Progress Report
1997

PDC
Parallelldatorcentrum

Progress Report
1997

KTH

Front Cover Picture: A computer image of the main computing resources at PDC. In the picture is shown counterclockwise from left, Strindberg, a 146 node IBM SP system, Selma, a Fujitsu VX/2 vector computer, the ImmersaDesk, a virtual reality projection system, Boye, an SGI Onyx2, and finally KALLSUP, a CRAY J932se. For more details see Section 1.4 on page 8. The ImmersaDesk is displaying results from an aircraft turbine simulation from Volvo Aero Corporation (VAC). This image was made by Calle Wilund, using the rendering package Alias Wavefront Studio 8.0 from SGI.

Parallelldatorcentrum (PDC)
Kungliga Tekniska Högskolan
S–100 44 Stockholm, SWEDEN
Telephone: +46–8–790 78 00
Telefax: +46–8–24 77 84
Email: info@pdc.kth.se
WWW: http://www.pdc.kth.se/

Publisher: Parallelldatorcentrum, © 1998
Editors: *Fredrik Hedman*, *Tomas Wilhelmsson*, *Ulf Andersson*
Typesetting & layout: *Fredrik Hedman*, *Tomas Wilhelmsson*
Printed by: *Ekblads, Västervik, April 1998*
ISBN 91-7170-246-6

Foreword

High performance computing in Sweden has reached a new level of maturity. A growing number of scientists find it natural to use high performance computing as an essential tool in their research. Both new research and commercial software are being developed for modern parallel architectures. PDC has played an important role in this process since the early 90s. One clear sign of the acceptance of parallel computing in the Swedish academic community is the increasing number of parallel computing centers. Today there are substantial parallel computing power not only at PDC but also in Göteborg, Linköping, Umeå and soon in Lund.

During the last year exciting research based on computations at PDC has been performed in many scientific fields. The sample of presentations in this Progress Report cover more than fifty projects. Most are in the basic sciences of physics, chemistry and biology. There are also important contributions from engineering science.

In 1997, HPDR and PDC signed a contract for the three years 1997–99. Unfortunately HPDR was eliminated in the last budget from the Department of Education. FRN has now taken on the responsibility of supporting high performance computing but it has of course many other responsibilities. We hope that this change in the form of funding will not reduce the focus and the continuity of support for leading edge computing in Sweden. It takes time to build a high quality computational infrastructure at a center.

In order to improve the service to the user community PDC has recently upgraded hardware and software. The development is briefly described in Chapter 1 and it follows the PDC strategy of protecting the valuable investment in all the programs developed by the research community.

PDC has also initiated a number of international contacts in order to better follow the rapid development in high performance computing. In a program from the European Commission a number of centers are set up to form a network of Technology Transfer Nodes. PDCTTN is the Swedish node and current activities is described in Chapter 2. The purpose of the initiative is to im-

prove the use of high performance computing and networking in small and medium size industries. Several interesting development projects have been started, based on cooperation between industry and academic groups. PDC has also learned from the interaction with the other European centers.

The leading academic supercomputer centers are located in the USA and the most progressive of those are the NSF centers. PDC has recently become an associate member to the partnership linked to the San Diego NSF Center. Globus is one communication project in which PDC participates together with several centers in the USA. A benefit from this cooperation will be software enabling a user to display high quality visualization at the home laboratory with data coming from interactive computation at PDC.

We feel that PDC has become a mature center which is respected internationally. We hope that what we have learned will benefit our users with improved service in many different ways and we are looking forward to future original research based on computations on the PDC facilities.

Björn Engquist
Director

Contents

1 Parallelldatorcentrum – PDC

This fifth progress report of Parallelldatorcentrum (PDC, Center for Parallel Computers) at Kungliga Tekniska Högskolan (KTH, Royal Institute of Technology) covers the activities of the center from June 1996 up until the end of 1997. A brief overview of the most important events at the Center during this period follows in Section 1.1. The PDCTTN is described in Chapter 2 and user projects are described in Chapters 3 through 8.

1.1 Background and Highlights

The Center was formed in January 1990 to act as a focal point and national forum for research on and use of parallel computers. Our goal is to stimulate research and disseminate information on the use of parallel computers.

This is achieved by providing high-performance parallel computers and expertise on their use to the technical and scientific computing community in Sweden.

The period covered in this report has been one of continued buildup and consolidation. At the end of October 1996 PDC was again evaluated by a committee appointed by HPDR. The members of the committee were: Professor Jan S. Nilsson, Knut and Alice Wallenberg's Foundation, Professor Risto Nieminen, Centre for Scientific Computing, Espoo, Finland, and Professor Odd Gropen, Departement of Chemistry, University of Tromsø, Norway. The overall impression of the committee was very positive and their final report summarized: "*... the committee concludes that PDC has in all respects met the criteria set out in the evaluation instruction.*"

Following this evaluation a new contract between HPDR and KTH for the period 1997–1999 was signed in May of 1997.

On the hardware side there has been a number of important events. The Fujitsu VX/2 was turned over to production in August of 1996. The Connection Machine CM200 (CM Bellman) was turned off in September 1996, after almost seven years of production. A visualization lab was set up with an ImmersaDesk 3D

vizualisation tool from Pyramid Systems as the main resource in October of 1996. The projected images on the ImmersaDesk are created by a Silicon Graphics Onyx2. The CRAY, owned by the KALLSUP consortium at KTH, and operated by PDC, was upgraded to a CRAY J932se in January of 1997. In December of 1997 a MaxStrat HiPPI disk was installed and attached to the CRAY and the Fujitsu VX/2. Finally, the IBM SP was upgraded to 110 nodes in October 1996 and at the end of 1997 to 146 nodes with 130 being the new 640 Mflop/s nodes.

1.2 Organization of PDC

PDC has a board, a scientific council and a director. P. G. Hedström, Corporate Technical Director of Electrolux AB is chairman of the PDC board, Professor S. Lennart Johnsson is chairman of the PDC scientific council and Professor Björn Engquist is the PDC director. Furthermore, there are three associate directors, four system managers, two system engineers, two program and application developers, one information officer and three secretaries. Affiliated with PDC there are also two researchers.

The associate directors each have a field of responsibility: Systems and Operations, Science and Customer Relations and Administration. The system managers have specific primary and secondary systems assigned to them where they act as respectively responsible or back-up. They report to the head for Systems and Operations. The program and application developers and information officer also have specific tasks and allocated to them. They report to the head of Science and Customer Relations.

To fulfill its major missions as a service provider of high performance computing and visualization, PDC has implemented a production organization that takes care of incoming user questions and the day-to-day running of the hardware resources.

User questions are primarily handled by the PDC help desk that is open Monday–Friday, 08:00–17:00. This service will respond to user requests made by email, phone and visits. All incoming user questions and other problems are logged in a problem tracking system. It is staffed by a group of operators that are also students at either KTH or Stockholm University. The group supervision is the responsibility of one of the permanent staff members. This task rotates in round robin fashion every two weeks.

Hardware resources are monitored regularly during the day all days of the week. This is done by the monitor person during off office hours and week ends and in collaboration with the operators during office hours. In case a serious problem occurs, the person responsible for monitoring can call the on-call expert for assistance. Both monitoring and on-call duties rotate in round robin fashion every week.

Corp. Tech. Dir., P. G. Hedström	Chairman, PDC Board
Prof. S. Lennart Johnsson	Chairman, Scientific Council
Prof. Björn Engquist	Director
Fredrik Hedman	Associate Director
Gert Svensson	Associate Director
Dr. Per Öster	Associate Director
Harald Barth	System Manager
Jonas Engström	System Manager
Johan Ihrén	System Manager
Lars Malinowsky	System Manager
Andreas Cedborg	System Engineer
Johan Danielsson	System Engineer
Peter Carlsson[a]	Information Officer
Tek. Lic. Nils Jönsson	Application Specialist
Anders Ålund	Application Specialist
Marina Backer Skaar	PDCTTN co-ordinator
Dr. Erik Aurell	Scientist
Dr. Mikhail Dzugotov	Scientist
Berith Bodelsson	Secretary
Britt Olsson	Secretary
Britta Svensson	Secretary

[a] Left PDC in November 1997.

1.3 Cost of Operation and Staff

The operational cost, including staff and investments, has during 1997 been covered by the Swedish Council for High Performance Computing, HPDR, and the Royal Institute of Technology.

Income 97	
HPDR	35 035 kSEK
KTH	5 639 kSEK
Other	2 401 kSEK
Reserve from 96	4 209 kSEK
Total	47 284 kSEK

Expenditure 97	
Operational Costs	17 416 kSEK
Investments[a]	25 972 kSEK
Reserved for future	3 896 kSEK
Total	47 284 kSEK

[a]Includes future costs for maintenance.

1.4 Hardware Resources

Networking

PDC is connected directly to SUNET via a dedicated FDDI connection. Internally, PDC has implemented a high-speed network infrastructure to support large-scale I/O and enable computational clusters of PDC systems. An Ascend/Netstar Gigarouter is the heart of the network, with a HiPPI connection to large systems and FDDI connections to various networks. All large systems are connected to a HiPPI network (800 Mbit/s) via an Essential HiPPI Switch. Other systems, such as AFS file servers, are connected to a number of FDDI (100 Mbit/s) rings separated by a Digital Equipment FDDI GigaSwitch.

Current Hardware

- Strindberg, a 146 node IBM SP, 130 T4 nodes, 16 wide nodes and around 720 Gbyte user available disk. The peak perfor-

mance of the whole computer is 87.7 Gflop/s and the total memory is 47.6 Gbyte.

- KALLSUP, a CRAY J932se managed by PDC for the KALLSUP consortium at KTH. Peak is 6.4 Gflop/s, total memory 8 Gbyte, and total disk 225 Gbyte.
- Selma, a vector computer from Fujitsu, with 2 processors, providing 2.2 Gflop/s and 2 Gbyte memory each. Equipped with 32 Gbyte SCSI and 60 Gbyte high performace HiPPI disk. System will be upgraded with one more processor to a total of 6.6 Gflop/s and 6 Gbyte memory in April, 1998.
- Boye, an SGI Onyx2 computer equipped with two Infinite Reality Graphics Pipelines and eight R10000 CPUs. The machine contains 2 Gbyte memory and 120 Gbyte disk.
- A projection-based system called ImmersaDesk enables 3D group viewing in a virtual reality environment. The ImmersaDesk is connected to the Onyx2 computer.

Mass storage

An IBM 3494 Tape Library Dataserver with four IBM 3590 Magstar tape drives. It can store up to 12 Tbyte of data. The HSM system currently runs on the CRAY J932se. HSM functionality is provided by the Data Migration Facility (DMF) from SGI/CRAY.

1.5 Events and Educational Activities

A large number of seminars, workshops, classes and conferences have been held at PDC during the period. In the tables below a selection of the most important events is given. In addition to this, the computing resources at PDC have been used in graduate and under-graduate courses at KTH, CTH and, Högskolan Gävle-Sandviken.

Event	Date
PDC Conference: Future Directions in High Performance Computing	971218–19
Meet Deep Blue Jr. (Deep Blue Jr. *vs.* Swedish Junior Class Chess Champion)	971017
Transport Processes in the Atmosphere and the Ocean (TAO), Workshop on diffusion (together with European Science Foundation)	971006–10
Computational Chemistry on Fujitsu Vector Parallel Computers	970924
PDC/PSCI Workshop on Parallel Libraries and Applications	970618–19
PDC Conference: Software for Parallel Computing	961216–17
Workshop on Computational Electro Magnetics	961211

Course	Date	Students
PDC Summer School: Introduction to High Performance Computing	Aug 97	45
Parallel Programming with MPI (at Högskolan Gävle-Sandviken)	May 97	30
Optimization on CRAY VPP systems	Mar 97	15
SGI CRAY from Fortran 77 to Fortran 90	Mar 97	12
Introduction to Parallel Computing on the IBM SP	Mar 97	7
SGI Origin 2000 Porting and Optimization	Apr 97	9
Introduction to Parallel Computing on the IBM SP	Apr 97	14
Introduction to Parallel Computing on the IBM SP	May 97	8
Optimization on CRAY VPP systems	Jan 97	11
Optimizing Application Code on CRAY VPP Systems	Aug 96	16
PDC Summer School: Introduction to High Performance Computing	Aug 96	37

Umeå collaboration

With the aim to improve the overall situation for HPC users in Sweden, PDC has established a collaboration with HPC2N at Umeå University. The objective is to improve both centers from the users' points of view by *e.g.*, streamlining applications for resources at both centers. As a result, the two centers now have common deadlines for applications, require similar information in the applications and also coordinate the granted computer time.

Another notable experiment is co-scheduling of resources between the IBM SP at HPC2N and the one at PDC. This effort showed the feasibility of scheduling large parallel job across both machines using 164 processors (see Section 1.6).

Globus project and SuperComputing97

The globally growing demand of easy access to large scale computing facilities is a challenge to computer science to further develop the basis for supercomputing applications. PDC is participating in one such project, Globus, conducted by Argonne's Distributed Supercomputing Laboratory and Information Sciences Institute, USC. For more information see `http://www.globus.org/`

The overall objective is to lay the groundwork for tomorrow's "High-Performance Computational Grids", in which access to supercomputing resources is consistent, dependable, and pervasive. Globus addresses the issues relating to security, communications, resource management, quality of service, programming methodologies, and tools. Important is to deploy applications, so as to allow practical exploration of the computational grid concepts.

In the fall of 1997, a testbed, Globus Ubiquitous Supercomputing Testbed (GUSTO), was set up and demonstrated during the SC97 exhibition in San José. The computational resources of 17 sites was gathered of which two were located outside the USA, Parallelldatorcentrum (PDC) and Rechenzentrum Garching der Max-Planck-Gesellschaft. This was the largest computational grid ever constructed with 330 computers, and 3600 processors, providing an aggregated peak performance of 2 Tflop/s. PDC contributed to this demonstration with the upgraded IBM SP Strindberg and an MPI based CEM application (see Section 5.1).

1.6 Resource Utilization and Scheduling

Currently, all scheduling on the IBM SP at PDC is performed by PDCs derivate of the EASY scheduler. After investigating several schedulers we found that our objectives were best met by the Argonne EASY Scheduler. It had fairness, simplicity, and efficiency as primary design goals which was well in line with our objectives. The original EASY was implemented for a homogeneous system. The combination of a system growing organically, such as our IBM SP, and the ever changing demands from users has encouraged us to develop EASY beyond the homogeneous platform and adding new functionality. Since 1994, when we first started to use EASY, we have incrementally modified the code leading to the version currently in use at PDC. Among the capabilities we have improved or added are recursive backfill, time-lock and mixed job resources.

All co-scheduled jobs are submitted to PDCs regular job queue, where HPC2N nodes show up as a special privileged node type (U). Co-scheduling in this context briefly means that an authorized user can submit jobs to both HPC2Ns and PDCs SP systems from a single point of control. It is also possible to submit single large jobs that runs on the two systems as a single job. Co-scheduling is enabled at the HPC2N site simply by not starting any jobs on a specified range of nodes for a particular period of time.

As of August 1997, successful experiments with large job scheduling has been performed; a 164-node test job has been started successfully.

The basic security and file system requirements has been addressed. A user with a synchronized account (same login and uid) can login across the SP systems and access his/her home directory in AFS or DFS at both sites.

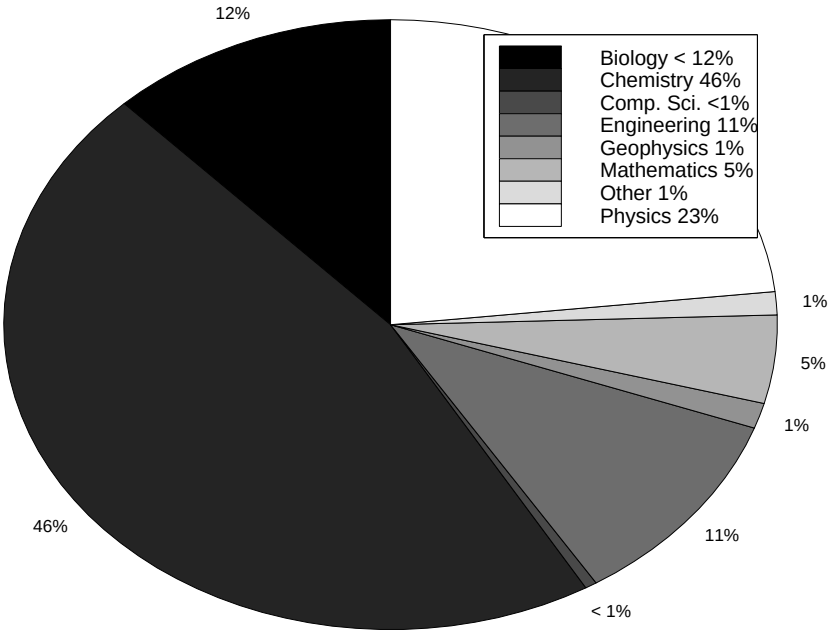

Figure 1.1. Percentage of total used computer time on the IBM SP for the different scientific disciplines during Q3–Q4 1997.

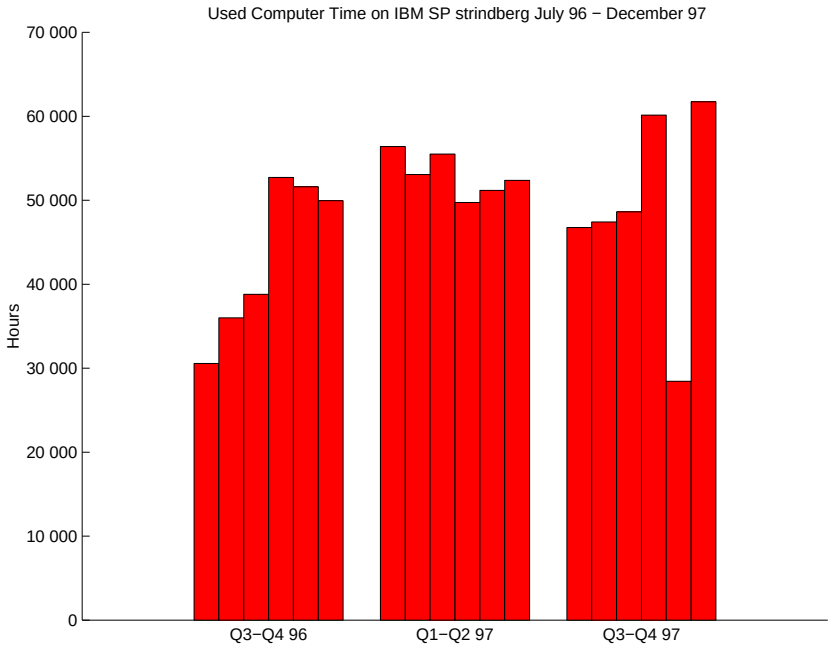

Figure 1.2. Used computer time per month on the IBM SP during the second half of 1996, first half of 1997 and second half of 1997. During November 1997 Strindberg was taken out of production for 12 days due to the major upgrade of its nodes and high-performance switch.

Figure 1.3. Percentage of total used computer time for the different Swedish universities. For each university the numbers are presented by period (Q2–Q3 96, Q1–Q2 97 and, Q3–Q4 97) from top to bottom. The label *free* is low priority jobs running free of charge and allocating otherwise unused computer time.

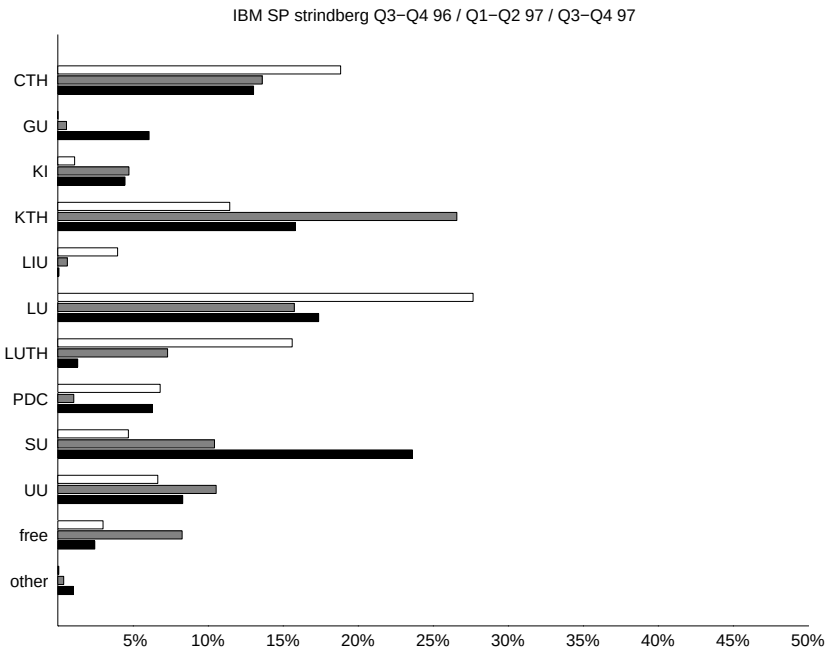

2 PDC Technology Transfer Node – PDCTTN

In 1997, PDC was selected a Technology Transfer Node (TTN) within the ESPRIT programme HPCN-TTN, initiated by the European Commission. The initiative started with the objective to improve industrial competitiveness across a wide range of industries through promotion of High Performance Computing and Networking (HPCN). The initiative specifically targets small and medium size organisations, which can now afford low-cost powerful systems made out of commodity components. Substantial emphasis is placed on novel HPCN applications to problems where it was previously too expensive or immature.

In order to encourage new users to adopt HPCN technology, a network of Technology Transfer Nodes (TTN) is established. Today there are 20 TTNs around the European Community (see Figure 2.1) where PDC was selected being a TTN in the beginning of 1997. The involvement is mainly co-ordinating groups of projects (activities) with important industrial applications but also involves demonstrations at industrial conferences, dissemination of publicity material, organisation of seminars and workshops, and publication of magazine and journal articles. The focus of all activities is on satisfying business requirements, rather than merely promoting technology.

The contract period for PDCTTN is April 1997 to April 1999 (with a possible extension until April 2000). By March 1998, there are five activities running and one under process to start — each one involving three partners; a small/medium size enterprise (end-user), a technology provider and an HPCN expert. They are:

- Simulation of flow pumps in paper industry (SIMMILL)
- Use of High Performance Computing in video and special effect productions (VIDEOGRAPH)
- Design of Fan blades (OPTIBLADE)
- Heat control in buildings (IDASTAR)

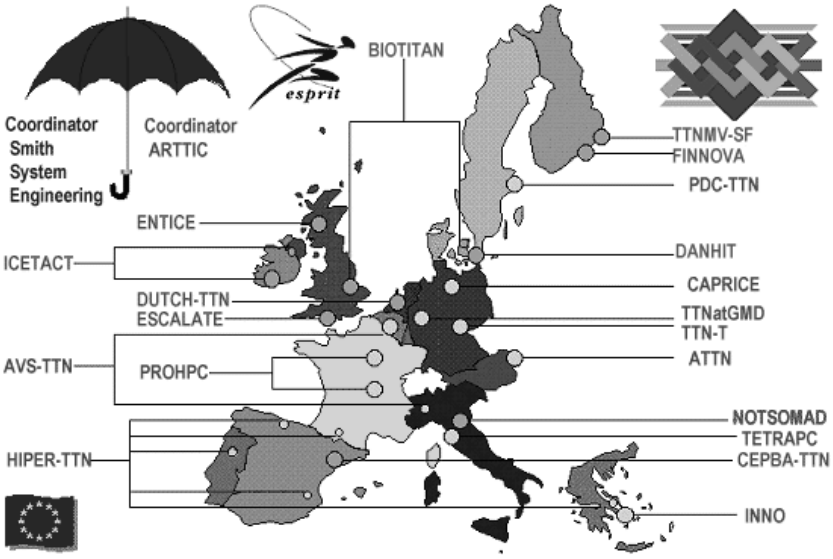

Figure 2.1. Locations of the European TTN network.

- Injection moulding optimisation in plastic industry (OPTIMOM)
- 3D photo modelling for architects and the building industry (3Demo)

During 1998 and onwards the TTN network including PDCTTN will concentrate on disseminating results. There are a total of around 200 activities from different industry areas in Europe and by focusing on a few well defined segments (see below) the aim is to create awareness about HPCN.

PDCTTN is appointed leader of all dissemination work towards European machinery industry and will therefore concentrate on creating awareness and disseminate results from relevant activities. Other important industry areas pointed out in the TTN network are; Aerospace, Automotive, Construction, Environment and transport, Finance, insurance and retail, Food, agriculture and fisheries, Forging, casting and moulding, Machinery, Medical, Pharmaceutical and chemical, Quality control and inspection, and finally, not to forget Security. In Europe, a lot of work will be directed towards these segments, in order to promote HPCN as a tool to improve industrial competitiveness.

More information is available from the PDCTTN co-ordinator Marina Backer Skaar or at `http://www.pdc.kth.se/pdcttn/`

SIMMILL

SIMMILL will demonstrate the use a materials model for non-Newtonian fluids in a CFD simulation. By implementing the materials model with a commercial CFD code it is expected to give quantitatively good results in simulations on real production processes. The ability to simulate non-Newtonian fluids is important to process industry in understanding and avoiding *e.g.*, "clogging" effects of suspensions. HPC resources in combination with simulation techniques for non-Newtonian fluids will have an impact on the whole process industry by enabling new and cost effective manufacturing methods. The end user is Kvaerner Pulping AB, a manufacturer of machines for pulp industry. The technology provider, Prosolvia AB will provide the knowledge and capability to perform CFD simulations and PDC, the HPCN partner will contribute with expertise in the field of non-Newtonian fluids.

VIDEOGRAPH

This demonstration is about the use of high performance computing in the video and animation special effects production business. Among customers such as television studios and film industry there is a strong demand for being able to produce complicated graphics effects fast to satisfy tight deadlines. Also, it is essential to continue using Adobe After Effects, a popular software package for adding graphics effects to film and video. This can be realised by porting Final Effects, "plug-in" effects to a parallel computer connected to a Apple Macintosh or a PC running Adobe After Effects. Cycore Computers AB, a Swedish SME of 10 people own the current code owner to Final Effects and is the industrial partner in this proposed action. The end-user is FilmEffekt, a a modern post-production company for both film and video in Norway. The HPCN expert is PELAB (Programming Environment Laboratory, Department of Computer and Information Science, Linköping University).

OPTIBLADE

The project demonstrates the feasibility of HPC parametric optimisation techniques for the design of fan and propeller blade profiles. A prototype will be developed called OPTFLO; an aerodynamic shape optimisation program by combining the parallel

flow solver NSMB with the CADOE parametric optimisation software. With better blade shapes for fans, propellers, and turbines, power consumption, motor size, noise, application regimes, and serviceability can all be improved. OPTFLO tries to reduce the number of flow simulations necessary for a design. The computational resources required are still large, and availability of cost-effective high performance computers is a prerequisite. The NSMB flow solver used is parallelized and scales up to more than 100 processors for large problems. Parallel CFD is complemented by the unique CADOE parametric solution technique, which offers efficient use of parallel computers in exploring the parameter space for optimisation.

IDASTAR

This demonstration concerns the use of HPCN technology in the construction and building industry. The business objective is to give the building industry a tool to do more detailed simulations on larger and more complex building models. This involves a more frequent and widespread use of simulations in designing and re-engineering buildings and subsequently to more optimal building designs. The most obvious results are better indoor climate and a reduction in the energy demand for heating, cooling and ventilation. The technical objective is to develop a parallel, distributed version of the IDA Solver, a state-of-the-art solver for systems of differential-algebraic equations.

OPTIMOM

The overall objective is to show the technical and economical benefits of High Performance Computing in Computer Aided Design, HPC/CAE technology for designing plastic parts as well as manufacturing injection moulded plastic products. A consortium with end-users from Finland, Norway and Sweden is formed by Saloplast OY, Dynoplast AS and PB Option AB. The technology providers are Cape Technology AB and the Department of Polymer Technology, KTH, where PDC, act as the HPCN expert.

3 Applications in Biology

3.1 Molecular Dynamics Simulations of Lipid Bilayers

Olle Edholm, Lars Sandberg
Department of Theoretical Physics, KTH
Aatto Laaksonen
Division of Physical Chemistry, Arrhenius Laboratory,
Stockholm University

Phospholipids are the essential components of biological membranes. In order to understand the function of membranes, it is necessary to have a knowledge of the structure and dynamical behavior of the lipids at atomic detail. Computer simulation techniques are a natural choice to achieve this goal. However, the understanding of molecular mechanisms lipid bilayers for the structure and dynamics is still a challenging problem to the community working with molecular dynamics simulations. The problem requires fairly large systems (the order of 10 000 atoms and upwards), long simulation times (order of nanoseconds) and some properties are extremely sensitive to details in the simulation protocol and the force field applied. A typical simulation of this type requires about 40 CPU-days of computing time on a fast workstation. If one needs to do several runs varying parameters in the force field or simulation protocol, one easily ends up with about a CPU-year of computing time on a fast workstation.

Doing several runs requires about a CPU-year of computing time on a fast workstation

The present work takes it starting point in the previous simulations [Berger *et al.*, 1997]. In that study a careful calibration of the Lennard-Jones parameters of the fatty acid chains of the dipalmitoylphosphatidylcholine (DPPC) molecules was done against experimental data for long chain liquid hydrocarbons. This gave good agreement with experiment for many parameters. Especially this work constituted better agreement with experiment for the volume density of lipid bilayers. (See Figure 3.1) However, this model is still crude. It uses a united atom description of the hydrocarbon groups of the lipids, a fairly short cutoff for the electrostatic interactions and the water model that although well tested and much used still could be improved. There are further still no consensus among various groups doing lipid simulations about the

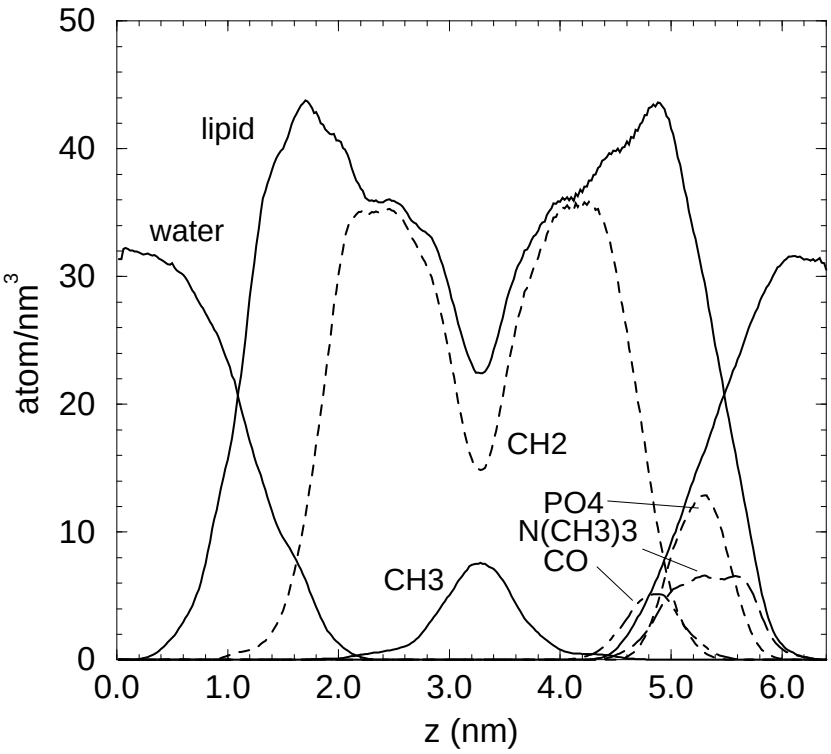

Figure 3.1. Profiles across the bilayer of the total lipid density, the water density, and the densities of certain lipid groups.

fractional charges for the different atoms in the lipid head group. Still that model gives good results for most of the quantities that are accurately available from experiments. The necessity for an improvement of the lipid simulations stems from that structure and dynamics in the head group region is very sensitive to several properties of the simulation protocol, as fractional charges, choice of cutoff and water model. Monitored through one variable, this is most clearly seen from the variation of the electrostatic potential across the membrane. The simulations that yet only have been started on the SP2 machine at the PDC aims at a systematic test of some properties of these lipid bilayer models and an improved description of especially the electrostatic part of the problem. (See Figure 6.5 on page 111)

The software is a state of the art molecular dynamics program [Lyubartsev and Laaksonen, 1997] developed and tested on simulations of smaller molecules. It has from the beginning been developed to use message passing techniques for efficient parallelization. Main features include the use of a double time step

algorithm to separate fast and slow motions and the inclusion of an Ewald summation to treat long-range coulombic interactions. The speedup is almost linear in the number of processors up to at least 32 processors. This makes simulations possible that could not have been done on single workstations.

A state of the art molecular dynamics program scaling almost linearly up to at least 32 processors

3.2 A Quantum Chemical Study of the Catalytic Mechanism for Ester Hydrolysis in Serine Hydrolases

Tore Brinck, Ching-Han Hu
Physical Chemistry, KTH
Karl Hult
Department of Biochemistry and Biotechnology, KTH

Serine hydrolases are important enzymes in many biological systems due to their unique ability to selectively catalyze the hydrolysis of amide and ester substrates. Serine proteinases and serine esterases are two important subclasses of the serine hydrolases. The main physiological function of the proteinases is to hydrolyze peptide bonds in proteins, while esterases break ester bonds, *e.g.*, in lipids. A common feature of most serine hydrolases is that the active site contains three residues, the catalytic triad (Asp-His-Ser), which play a key role in the catalytic process. In addition, the so called oxyanion hole, which consists of two or more hydrogen donating groups, is known to be important for the catalytic activity. The purpose of the oxyanion hole is to stabilize the negatively charged carbonyl oxygen that appears in the tetrahedral intermediates and transition states by hydrogen bonding.

The objective of the current work has been to study the catalytic mechanism of ester hydrolysis in serine hydrolases using *ab initio* and density functional theory (DFT) methods. For this purpose, a model system was constructed which contains the key components of the enzymatic reaction center (see Figure 3.2). The Asp, His and Ser residues of the catalytic triad were modeled by formate anion, imidazole and methanol, respectively. The oxyanion hole was represented by two water molecules. Finally, methyl formate was used as the substrate. Using this model system, we have calculated the full reaction pathway, including the geometries and energies of the relevant intermediates and transition states [Hu *et al.*, 199X]. This has, for example, involved optimizing transi-

Very few transition state optimizations on systems of this size have previously been reported

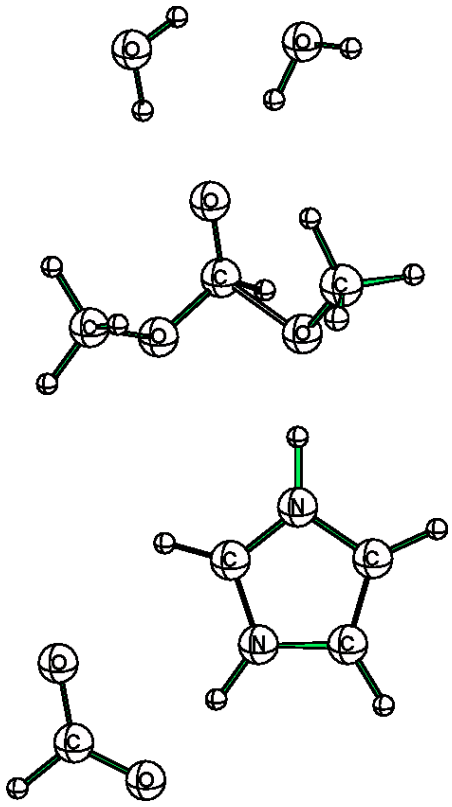

Figure 3.2. The model system for enzyme hydrolysis in serine hydrolases represented by the DFT-B3LYP/6-31+G* computed transition state of the acylation step.

tion states at the *ab initio* HF and DFT-B3LYP levels of theory for systems containing up to 33 nuclei and 322 contracted basis functions. Very few transition state optimizations on systems of this size have previously been reported. Single point energies at the *ab initio* MP2 level of theory have been computed for the optimized geometries.

In excellent agreement with the results of measurements

Our computed activation energies for the different steps of the catalysis are in good agreement with experimental data. This indicates that the selected model system gives a good representation of the enzymatic reaction center and that the computational level is appropriate. We have also studied the catalytic effects of the Asp residue and the oxyanion hydrogen bonds by performing calculations on systems where the models for these groups have been left out. Our results show, for example, that the Asp residue reduces the activation energy by approximately 6 kcal/mol. This is in excellent agreement with the results of measurements on enzymes where this residue has been removed by site-directed mutagenesis.

Finally, we have compared our computed transition state structure for the acylation step with the crystal structure of the reaction center in chymotropsin (a serine proteinase) with a bound transition state inhibitor. There is a very good agreement between the two structures as can be seen from Figure 6.7 on page 112. Since our geometry optimization was conducted without any geometrical constraints, this supports the generally accepted hypothesis that enzymes are optimized towards transition state stabilization.

3.3 MD Simulations of Escherichia Coli Thioredoxin

Robert Garemyr, Arne Elofsson
Department of Biochemistry, Stockholm University

Proteins are the most complex biological macromolecules both to structure and function. The structure of proteins can be determined by X-ray crystallography or NMR, but the unique function of proteins do not only depend upon their structure as the dynamic features of proteins are of great importance. Even if experimental methods can give some information about the dynamics of a protein, it is necessary to use theoretical methods to fully understand the dynamics of proteins.

The most commonly used method to study protein dynamics is Molecular Dynamics simulations (MD). The fundamental idea of MD is to use Newtons equations of motion for every atom in the molecule, treating each atom as a classical particle, ignoring all quantum effects. The energy function, or its gradient *i.e.*, the force field, used to study proteins normally consists of two parts, the bonded and the nonbonded part. The bonded interactions include all interactions between atoms that are covalently bound to each other, this includes energy terms for bond length, bond angles and torsion angles. The potentials for these terms are usually taken to be harmonic. The nonbonded interactions normally includes a van der Waals term and an electrostatic energy term, plus in some force fields a term for hydrogen bonds. As the number of nonbonded interactions is proportional to the square of the number of particles, whereas the number of bonded interactions are equal to the number of particles, most of the computational burden lies in computing the former interactions. To speed up the MD-simulations the nonbonded interactions are most often neglected beyond a chosen cutoff radius. However, simply

truncating long range interactions terms in MD-simulations will introduce nonphysical artifacts, *i.e.*, an effective impulsive force resulting from the discontinuity in the gradient of the potential. In this study, as well as most current simulation studies, we use a bath of explicit solvent molecules, and for dipolar systems like water a simple truncation of the nonbonded interactions may lead to the following scenario: molecules crosses the cutoff boundary, then reorients without "feeling" each other, and then recrosses the boundary with higher energy [Tasaki *et al.*, 1993]. For this reason smoothening functions are often used to make the nonbonded interactions go to zero in a continuous fashion. This can be done on an atom by atom or on a group by group basis, where the latter one avoid the problem of truncating dipoles. Two of the most widely used smoothing schemes are the "switching" and "shifting" functions, [Loncharich and Brooks, 1989], implemented in the CHARMM molecular mechanics program [Brooks *et al.*, 1983].

We have chosen to study thioredoxin since it is a small and well studied protein of a rather small size. The method used to incorporate water is the stochastic boundary method. This method places a watersphere around the protein and treats the outer water layer with Langevin dynamics, *i.e.*, trying to reproduce interactions with water outside the sphere. The water molecules are kept in place by a potential calculated from interactions with water outside the sphere.

All simulations were performed using the CHARMM program, simulating for 250 ps using the last 150 ps collecting data. The simulation models tested the following parameters:

- constant and linear distance dependent dielectric
- different cutoff radii and one without cutoff
- smoothening by using a switching function or a shifting function on atom by atom or group by group basis.

The parameters used to judge the various models are the following:

- RMSD from the crystal structure.
- a comparison between the experimentally obtained temperature factors and the rms fluctuatons for each residue from the simulations, see Figure 3.3.

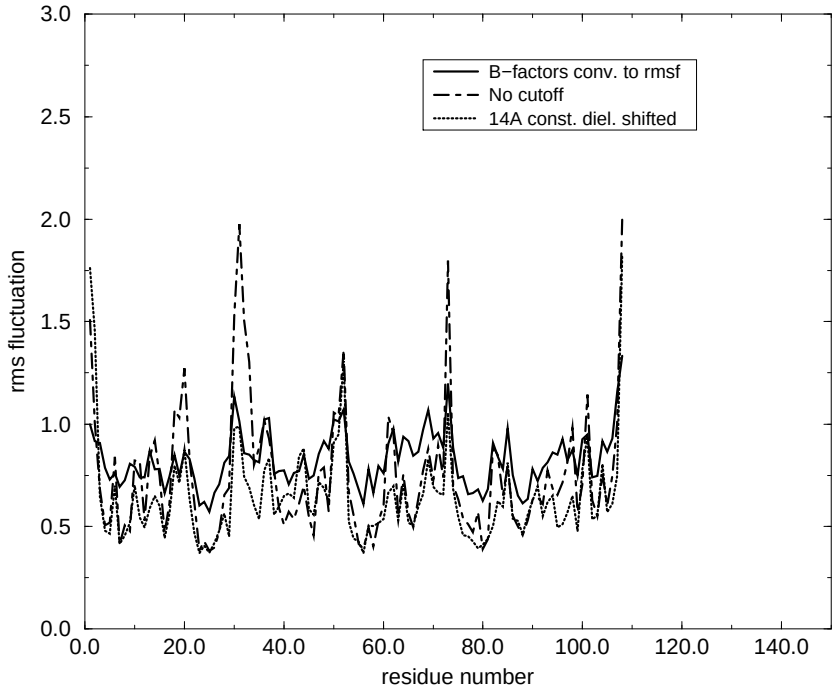

Figure 3.3. Comparison of the rms fluctuations for the model with no cutoff, the one with a 14 Å cutoff (constant dielectric and smoothening by the shifting function) and the experimentally obtained B-factors converted to rms fluctuations.

- the time development of the accessible surface area and its average value.

The simulation without cutoff is of course very computationally burdensome, therefore we have chosen to perform this simulation on the IBM SP-2 using a parallel version of CHARMM.

3.4 Optimal Plasmid Copy Number Control

Johan Paulsson, Måns Ehrenberg
Department of Molecular Biology, Uppsala University

Plasmids are small gene clusters separate from the chromosome with independent replication control and inheritance mechanisms. Plasmids are popular model systems for replication control of chromosomes or viruses [Paulsson *et al.*, 1998], but are also very common both *in vivo* (a common cause of antibiotic resistance in bacteria) and in biotechnology. Since plasmids must compete with the cell for ATP, enzymes etc., they inevitably become a metabolic burden and reduce the growth rate of the host. If plasmids cannot compensate by conferring some selective advantage, plasmid-free

cells will eventually outgrow plasmid-containing cells in the course of evolution. Plasmids can also be lost directly if one of the daughter cells fails to receive a plasmid copy at cell division. This means that there is a selective pressure on plasmids to obtain a high segregational stability at a minimal metabolic burden. To understand the evolutionary strategy of plasmids it is therefore necessary to relate the molecular details of replication control to both segregational stability and metabolic burden [Paulsson and Ehrenberg, 1998].

Plasmid ColE1 is perhaps the most studied replicon of all and is commonly used as a cloning vector in bioengineering. There are two control elements in replication control: RNA I and RNA II. Constitutive transcription of RNA II starts upstream of the replication origin (*ori*) and proceeds through *ori*. In the absence of RNA I, RNA II forms an RNA-DNA hybrid (at the *ori* of the plasmid from which it was transcribed) that acts as a primer for plasmid replication. RNA I is antisense to RNA II and is constitutively transcribed from the opposite strand and subsequently released in the cytoplasm. Replication priming by a cis-acting RNA II can be inhibited by a trans-acting RNA I during a certain period in primer formation called the inhibition window, extending approximately from base 110–360 in the coding region for RNA II. If RNA I forms a duplex with RNA II in this window, the conformation of RNA II changes and the replication primer cannot form.

Segregational stability

Segregational stability is quantified by *P(loss)*, the probability that a plasmid-containing cell gives rise to a plasmid-free segregant at cell division. When the probability distribution of plasmids at the end of the cell cycle is known, *P(loss)* can be easily calculated [Paulsson and Ehrenberg, 1998]. To predict the plasmid distribution, the different chemical reactions involving RNA I and RNA II have been modelled as master equations governing the stochastic process of plasmid replication in a growing cell population. This set of differential equations has been integrated over many cell cycles to obtain self-consistent initial conditions. The code was written in Fortran 77 and in some cases we were forced to use a grid size of 200×1000, each node corresponding to a differential equation. Segregational stability can be increased either by increasing the average copy number or by reducing copy number variation. A

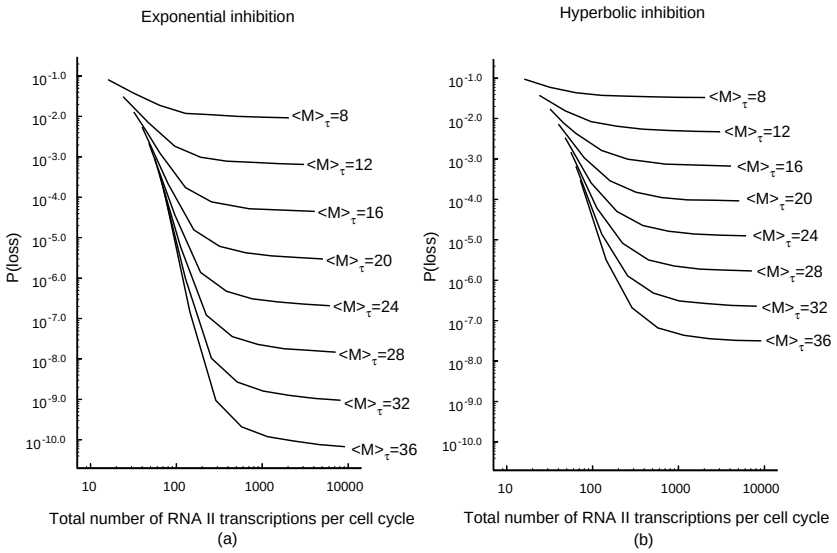

Figure 3.4. *P(loss)* as a function of the total number of RNA II transcriptions per cell cycle for different average copy numbers and for exponential **(a)** and hyperbolic **(b)** inhibition. All curves were obtained for the same set of rate constants, with the normalized RNA II transcription frequency varying from 2 to 256. The total number of RNA II transcriptions per cell cycle depends on both the normalized RNA II transcription frequency and the average copy number at the end of the cell cycle.

higher average copy number inevitably brings a higher metabolic burden in terms of plasmid replication. An efficient copy number control that reduces copy number variation requires a sensitive regulation mechanism and rapid turnover of the regulatory elements and hence also imposes a metabolic burden on the host. The quality of copy number control depends on how sensitively the replication frequency responds to changes in RNA I concentration and the relation between plasmid and RNA concentrations. Two different inhibition mechanisms have been suggested in the past, hyperbolic inhibition, corresponding to a single rate limiting step in the inhibition process and exponential inhibition, corresponding to a saturating number of rate limiting steps. When plasmid and RNA I concentrations are proportional throughout the cell cycle, *P(loss)* depends on the average copy number, the inhibition mechanism and the transcription frequency of RNA II (see Figure 3.4). Exponential inhibition was found to reduce copy numbers variation much more efficiently than hyperbolic inhibition. Clearly, the optimal strategy to increase segregational stability depends on the growth rate reductions associated with replication versus transcription. Efficient copy number control requires that plasmid and RNA I are approximately proportional. If free RNA I is not rapidly degraded, the RNA I concentration will not be "up to date" with the current plasmid concentration, drastically decreasing segrega-

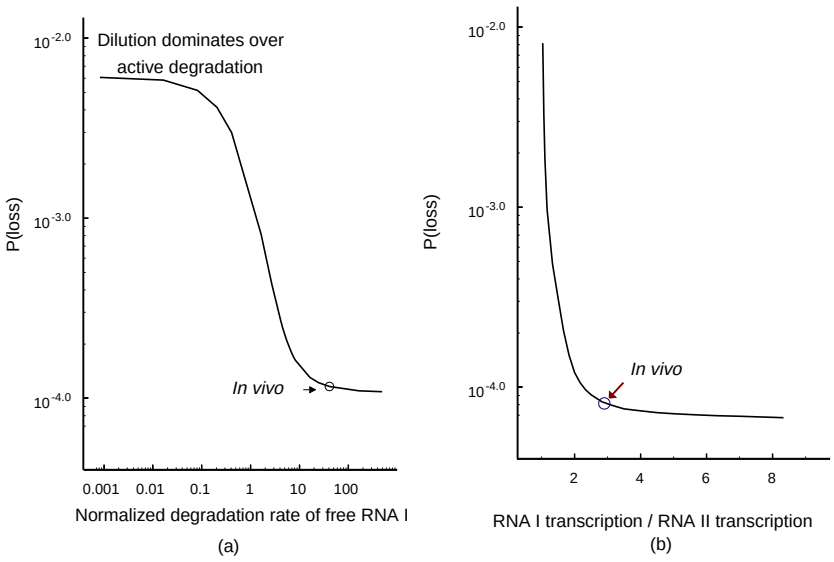

Figure 3.5. *P(loss)* dependence on RNA I turnover for exponential inhibition. The average plasmid copy number was kept at 16 in the simulations and all other rate constants were chosen from experimental estimates of in vivo data. **(a)** *P(loss)* as a function of the normalized RNA I degradation rate constant. The *in vivo* estimate of the RNA I degradation rate constant is marked. **(b)** *P(loss)* as a function of the ratio between the transcription frequencies of RNA I and RNA II. The *in vivo* estimate of this ratio is marked.

tional stability (see Figure 3.5(a)). RNA I is also degraded after duplex formation with RNA II. If RNA I is not transcribed much more frequently than RNA II, there will be large random fluctuations in the number of RNA I molecules in the cell, leading to a randomised copy number control and low segregational stability (see Figure 3.5(b)).

Optimality

New aspects of molecular biology ... gives the model predictive rather than just descriptive powers

ColE1 plasmids can provide the host cell with antibiotic resistance or code for systems that selectively kill plasmid-free cells. In all situations where plasmids are essential for the survival of the host, the "net" growth rate of the plasmid-host system is reduced by the metabolic burden of plasmids, but also by plasmid loss since it kills one of the daughter cells. Under such conditions, there is an optimal set of rate constants that depends on both types of growth rate reductions, maximising the net growth rate of the plasmid-host system. Computer simulations predict threshold values in the rate constants for turnover of RNA I and RNA II such that an increase has virtually no effect on *P(loss)* but a decrease can be devastating. However, to establish the relevance and impact of these thresholds on the behaviour of ColE1 *in vivo*, a full cost-benefit analysis must be carried out by optimising the net growth rate, keeping RNA I and RNA II turnover rate

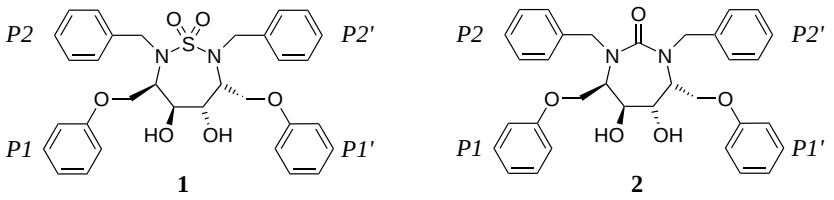

Figure 3.6. Seven-membered cyclic sulfamide (left) and urea derivatives (right).

constants and average copy number as free parameters. This way, qualitatively new aspects of molecular biology, only available using quantitative methods, link operational efficiency and energy costs in a way that gives the model predictive rather than just descriptive powers. A deeper understanding of the regulation of plasmids could also eventually lead to more efficient ways of dealing with the plasmid dependent problem of antibiotic resistant bacteria.

3.5 Sulfamide Containing HIV-1 Protease Inhibitors: Development of Force Field Parameters.

Wesley Schaal, Anders Hallberg, Anders Karlén
Organic Pharmaceutical Chemistry, Uppsala University

Guided by the knowledge of the mechanism of action of HIV-1 protease, which is an aspartyl protease, a large number of transition state based analogues exhibiting high inhibition constants have been designed. These inhibitors retain substantial peptide character and the difficulties in combining a high enzyme binding affinity with oral bioavailability is well recognized. Considering that peptide-based inhibitors in general are rapidly metabolized and more importantly are poorly absorbed has led to an intensive search after nonpeptidic inhibitors.

We have synthesized C2 symmetric cyclic urea and sulfamide derivatives from L-mannoic gamma-lactones and D-mannitol to be used as inhibitors of HIV-1 protease, [Hultén *et al.*, 1997, Bäckbro *et al.*, 1997]. Among these, sulfamide 1 and urea 2 (see Figure 3.6) inhibit the protease with Ki values of 19.1 and 12.2 nM, respectively.

X-ray analysis of the complexes of 1 and 2 with the protease, performed by Docent Torsten Unge (Uppsala University), showed that these inhibitors bind in unexpectedly different conformations. The urea 2 binds symmetrically (as expected by comparison with other cyclic urea HIV-1 protease inhibitors [Lam *et al.*, 1994])

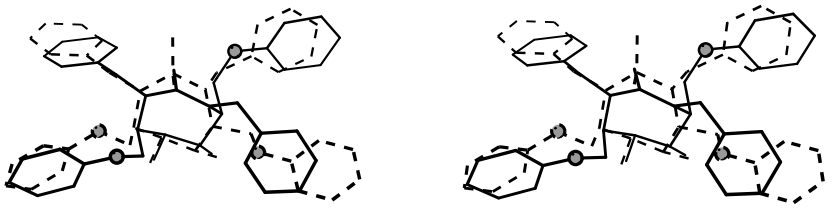

Figure 3.7. Stereodrawing comparing the x-ray conformations of inhibitors 1 (dashed) and 2 (solid). The P1/P1' oxygens are marked on each.

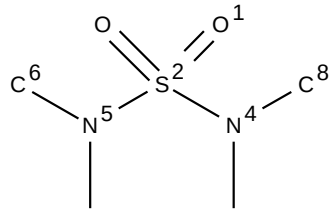

Figure 3.8. Model compound 3 which was used for *ab initio* calculations.

while sulfamide 1 diplayed an unpredicted, unsymmetrical mode of binding. A superimposition of the bound conformations of 1 and 2 in the protease revealed that the P1' of 1 corresponds to the P2' of 2 and vice-versa (see Figure 3.7). This finding has a strong implication for the future design of sulfamide analogues since a different structure-activity relationships can be expected for 1 as compared to 2.

We are studying the binding conformation of 1 in more detail since it has consequences for the future design of compounds in this series. More specifically we are investigating if the unexpected binding mode of 1 could have been predicted from docking studies of the inhibitor in the active site of the protease. It would be very useful to understand the generality of this conformational flip and whether or not it could be controlled through appropriate functionalization.

Due to the size of the problem, we have chosen to use molecular mechanics calculations. We have worked out a Monte Carlo (MC) docking protocol using the AMBER* force field in BatchMin of the MacroModel package at PDC.

The AMBER* force field lacks specific parameters for the sulfamide moiety of 1. Since the only difference between 1 and 2 is in the replacement of a sulfamide for a urea, generation of high quality parameters around the sulfamide was imperative. Compound 3 (see Figure 3.8) was chosen as the model compound for *ab initio* calculations (Gaussian94 at PDC) to be used in the parameterization.

Nodes	Wall time	Total time
1	249	249
5	50	250
10	27	270
20	17	340

Table 3.1. Scalability of MC calculations in MacroModel. On 10 processors the efficiency is 92 % and on 20 processors it is 73 %.

Coarse torsional scans of model compound 3 at the HF level suggested a starting conformation (torsion 6–5–2–1 = 179, torsion 8–4–2–1 = 116) for subsequent geometry optimization to the global energy minimum at B3LYP/6-31G*. Convergence was difficult to reach (undamped oscillations) and a CalcAll keyword was added to reach a stable point. A frequency calculation (B3LYP/6-31G*) revealed a small negative frequency of -4 Å. Additional calculations suggested that this geometry corresponded to a shallow sadle-point and that the true global energy minimum (at B3LYP/6-31G*) could be found in a different local energy mimimum identified in the above HF/6-31G* torsional scan (torsion $6-5-2-1 = 339$, torsion $8-4-2-1 = 116$).

A new frequency calculation from this optimized geometry, followed by several single point calculations on different rotamers, and x-ray crystallographic data provide the bulk of the data used for parameterization of the the sulfamide moiety. The parameter fitting is being done offsite in cooperation with Per-Ola Norrby (DFH) [Norrby and Liljefors, 1998].

Distributed Monte Carlo calculations showed reasonably good scaling.

With these new parameters in hand, we can now attempt to predict the binding of 1 and, more importantly, new derivatives of 1 with the Monte Carlo docking routine. Preliminary distributed Monte Carlo calculations on a small docking problem showed reasonably good scaling behavior, see Table 3.1. Calculations for larger molecular systems are expected to scale even better.

In conclusion, force field parameters have been developed for the sulfamide moiety. Work is in progress to apply these parameters to the development of novel cyclic sulfamide HIV-1 protease inihibitors.

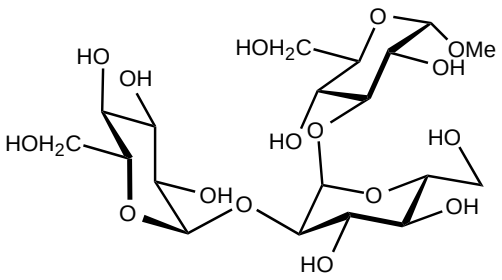

Figure 3.9. Schematic drawing of the trisaccharide $\alpha-\mathrm{D}-\mathrm{Glcp}-(1\rightarrow 2)-\alpha-\mathrm{D}-\mathrm{Glcp}-(1\rightarrow 3)-\alpha-\mathrm{D}-\mathrm{Glcp}-\mathrm{OMe}$.

3.6 Molecular Dynamics Simulation of the Terminal Glucotriose Unit in the Oligosaccharide of Glycoprotein Precursors

Christer Höög, Göran Widmalm
Department of Organic Chemistry, Arrhenius Laboratory, Stockholm University

One of the most important functions of glycosylation is to serve as recognition markers in molecular processes. Oligosaccharides may also modify the properties of proteins by altering their stability [Mer *et al.*, 1996], protease resistance or quaterny structure [Dwek, 1996]. Abnormal glycosylation is diagnostic in disease, *e.g.*, cancer and rheumatoid arthritis. The glycan chains in glycoproteins are commonly either N- or O-linked via asparagine or threonine/serine, respectively. The oligosaccharides may range from a few residues to multibranched, such as pentaantennary structures. In human only a small number of monosaccharides are used in the synthesis of these structures, although the number of structures formed may be large. Structural characterization of glycoproteins often identify different variants with respect to the carbohydrate chains of the polypeptide, denoted glycoforms. The trisaccharide (Figure 3.9)

$$\begin{aligned}&\alpha-\mathrm{D}-\mathrm{Glcp}-(1\rightarrow 2)-\alpha-\mathrm{D}-\mathrm{Glcp}-(1\rightarrow 3)\\&-\alpha-\mathrm{D}-\mathrm{Glcp}-\mathrm{OMe},\end{aligned}\tag{3.1}$$

is a model for the terminal glucotriose in $\mathrm{Glc_3Man_9GlcNAc_2}$ in glycoprotein precursors. It has been investigated by molecular dynamics simulation for 1 ns in aqueous solution using the molecular mechanics program CHARMM. An inter-residue intramolecular hydrogen bond, O6'-HO6'...O2, where O6' is a donor in the 2-linked residue and O2 is an acceptor in the 3-linked residue was

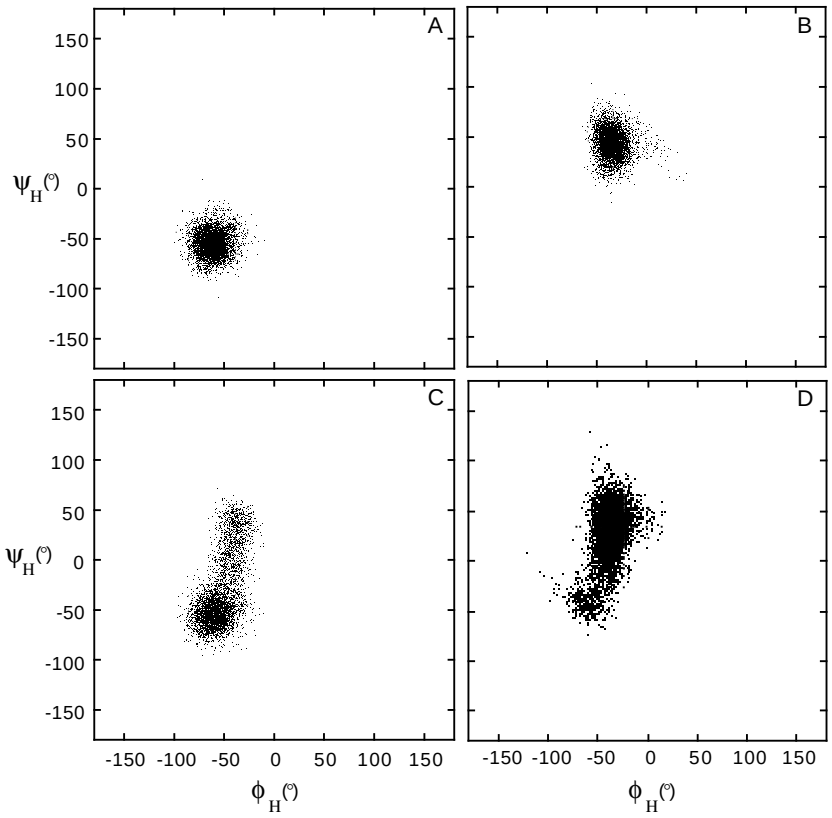

Figure 3.10. Scatter plots of Φ *vs.* Ψ from the aqueous MD simulations of 1. **A**: $(1 \rightarrow 2)$-linkage of structure (3.1) from simulation I; **B**: $-(1 \rightarrow 3)$-linkage from simulation I; **C**: $(1 \rightarrow 2)$ linkage from simulation II; **D**: $(1 \rightarrow 3)$-linkage from simulation II.

found to persist more than half of the time when the ω' dihedral of the hydroxymethyl group of the central residue populated the gt-conformer. In contrast to earlier studies [Alvardo *et al.*, 1991, Stenutz and Widmalm, 1998] hydrogen bonding between O2" and O4 was found only to a limited extent. The results obtained from this simulation, in conjunction with previous information, show that the glucotriose unit can be stabilized by different hydrogen bonds leading to a quite defined structure that the oligosaccharyltransferase should be able to recognize more easily, which is of particular interest since the terminal glucotriose unit is situated on a rather flexible oligosaccharide chain.

Methods

Atoms in the terminal glucose residue are denoted by a double prime, in the middle residue they are labelled by a prime, and in the O-methyl residue the atoms are unprimed. The torsional an-

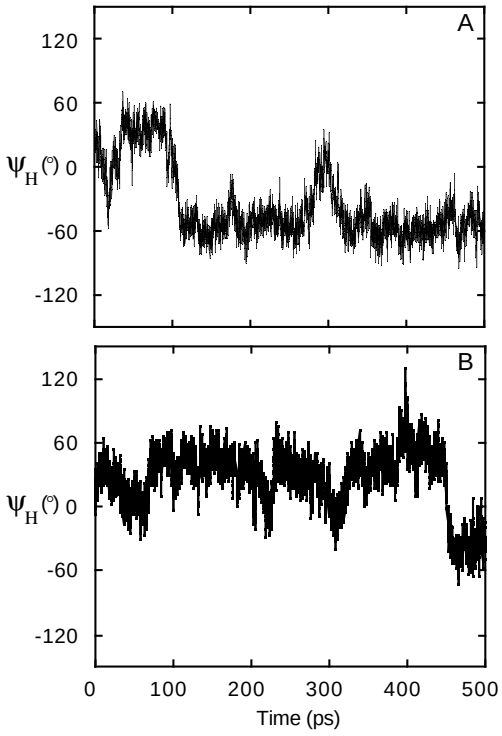

Figure 3.11. Molecular dynamics trajectory of equation (3.1) from simulation II of the Ψ dihedral angles of the (1 → 2)-linkage (**A**) and the (1 → 3)-linkage (**B**).

gles at a glycosidic linkage are denoted by Φ = H1-C1-OX-CX and Ψ = C1-OX-CX-HX, where X is the linkage atom. The torsional angle of a hydroxymethyl group is denoted by ω = O5-C5-C6-O6 and the three staggered conformers are given by gt (+60°), gg (−60°) and tg (180°). Simulations were performed on Strindberg, using 32 nodes resulting in a CPU time of approximately 4 hours per 100 ps.

Results

The conformational space sampled over a dynamics trajectory can be visualized in a scatter plot of Φ *vs.* Ψ where higly populated regions show clustering (Figure 3.10). In simulation I only one conformational state was observed whereas in the second simulation two additional states with changes in the Ψ dihedral angles occurred. In simulation II larger fluctuations were observed for Ψ' and Ψ" that each populated two states (Figure 3.11). The dihedral angles ω" and ω of the exocyclic hydroxymethyl groups showed no occurrence of the tg-conformer and relative populations

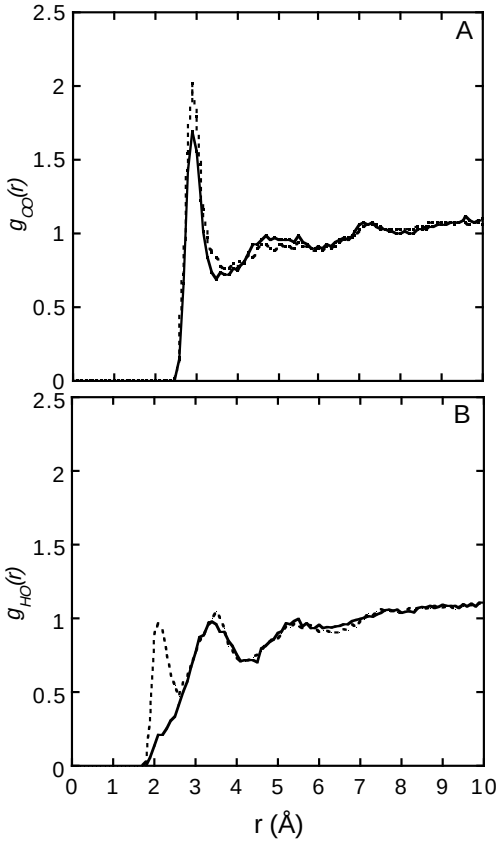

Figure 3.12. Radial distribution functions from simulation I. **A**: $g_{OO}(r)$ around O6' (solid line) and O6" (dashed line). **B**: $g_{HO}(r)$ around HO6' (solid line) and HO6" (dashed line).

for gt:gg as 88:12, wich is an overestimate of the gt-conformer in this force field (unpublished results) compared to an anticipated ratio of ≈40:60, which is observed for α-glucose [Nishida *et al.*, 1984]. The ω' dihedral of the middle glucosyl residue showed a small change in the relative population of gt:gg to 96:4. The rms fluctuation for dihedral angles ω" and ω were $\approx 30°$, whereas for ω' it was decreased to $\approx 20°$. Solvent interactions can be investigated using an atomic radial distribution function(RDF). This is given by $g_{nm}(r)$ where the first index n refers to a solute atom and the second index m refers to a solvent atom. Three kinds of RDFs were studied, namely, (I) were studied, namely, (i) $g_{OO}(r)$, (ii) $g_{HO}(r)$, (iii) $g_{HO}(r)$. Integration of $g_{OO}(r)$ out to the first minimum at 3.5 Å yields the average number of water molecules in the first shell around a particular oxygen, *i.e.*, the coordination number n_{OO}. The number of hydrogen bonds can in

Table 3.2. Coordination numbers of equation (3.1) obtained from the RDFs.

Oxygen	n_{OO}	n_{OH}	n_{HO}	n_H
Hydroxyl groups				
O2	2.5	0.8	0.8	1.6
O2"	3.4	1.3	0.8	2.1
O3'	3.4	1.2	0.9	2.1
O3"	3.8	1.3	1.0	2.3
O4	2.6	1.2	0.7	1.9
O4'	3.4	1.3	1.0	2.3
O4"	3.5	1.3	0.9	2.2
O6	3.8	1.8	0.8	2.6
O6'	3.5	2.0	0.4	2.4
O6"	3.9	1.8	0.8	2.6
Ring/bridge groups				
O1	1.6	0.3	–	0.3
O2'	1.0	0.1	–	0.1
O3	0.6	0.1	–	0.1
O5	1.3	0.2	–	0.2
O5'	1.1	0.3	–	0.3
O5"	1.4	0.2	–	0.2

the same way be investigated by integration of oxygen-hydrogen distributions out to 2.5 Å to give the coordination numbers n_{OH} and n_{HO}. The total number of hydrogen bonds between a specific hydroxyl group and solvent molecules is then given by the coordination number $n_H = n_{OH} + n_{HO}$. Radial distribution functions of the hydroxymethyl groups of the terminal and 2-linked glycosyl residues are shown in Figure 3.12. The $g_{OO}(r)$ show a typical maximum around 2.9 Å, which is indicative of hydrogen bonding with the solvent. A small difference between these two RDFs can be identified. The difference is much more pronounced if instead the $g_{HO}(r)$ is investigated, where the first maximum around 2 Å is absent for the hydroxyl hydrogen HO6', which thus is shielded from solvent. Inspection of coordination numbers for solute oxygens and hydrogens (Table 3.2) reveal that the lowest values of n_{OO} and n_{OH} are observed for O2, which therefore has a decreased ability to act as an acceptor in hydrogen bonding from solvent. On the same residue low values of the coordination numbers for O4 are also observed, thus HO4 as a donor to solvent is reduced. Of the hydroxymethyl groups the one in the middle

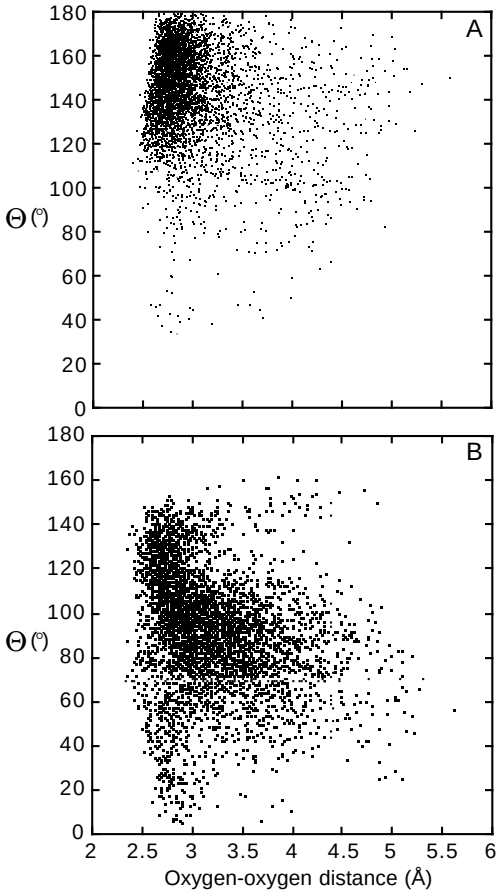

Figure 3.13. Scatter plot from simulation I of donor-acceptor distance *vs.* donor- hydrogen...acceptor angle. **A**: O6'-O2 *vs.* O6'-HO6'...O2. **B**: O2"-HO2"...O4.

sugar residue shows a higher value for n_{OH}, whereas for n_{OO}, n_{HO} and n_H the coordination numbers are reduced. The oxygen atom in the hydroxymethyl residue is thus more accessible for hydrogen bonding from hydrogens of the solvent and at the same time the hydroxyl hydrogen is significantly less accessible to solvent hydrogen bonding. Ring and bridge oxygens show solvent interactions and hydrogen bonding to a lesser extent. Inter-residue intramolecular hydrogen bonding in (3.1) can be monitored in the simulation by applying criteria for hydrogen bonding, namely theta $> 135°$ and an oxygen-oxygen distance < 3.5 Å. In earlier studies hydrogen bonding has been investigated for O4-O2". From the RDFs some differencees were observed for this pair. The above results also indicates that another pair, namely, O6'-O2 may be involved in hydrogen bonding. For a pair of atoms where both can act

as a donor or an acceptor the direction of the hydrogen bond is important. A hydrogen bond is present when both of the above criteria are fulfilled. Thus a hydrogen bond was found to persist as O6'-HO6'...O2, where O6' is a donor and O2 is an acceptor (Figure 3.13). During the simulation this hydrogen bond occurred for $\approx 60\%$ of the time whereas a hydrogen bond with the reverse direction was non-existent. When the dihedral angle Ψ' shows a distinct negative value, as is the case for the last part of simulation II (Figure 3.11), this hydrogen bond is not present. Hydrogen bonding in the O4-O2" pair occurred only to a limited extent, *i.e.*, 4.9% for the direction O2"-HO2"...O4 (Figure 3.13) and even less, 0.1%, for the reverse direction O4-HO4...O2". The decreased hydrogen bonding of HO4 to solvent (Table 3.2), is relieved by hydrogen bonding to O2' to some extent. The occurence of O4-HO4...O2' was 3.7% and 9.8% in the two simulations. In the present aqueous simulation an inter-residue hydrogen bond is formed to a significant extent for O6'-HO6'...O2, whereas for the O4-O2" pair intra-molecular hydrogen bonding occurs only to a limited extent.

4 Computational Fluid Dynamics

4.1 Large Grid Simulations of the Flow Field in a Draft Tube

John Bergström
Department of Mechanical Engineering, Division of Fluid Mechanics, Luleå University

In this project a test account on KALLSUP was used to investigate the numerical accuracy of a simulation of the flow field in a hydro power draft tube using CFX, see Figure 6.21 on page 119. A paper on this subject has been submitted to Computers and Fluids [Bergström and Gebart, 199X].

The potential for overall efficiency improvements of modern hydro power turbines is of the order a few percent.

The potential for overall efficiency improvements of modern hydro power turbines is of the order a few percent. A significant part of the losses occur is in the draft tube. To improve the efficiency by analyzing the flow in the draft tube, it is therefore necessary to do this accurately, *i.e.*, one must know how large iterative and grid errors are. This was done by comparing some methods to estimate errors. Four grids (122976 to 4592 cells) and two numerical schemes (hybrid differencing and CCCT) were used in the comparison. To assess the iterative error, the convergence history and the final value of the residuals were used. The grid error estimates were based on Richardson extrapolation and least square curve fitting. Using these methods we could, apart from estimate the error, also calculate the apparent order of the numerical schemes. The effects of using double or single precision and changing the under relaxation factors were also investigated. To check the grid error the pressure recovery factor was used. The iterative error based on the pressure recovery factor was very small for all grids (of the order 10^{-4}% for the CCCT scheme and 10^{-10}% for the hybrid scheme). The grid error was about 10% for the finest grid and the apparent order of the numerical schemes were 1.6 for CCCT (formally second order) and 1.4 for hybrid differencing (formally first order). The conclusion is that there are several methods available that can be used in practical simulations to estimate numerical errors and that in this particular case, the errors were too large. The methods for estimating the errors also allowed us to compute the

necessary grid size for a target value of the grid error. For a target value of 1%, the necessary grid size for this case was computed to two million cells.

Simulations using KALLSUP

We want to use KALLSUP to be able to do a simulation using very large grid sizes

We want to use KALLSUP to be able to do a simulation using very large grid sizes and check that it is possible to extrapolate results from smaller grids. A grid with two million cells requires a lot of memory and this is available at the KALLSUP computer. First a simulation previously done was used as a test, to check the speed of the KALLSUP computer. It was concluded that there was no decrease in CPU time compared to a DEC Alpha 4/266. However, since there is only 256 Mbyte memory available at the DEC Alpha, we still want to use the KALLSUP computer because of the large memory requirements. Some tests using a grid with about one million cells has been done but the submitted jobs has so far not been successful because we do not know the memory requirements for grids of this magnitude. The time spent in the queue system was very long (about one week) for these test, probably because we required a lot of memory (2000 Mbyte). When we manage to simulate the draft tube flow using these large grids, we will compare this to the extrapolated results from previously grids of smaller size, and hopefully they will match.

4.2 Direct Numerical Simulations of Turbulent Boundary Layer and Channel Flow

Martin Skote, Krister Alvelius
Department of Mechanics, KTH

The Fortran code used for direct numerical simulations of turbulent boundary layer and channel flow has been implemented and run on the Fujitsu VX/2, Selma, at PDC. The spectral method used in the code is a very efficient way to get high accuracy at a very high computational speed. Due to the spectral representation in Fourier series the degree of vectorization is very high. The vectorization is dependent on the size of the problem, a large problem will in a natural way contain long vectors. For small problems the size of the vectors can be increased by arranging the arrays in the code in a proper way. This can be achieved either by tuning pro-

Due to the spectral representation in Fourier series the degree of vectorization is very high.

gram parameters or, in the absence of that possibility, letting the precompiler, `fpp`, of the KALLSUP computer vectorize the code.

If we have a two-dimensional problem with 100×40 grid-points and using 40 vectors of length 100, the performance is very poor. If we instead use only one vector of length 4000, the speed-up is about 10. The code runs at about 800 Mflop/s which is equivalent to 10 processors on the KALLSUP machine. Selma is much more sensitive to the size of the vectors than KALLSUP. The speed-up on KALLSUP was only 10% while for Selma the same increase of length gave a speed-up of 100%. To obtain useful results from a simulation of turbulence, one has to let the simulation run for a long time, for the collection of statistics. This means that 10 CPU hours is a very small amount of time and the job has to be restarted over and over again. This can not yet be done on Selma automatically, which has so far limited our usage of the computer.

The code runs at about 800 Mflop/s

4.3 Navier-Stokes Calculations on a Full Configuration Aircraft using Parallel Computers[1]

Anders Ytterström
Center for Computational Mathematics and Mechanics, KTH
Arthur Rizzi
Department of Aeronautical Engineering, KTH
Carlos Weber
CERFACS, France
Jan Vos
EPFL, Switzerland

The work presented here is a result of the EC ESPRIT III project Parallel Aero, which was part of the EUROPORT 1 project. The objectives of the Parallel Aero project were twofold, first to investigate whether the current generation of massively marallel computers is capable of solving the Navier–Stokes equations for aerodynamic design in a turn around time required by a design office, and second to study the feasibility of a machine-independent and

[1]The development of the Parallel Version of NSMB was done in the frame of the ESPRIT III Project Parallel Aero. The Swedish participation in this project was funded by NUTEK, the Swedish National Board for Industrial and Technical Development. The Swiss participation in this project was funded by the Swiss Ministry of Education and Science (OFES).

Aerospatiale, Toulouse is gratefully acknowledged for providing the AS28G mesh and windtunnel data.

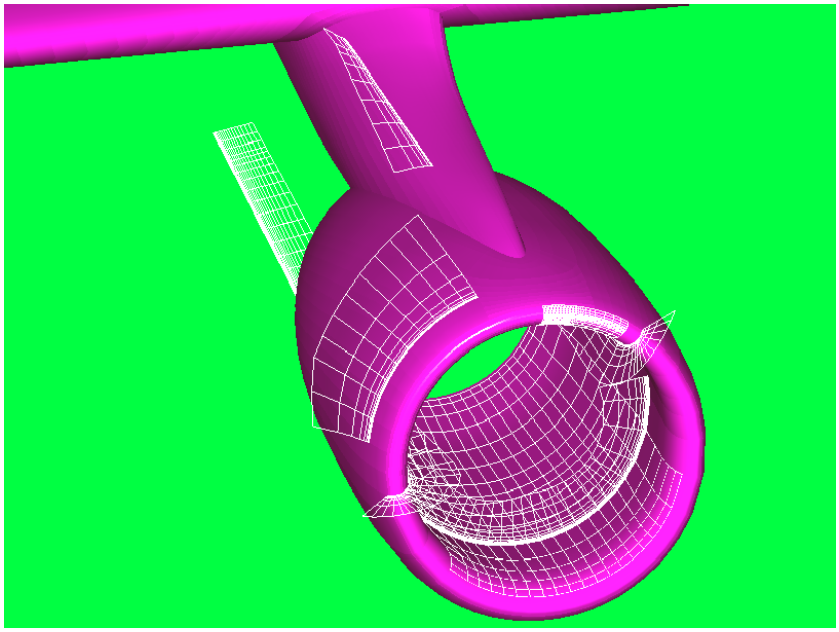

Figure 4.1. A part of the AS28G mesh, at the pylon and nacelle, where flow separation occurs for this full aircraft configuration.

scalable parallel Navier–Stokes code by porting the NSMB [Vos *et al.*, 1997, Leyland *et al.*, 1995] code to several different parallel platforms using standard message passing libraries.

The turbulent flow over a full configuration (body, wing, nacelle and pylon) aircraft, the AS28G, using a parallelized Reynolds average Navier–Stokes solver, NSMB [Vos *et al.*, 1997, Leyland *et al.*, 1995], on two parallel computers: IBM SP-2 (PDC) and NEC SX4 (CSCS, Switzerland) and Fujitsu VX/2 (PDC).

The NSMB code solves the Navier–Stokes equations on multi block structured grids.

Numerical scheme in the NSMB *code*

The NSMB code solves the Navier–Stokes equations on multi block structured grids. The Navier–Stokes equations are discretized using a space centered finite volume scheme. The equations are integrated in time using either explicit Runge-Kutta time stepping, or the implicit LU-SGS scheme [Yoon and Jameson, 1986, Klopfer and Yoon, 1993, Weber, 1996]. It is also possible to use Diagonal-ADI [Caughey, 1988] for the Runge-Kutta scheme [Jameson, 1985].

Various turbulence models of different complexity are available in NSMB. For the Parallel Aero project the Baldwin-Lomax model [Baldwin and Lomax, 1978] was used in all benchmark test cases. The Baldwin-Lomax model has also been used for the present com-

putations. It has been implemented in a general way for complex geometries and multi-block computations [Gacherieu, 1996].

Parallelization strategy

Two design choices were made in the development of parallel NSMB, first the domain partitioning is executed before the execution of parallel NSMB, and second the parallel implementation in NSMB is based on a master/slave paradigm. This latter choice permits an easy porting of NSMB to different parallel platforms.

Domain partitioning tool MB-Split

Within the Parallel Aero project, a domain decomposition tool MB-Split [Ytterström, 1997] was developed at KTH. MB-Split is written in C++. It can read a NSMB database with an arbitrary number of blocks, and generates a new database with a new number of blocks such that a balanced calculation is obtained on a parallel computer, using different load balancing algorithms.

AS28G full aircraft

The AS28G test case is representative of a full aircraft configuration, which includes the engine/airframe integration where viscous effects are important, especially on the pylon, where flow separation occurs. The finest grid contains 62 blocks with 3.5 million grid points. Figure 4.1 shows a part of the grid.

The finest grid contains 62 blocks with 3.5 million grid points.

The flow condition presented here represents the cruise condition, for which the pylon are optimized: $Re/m = 11.16 \times 10^6$, $\alpha = 2.2^\circ$ and $M = 0.8$.

Parallel performance

Load balancing on the IBM SP-2 has been made using MB-Split and the so called GreedyXtra Load balancing algorithm, giving a mesh that has 75 blocks, compared to the original 62 blocks.

Measured computational timings from NSMB shows a large deviation for some cases, possibly explained by different amount of work performed for different boundary conditions, or different computational efficiency for different vector lengths. Both the approximated times and the measured times are only for the computational work and does not involve communication. The abso-

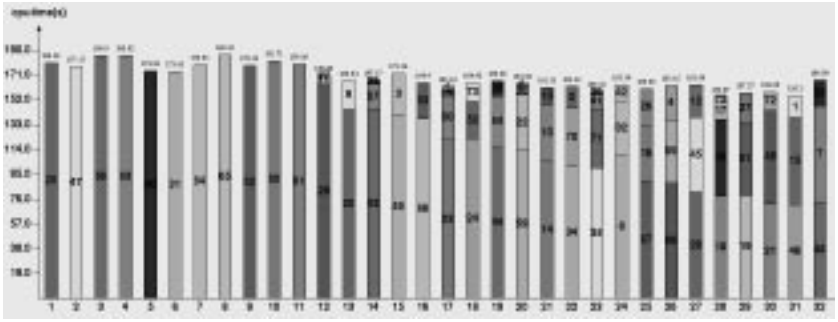

Figure 4.2. Load balance based on real timings on 32 IBM SP-2 processors, using the implicit LU-SGS scheme and Baldwin-Lomax.

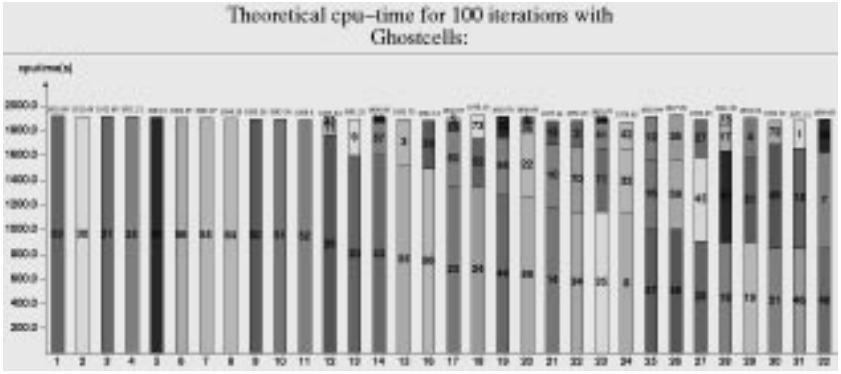

Figure 4.3. Theoretical load balance on 32 IBM SP-2 processors. Approximate timings for 100 iterations.

lute levels do not have to coincide, as they could be for different number of iterations, but the distribution should be the same.

The difference in load balance between theory and reality is not consistent for different numerical schemes. Figure 4.2 shows the load balance on 32 SP-2 processors using the implicit LU-SGS scheme. This should be compared to the theoretical load balance presented in Figure 4.3 and the measured load balance in Figure 4.4, for the ADI scheme. The maximum time for the LU-SGS scheme is 186 seconds, which is about 10% from the average 169 seconds and 230 seconds as maximum for the ADI scheme which is 37% from the average 168 seconds, compared to the theoretical 193 seconds, which is 2% from the average 190 seconds.

The grid has been split into 109 blocks for the computation on the CRAY T3D using 64 processors. Only the standard Greedy load balancing algorithm in MB-Split has been used to split the mesh which gave a somewhat unevenly distributed load on the processors. The ratio of communication time to the elapsed time in the time stepping loop is 32.5%. The large amount of communication time is due to the load balancing which might be improved

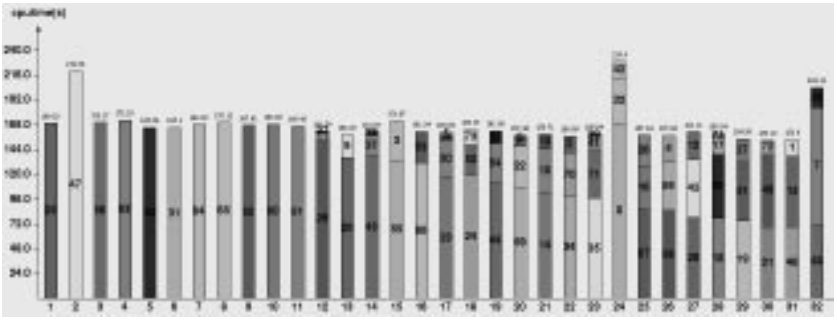

Figure 4.4. Load balance based on real timings in seconds on 32 IBM SP-2 processors, using the ADI scheme and Baldwin-Lomax.

Computer	Elapse time per iter (s)	Elapse time, timestepping routine (s)
Fujitsu VX/2 (LU-SGS)	42	40
NEC SX4 (LU-SGS)	29	27
32 p. IBM SP-2 (ADI)	41	23
32 p. IBM SP-2 (LU-SGS)	41	20
64 p. IBM SP-2 (ADI)	31	16
64 p. IBM SP-2 (LU-SGS)	30	11
64 p. CRAY T3D (LU-SGS)	22	21

Table 4.1. Timings for the fine AS28G mesh using the ADI and LU-SGS schemes on different computers.

by using the GreedyXtra Load balancing algorithm.

Timings for the parallel computations using 32 and 64 processors on the IBM SP-2 and 64 processors on the CRAY T3D has been compared with timings using a single processor on two vector computers, NEC SX4 and Fujitsu VX/2. Table 4.1 shows timings per iteration for the different computers. The Fujitsu VX/2 timings are for the original 62 block mesh, while the timings for the SP-2 are for a 75 block mesh using 32 processors and a 106 block mesh using 64 processors. The CRAY T3D and NEC SX4 timings are for a 109 block mesh. Computational time without communication are given in the second column. The whole difference between the timings for the timestepping routine and the total elapse time could not be considered to be communication, but a large part of it could. All computations have been made with the Baldwin-Lomax turbulence model and all communication have been made with PVM message passing library. The performance rate for the NEC SX4 calculation is around 500 Mflop/s.

The LU-SGS and the ADI schemes takes about the same time

per iteration, as shown for the 32 processor SP-2 cases in Table 4.1. The performance rate on the SP-2 is very low, which could be explained with the low communication bandwidth for the public domain PVM on the SP-2 (less than 10 Mbyte/s). This is more evident for the fine AS28G mesh than for smaller testcases. The performance rate using NSMB on the Fujitsu VX/2, for a case with a favorable vectorlength, could be as high as 900 Mflop/s and slightly higher for the NEC SX4 and around 40 Mflop/s for the "thin" SP-2 processor. This would demand around 20–25 SP-2 processors to get the same performance as the Fujitsu VX/2 and NEC SX4 without considering communication, but the problem with load balancing and efficient parallelization makes it difficult to get close to the theoretical performance, why vector computers like the Fujitsu VX/2 and NEC SX4 achieves a good price/performance compared to modern parallel computers.

Flow analysis and comparison with experiments

The CFL number has been increased from 1, continuously up to 10^9 after approximately 700 iterations, using the LU-SGS scheme. After 5000 iterations the L_2 norm of the residual (ρ) has been reduced by four orders of magnitude. This corresponds to a total elapsed time of approximately 30 hours on the CRAY T3D and 55 hours on the IBM SP-2. Lift and drag coefficient histories are given in Figure 4.5 and show converged values after about 4000 iterations.

Computed lift (CL) and drag (CD) coefficients based on wind-axis are given in Table 4.2 and compared with windtunnel measurements, for different computers and block splitting. Artificial dissipation of second order was reduced to 0.4 for the second test using the Fujitsu VX/2 and to 0.25 for the second test using the CRAY T3D compared to 0.8 for the other cases.

Figures 4.6 and 4.7 plots the pressure coefficient, -Cp, at two different positions on the wing. The Cp distribution on the lower side of the wing is very good computed for all stations, but the shock positions are predicted slightly behind the correct position, especially for station 3 (Figure 4.6), close to the pylon The shock positions closer to the wing-tip, *e.g.*, at station 6 (Figure 4.7) are much better predicted. The shock position could also be seen in Figure 6.4 on page 110, showing isopressure plots ontop of the wing.

The shock positions closer to the wing-tip are much better predicted

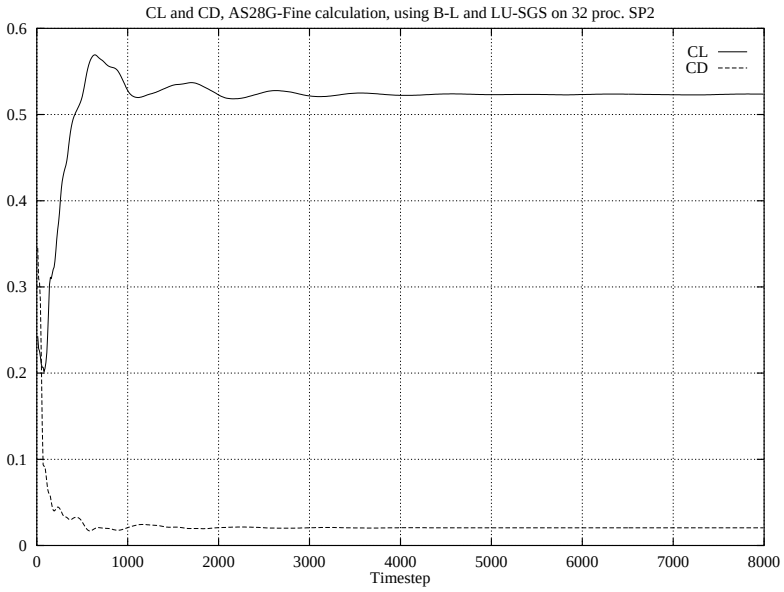

Figure 4.5. Lift (CL) and drag (CD) coefficients as a function of iteration, for the AS28G mesh, using LU-SGS and Baldwin-Lomax. Converged values are reached within 4000 iterations.

	CL	CD
32 processor IBM SP-2	0.5234	0.0307
64 processor CRAY T3D	0.5231	0.0307
Reduced Artdiss2, CRAY T3D	0.5300	0.0305
Fujitsu VX/2	0.5247	0.0306
Reduced Artdiss2, Fujitsu VX/2	0.5297	0.0303
Windtunnel	0.5145	0.0289

Table 4.2. Lift (CL) and drag (CD) coefficients for the AS28G, using LU-SGS and Baldwin-Lomax in NSMB.

Summary and conclusions

It could be concluded that a complete aircraft with a large Reynolds number ($\sim 10^7$) can be correctly calculated within 2 days using a modern vector or parallel computer, with an error in lift of around 2% and in drag of about 4%.

The use of modern vector computers is a competitive choice for large, complicated, flowcases, regarding the price/performance. The computational time for the fine, 3.5 million gridpoint mesh, on a single NEC SX4 processor took as long time as approximately 50 CRAY T3D processors and 45 processors on the IBM SP-2. The same figures for the Fujitsu VX/2 were 34 and 32 respectively.

The use of modern vector computers is a competitive choice for large, complicated, flowcases

A dynamic load balance, based on real timings, would be preferred for parallel computations, in order to be more efficient.

Figure 4.6. Cp (pressure coefficient) distribution on the wing of AS28G, at station 3, 42% of half-span, which is close to the pylon. Calculation (line) is compared with measurements(dots).

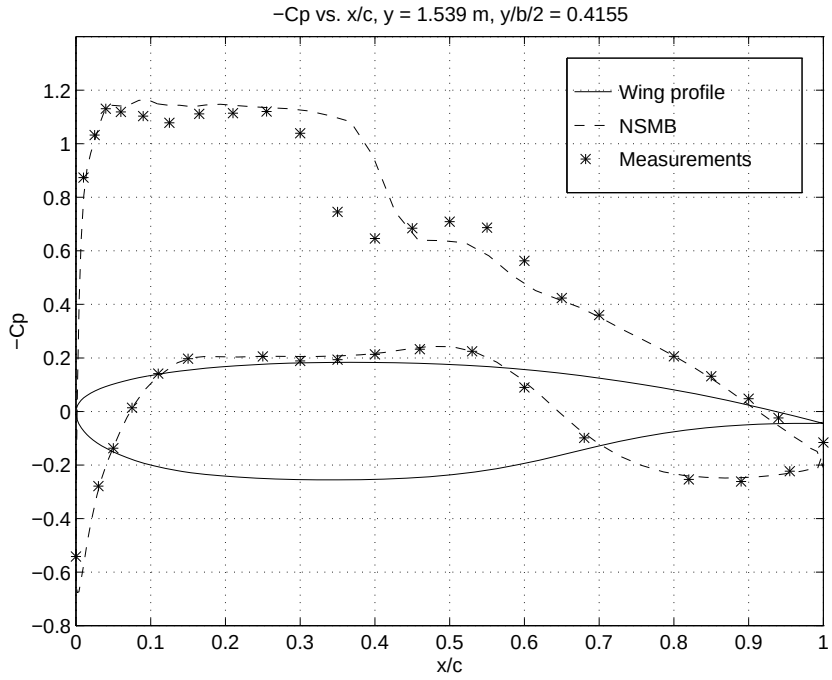

Figure 4.7. Cp (pressure coefficient) distribution on the wing of AS28G, at station 6, 78% of half-span. Calculation (line) is compared with measurements (dots)

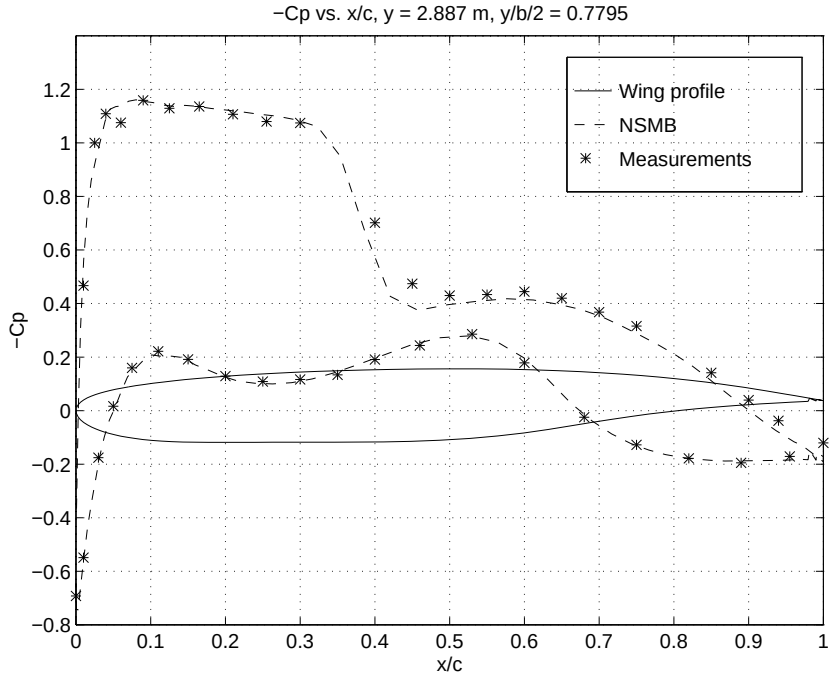

4.4 TURMUNSFLAT: Turbulence Modeling of Unsteady Flows in Axial Turbines

Virgine Casanovas
Department of Energy Technology, KTH

Background

TURMUNSFLAT is an european project whose aim is to better understand the flow conditions in axial low pressure turbine. Indeed, the unsteady phenomena due to stator-rotor interactions create complex transition from laminar to turbulent flows. The characteristics of turbulence are not well known under these conditions and the overall aim of the project is to find out new turbulence models simple enough to be practical in the design process of a turbine, but sufficiently accurate to obtain valid information on unsteady blade forces and unsteady aero-thermal stage performances.

The Chair of Heat and Power at KTH is involved in the task of doing unsteady 2D and steady 3D blade row and stage calculations.

Objectives

The objectives of the first calculations are to compare calculations on the whole stage with calculations on the rotor blades only with a prescribed incoming unsteady wake simulating the wake creating by the stator blades row. This aims at evaluating the relative importance of the two-way interaction effects in which the downstream blade row influences the upstream blade row compared to the one-way interaction effects. This first study should enable to justify the unsteady calculations on one blade row only with a rightly prescribed incoming wake instead of doing calculations on a whole stage. This would allow to save a considerable amount of CPU time.

The second objective of the project is to experiment new turbulence models developed by some others partners of the project in case of 2D unsteady blade row calculations as well as 3D steady whole stage calculations.

Method of attack

The study is being done on two test cases which are the single stage BRITE EuRam turbine from the Von Karman Institute (with 43 stator blades and 64 rotor blades) and two different configurations of the GEC Alsthom single stage turbine with 32 stator blades and 55 or 44 blades for the rotor, depending on the configuration. These test cases will allow to compare numerical and experimental results obtained from the different partners of the project.

The comparison of one-way and two-way interference effects is performed using an unsteady 2D Navier–Stokes code UNSFLO, a steady 3D Navier–Stokes code VOLSOL*v2.5 from Volvo Aero Corporation (VAC) and an unsteady 2D code Sara2D from VAC as well.

First viscous calculations using standard turbulence models (algebraic or two-equation models like the $k-l$ model) are performed.

Actual results

The work which has been performed until now consists in 2D steady and unsteady stator-rotor analysis as well as unsteady wake/rotor analysis with an algebraic and the $k-l$ turbulence models.

The main results obtained from the comparison of different calculations show that the unsteady effects on the flow on the stator are negligible and that the calculations on the rotor blade row only are in agreement with those on the whole stage, on condition that a correct velocity deficit and a correct pressure disturbance at the inlet of the rotor are stated.

Further work

The next steps of the project are to do 2D unsteady blade row calculations using the $k-\epsilon$ turbulence model as well as to perform 3D steady calculations on the whole stage with also the $k-\epsilon$ turbulence model.

4.5 Modeling Combustion using Computational Fluid Dynamics

Thomas Badinard, Dean R. Eklund
Department of Energy Technology, KTH

The subject of the work was the study of turbulent combustion. The aim of this project was to simulate one reacting flow test case for which extensive experimental data were available (experimental data from ENEL). The code used to run the simulation was a CFD code developed by Volvo Aero Corporation named VOLSOL [Eriksson, 1996]. The test case was run both inert and reacting on two grids.

A small scale axi-symmetric methane-air flame stabilized by a bluff body configuration was investigated

A small scale axi-symmetric methane-air flame stabilized by a bluff body configuration was investigated [Ele, 1994]. A methane jet passes through a cylinder of 50 mm diameter. Air was supplied through a coaxial cylinder of diameter 100 mm. The bluff body was then formed by the wall between the two coaxial cylinders.

The methane jet velocity profile was considered to have the form of a fully developed pipe flow, while the air was approximated as having a constant axial velocity.

The reacting results

To compute the experiment, the following models were used:

- The *standard* $k - \epsilon$ *model* for turbulence modeling.
- Two different models for combustion to allow comparison: the *Eddy Dissipation Concept* of Magnussen and his simplified EDC model [Magnussen, 1989]. Kinetic rates were not considered in the calculations.

A structured grid was used of two different size 161×185 and 81×93. The reacting results are all done on the 81×93 grid. Around 220 hours on a single node of the IBM SP-2 were needed for each reacting flow calculation.

It is observed in Figure 4.8 that the simulation recreates the two recirculation zones shown by the experimental results. The general shape of the flow is quite well simulated. However, the place of the reaction zone (corresponding to high temperatures) is not well simulated, see Figure 4.9 and the temperature contour plots in Figure 6.1 on page 107.

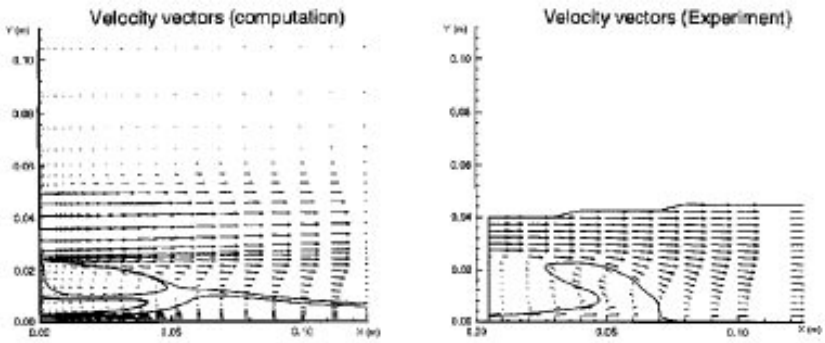

Figure 4.8. Vector plots of the flow field for the calculations and the experiment

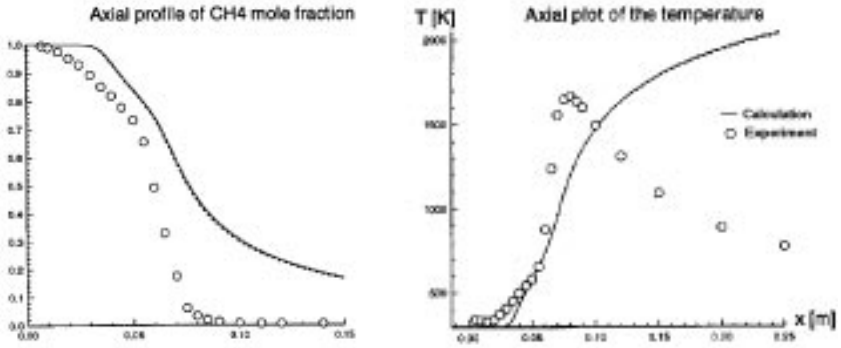

Figure 4.9. Plot of the methane mole fraction and the temperature on the centerline

The reaction zone is situated around $x = 0.08\,\mathrm{m}$ for the experiment matching the end of the penetration of the methane jet. The computation creates a reacting zone only in the shear layers between the coaxial air jet and the pocket created by the recirculation zones. The methane mole fraction on the axis of the combustor is then not consumed as well as in the experiment: at $x = 0.15\,\mathrm{m}$, no methane is left for the experiment while the simulation shows still a methane mole fraction of 0.2. The methane is not consumed in the same place for experiment and the simulation.

Conclusions

This work has shown the ability of the VOLSOL code to simulate a reacting flow. Though large differences in the calculated and experimental results were found, good agreement with other simulations using the same combustion models was observed. Modifications to the turbulent combustion modeling are being investigated. The experience acquired and the study of these results are of importance for the project to model radiation from combustion flow fields.

5 Applications in Physics

5.1 Large Scale FDTD

Erik Abenius, Ulf Andersson, Gunnar Ledfelt
Parallel and Scientific Computing Institute, KTH

Introduction

This project is a collaboration between Saab Military Aircraft, the Swedish Defence Research Establishment (FOA), the Swedish National Testing and Research Institute (SP) and NADA at KTH. It is one of the project conducted within the Parallel and Scientific Computing Institute (PSCI) competence center. The goal of this project is to develop methods for numerical simulation of electromagnetic phenomena in complex systems, for instance an aircraft. Electromagnetic fields are governed by the Maxwell equations. For linear, isotropic and nondispersive media they are:

$$\begin{aligned} &\nabla \cdot (\epsilon \bar{E}) = 0, && (Gauss) \\ &\nabla \cdot (\mu \bar{H}) = 0, && (Gauss) \\ &\tfrac{\partial \bar{H}}{\partial t} = -\tfrac{1}{\mu}\nabla \times \bar{E} - \tfrac{\rho'}{\mu}\bar{H}, && (Faraday) \\ &\tfrac{\partial \bar{E}}{\partial t} = \tfrac{1}{\epsilon}\nabla \times \bar{H} - \tfrac{\sigma}{\epsilon}\bar{E}, && (Ampere) \end{aligned} \tag{5.1}$$

where $\bar{E}$ is the electric field in $[V/m]$, $\bar{H}$ is the magnetic field in $[A/m]$, ϵ is the electric permittivity in $[F/m]$, μ is the magnetic permeability in $[H/m]$, σ is the electric conductivity in $[S/m]$ and ρ' is an equivalent magnetic resistivity in $[\Omega/m]$.

The Maxwell equations are a first order hyperbolic system of PDE:s. They can not be solved analytically except for a few simple geometries, such as spheres and circular cylinders. For more complex structures one has to rely on numerical methods, *i.e.*, computational electromagnetics (CEM), and/or experiments.

There is a wide range of applications for CEM. Some of the more important ones are electromagnetic compatibility (EMC), antenna analysis, cellular phone-human body interaction, microwave ovens and radar cross section (RCS) calculations.

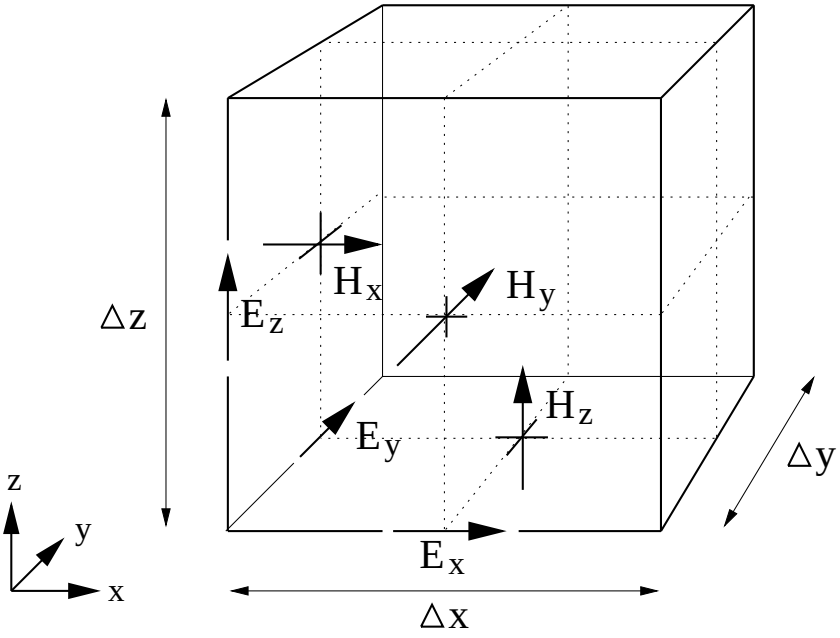

Figure 5.1. Position of the electric and magnetic field vector components in a unit Yee cell.

Regarding EMC there are several threats that an aircraft has to be verified against where some examples are lightning, radio and radar fields, electrostatic discharge, fields emitted by electronic equipment and high power directed microwave weapons. All these threats can, if the electronic equipment of the aircraft is not sufficiently protected, disturb or damage the electronic equipment causing EMC problems that would jeopardize flight safety. A well known example is the prohibition of using cellular phones aboard airliners.

The Yee method

In 1966 a Finite-Difference Time-Domain (FDTD) method for the Maxwell equations was introduced by K. S. Yee. This method uses a leapfrog scheme on staggered Cartesian grids. Figure 5.1 shows the positions of the electric and magnetic components in a unit cell of the staggered grid. The Yee scheme explicitly discretizes Ampere's law and Faraday's law and implicitly enforces the two Gauss's law relations.

For open problems an absorbing boundary condition (ABC) is needed to truncate the computational domain. Incident plane waves can be generated by Huygens surfaces, *i.e.*, by dividing the

computational domain into two parts, a total field part surrounded by a scattered field part. The fields can also be excited by a point source or by using a thin wire model. For a thorough description of the FDTD method see the book by Taflove [Taflove, 1995].

The Yee method has several advantages. It is robust, fast and easy to understand. Furthermore it is possible to achieve the response in a chosen frequency band in one calculation by using a pulse excitation. This can not be achieved with a frequency domain method. On the other hand the Cartesian grid conforms badly to the real geometry, thus introducing so called stair stepping errors. Furthermore, it does not exist a general subgridding scheme. This means that structures smaller than the grid resolution have to be treated by subcell models. In spite of these disadvantages we believe that the Yee method will remain in use for many years. Therefore, the subcell models have to be improved and new subcell models must be developed. Some of the geometric structures in need of (better) subcell models are thin wires, bundled wires, thin layers and thin slots.

Code description

We have implemented the Yee method using Fortran 90. We use the first order Mur boundary condition as ABC. The recently introduced Perfectly Matched Layer (PML) is under implementation. PML is regarded as a major breakthrough in electromagnetic modeling. It has been shown to be superior to classical absorbing boundary conditions, such as the Mur boundary condition.

The code is portable and performs well on the various platforms at PDC

The code is portable and performs well on the various platforms at PDC. On one thin IBM SP-2 node the performance is 70 Mflop/s and on one CRAY J932 node the performance is 100 Mflop/s. On a Fujitsu VX/2 node the code performs extremely well. It is possible to achieve 1.4 Gflop/s. This is more than half of the peak performance (2.2 Gflop/s) of a Fujitsu VX/2 node. This performance is however very problem-size dependent. It has been reached on a grid with $2045 \times 59 \times 59$ nodes. The calculations in Figure 6.2 on page 108 and Figure 6.3 on page 109, with grid sizes of $80 \times 80 \times 200$ and $200 \times 200 \times 200$, had a performance of about 900 Mflop/s. In our equations there are twice as many additions as there are multiplications which means that the full arithmetic capacity of the Fujitsu VX/2 (eight additions and eight multiplications each clock cycle) can not be used. There-

On a Fujitsu VX node 1.4 Gflop/s can be achieved

fore, the upper limit of the peak performance is 1.7 Gflop/s in our application.

Parallelization is under implementation using MPI. Preliminary results on the two node Fujitsu VX/2 shows a performance of 2.7 Gflop/s for $2045 \times 118 \times 59$ nodes. CEM calculations needs a lot of memory. The 2 Gbyte per node at the Fujitsu VX/2 enables us to make larger simulations than we could perform on a workstation On 64 thin SP-2 nodes we have reached 3.8 Gflop/s which corresponds to 60 Mflop/s per node and 23% of the peak performance of the SP-2 nodes.

On 64 thin SP-2 nodes we have reached 3.8 Gflop/s

Thin wires

If an electromagnetic problem contains a wire of radius less than the cell size of the FDTD-grid one must use a thin wire model. The purpose of the model is to govern the influence of a wire running through the FDTD-grid without resolving the small wire radius. We have implemented a model that introduces a one-dimensional hyperbolic system of PDE:s describing the current (I) and voltage (V) along the wire, see [Abenius, 1997]. If the wire lies along the z-axis we have,

$$L\frac{\partial I}{\partial t} + \frac{\partial V}{\partial z} = E_z \tag{5.2}$$

$$C\frac{\partial V}{\partial t} + \frac{\partial I}{\partial z} = 0 \tag{5.3}$$

where L and C are the characteristic inductance and capacitance of the wire. Equations (5.2) and (5.3) are also discretized using a leapfrog scheme on staggered grids. The coupling between the thin wire model and the Yee algorithm is straightforward. The right hand side of (5.2) couples the Yee algorithm to the thin wire model. The coupling from the thin wire model to the Yee algorithm is done by including the current I as a current density term in the right hand side of Ampere's law.

By forcing the current in a wire-segment, the thin wire model can be used for simulating antennas. This procedure has been used in the calculations shown in Figure 6.2 on page 108 and Figure 6.3 on page 109. Figure 6.2 shows an E-shaped open waveguide, with a radiating antenna. Figure 6.3 shows a model setup for studying the induction of currents on a wire connecting two electronic devices in the presence of a transmitting cellular phone.

Further information

More information about this project can be found in the proceedings from RVK-96 [Andersson and Ledfelt, 1996] and at the project homepage `http://www.nada.kth.se/~ulfa/CEM.html`.

5.2 Nuclear Spin Relaxation in Paramagnetic Complexes (S = 1) of Arbitrary Symmetry

Tomas Nilsson, Jozef Kowalewski
Division of Physical Chemistry, Arrhenius Laboratory,
Stockholm University

Introduction

The field-dependence of nuclear spin relaxation rates, commonly called nuclear magnetic relaxation dispersion (NMRD), gives insight into microscopic structural and dynamic properties. We are interested in the proton relaxation enhancement (PRE) of ligands (*e.g.*, water molecules) in paramagnetic transition metal complexes, exchanging rapidly with the bulk. NMRD-profiles give an indirect way of studying the electronic structure as well as the electron spin dynamics.

NMRD-profiles give an indirect way of studying the electronic structure as well as the electron spin dynamics

Traditionally, the modified Solomon-Bloembergen (MSB) equations [Kowalewski *et al.*, 1985] (or the Solomon-Bloembergen-Morgan (SBM) theory) are used to interpret the NMRD-profiles. However, in order for the MSB equations to be applicable the strong narrowing condition (or more commonly, the Redfield limit) has to be fulfilled. For systems such as Ni(II) complexes ($S = 1$), with which we shall be concerned here, the Redfield limit is generally not fulfilled due to the very fast electron spin relaxation and the SBM theory breaks down.

A general theory that can allow for the electron spin to be outside the Redfield limit (in the slow-motion regime) as well as within it, was developed by Kowalewski and coworkers (the Stockholm-group) [Benetis *et al.*, 1983] in the early 1980s (*i.e.*, the slow-motion theory). We have now generalized one of the most recent models developed by Larsson *et al.* [Larsson *et al.*, 1994], which allows for the static and transient zero-field splitting (ZFS) to be present simultaneously. The subject of the present research are the symmetry-breaking properties and how they affect the NMRD-profiles. The effect of rhombic symmetry in the static ZFS tensor

will be discussed, where the tensor is described by the axial (D_S) and rhombic (E_S) terms. Furthermore, we have also investigated the case when the principal axis system of the static ZFS tensor is allowed to deviate from the molecule-fixed frame of the dipole-dipole vector between the nuclear spin and the electron spin. The transformation between these two frames is described by the polar angle (θ) and the azimuthal angle (ϕ), where the latter is set to zero in all calculations.

One of the objectives of the present research is to provide a standard set of "exact" calculations, against which simplified models may be tested. One such model is the so-called "low-field theory" developed by the Florence-group of Bertini and coworkers [Banci *et al.*, 1991]. In their theory they treat the Zeeman interaction as a perturbation in the ZFS regime using the Kubo and Tomita formalism.

We will present NMRD-profiles for some cases and discuss the effects of the symmetry-breaking properties mentioned above and also make a comparison between the Stockholm- and Florence-approach.

Theory

The framework of the slow-motion theory will be given very briefly. Under fast exchange conditions the PRE of ligand protons in paramagnetic transition metal complexes depends on modulation of the hyperfine interaction between the nuclear spins (the protons in our case) and the unpaired electron spins. This hyperfine interaction contains the through space dipole-dipole (DD) interaction and the through bonds Fermi contact (FC) interaction. The latter is sometimes called the scalar (SC) interaction. We shall only consider the dominating DD interaction throughout the rest of this text.

The slow-motion theory is based on the idea that if the electron spin degree of freedom is considered to be a part of the lattice, the Redfield theory can be used for the nuclear spin relaxation caused by the weak coupling between the nuclear spins and the lattice.

The expression for the nuclear spin-lattice relaxation rate is given in Eq. (5.4) in terms of the real part of the complex spectral density taken at the nuclear spin Larmor frequency.

$$T_{1I}^{-1} = 2Re\left\{K_{1,1}^{DD}\left(-\omega_I\right)\right\} \tag{5.4}$$

The spectral density in Eq. (5.4) is given as the Fourier-Laplace transform

$$K_{1,1}^{DD}(-\omega_I) = \int_0^\infty G_{1,1}^{DD}(-\tau)\, e^{-i\omega_I \tau} d\tau \tag{5.5}$$

where the auto-correlation function for the lattice, $G_{1,1}^{DD}(\tau)$, is defined as

$$G_{1,1}^{DD}(-\tau) = Tr_L \left\{ T_1^{1^\dagger} e^{-i\mathcal{L}_L \tau} T_1^1 \rho_L^{eq} \right\} \tag{5.6}$$

The auto-correlation function in Eq. (5.6) contains the lattice T_1^1 tensor operators, which are components of irreducible spherical tensor operators, the lattice Liouville superoperator, $\mathcal{L}_L$, (lattice Liouvillian), which determines the time-evolution of the system and the lattice density operator, ρ_L^{eq}, which is assumed to be in thermal equilibrium at all time.

The actual computation of the spectral density at the nuclear spin Larmor frequency is performed by setting up and inverting the supermatrix $\mathbf{M} = i(\mathbf{L}_L + \omega_I \mathbf{1})$, which gives for the case of electron spin $S = 1$ the following expression of the nuclear spin-lattice relaxation rate

$$T_{1I}^{-1} = \frac{8}{3} \left(C^{DD}\right)^2 Re\left\{ \mathbf{c}_1^* \mathbf{M}^{-1} \mathbf{c}_1 \right\} \tag{5.7}$$

Actually, only a 3×3 fragment of the inverse supermatrix is required due to the multiplication of the projection vectors $\mathbf{c}_1$ in Eq. 5.7. This supermatrix is expressed in an orthonormal basis set defined in Liouville space. The supermatrix is very large but sparse and the dimension depends upon the convergence in the numerical calculation. Because of the fact that the reorientational and distortional motions are described with classical degrees of freedom the supermatrix is in principle infinitely large, which means that we have to truncate the matrix at a certain size. The convergence is tested by increasing the basis set. We have found that if the relaxation rates has converged so that the difference is less than 2% a dimension of 100 000 is necessary for magnetic field strengths between 1 and 10 Tesla. However, at low magnetic field (less than 1 Tesla) and at very high magnetic field (more than 10 Tesla) the convergence is better than 0.1% for a dimension of 30 000 of the supermatrix. The inversion procedure is accomplished by using the Lanczos algorithm. The main reason for using parallel computers is to be able to test the convergence in the numerical calculation

The main reason for using parallel computers is to be able to test the convergence in the numerical calculation involving these huge matrices

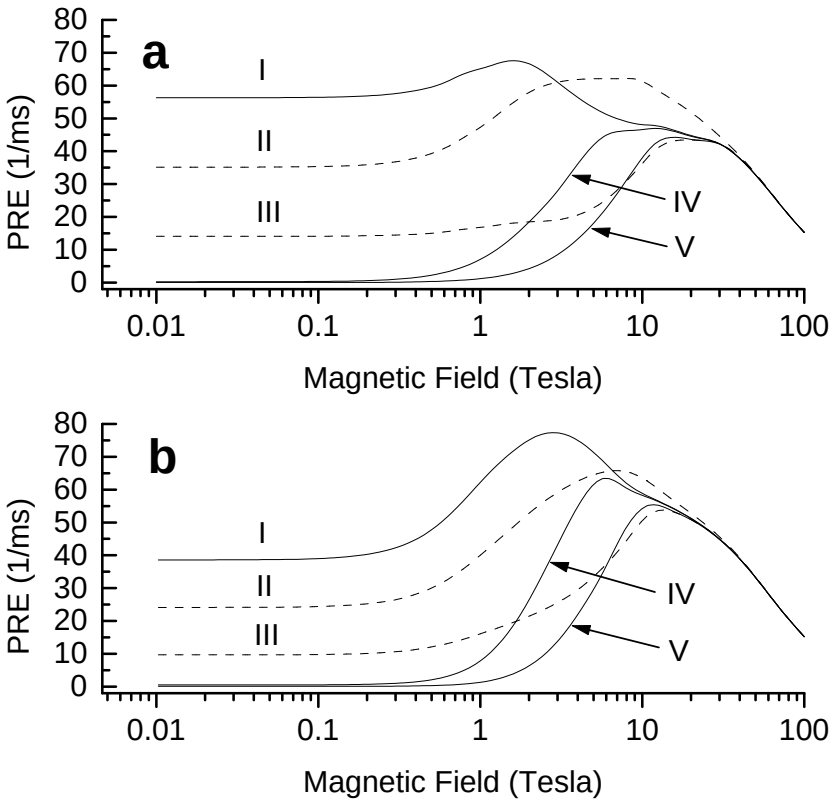

Figure 5.2. NMRD-profiles for an asymmetric ($\Delta_S = 10$ cm^{-1}) weakly deformable ($\Delta_T = 0.5$ cm^{-1}) complex with increasing polar angle and rhombicity in the following way: $\theta = 0°$, $E_S/D_S = 0$ in curve I; $\theta = 45°$, $E_S/D_S = 0$ in curve II; $\theta = 90°$, $E_S/D_S = 0$ in curve III; $E_S/D_S = 0.1$, $\theta = 0°$ in curve IV; $E_S/D_S = \frac{1}{3}$, $\theta = 0°$ in curve V. The same parameters are used in a) the Stockholm-approach and in b) the Florence-approach.

involving these huge matrices in the case of $S = 1$. However, even the matrices after convergence has been reached (which are used for production) are quite large (about 500 Mbyte).

Asymmetric weakly deformable complexes

The NMRD-profiles I–III in Figure 5.2 show the effect of increasing the polar angle θ, without introducing the rhombicity of the ZFS, for the case of an asymmetric (large static ZFS) weakly deformable (small transient ZFS) complex. Increasing the angle has the effect of reducing the PRE substantially at low magnetic fields up to about 10 Tesla. The physical picture of increasing the angle is that the effective dipolar field is reduced, which is the same as to say that the dipole-dipole interaction strength has decreased. The NMRD-profiles I, IV and V in Figure 5.2 show the effect of increasing the rhombicity when the angle θ is zero for the same case. Increasing the rhombicity has the effect of drastically re-

ducing the PRE at low magnetic fields. The physical explanation of the rhombicity effect is that a new precessional motion around the quantization axis in the principal axis system becomes operative. This removes the permanent magnetic moment, which is present with a cylindrically symmetric ZFS tensor. This new motion in the electron spin system effectively quenches the nuclear spin dipole-electron spin dipole interaction. If we compare Figure 5.2a and 5.2b they show the same trends concerning the angular and rhombicity effect. However, the differences that do appear is due to the fact that the Florence-approach uses a phenomenological description of the electron spin relaxation, while the Stockholm-approach does not. Furthermore, the Florence-approach separates the electron spin system from the rest of the lattice, while the Stockholm-approach takes cross-correlation effects into account.

5.3 Meta-Stable States of the ppπ^- Molecular Ion

Svante Jonsell, Piotr Froelich
Department of Quantum Chemistry, Uppsala University
Jan Wallenius
Department of Reactor Physics, KTH

As a beam of negative pions hits a source of molecular hydrogen highly excited pionic hydrogen atoms are formed

As a beam of negative pions hits a source of molecular hydrogen highly excited pionic hydrogen atoms ($p\pi^-$) are formed. These atoms are de-excited through a number of different channels. Finally the pion will be captured by the proton through the nuclear reaction

$$\pi^- + p \longrightarrow \pi^0 + n. \tag{5.8}$$

From time of flight studies of the neutrons produced in this reaction the mass difference between the neutral and the charged pion can be deduced [Crawford *et al.*, 1991]. If the initial velocity of the pionic atoms would be zero, the energy of all neutrons would be the same and could be related to the particle masses through the energy balance:

$$\begin{aligned} m_{\pi^- p} &= m_{\pi^-} + m_p - E_b = E_n + E_{\pi^0} = \\ &= (m_n^2 + p_n^2)^{\frac{1}{2}} + (m_{\pi^0}^2 + p_{\pi^0}^2)^{\frac{1}{2}} \end{aligned} \tag{5.9}$$

where E_n, E_{π^0} are total energies of the neutron and the pion, respectively, E_b is binding energy of the pionic atom, p_n is the

Figure 5.3. The Jacobian coordinate systems used. The origin of $\mathbf{R}_i$ is at the center of mass of the two particles connected by $\mathbf{r}_i$.

momentum of the neutron, $p_n = p_{\pi^0}$. However, the experimental analysis is sensitive to the initial kinetic energy of the pionic atoms, and therefore to the details of the pionic cascade [Aschenauer and Markushin, 1996]. We hope that the unexpected excess of very energetic pionic atoms noticed in recent experiments [Crawford *et al.*, 1991, Aschenauer *et al.*, 1995, Badertscher *et al.*, 1997] can be clarified with the help of our recently presented side-path theory [Froelich and Flores, 1993, Froelich and Wallenius, 1995, Wallenius and Froelich, 1996].

Our research has shown the existence of three-body resonances of muonic molecules [Froelich and Flores, 1993, Froelich and Wallenius, 1995, Wallenius and Froelich, 1995, Wallenius and Froelich, 1996]. Presently we investigate whether similar states exist in pionic molecules. These states are situated in the dissociative continuum of $pp\pi$ just below the $p\pi(nl) + p$ thresholds. Fast formation of these states in $p\pi(nl)$ - H_2 collisions, and their following decay into $p\pi(n'l') + p$ channel can be considered as resonantly enhanced pion transfer, resulting in very energetic pionic atoms. This opens a new and previously unconsidered acceleration mechanism for pionic atoms during the pion cascade.

The formation rates of $pp\pi$ molecules in $p\pi$-H_2 collisions can be obtained by means of scattering-theoretical methods, where exact binding energies and wave functions of the $pp\pi$ states are needed as input to the calculation of the relevant transition matrix elements.

The three-body wave functions $\Phi_{JM}(\mathbf{r}, \mathbf{R})$ were obtained variationally by use of the Coupled Rearrangement Channel method devised by Kamimura [Kamimura, 1988]. Φ_{JM} is expanded in terms of Gaussian basis functions spanned over the two rearrangement channels $\alpha = 1, 2$ shown in Figure 5.3.

$$\Phi_{JM} = \sum_{\alpha} \sum_{l,L} \sum_{i=1}^{i_{\max}} \sum_{I=1}^{I_{\max}} c_{\alpha i l I L} (1 + (-1)^{p+J} \mathcal{P}) g_{\alpha i l I L} \quad (5.10)$$

$$g_{\alpha i l I L} = r^l R^L e^{-(r/r_{\alpha i})^2} e^{-(R/R_{\alpha I})^2} \left[Y_l(\mathbf{r}_\alpha) \otimes Y_L(\mathbf{R}_\alpha) \right]_{JM}$$

The non-linear variational parameters r_i and R_I are chosen as

$$r_{\alpha i} = r_{\alpha 1}\left(\frac{r_{\alpha n}}{r_{\alpha 1}}\right)^{\frac{i-1}{n-1}}, R_{\alpha I} = R_{\alpha 1}\left(\frac{R_{\alpha N}}{R_{\alpha 1}}\right)^{\frac{I-1}{N-1}} \tag{5.11}$$

The geometrical progression allows for an accurate description of both short and long range behavior.

Since the two protons are identical the third rearrangement channel was not needed after the program had been modified to include the exchange contribution. Thus the number of Gaussians could be halved, and consequently execution times and memory requirements were reduced by almost 75%. The price to pay is that the program has to be run twice, once for each parity ($p = 0$ or $p = 1$) of the proton exchange operator $\mathcal{P}$.

Execution times and memory requirements were reduced by almost 75%

Since the resonances sought for are embedded in the scattering continuum of free $p\pi(n = 1, 2)$ atoms, the Rayleigh-Ritz procedure will not yield absolute bounds of the resonance energies. Instead we apply the stabilization technique, where one introduces a real scaling parameter α through the transformations

$$r \to r\alpha, \quad T \to T/\alpha^2, \quad V \to V/\alpha \tag{5.12}$$

where T and V are the kinetic and potential energy matrix elements, respectively. Varying α one obtains a stabilization graph as shown in Figure 5.4.

We have investigated the energy range up to the third atomic threshold, for total angular momentum $J = 0$ and $J = 1$. Our calculations show a rich structure of meta-stable states of all possible symmetries under each threshold. The ground-state energy was found to be $-294.858\,\text{eV}$ relative the first atomic threshold.

The work to determine the relevant formation and decay rates for these states is in progress. In particular we try to determine the Coulombic life time through the method of complex scaling. These rates will be used in a Monte Carlo simulation of the cascade process to determine the impact of the side-path mechanism on the pion cascade. This in turn will allow more precise conclusions regarding the capture widths of the nuclear reaction (5.8), and the mass difference $m_{\pi^0} - m_{\pi^-}$.

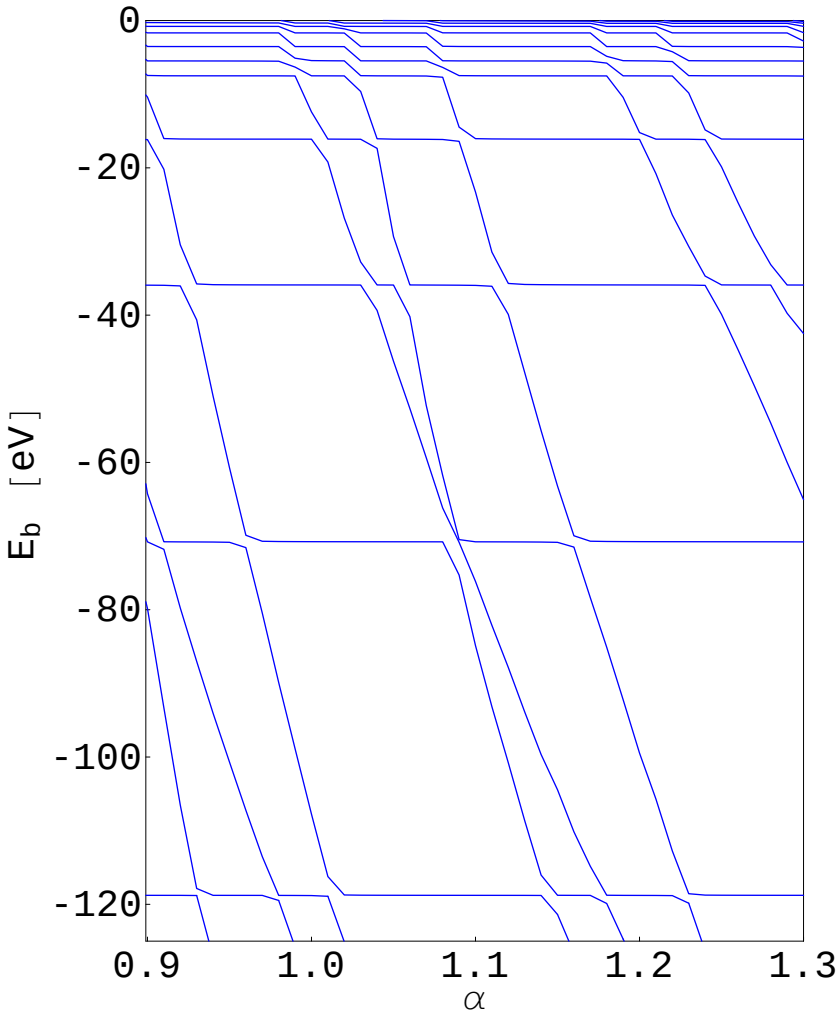

Figure 5.4. Stabilization graph showing meta-stable states of the $pp\pi$-molecule below the $3s$ threshold. The total angular momentum $J = 0$, and the parity under proton exchange $p = 0$.

5.4 Non-Linear Properties of Oligomers and Fullerenes

Patrick Norman, Dan Jonsson, Yi Luo, Olav Vahtras, Hans Ågren
Department of Physics, Linköping University

The basic goal of our current research is to relate the appearance of the strong non-linearity with both electronic and geometric structures of materials, with the ultimate goal in mind to design optically active and conducting devices through the use of molecular modeling and computations. We focus on quantum first-principle methods, since their inherent fulfillments of rigorous computa-

tional criteria are very useful for pinpointing specific properties and functions of particular chemical groups and substituents. The response theory methods have been developed in a broad Scandinavian collaboration and is now routinely applied to a number of non-linear properties, be it magnetic and electric, internal and external, time-dependent and time-independent, etc. Some of these are exotic, others have a very strong potential for technical applications and material science in general as we try to describe in this application. Our efforts are collected into the DALTON [Helgaker *et al.*, 1997] quantum chemistry program, which has been used for all the present communication. In Linköping we have, so far, focussed our applications on the following three non-linear effects.

Others have a very strong potential for technical applications

- Materials with strong second and third harmonic generations, SHG and THG. Such materials can be used for doubling, respectively, tripling of laser frequencies, introducing laser technology into the blue and near-UV wavelength regions. The SHG and THG capabilities are directly connected with hyperpolarizability tensors that we now can compute for polymeric compounds, metal-polymer interfaces, bucky molecules and solid charge transfer complexes, all with exceptional properties in this area. The industrial impact of UV lasers in the electronic industry is obvious, only to mention the possibility to manufacture extremely compact storage disks (CD:s). We use here the double direct random-phase approximation (RPA) and also the quadratic and cubic response extensions of RPA.

- Electro-optic and magneto-optic Kerr effects. These effects, connected to the electric, respectively magnetic, hyperpolarizabilities and susceptibilities, describe the action of external fields (electric or magnetic) on the polarization directions of light. A switch (or not) of the polarization plane gives an efficient representation of binary 0:s or 1:s, and Kerr compounds, like, probably, some first row transition metal alloys, therefore hold great promises as materials in future optical computers.

Hold great promises as materials in future optical computers

- Strong charge transfer complexes with potential use as optical switches. Simulations of 1-dimensional charge transfer complex for which a strong in-plane longitudal excitation dominates the hyperpolarizability, are now being extended to 2- and 3-dimensional charge-transfer compounds with several donors

and/or acceptors connected to the ring systems (so-called quadrupolar and octo+-polar molecules). Due to competing in-plane orthogonal excitations and "phase-matching" these are suitable non-linear materials. With reaction field response model calculations the critical role of the surrounding solvent can be monitored. The calculations of non-linear electric properties have mostly focussed on hyperpolarizabilities that connect directly to measured non-linear susceptibilities. These quantities play a key role in the understanding of non-linear optical response of molecules. The molecular systems that we have accessed fall largely into three categories; small systems, such as neon isoelectronic hydrides, for which extensive computational tests on electron correlation, basis sets, role of frequency dependence and vibrational dependence have been accomplished; oligomer sequences, in particular polyenes and polyenes for which the length dependence and convergence to the polymer value of the hyperpolarizability is of interest, and; special donor-acceptor compounds, in particular disubstituted benzenes, for which the charge transfer character of the HOMO-LUMO (highest occupied to lowest unoccupied molecular orbital) excitations implies large polarizabilities and hyperpolarizabilities.

Why do we need parallel computing?

The development of *ab initio* methods is driven by on one hand the theoretical improvements and on the other hand the development of more powerful computing resources and is aiming at an improved description of large scale systems. Solving the Schrödinger equation for a molecule at the *ab initio* level forces us to compute a vast number of integrals for the two-electron Coulomb operator. Traditionally a quantum chemistry calculation is preceded by computing all the needed integrals and storing them on disk. However, since the number of integrals grows as the number of basis functions to the fourth power we soon end up with a problem of storage. As the speed of computers has drastically increased we have been lead to a different (*direct*) strategy namely to recompute the integrals whenever needed for which the efficiency is determined by the ratio of I/O and computing speed. The former method is at present faster but as mentioned it suffers from the disk space deficiency. Thus by combining *direct* methods with parallel computing, we not only avoid the bottleneck of disk space but

Thus by combining direct methods with parallel computing, we drastically improve the speed of large-scale calculations

Number of rings	Number of nodes	Slave efficiency	Total efficiency	Theoretical efficiency
1	9	98.5	85.2	88.9
2	8	99.1	86.8	87.5
3	9	99.0	87.5	88.9
4	8	99.1	86.5	87.5
5	8	99.2	86.6	87.5
6	10	98.9	88.8	90.0

Table 5.1. Parallel efficiency. The number of nodes is the total number of nodes (including the master), and the number of slaves is this number minus one.

also drastically improve the speed of large-scale calculations. Furthermore, the CPU demanding tasks are strongly localized to a few subroutines so that our parallel implementation is relatively easy to perform and, in addition, will be most effective, *cf.* Table 5.1. Recently, we have presented this technique by calculating the polarizability and second hyperpolarizability at the RPA (Random Phase Approximation) level for a number of π-conjugated compounds, see below.

As a selection of recent publications we would like to refer to [Norman *et al.*, 1996a, Norman *et al.*, 1996b, Jonsson *et al.*, 1996]. More information can be found at:
`http://www.ifm.liu.se/Compphys/html/publicat.html`

Recent results with parallel computations

Oligomers

It has for a long time been recognized that conjugated molecules play an important role in the search for materials with large nonlinear optical (NLO) responses, and that modern theoretical techniques can be helpful in this search. Computations can pinpoint the microscopic origin of NLO properties and also reveal special structure to property relations. The (hyper)polarizabilities of conjugated polymers increase exponentially with increasing size of the oligomers until a linear dependence, or a saturation region, is reached.

When the molecular head-to-tail length L is adopted as an overall parameter, a unified picture for E_g, α and γ appears. It is noticable how much better the molecular length provides a unified despription for various types of oligomers in comparison to for instance the number of π-electrons, which also has been used in this

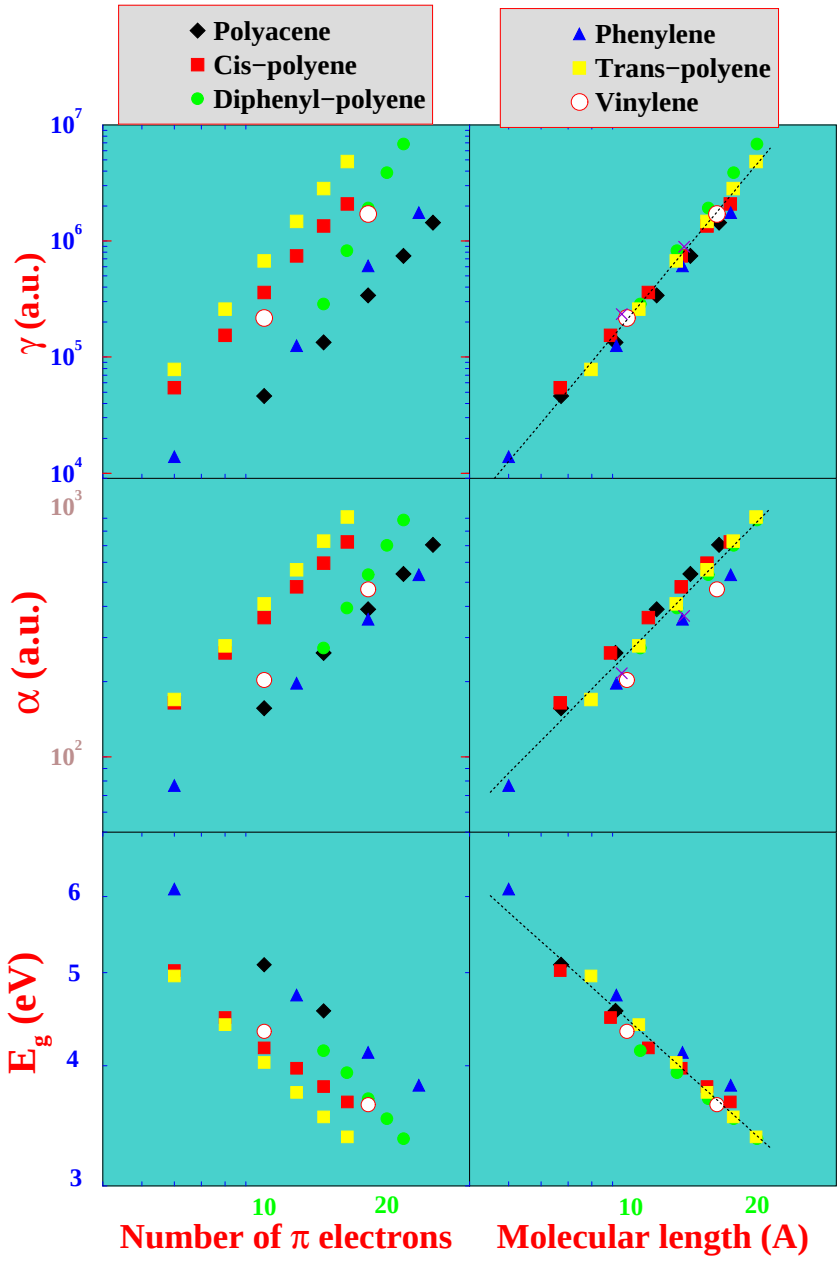

Figure 5.5. Optical gap (E_g), static polarizability (α) and hyperpolarizability (γ) versus number of π electrons (left) and molecular length for polyacenes (diamond), *cis*-polyenes (square), diphenyl-polyenes (circle), phenylenes (triangle), *trans*-polyenes (filled square) and vinylenes (star). The dotted lines show the obtained power law dependence, *cf.* Equation 5.14.

α (10^{-24} cm^3)	γ (10^{-36} esu)	Method
75.3	57.3	DD-CRPA

Table 5.2. Calculated values for static polarizability and hyperpolarizability of C_{60}

context previously in the literature (compare the left-most graphs to the right-most in Figure 5.5). For all compounds considered here, a common power law length dependence is obtained with the molecular length as structure parameter;

$$\begin{aligned} E_g &= 10.6L^{-0.38\pm0.02}, \\ \alpha &= 6.06L^{1.65\pm0.07}, \\ \gamma &= 14.83L^{4.19\pm0.10}. \end{aligned} \tag{5.13}$$

We believe that the predicted power law dependence of the optical energy gap versus molecular length can be of importance in applications. It means that a power law dependence for molecular properties versus the optical energy gap can be anticipated and that one can predict the polarizabilities by measuring the optical energy gap (or the so-called absorption edge). The power law exponent of -11.02 obtained for γ versus E_g is in close agreement with experiment for some of low-molecular-weight compounds. We refer to the original work for details [Luo *et al.*, 1997].

Fullerenes

It is well known that the hyperpolarizability of conjugated molecules is strongly associated with the delocalized nature of π-electrons. The hyperpolarizability is the nonlinear correction to the linearly induced dipole moment of a molecule, see Figure 6.6 on page 112. The optical nonlinearity of C_{60} has often been compared to that of the benzene molecule, and different values for the ratio between (hyper)polarizabilities of C_{60} and benzene have been reported previously in the literature, see our publications for a complete set of references [Norman *et al.*, 1997, Jonsson *et al.*, 1997]. For this purpose, we have calculated the polarizability and hyperpolarizability of benzene at the same level of approximation and with the same carbon basis set. We note that this is the first attempt to do this at the *ab initio* level. For the hydrogens we used a standard 4-31G basis set which matches the carbon basis set. The average values for the polarizability and hyperpolariz-

This is the first attempt to do this at the ab initio level

ability of benzene are found to be 9.3×10^{-24} cm^3 and 7.4×10^{-36} esu, respectively, which are 8 times smaller than the corresponding values for C_{60}. It thus confirms the increase of nonlinearity going from benzene to C_{60} although this increase is not as steep as previously suggested, see our publications for a complete set of references. We note that a ratio of 57 has been predicted although the hyperpolarizability for C_{60} in the same work is smaller than our theoretical value. This is probably a consequence of assuming an experimental γ value of benzene that is far smaller than what can be found elsewhere in the literature.

5.5 Correlation Phenomena in Atomic Collision Cascades

Rumjana Chakarova, Imre Pázsit
Department of Reactor Physics, CTH

Cascades of displaced atoms and vacancies are created in the material as a result of the stochastic slowing down of the projectile and the recoils. They cause radiation damage, sputtering as well as secondary emission of neutral or charged particles. Fluctuation effects in the processes above can be investigated by analysing the characteristics of higher moments, *i.e.*, variance and correlations [Pazsit and Chakarova, 199X]. The correlation functions or two-point densities describe joint cascade statistics at two phase space points. The variances of the yields can be obtained as integrals over the correlations. Although it is possible to give an explicit transport solution for both the variance and the correlations, the numerical or analytical evaluation of these formulae is extremely complicated and has not been achieved so far except in one very simple model case.

In this work various aspects of the variance behaviour and the correlation structure have been investigated by using the Monte Carlo method . A Monte Carlo code has been written based on a binary collision and power law interaction model. Varying the power parameter allows to consider different interaction regimes: high energy approximation where the scattering is determined by the Coulomb repulsion between the nuclei, as well as lower energies where the screening of the Coulomb interaction is essential. Energy losses due to interaction with electrons are taken into account. The conventional particle transport Monte Carlo algorithm

involves statistical simulation of one particle at a time moving through a given medium. To obtain realistic results, many particles have to be tracked. For example the variance estimation of the sputtered yield with statistical error less than 8%, requires simulation of one million ions with thousands of primary and secondary recoils for each of them. Thus the calculations are very demanding on CPU time. Fortunately, the algorithm is suitable for parallelization due to the independence of the cascades initiated by independent projectiles or recoils atoms.

The algorithm is suitable for parallelization due to the independence of the cascades initiated by independent projectiles or recoils atoms

The parallel Monte Carlo code using the MPI library has been implemented on the IBM SP-2 system at PDC. The total number of projectile histories is divided among the processors. The results obtained are then collected for further statistical evaluation. An important point is the generation of independent random number sequences for each processor. A linear speed-up of the calculations has been achieved. The code was successfully ported without changes to other parallel systems as well, *e.g.*, SGI Origin 2000 at UNICC, CTH, and CRAY T3E at NSC, since the MPI library as a message passing standard is available on all of them.

The mean and variance of the sputter yield and the vacancies have been obtained as functions of the ion energy. The effect of the free boundary on the structure of the vacancy correlation functions was investigated. Depth correlations of the vacancies created by a 100 keV Si ions when penetrating a Si semi infinite medium are shown in Figure 6.8 on page 113 as function of the depth variables Z_1 and Z_2. The positive correlations are sharply concentrated at $Z_1 = Z_2$ which means that the concurrent generation of vacancies is most probable to occur in depth layers very close to each other. The probability diminishes fast with increasing the distance between the layers. This behaviour is related to features in the space distribution of the vacancies in each particular cascade process. Soft collisions with small energy transfer are dominating which results in a tendency of small deflection angles of the projectile and nearly perpendicular ejection of recoils. The vacancies are not homogeneously distributed in the cascade volume but tend to form clusters at different depth layers. The effect is clearly seen in Figure 6.9 on page 113 where snapshots of the vacancies of three cascades are plotted.

5.6 Two-Photon QED Correction in Highly-Charged Ions

Björn Åsén, Martin Gustavsson, Sten Salomonson, Per Sunnergren
Department of Physics, CTH and Göteborg University

Background

The interest in QED (Quantum Electrodynamics) applications to atomic systems has been enhanced significantly in recent years, mainly through the experimental success in producing and studying very highly charged ions. In heavy-ion accelerators, like UNILAC at GSI in Darmstadt, GANIL in Caen, Super-EBIT in Livermore and the SUPER-HILAC at Berkeley, highly stripped atoms ions can be produced and accurately measured up to hydrogen-like uranium. These heavy few-electron systems are extremely relativistic and provide an excellent test of both relativity and QED in a region not previously carefully investigated. The basic theory of electronic structure is *quantum electrodynamics*, QED. The three main actors in QED are the electron field, the photon field and the emission and absorption of a photon by the electron. The physical picture is that electrons are particles surrounded by a virtual photon cloud. All physical interactions are described as the exchange of photons. Since the coupling constant $\alpha \approx 1/137$, which is characteristic for the emission of a photon by the electron, is small compared to unity, it is appropriate to make an expansion of the total electromagnetic interaction in terms of the number of exchanged photons.

These heavy few-electron systems are extremely relativistic

The term *bound state QED* refers to QED in atoms. In an atom the electrons are propagating in the field from the nucleus. For these systems it is sufficient to treat the nuclear field as a classical field. The reason is that we can as a first step approximate the nucleus as an infinitely heavy fixed particle in relation to the electron. We can then solve the Dirac equation for an electron in a static Coulomb field and consider the solutions as describing the electron field. The effect of nuclear recoil and other left out effects in this approximation can be treated separately.

The lack of a simple analytic structure of the Coulomb propagator compared, *e.g.*, to the free electron propagator restrict the analytical treatment of these systems. The old methods of solving bound-state QED problems were mainly restricted to lighter systems, where it is appropriate to make an expansion of the inter-

Effect	Value
First order self-energy (SE)	355.05
First order vacuum polarisation (VP)	-88.60
Second order VPVP	-0.94
Second order SEVP	1.14
Second order SESE	
Second order S(VP)E	
Nuclear size	198.68
Nuclear recoil	0.51
Nuclear polarization	-0.18
Lamb shift(theory)	465.23
Lamb shift(exp)	470(16)

Table 5.3. Contributions of various effects to the 1s Lamb shift in H-like uranium. The SESE and S(VP)E contributions are not yet fully calculated. All values are in eV.

action between the electron and the nucleus with charge number Z. The characteristic coupling constant of this expansion is $Z\alpha$, which tends to unity for heavy systems. To obtain sufficient accuracy in this high Z region, it is essential to treat most of the problems without using the $Z\alpha$ expansion. To summarize, the problem is to give an adequate description of electrons moving in a strong nuclear field. This cannot be done strictly analytically, but in combination with numerical techniques we can obtain a rigorous calculation scheme. The development of finite basis-sets to construct the electron propagators has simplified the building scheme of QED calculations and many complicated processes are now possible to evaluate in a more straight-forward manner than before.

One-electron Lamb shift in high-Z systems

The Lamb-shift for a single energy level in a one-electron ion includes, by convention, all corrections (except hyperfine structure and the non-relativistic reduced mass correction) beyond the point nucleus Dirac eigenvalue. This value can be obtained by a simple formula and assumes an infinitely heavy point nucleus.

To get a brief overview of the theoretical situation on the Lamb shift in highly charged ions, we list in Table 5.3 the different contributions which have to be included to obtain correct energy levels at the 0.1 eV level for the 1s-state in H-like uranium, although this is well below the present experimental error. This error, however,

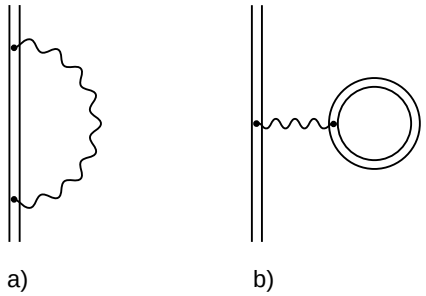

Figure 5.6. First order (one photon) QED effects, **a)** The bound electron Self Energy (SE), where the electron emitts and reabsorbs a virtual photon and **b)** the Vacuum Polarization VP. The double lines denote electrons propagating in an atomic potential field, and the wavy line a propagating photon.

is expected to be reduced by at least a factor of ten in the near future.

The finite nuclear-size effect on the energy levels can be included by the use of realistic nuclear charge distributions such as the two-parameter Fermi and deformed Fermi models. However, this introduces a non-negligible uncertainty at the 0.1 eV level and these effects will eventually set an accuracy limit of the QED test. To go beyond this, the knowledge about nuclear structure has to be improved. The correction that takes into account the nuclear motion (recoil) also has to be included. This can now be done to the relevant accuracy. Finally, also a small effect from the polarization of the nucleus by the electron field, has to be included.

The one-photon QED corrections, the self-energy (SE) and the vacuum polarization (VP), see Figure 5.6, which contribute to the Lamb shift, can now be accurately calculated. Considering the two-photon QED effects, Figure 5.7, the contributions can be separated into SESE, VPVP, SEVP and S(VP)E corrections. The SEVP and the VPVP corrections have recently been calculated.

To obtain a rigorous test of the Lamb shift in strong fields at the 0.1 eV level one has to calculate the remaining two-photon QED effects; the SESE, which, by using rough scaling laws, can be estimated to be of the order of 2 eV for H-like uranium, and the S(VP)E contribution.

A challenge for the numerical analysis will be the high-precision computation of multi-dimensional integrals. Here, parallel computer facilities will be of great importance.

The evaluation of the two-photon corrections represents a difficult task and a challenge for the numerical analysis will be the high-precision computation of multi-dimensional integrals. Here, parallel computer facilities will be of great importance in the calculations.

We have started a project to calculate the S(VP)E contribution. This will give us good experience and a solid basis when attacking the more difficult SESE contribution.

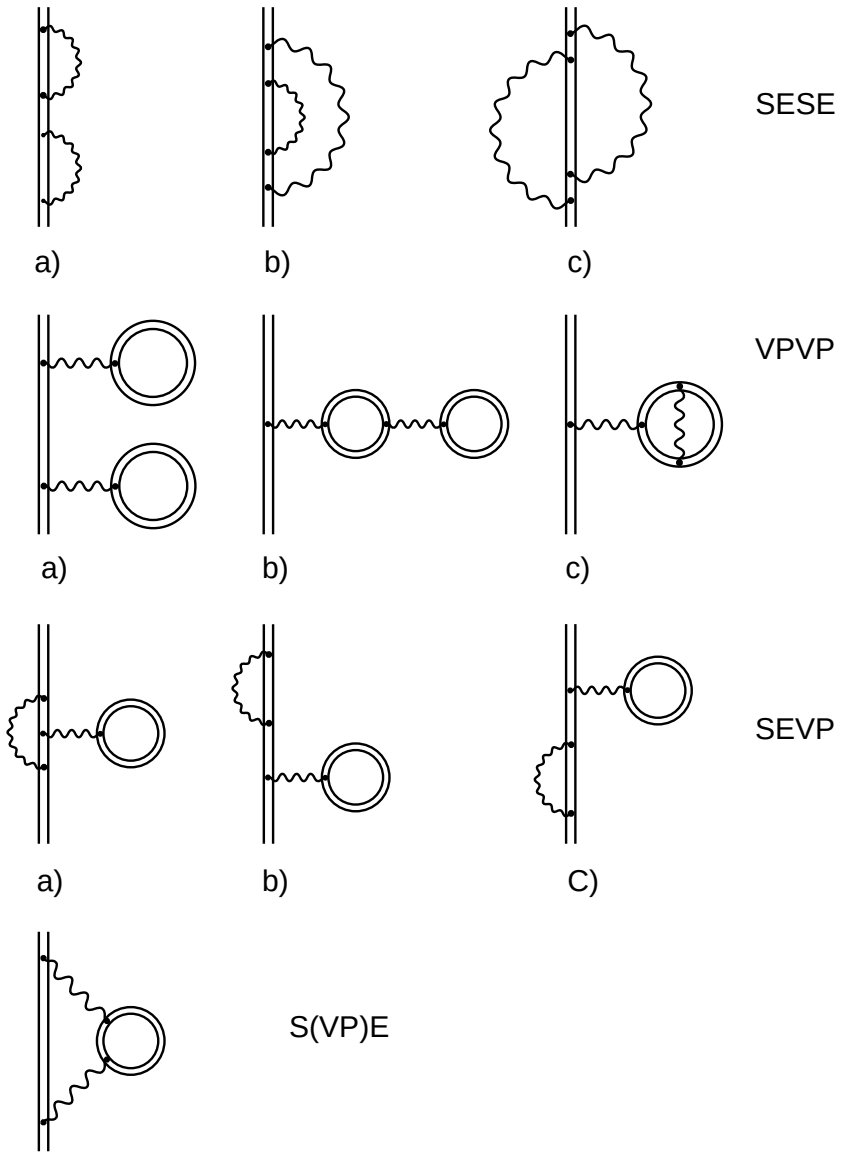

Figure 5.7. Second order (two photon) QED effects.

5.7 Radicals in Biophysical Systems

Leif A. Eriksson
Department of Physics, Stockholm University

Radical systems are of great importance as precursors or intermediates in a large number of biologically important reactions. They occur both naturally, as a means to catalyse certain reactions, enhance proton transfer mechanisms, *etc.*, as well as induced by external sources (direct radiation damage; radiation induced precursors; byproducts in metabolism mechanisms). Due to the short lifetimes associated with most radical species, complicated spectral analysis and interpretation, and the problems associated with maintaining the biological activity and function of the sample in question, theoretical calculations can provide a useful complementary tool for analysis. In recent years, the development of cost-effective computational techniques (*e.g.*, density functional theory) coupled with hardware development (parallel- and supercomputing fascilities) have enabled the use of accurate theoretical calculations for direct comparison with precise experimental measurements of processes of vital importance in biological material.

We have recently initiated an extensive research program, whereby radical structures and properties, and radical catalysed or radical controlled reaction mechanisms are investigated using gradient corrected DFT. Throughout, comparisons are made with available experimental data, and the work is often done in close collaboration with leading experimental research groups world wide. The main focus has to date been on three main areas of research: (i) stable or transient amino acid radicals, (ii) the structure and functionality of quinones in photosynthesis, and (iii) the effects of radiation damage to DNA. In the follwing a short description of the results is presented. In the bibliography section, the references resulting from computations hitherto performed on the computers at PDC are listed. It is clear that the resources made avaliable for our usage at PDC have played a key role in the success of the project to date.

It is clear that the resources at PDC have played a key role in the success of the project to date

Amino acid radicals

We have in this project concentrated on model systems of stable or transient radicals detected in various enzymes and proteins, where they serve as "storage units" for enzyme reactivity or act as cat-

alysts in chemical reactions [Eriksson, 1997, Himo and Eriksson, 1998, Lassmann *et al.*, 199X, Eriksson, 199X, Eriksson and Himo, 1997, Himo and Eriksson, 199X]. On the basis of equilibrium geometry and hyperfine parameter calculations we have located a possible source to the difference between glycyl radicals ecountered in various anaerobic enzymes [Himo and Eriksson, 1998], and determined the geometry and protonation state of the sulfinylimine radical observed upon destruction of the active site of ribonucleotide reductase by means of a modified substrate [Eriksson, 199X]. We have also determined the reaction products between histidine and OH radicals [Lassmann *et al.*, 199X] as well as developed a detailed scheme for the conformational dependence of the hyperfine parameters in *e.g.*, tyrosine and tryptophan radicals observed in several proteins, as a tool for structural analysis [Eriksson and Himo, 1997]. For one system (Pyruvate Formate Lyase), where the reaction mechanism is catalysed by a stable glycyl radical, a detailed study has been performed of the full reaction mechanism [Himo and Eriksson, 199X]. Further work involves studies of the radical transfer mechanism in ribonucleotide reductase, effects of molecular oxygen to anaerobic protein centered radicals, and the radical catalysed reaction mechanism of galactose oxidase.

A detailed study has been performed of the full reaction mechanism

Quinones

Quinones play a central role in photosynthesis, where they act as acceptors and mediators of the electrons released from the light excited chromophors, and subsequently as proton carriers across the thylakoid membranes. These protons are subsequently used by the ATP-synthetase protein in the cell energy storage reactions. In the first of our papers on quinones [Eriksson *et al.*, 1997] we determined the hyperfine structures of different model systems, as well as the plastoquinones employed by green plants. We could also show the importance of hydrogen bonding for various key properties of quinones, such as electron affinities, and were able to confirm a recent experimental proposal for the order of the 2 electron + 2 proton uptake. In a comparative structural analysis of the quinones employed by green plants vs those used by photosynthetic bacteria, we were subsequently able to determine a clear relation between quinone head-to-tail orientation and organism specificity [Himo *et al.*, 199X]. We are now extending the

models by incorporating parts of the surrounding and the molecular framework connecting the quinone pairs in green plants and in bacterial reaction centers, in order to gain more detailed knowledge about the very fine-tuned electron transfer mechanisms of photosynthesis.

Radiation damage to DNA

There is a direct relation between the increased UV-radiation due to ozone depletion and increased rates of skin cancer

It is well known that *e.g.*, UV and gamma-radiation on living material results in a large number of reactions in and around DNA, resulting in *e.g.*, DNA strand breakage, protein-DNA cross links, or DNA base modifications. There is a direct relation between the present reports of increased UV-radiation due to ozone depletion and increased rates of skin cancer. As a means to gain insight of the detailed mechanisms behind radiation induced modifications to DNA, we have therefore initiated a research program where we investigate DNA-based radicals, their possible sources and subsequent reaction steps. Thus far two publications have been submitted in which we investigated the role of OH radicals to the formation of cytosine radicals [Wetmore *et al.*, 199Xb], and performed a comparative study of all possible dehydrogenation, hydrogenation and hydroxylation products of the structurally related thymine and uracil DNA bases [Wetmore *et al.*, 199Xa]. Further work involves similar studies of the larger adenosine and guanine bases, sugar radicals, and radical induced reactions within DNA as well as between DNA and surrounding proteins.

5.8 Monte Carlo Simulations of Vortices in High Temperature Superconductors

Jack Lidmar, Mats Wallin
Department of Theoretical Physics, KTH

A type II superconductor placed in a magnetic field shows many unusual properties. The magnetic field will not penetrate the sample homogeneously as one might have expected, but will instead be concentrated to small flux tubes called vortices. These line-like objects interact strongly with each other, and with various types of imperfections in the material, thereby offering the opportunity to investigate a variety of physical phenomena of great theoretical as well as experimental interest.

The phase transition between the superconducting and the normal state is strongly affected by the motion of vortices. Even in the absence of an external magnetic field, vortex fluctuations have important effects on both static and dynamic quantities. When a current is applied to a superconductor, a vortex will experience a Lorenz force. If the vortex is free to move in response to this force, a voltage will be induced according to the Maxwell equations, leading to dissipation and loss of superconductivity.

In Monte Carlo simulations of vortex systems we can calculate several key quantities of direct experimental relevance. By driving a current through the system, simulated by applying a force on each vortex, and measuring the voltage response, we obtain the nonlinear IV characteristics directly from the simulation. In the case of no applied force, vortex fluctuations will still induce voltage fluctuations, and the linear resistance can be calculated from the Kubo formula,

$$R = \frac{1}{2T} \sum_{t=-\infty}^{\infty} \Delta t \, \langle V(t)V(0) \rangle \, .$$

Close to a continuous phase transition this quantity and the IV characteristics follow simple scaling laws, allowing universal critical exponents to be extracted from the Monte Carlo data. In this way we have determined the dynamical critical exponent $z \approx 2.7$ for the transition in zero external magnetic field for a lattice vortex model with short range interactions in both clean systems and systems with quenched point disorder [Lidmar *et al.*, 1997]. This result is relevant for interpreting recent experiments on high temperature superconductors.

This result is relevant for interpreting recent experiments on high temperature superconductors

In the case where there is an external magnetic field, and therefore a net number of vortices, it is extremely important to take into account the interaction with various types of disorder – point defects, columnar defects, twin boundaries, *etc.* The transition temperature and the critical current of a superconductor can be significantly increased by pinning the vortices to these defects, thereby reducing their mobility. A way to enhance the pinning is by artificially introducing columnar defects into the material by heavy ion irradiation. Apart from the practical importance in applications this is also a theoretically very interesting problem which has received considerable attention recently. At low temperatures the vortices are pinned by the disorder and the system is in

a glassy state characterized by a highly nonlinear current-voltage dependence and a vanishing linear resistivity. As the temperature is raised the vortices delocalize and the system turns into an entangled flux liquid. The phase transition between these states is subject to current investigation.

The problems we study are ideally suited for the parallel computing resources at PDC

The problems we study are ideally suited for the parallel computing resources at PDC. The simulations are very computer intensive, especially the problems with disorder, since they involve extensive averaging both over vortex configurations and over different realizations of the quenched disorder. Our codes implement this averaging process by sampling disorder realizations independently on each node, leading to a very efficient parallelization. The success of these difficult computations depend crucially on the use of the supercomputer facilities at PDC.

5.9 Medium-Range Order in a Simple Monatomic Liquid

Mikhail Dzugutov[1]
Center for Parallel Computers, KTH
Babak Sadigh
Department of Theoretical Physics, KTH
Stephen R. Elliott
Department of Chemistry, University of Cambridge, UK

Introduction

Medium-range structural order (MRO) is found in a wide range of amorphous solids. A prominent structural feature of these systems, from which the presence of MRO is inferred is the so-called *first sharp diffraction peak* (FSDP) which usually occurs in the structure factor, $S(Q)$, at a value of the scattering vector Q in the range $1 < Q < 2\,\text{Å}^{-1}$ [Moss and Price, 1985]. As well as corresponding, apparently, to real-space structural correlations with a period $2\pi/Q = 3 - 6\,\text{Å}$, *i.e.*, on the length scale corresponding to MRO [Elliott, 1991], the FSDP behaves in an anomalous away in relation to the other peaks in $S(Q)$ as a function of temperature, pressure and composition [Elliott, 1992]. The structural origin of the FSDP is still the subject of considerable dispute (see *e.g.*, [Moss and Price, 1985] and [Elliott, 1992] for reviews).

A most intriguing aspect of the FSDP is that it is a rather

[1]MD would like to thank the Swedish Natural Science Research Council (NFR) for supporting this project.

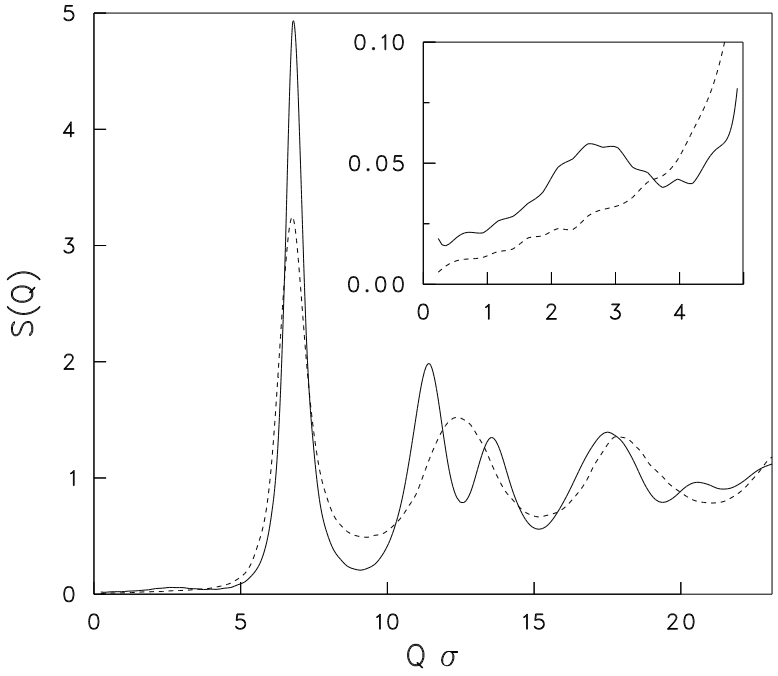

Figure 5.8. The structure factor of the IC liquid (solid line) and for the LJ liquid (dashed line). The long-wavelength part is presented in the inset.

universal feature which cannot be associated with any particular type of local order, or chemical order effects. An interpretation of this universality that has been previously suggested [Elliott, 1990, Cervinka, 1985, Cervinka, 1987] is that the presence of void-regions in the structure of covalently bonded non-crystalline materials gives rise to the FSDP in the overall structure factor. This void-based interpretation has the merit of complete generality, *i.e.*, it is not restricted to a particular type or structure of non-crystalline material. In this approach, the structure is treated as a mixture of spherical atoms and voids, and these two entities are regarded as different atomic species. Such an analysis for a monatomic amorphous system was first performed by Blétry [Blétry, 1990].

In this study, in order to test the above void-based approach, we have analyzed the medium-range atomic structure of a simple monatomic liquid simulated by molecular dynamics (MD). A singular structural feature of this liquid which we exploit in this study is the presence of MRO manifested by a well-defined pre-peak in $S(Q)$, see Figure 5.8. By contrast, $S(Q)$ of the Lennard–Jones (LJ) liquid, also shown in Figure 5.8, is entirely featureless in the respective range of Q. The results we present here provide con-

vincing evidence that the MRO structure featured by this liquid can be well accounted for by vacancy ordering.

Model

The liquid structure investigated here was generated in a molecular dynamics simulation (MD) utilizing a judiciously designed pair potential [Dzugutov, 1992] which was tailored to favour an icosahedral configuration of the first shell of neighbours. This type of short-range order, which has never been observed in any real monatomic simple liquid, is known to play a crucial role in the glass formation of metallic systems of simple constitution [Hafner, 1987]. This model, hereinafter referred to as IC, can thus be regarded as a monatomic template for multicomponent metallic glass-formers. Indeed, it has been found to exhibit a pronounced glass-forming ability. It could be cooled down to an anomalously high viscosity while remaining in the thermodynamically stable liquid state [Dzugutov, 1992, Dzugutov, 1994], demonstrating strongly non-Arrhenius behaviour as well as stretched-exponential relaxation [Dzugutov, 1994]. These are typically associated with the liquid dynamics close to the liquid-glass transition [Götze and Sjögren, 1992]. Besides this, its diffusive dynamics revealed a substantial rate of vacancy-assisted hopping [Dzugutov, 1994]. Another remarkable distinction of this liquid is that it was found to freeze into a dodecagonal quasicrystal [Dzugutov, 1993].

The model could be cooled down to an anomalously high viscosity while remaining in the thermodynamically stable liquid state

The prepeak we analyse here is situated at approximately 40% of the position of the main diffraction peak. This structural peculiarity distinguishes the liquid simulated here from all the known simple monatomic liquids. It allows to test the void-based interpretation of MRO. The apparent advantage of using a monatomic liquid for this purpose is that it allows the effects of topological ordering on MRO to be distinguished from chemical-order effects which can also contribute to this structural effect [Hafner, 1987].

Simulation

The MD simulation producing the liquid configurations that we analyse here was carried out using a system of 16 384 atoms. Note that all the quantities hereinafter are given in the Lennard–Jones reduced units which were used to define the pair potential employed here. The IC liquid was simulated at a reduced number

density, ρ, of $0.85\sigma^{-3}$ and a reduced temperature, T, of 0.5ϵ which corresponds to its estimated freezing point [Dzugutov, 1993]. We also analysed the structure of the LJ liquid, simulated at the same reduced number density and at a reduced temperature T, of 0.7ϵ, which approximately corresponds to its triple point. The LJ structure was taken as a reference since, as one can see from its structure factor in Figure 5.8, it does not possess the MRO observed in the IC liquid. Before applying the structural analysis, the instantaneous configurations generated in MD runs were subjected to the steepest descent minimization routine. This procedure removes the temperature-induced perturbation thus revealing the so-called "inherent liquid structure" [Stillinger and Weber, 1984], which allows structural features of the two liquids to be contrasted.

Results

To identify the voids in the structure, we employed the following procedure. We assumed that all the atoms can be regarded as hard spheres with an effective diameter 1.01σ. At this distance, the radial distribution function $g(r)$, starts to deviate from zero. We located and sorted out structural vacancies which were identified as non-overlapping spherical voids of a chosen diameter. By varying the void diameter, we could investigate the effect of this parameter on the ordering of voids, and its contribution to the intermediate-range structural order of interest. Figure 5.9 shows the statistics of vacancies as a function of the vacancy diameter for both liquids. The LJ liquid apparently contains remarkably few vacancies in the atomic-size range as compared with the IC liquid. The main contribution to its total free volume arises from the relatively high number of smaller-size vacancies. The latter comprise irregularly shaped structural voids which accounts for the main share of the available free volume. This indicates that the LJ liquid, as compared with the IC liquid, is characterized by a much looser local structure. Note that in the IC liquid the first minimum of the pair correlation function is much deeper than the one in the LJ liquid [Dzugutov, 1992]. In the former case, separation between the first shell of neighbours and the rest of the structure is more pronounced. This is apparently related to the more compact character of the icosahedrally ordered structural units as compared with the FCC-related ones in the LJ liquid. To investigate the connection between the presence of well-defined vacancies

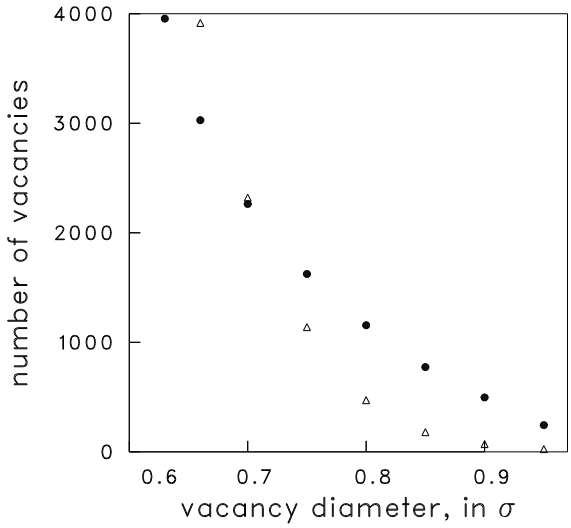

Figure 5.9. The number of spherical vacancies identified in the structure as a function of the assumed vacancy diameter. Solid dots, IC liquid; triangles, LJ liquid.

in the IC liquid and the MRO, we use an approach suggested by Blétry [Blétry, 1990], whereby the structure is regarded as a binary mixture of atoms and spherical voids. The structural correlations in the atom-void binary mixture may be characterized by calculating the respective partial structure factors. We used the definition of the partial correlation functions as formulated by Ashcroft and Langreth [Ashcroft and Langreth, 1967]

$$\begin{aligned} S_{AV}(Q) &= \delta_{AV} + 4\pi\rho_0\sqrt{x_A x_V}\int_0^\infty [g_{AV}(r)-1]\,\frac{\sin Qr}{Qr}r^2 dr \\ S(Q) &= \sum_A\sum_V \sqrt{x_A x_V}\frac{b_A b_V}{\langle b^2\rangle}S_{AV}(Q) \end{aligned}$$

The indices A and V above refer to the two species involved, atoms and voids, respectively. b_A and b_V are the respective scattering lengths, x_A and x_V the number concentrations, $g_{AV}(r)$ is partial pair correlation function, δ_{AV} is the Kronecker symbol and ρ_0 is the total number density. Since the scattering length of a void is zero, the total structure factor $S(Q)$ reduces to the partial atom-atom structure factor.

Figure 5.10 shows the atom-void and void-void partial structure factors for several values of vacancy diameter. Both of these latter structure factors feature well-defined prepeaks, the positions of which agree well with the location of the prepeak in the total structure factor in Figure 5.8. However, the intensity of these

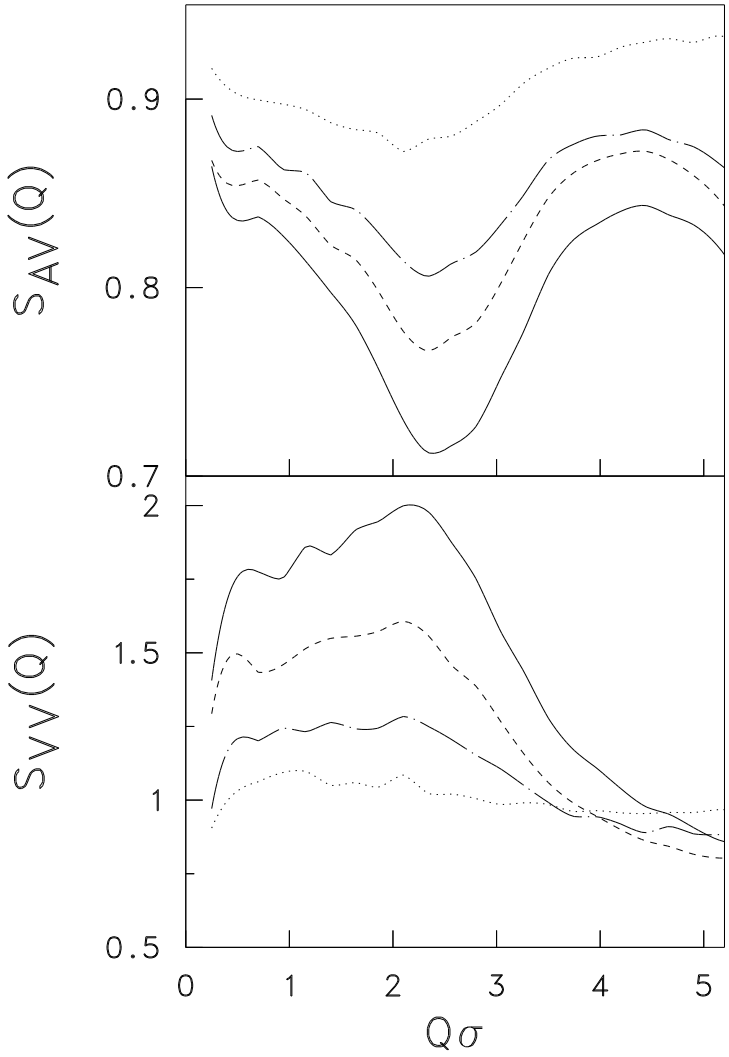

Figure 5.10. Ashcroft-Langreth partial structure factors of IC liquid for different values of vacancy diameter d. **Top:** atom-vacancy correlations; **Bottom:** vacancy-vacancy correlations. Solid line, $d = 0.63$; dashed line, $d = 0.7$; chain-dotted line, $d = 0.8$; dotted line, $d = 0.95$.

peaks reduces as the size of the vacancies increases. This can be ascribed to the respective decrease in the number densities of the vacancies. On the other hand, the atom-void partial structure factor for the LJ liquid in Figure 5.10 is structure-less in the same domain of Q, which is entirely consistent with the absence of the FSDP in its total structure factor, Figure 5.8.

Discussion

The above analysis demonstrates the key role of atom-vacancy correlations in generating the FSDP observed in the structure factor of the IC liquid. These results thus support the hypothesis of the origin of MRO as being induced by the ordering of vacancies.

Based on these results, we may suggest the following picture of MRO in the liquid investigated here. The icosahedrally ordered local structural units, comprising the structure of this liquid, are rather stable, and have a tendency to form a network; this may be concluded from the pronounced viscosity of this liquid and its glass-forming ability [Dzugutov, 1992]. The rigidity of the icosahedrally ordered structure leads to the creation of a well-defined network of atom-size vacancies, producing the observed FSDP. This conclusion is of immediate relevance for simple metallic glass-formers possessing a similar kind of structure. We also conclude that the formation of the intermediate-range order observed in amorphous solids begins in the equilibrium liquid phase.

It has to be noted that vacancies can be directly observed in the quasicrystal structure [Dzugutov, 1993] into which this liquid was found to freeze. Moreover, the presence of vacancies in this phase explains phason dynamics [Dzugutov, 1995], a generic form of structural relaxation in the quasicrystal which leads to its formation and thermodynamical stability. In the glassy state [Mattila *et al.*, 1996], systems with icosahedral local order demonstrated a pronounced ability to sustain radiation-induced vacancies.

This study convincingly demonstrates the FSDP, should not necessarily be associated with the network structure arising from the complex geometry of constituent molecules or strong bonding. We have demonstrated that it may arise in a simple glass-forming liquid from the ordering of vacancies induced by the icosahedral local order.

5.10 Electronic Structure Calculations for the Physics and Chemistry of Surfaces[2]

Lennart Bengtsson, Thomas Mattsson, Johan Strömqvist, Mats Persson, Göran Wahnström
Department of Applied Physics, CTH

In the past decade, tremendous progress has been made in the developments of techniques for first principle calculations of the total energy of solids, surfaces and molecules. Plane-wave and pseudopotential methods that are based on density functional theory have now progressed to a point where accurate and reliable calculations can be performed on systems containing hundreds of atoms [Payne *et al.*, 1992]. Our project concerns electronic structure calculations of atom- and molecule-surface interactions using these methods. The main goal has been to develop potential energy surfaces (PESs) that can be used in quantum and classical molecular dynamics calculations to develop our understanding of elementary physical and chemical processes at surfaces on an atomic scale. Our specific projects concerns surface reaction dynamics, quantum diffusion on surfaces, and structure and energetics of oxide surfaces. A most important ingredient of our work has been the close contacts and collaborations with Dr Hammer and associates at DTH, Lyngby, Denmark. For instance, through these contacts, we have access to a message passing version of the plane wave code called DACAPO [Hammer and Nielsen, 1995].

Potential energy surfaces for hydrogen atoms on metal surfaces

Using the electronic structure code DACAPO on the SP-2 machine, we have determined the total energy of the (1×1) structure of H on Ni(100) in 16 different configurations. The results for vibrational frequencies, adsorption energies, and heights are in very good agreement with available experimental data [Mattsson *et al.*, 1997]. As discussed below, we have used the calculated data to construct a model potential that is used in quantitative Monte Carlo calculations of quantum diffusion of H and D.

Using the same code on the SP-2 machine, we have also calculated the total energy for a (2×2) structure of H atoms adsorbed on and absorbed inside a Cu(111) surface in three major high

[2]This work was supported by NFR and the NUTEK/NFR interdisciplinary materials consortium: Theoretical and Computational Materials Physics.

symmetry configurations [Strömquist *et al.*, 199X]. The derived binding parameters from this calculation are in good agreement with available experimental data. A somewhat unexpected finding is the relative low potential barrier for absorption of the H atom into the bulk. From the calculated energy points, we have constructed a model model PES that have been used to study the classical dynamics of H absorption in and absorption on a Cu(111) surface.

Quantum tunneling and diffusion

Hydrogen diffusion on metal surfaces has been subject of great theoretical effort over the years with a renewed interest caused by recent experiments on hydrogen diffusion on nickel surfaces in the low-temperature regime [Zhu *et al.*, 1992].

Our recent work [Mattsson *et al.*, 1995] has successfully shown that it is possible to gain qualitative understanding of the quantum behavior of hydrogen diffusion on metal surfaces, especially concerning the transition from semi-classical diffusion to quantum tunneling when lowering the temperature (see Figure 6.10 on page 114). However, fundamental questions still remain unsolved, in particular the experimentally observed absence of a pronounced isotope effect [Lin and Gomer, 1991]. Both the transition temperature between semi-classical and quantum behavior as well as the magnitude for the diffusion constant in the quantum regime are found to be similar for both hydrogen and deuterium.

We are now able to treat all atoms fully quantum mechanically

We have improved our treatment by developing a Quantum Monte Carlo (QMC) program and we are now able to treat all atoms fully quantum mechanically. An accurate model potential has been developed based on extensive *ab initio* calculations of the total energy for the adsorbed H atom, which were performed on the SP-2 at PDC (see previous section). This information has been used to make a detailed investigation of hydrogen tunneling utilizing the improved description of the interaction potential [Mattsson and Wahnström, 1997a, Mattsson and Wahnström, 1997b].

In the future we plan to perform *ab initio* calculations of the total energy for lower hydrogen coverages, in particular for H adsorbed on the Ni(111) surface. We would also like to include electronically non-adiabatic effects to be able to understand the relative importance of the coupling to the lattice vibrations compared with electronic excitations.

Potential energy surfaces for an Eley-Rideal reaction of hydrogen atoms on a Cu(111) surface

We have performed calculations of various sections of the PES for the Eley-Rideal reaction of H atoms on a Cu(111) surface in which an incident H atom reacts directly with an adsorbed atom. The aim was to construct an accurate model PES that can be used in reaction dynamics calculations. We have more or less completed this project and the results have been presented at the Euroconference on "Total Energy Methods to study the Dynamics of Surface", Corfu. As a first step, we have investigated the effects of the surface corrugation on this reaction using the calculated energy points for the (2×2) structures of H atoms to construct a corrugated version of our semi-empirical PES [Caratzoulas *et al.*, 1997]. In order to have a more accurate description of the reaction region of the PES, we have mapped out three two-dimensional sections of the PES: (1) the collinear configuration of the two H atoms, (2) the hollow-bridge-hollow and (3) hollow-top configurations in which one H atom is fixed in the equilibrium position at the hollow site and the other atom is in the plane spanned by the surface normal and the $[\bar{1}10]$ and the $[\bar{2}11]$ surface directions, respectively. The results for the collinear configuration shows that the PES is attractive in the sense that the exothermicity is predominantly released in the entrance channel, which is consistent with state-to-state molecular beam experiments by Rettner and Auerbach [Rettner and Auerbach, 1995].

The most computationally demanding configurations have been those where it has been necessary to include spin polarization

In total, we have calculated about 150 energy points for the interacting H atoms on the Cu(111) surface and each configuration has involved from 6 to 15 nodes. In particular, the most computationally demanding configurations have been those where it has been necessary to include spin polarization.

5.11 Paper Optics on Fujitsu VX

Teresita Quinteros, Måns Bjuggren
Institute of Optical Research, Stockholm

Introduction

In the manufacturing of paper it is well known that the addition of small irregular particles (fillers and coating pigments) enhances the light scattering and therefore the visual quality of the paper

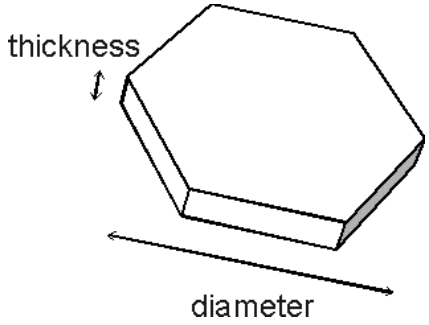

Figure 5.11. Scheme of a simulated single clay particle.

and print. Traditionally, the analytical study of paper optics is done by using the so-called Kubelka-Munk equations [Kubelka and Munk, 1931, Kubelka, 1948], *i.e.*, a two-stream radiative transfer theory [Schuster, 1905]. The Kubelka-Munk equations adequately describe the experimental results provided several limiting conditions are met. However, the real structure and physical characteristics of paper are not considered.

We wanted to study the optical behavior of pigments in paper coatings. With that purpose, we performed numerical simulations of the light scattering by clusters of pigments using formal scattering theory. Our aim was to depict the basic mechanisms involved in the scattering of light by the bulk of paper coating layers and develop a suitable technique for coating optimization.

Pigments in paper coatings are irregular particles of sizes comparable with the wavelength of visible light. Many different numerical methods to calculate the light scattering by particles have been developed [Wriedt, 1998] and computer programs are nowadays available to the research community.

Numerical method

To perform our simulations we used the discrete dipole approximation (DDA) [Draine, 1988, Draine and Flatau, 1994], a method that has proved to fairly well describe the light scattering by particles with complicated geometries. In the DDA particles are represented as a lattice of dipole fields and the scattering of light is calculated as the sum of the light irradiated from each dipole when receiving the incident light and the light from all other dipoles. Our calculations were done with Selma, PDC's Fujitsu VX/2 vector computer. The clusters of pigments were built following the

characteristics presented by commercial pigments regarding size distribution and refractive index. We described the clay pigments as hexagonal flakes with diameters chosen following the size distribution of a commercial clay, and thickness randomly selected in a given interval (Figure 5.11). Each particle was randomly located in the volume of the cluster. Preferential orientation of individual pigments and porosity of the cluster could be selected.

We simulated the light scattering by clusters of clay pigments in the bulk of the coating layer [Quinteros and Bjuggren, 1998]. Becasue of the current memory limitation of 2 Gbyte we could not simulate a cluster big enough for edge effects to be small. We chose the cluster's outer shape to be a sphere. A spherical volume was cut from a larger, cubic cluster, see Figures 6.12 and 6.13 on page 115. We compared the scattering properties of these porous spheres with those of a solid of a solid sphere of the same size, the last calculated using Mie theory.

Some examples and discussion

We studied the influence of the cluster porosity on the light scattering. Figure 5.12 shows the scatterd power, *i.e.*, the flux of the scattered irradiance for spherical clusters, $4\,\mu$m in diameter and with two different porosities, as function of the polar scattering angle. The results are compared with those for a solid sphere of the same size, which were calculated with Mie theory. The scattering at angles smaller than 20° is dominated by the spherical shape of the clusters as a whole. The relative difference in the scattered power (dP/P), averaged over the scattering angle is 1.77, between the 66% and the 33% porosity samples.

The extinction coefficient[3] obtained in the calculations does not depend appreciably on the porosity in the calculated range (up to 75% porosity) while the asymmetry factor[4] decreases with porosity. The effect, for a dilute gas of porous clusters, is a reflectance that increases with the clusters porosity. This, in turn corresponds

[3]The extinction coefficient is defined as the probability for the incident light to be absorbed or scattered, divided by the projected area the cluster presents to the incident light. In our simulations, the projected area is defined as πa^2, a being the radius of the sphere we use to cut the clusters with.

[4]The asymmetry factor is defined as the mean value of the cosine of the scattering angle, weighted with the phase function, *i.e.*, the amplitude scattered in each direction.

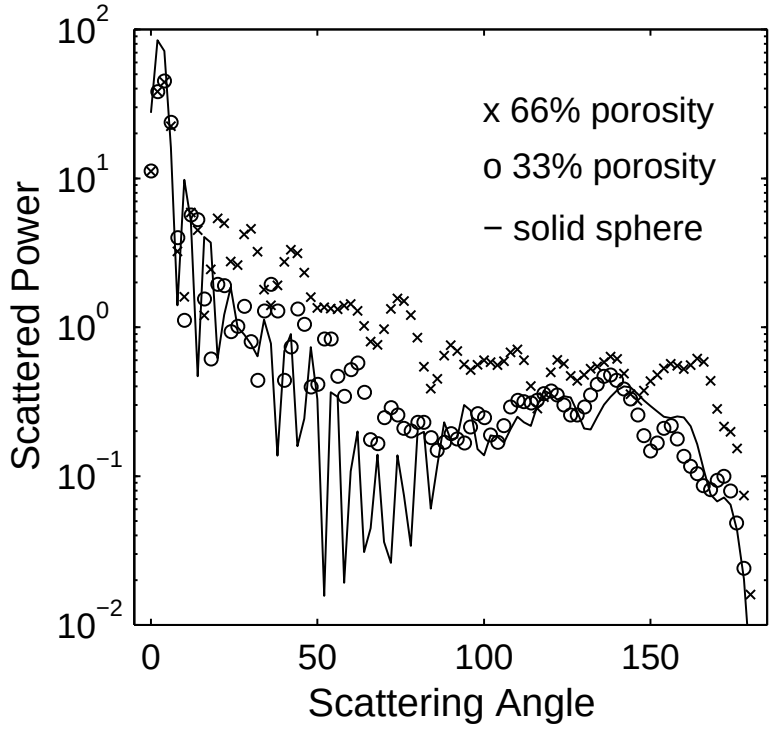

Figure 5.12. Scattered power for spherical clusters of clay particles with two different porosities and $4\,\mu$m total diameter, and for a solid sphere of the same size.

to an increasing scattering coefficient in the sense of the Kubelka-Munk theory. Measurements of the Kubelka-Munk scattering coefficient for clay and calcium carbonate coatings also show an increase with porosity [Engström and Rigdahl, 1992]. The results of the simulations follow this trend in the porosity dependence.

We further studied the wavelength dependence of the light scattering in the visible range, again using $4\,\mu$m spherical clusters, now all with 40% porosity. The extinction coefficient we obtained did not depend appreciably on the wavelength. On average it was 1.2 to 1.5 times higher than that of a solid sphere with $4\,\mu$m diameter. Analysis of the asymmetry of the scattered irradiance for the porous spheres indicated that the Kubelka-Munk scattering coefficient for a dilute gas would increase with the wavelength. However, experimental results on clay coatings have shown that it decreases by 50% in this wavelength range [Engström and Rigdahl, 1992]. We think our calculations overlooked the contribution to the total scattering of the shorter wavelength by small pores in the sample. Further studies are needed to clarify this point.

Conclusion

We have exemplified the applicability of the DDA to the study of the optical behavior of simulated paper coating clusters about 10 wavelengths cube. In particular we have studied the dependence of the light scattering on the wavelength of the incident light and the porosity of the sample. Results from the porosity scan followed the expected trend from experimental data while the wavelength scan did not. Further theoretical and experimental studies are needed to fully understand the capability of the method to study effects on light scattering from properties such as the porosity, structure, and surface roughness of the samples. However, the results indicate that our methodology can provide a powerful tool to address the problem of light scattering in dense particulate media such as paper coatings.

5.12 Spin Chains in a Random Field: A DMRG Analysis

Ausrius Juozapavicius, Sergio Caprara, Anders Rosengren
Department of Theoretical Physics, KTH

Spin chains in a transverse random field have been of an increased interest in recent times because of their disorder-driven quantum transitions and especially due to the fact that the critical point of such systems is not an isolated point of nonanalyticity, but a wide region, where the zero-field susceptibility diverges. The system of our study is an anisotropic XY spin-1/2 chain in a random field (XYRF), described by the Hamiltonian

$$\mathcal{H} = -J \sum_i S_i^z S_{i+1}^z - \gamma J \sum_i S_i^y S_{i+1}^y - \sum_i h_i S_i^x - H \sum_i S_i^z,$$

where the spin matrices S^α are just one half of the corresponding Pauli matrices $S^\alpha = \sigma^\alpha/2$, h_i are random-field values uniformly distributed in the interval $-h_0 < h_i < h_0$, H is a constant field in the z direction, added to produce spontaneous symmetry breaking in our calculations, and $0 \leq \gamma \leq 1$ is a factor of anisotropy: when $\gamma = 0$, we have totally anisotropic spin-1/2 quantum Ising model in a transverse random magnetic field (QIMRF), while $\gamma = 1$ gives the standard XY model. We take the units of energy such that $J = 1$. Recently the QIMRF has been obtained as an effective model for the one-dimensional Kondo lattice model and some features of the latter can be explained in terms of the QIMRF. Quantum

transitions in general are believed to be of great relevance to the physics of high-T_c superconductors. However, random systems are extremely difficult to solve analytically. There are two cases, when we have analytical results for the XYRF model - the exact solution for this system with zero random field was obtained by Lieb, Schultz and Mattis, and many exact critical properties for $\gamma = 0$ system were calculated by Fisher by means of the real-space renormalization group. However there is no knowledge of the dependence of the critical properties of the XYRF system on the factor of anisotropy γ and our calculations are supposed to fill in this gap.

The density-matrix renormalization group (DMRG) approach is used for solving the XYRF system. The DMRG was developed by White, who improved Wilson's real-space renormalization group. The main idea of the DMRG method is to take two blocks (most often they consist each of two spins of the chain), add them together into a superblock, calculate the Hamiltonian of this system, and project out some small number of the block states that are the most probable in constructing the ground state of the superblock. At the next step of iteration, one new spin is inserted into each block, which are joined again to make a new superblock. The Hamiltonian of this new system is calculated and the iteration is repeated. Since only a small number of relevant states is kept at each step, the Hamiltonian always has the same size, while the system size increases. We calculate the desired properties of the system at each iteration until they converge to their infinite-size values. Usually, for ordered systems this convergence is very fast, and even for random systems some 150 renormalization group steps (the system then consists of 300 spins) are enough, as was in our case. However, to obtain satisfactory statistics, the process must be repeated a number of times with different random field configuration. In the case of strong anisotropy ($\gamma \to 0$) 100 field configurations are enough, while we need at least twice that number for $\gamma \to 1$. The accuracy of the calculation strongly depends on the number of the projected states kept. The more states are thrown away, the larger is the truncation error, but the speed of calculations decreases drastically with the increasing number of states kept. We have used 8 states in most of the calculations except for $\gamma > 0.9$, where the number was 16. The average time of one RG step takes 6 seconds on a computer like Strindberg, so 150

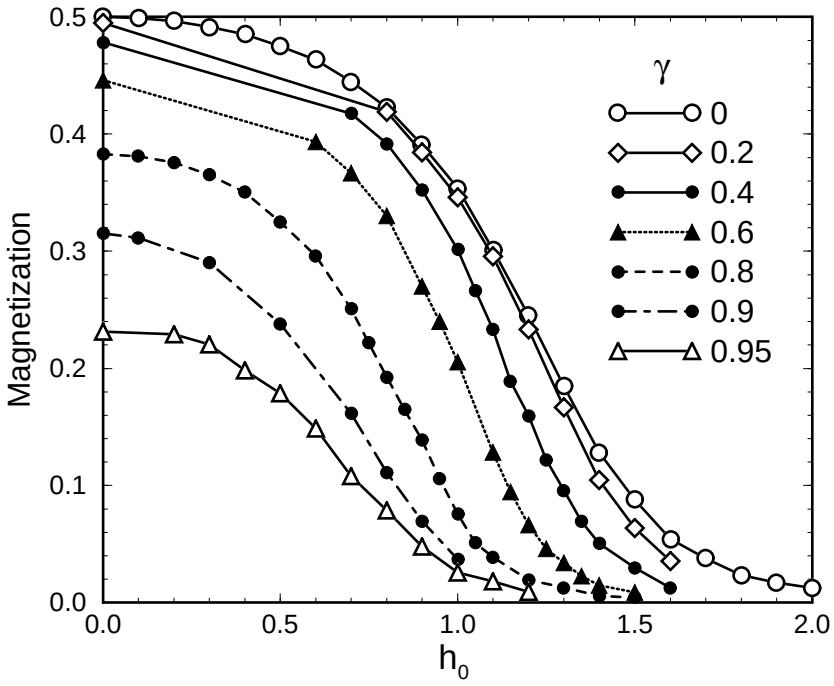

Figure 5.13. The magnetization dependence on the amplitude of the random magnetic field h_0 and on the factor of anisotropy γ at the uniform magnetic field $H = 1 \times 10^{-5}$. The error bars are smaller than the symbols.

DMRG steps times 100 field configurations takes around 25 hours on one processor. Since the problem is purely statistical, each of the field configurations being independent, the parallelization of the problem is almost natural - we run the same program on all the processors we have, except that we give a different seed for the random number generator. The algorithm is not very complicated, so the program is written in Fortran 77, which has still the best performance. The NAG library routines for matrix diagonalization are used.

Four main properties of the XYRF system are calculated: the magnetization M in the z direction, the ground state energy E, the energy gap G between the ground state and the first excited state, and the spin-spin correlation function. The DMRG calculations are carefully tested against the previously known analytical results and the agreement is perfect. *E.g.*, the difference between the exact ground state energy (found by Lieb *et al.*) and the calculated one is of the order of 10^{-5} for big γ values and as small as 10^{-15} for $\gamma \to 0$. The magnetization dependence on both the uniform field H and the amplitude of the random magnetic field h_0 for $\gamma = 0$ has the same behavior and critical exponents as obtained

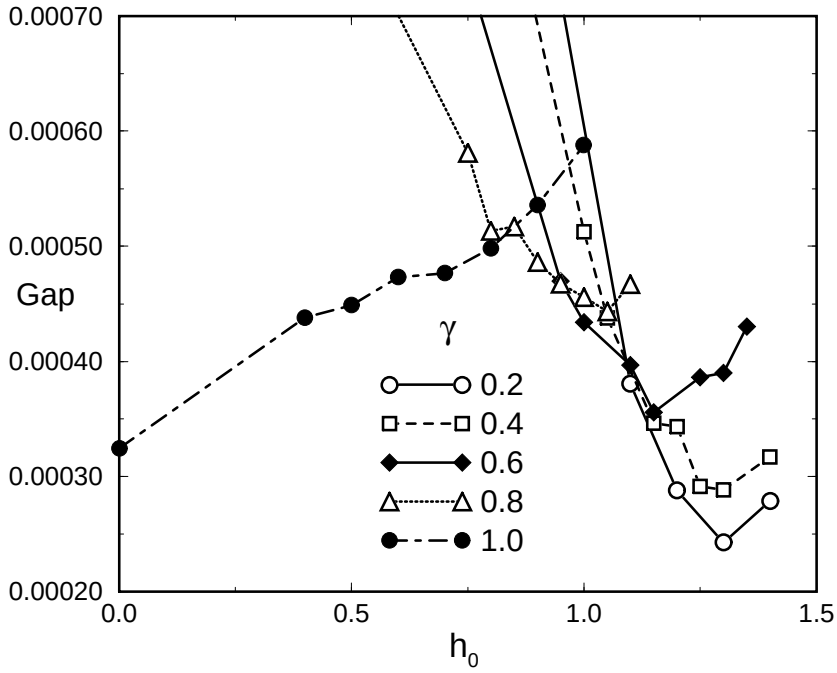

Figure 5.14. The energy gap dependence on the amplitude of the random field h_0 and on the factor of anisotropy γ at $H = 1 \times 10^{-5}$. The minima point out the phase transition points of the system.

by Fisher. The scaling laws of the two-point spin-spin correlation functions give the exponent $\tilde{\nu} = 1.04$ which is very close to the Fisher's predicted $\tilde{\nu} = 1$.

The magnetization dependence on the amplitude of the transverse random magnetic field h_0 and on the factor of anisotropy γ for the uniform magnetic field $H = 1 \times 10^{-5}$ is shown in Figure 5.13. The system is in a ferromagnetic state at low fields and the system is driven towards the paramagnetic state by increasing h_0. To obtain the exact point of the phase transition (PT) it is necessary to find where the spontaneous magnetization $M_0 = M(H = 0)$ turns to zero. The picture similar to Figure 5.13 is thus obtained for a number of different H values and the magnetization is extrapolated to M_0. So far we have obtained M_0 for $\gamma = 0$ and $\gamma = 1$ only. The transition occures close to $h_0 = 1.36$ for $\gamma = 0$, and the value is in good agreement with the exact Fisher's value $h_0 = e/2 \approx 1.3591$. The spontaneous magnetization for $\gamma = 1$ is obtained to be zero for any random field strength, as was expected from the exact solution of the XY model (Lieb *et al.*). The transition points for other γ values are estimated by calculating the energy gap dependence on h_0. Figure 5.14 shows the

energy gap curves for some values of the factor of anisotropy and the minima of the curves point to the corresponding PT points. In the nearest future it is necessary to complete the calculation of the spontaneous magnetization for intermediate values of the anisotropy factor (which automatically gives the critical exponents of the magnetization), to compare the results with those obtained from Figure 5.14, and to determine the scaling laws of the spin-spin correlation functions at the points of phase transition.

In summary, we have analyzed some properties of the anisotropic XY spin chain model in a transverse random magnetic field by means of the density-matrix renormalization group (see also [Juozapavičius *et al.*, 1997, Caprara and Rosengren, 1997b, Caprara and Rosengren, 1997a]). Our results stand not only as the accurate test of predicted scaling relations or as the newest estimates of other properties, but they also point out the wide applicability of the DMRG method described above to the problems of quantum phase transitions in disordered systems, which makes this algorithm a good and reliable alternative to other numerical methods.

Our results point out the wide applicability of the DMRG method to the problems of quantum phase transitions in disordered systems

5.13 Ab Initio Calculations of Doubly Excited States in Two-Electron Systems

Andre Bürgers[5]
Department of Atomic Physics, Stockholm University

Introduction

Doubly excited states in two-electron systems are studied in photo ionization and electron-ion scattering experiments. In the former, a photon is absorbed by the target atom (or ion) which has an energy lying between the first single-ionization threshold and the threshold for double ionization. In helium *e.g.*, these thresholds lie 24.6 eV and 79.0 eV above the ground state. In this interval, direct single ionization occurs at any energy. However, if the photon energy matches that of a doubly excited state, this state can be formed and then auto-ionize leading to the same final state as the direct ionization. Both paths interfere, leading to asymmetric resonances in the photo-ionization cross section. By this means,

[5]I'd like to thank Anders Ålund from PDC for numerical advice when vectorizing the code for Selma. This project is supported by the European Communities TMR programme under contract number ERBFMBICT961473.

doubly excited states have been studied using synchrotron light at BESSY in Berlin and at the Advanced Light Source in Berkeley.

The time reversed process to photo-ionization are recombination processes between ions and electrons. Here, the ion can capture an electron to a bound state (singly excited or ground state) by emitting a photon (radiative recombination, RR), or it can capture an electron resonantly to a doubly excited state. This resonance can then either auto-ionize, or it can stabilize to the new charge state by emitting a photon, thus completing the dielectronic recombination (DR) process. This process is studied in storage ring experiments like CRYRING in our group. Dielectronic recombination processes are very interesting in applications like accelerator physics, plasma physics, and star models.

But the doubly excited states are also interesting in themselves due to the strong correlation in the movement of the electrons, which causes a severe breakdown of the single-particle model which describes the movement of one electron in an averaged field of all the other electrons and the nucleus. This lead to the development of several models describing the two-electron system by new, collective quantum numbers [Herrick, 1983, Feagin and Briggs, 1986]. Since the problem is not separable, these quantum numbers are of course only approximately "good" quantum numbers. Moreover, the classical three-body Coulomb problem is mainly chaotic, so doubly excited states are also interesting in the search for *quantum chaos*. To understand all these features, highly accurate *ab initio* calculations of doubly excited states are needed.

Highly accurate ab initio calculations of doubly excited states are needed

Computational method

The non-relativistic Hamiltonian for the relative motion of the two-electron atom or ion with nuclear charge Z reads (in atomic units)

$$H = -\frac{\nabla_1^2}{2\mu} - \frac{\nabla_2^2}{2\mu} - \frac{\nabla_1 \cdot \nabla_2}{M} - \frac{Z}{r_1} - \frac{Z}{r_2} + \frac{1}{r_{12}} \,.$$

Here, $-i\nabla_1$ and $-i\nabla_2$ are the momentum operators in position representation, r_1 and r_2 are the distances of the electrons from the nucleus, r_{12} is the inter-electronic distance, and μ the reduced mass of the electron-nucleus system. The term $\nabla_1 \cdot \nabla_2/M$ is the so called *mass polarization term* and accounts for the movement of the nucleus with mass M. If one is not especially interested in

the effects of the nuclear mass, the limit $M \to \infty$ is usually taken.

The wave function of the two-electron atom is expanded as

$$\Psi^{\pi}_{L,M}(\boldsymbol{r}_1, \boldsymbol{r}_2) = \sum_{-L \le M' \le L} {\mathcal{D}^{L}_{MM'}}^{*}(\psi, \theta, \phi)\, \Phi^{\pi}_{M'}(r_1, r_2, r_{12})\,,$$

where the ${\mathcal{D}^{L}_{MM'}}^{*}(\phi, \theta, \phi)$ are the rigid-top wave functions describing the rotation from a laboratory frame with the Euler angles ψ, θ, ϕ. Since the rigid-top wave functions are known, the integration over the Euler angles can be carried out, leaving us with an effective Hamiltonian for each pair of good quantum numbers L and M containing Coriolis-like couplings of the $\Phi^{\pi}_{M'}$. We transform the three-dimensional problem into perimetric coordinates

$$\begin{aligned} x &= r_1 + r_2 - r_{12} \\ y &= r_1 - r_2 + r_{12} \qquad\qquad x, y, z \ge 0\,. \\ z &= -r_1 + r_2 + r_{12} \end{aligned}$$

We choose to use a basis set representation of the Hamiltonian which shifts the problem to solving a (generalized) eigenvalue problem. Our basis set consists of Sturmian type product functions in the perimetric coordinates. The basis functions for the case $L = 0$ read

$$\Phi^{\pi}_{nkm}(x, y, z) = \phi_n(\alpha x)\ [\phi_m(\beta y)\, \phi_k(\gamma z) + (-1)^{\pi} \phi_k(\gamma y)\, \phi_m(\beta z)]$$

and for $L = 1$

$$\Phi_{nkm} = \phi_n(\alpha x)\, \phi_m(\beta y)\, \phi_k(\gamma z)\,,$$

with $\phi_n(u)$ is defined as

$$\phi_n(u) = L_n(u)\, e^{-u/2}\,,$$

where the $L_n(u)$ are the Laguerre polynomials. The usage of the perimetric coordinates together with this basis set has several computational advantages. To start with, the volume element

$$\mathrm{d}V = \frac{8\pi^2}{32}(x + y)(x + z)(y = z)\, \mathrm{d}x\, \mathrm{d}y\, \mathrm{d}z$$

cancels all the divergences in the Hamiltonian when matrix elements are calculated. Further, all these matrix elements can

be calculated analytically using the recursion relations and orthogonality of the Laguerre polynomials. These guarantee also that most of the matrix elements vanish exactly, and by ordering the matrix elements in an appropriate way, a highly banded matrix representation can be achieved. In our calculations, we used $\alpha = 2\beta = 2\gamma$ to further reduce the bandwidth of the matrix. We have used basis sets with a maximum node number $\omega = n + m + k = 64$ in the $L = 0$ case, leading to a basis size of 24 497 states and a bandwidth of 1 142, consuming about 900 Mbyte on Selma. In the case of $L = 1$, the maximum node number was $\omega = 56$ leading to 32 509 basis states and a bandwidth of 2 898, consuming little less than 1800 Mbyte.

Consuming little less than 1800 Mbyte

This type of solution of a quantum mechanical problem is known as the *variational method*, where the expansion coefficients of the state vector in the basis set are regarded as linear variational parameters. It can be refined by using β as an additional, nonlinear variational parameter. However, the variational method is restricted to the calculation of *bound* states. This method can be generalized to *resonant* states by using the *complex scaling* technique, which is essentially an analytic continuation. It is achieved by formally writing

$$\beta = b\, e^{i\vartheta}$$

with b and ϑ real. In this formalism, also resonant states become square integrable. The complex scaled Hamiltonian is no longer hermitian, but complex symmetric, allowing for complex eigenvalues. Those eigenvalues which are stable with respect to a variation of ϑ represent the resonances; their position is given by the real part of the complex energy eigenvalue and their width is given by its imaginary part,

$$E_{res} = E_R - i\Gamma/2\,.$$

For actually obtaining the resonance energies we use two different numerical schemes. In a first step, a number of eigenvalues around a (complex) energy are calculated using a fast Lanczos algorithm [Ericsson and Ruhe, 1980]. In this way, we get a number of candidates with one program call. The eigenvalues are checked for convergence by systematically increasing the basis size. Note that at this stage, the variational parameter β is not optimized.

In a second step the matrix equation is solved using an inverse iteration procedure on an LDL^T decomposition of the Hamilton

matrix with the results from the Lanczos step as starting values. The complex scaling parameter β is optimized iteratively in this procedure such that the complex energy becomes stationary, $\partial E/\partial\beta = 0$. It turns out, that most of the (well converged) eigenvalues obtained with the Lanczos algorithm fulfill the stationary criterion to the specified accuracy already after very few (sometimes even the first) iteration; for large basis sets the energy depends only very weakly on the parameter β. The inverse iteration method is also used to calculate several expectation values which characterize the doubly excited states.

Both schemes, the Lanczos and the inverse iteration algorithms, are suitable for vectorization, which is why we choose Selma as the platform for the calculations

Both schemes, the Lanczos and the inverse iteration algorithms, are suitable for vectorization, which is why we choose Selma as the platform for the calculations. Additionally, we profit from the large memory which is associated to each node on Selma, so that we up to now did not need to parallelize the code.

Results

Here, we want to give a general overview over the results we have obtained. They have been published in more detail in [Bürgers and Wintgen, 1994, Bürgers *et al.*, 1995, Bürgers and Rost, 1996, Bürgers and Bachau, 1997, Bürgers *et al.*, 1998].

An analysis of the energies of the helium doubly excited states of S symmetry ($L = 0$) by means of the quantum defect theory showed that for moderate excitation energy the Rydberg series converging to the various He^+ thresholds followed the predicted propensity rules for non-radiative decay and could be classified according to the approximate quantum numbers [Rost and Briggs, 1991, Bürgers and Wintgen, 1994]. However, for higher energies, the propensity rules do no longer apply to *all* the series. Those states which have a configuration close to a collinear one where both electrons are situated on opposite sides of the nucleus continue to behave regularly, while others with a configuration far from the collinear one start to behave very unregularly. In addition, their reduced width (*i.e.*, their width measured in relation to their mutual distance) increases, and individual states begin to overlap. Since the propensity rules were derived for adiabatic basis states described by approximate quantum numbers, a fulfillment of the propensity rules was interpreted by the former states being in "pure" basis states, while the latter are interpreted as "mixed" states [Bürgers *et al.*, 1995]. The first such "mixed" states were

found above the He^+ ($N = 5$) threshold, while overlapping states occur for the first time above the He^+ ($N = 7$) threshold.

The examination of *complex expectation values* [Bürgers and Rost, 1996] showed, however, that this picture is even more complicated as it was assumed earlier. Complex expectation values (and especially their imaginary part) turned out to be much more sensitive to accidental degeneracies in the energy spectrum as the energies themselves. The most recent investigation of the *inter-electronic angle* [Bürgers *et al.*, 1998] showed that also those states which have a close-to-collinear configuration with both electrons on the *same* side of the nucleus behave irregular and have to be viewed as superposition of adiabatic basis states. A detailed comparison of the calculated inter-electronic angles in helium with the (asymptotic) values from the adiabatic model (or others) shows that it is only the states with a configuration close to a collinear configuration with both electrons on *opposite* sides of the nucleus which remain regular and can be approximated by adiabatic basis states. Moreover, "mixed" states are found even for the lowest doubly excited states, *i.e.*, for much lower energy as assumed previously.

5.14 Simulated Scattering of Seismic Waves in Random Media

Lena Frenje, Christopher Juhlin
Department of Geophysics, Uppsala University

We have developed a new code on the IBM SP-2 for 2D and 3D acoustic and elastic modeling in randomly varying media. With this code we simulate scattering of seismic waves as they propagate through a heterogeneous media. The purpose is to investigate if we can produce synthetic seismograms which are realistic when compared to data recorded over and in the Earth's crust.

Random velocity models

A heterogeneous medium can be modeled with a deterministic background velocity plus a random component. We use a Self-similar medium, which has fractal properties with similar velocity fluctuations on several length scales. The parameters needed to generate the medium can be extracted from sonic velocities measured in boreholes [Holliger, 1997]. We have used a sonic log from

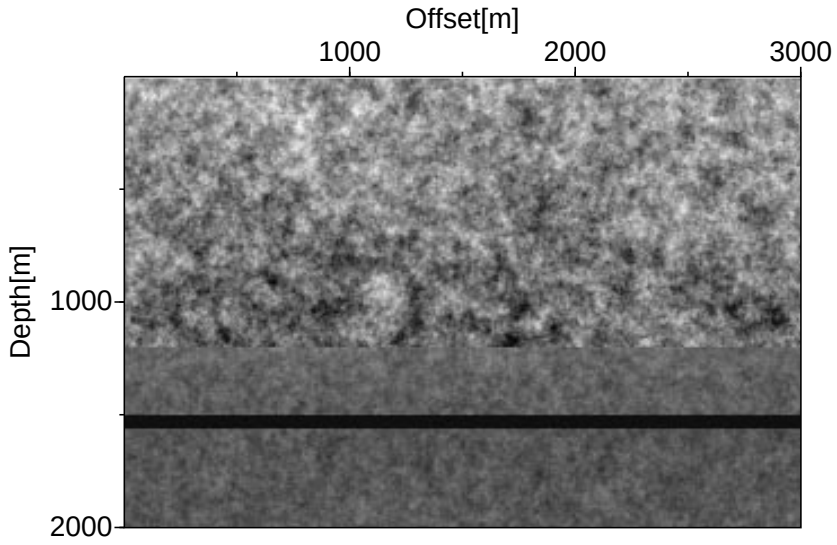

Figure 5.15. 2D velocity model simulating the upper crust in the Siljan Ring area, central Sweden.

the Gravberg-1 borehole in the Siljan Ring area in central Sweden. This area is well suited for our investigation since a considerable amount of seismic data has been collected in the area and allows us to compare real data with our synthetics.

Figure 5.15 shows our 2D velocity model with random velocity fluctuations simulating the heterogeneous granite of the upper crust in the Siljan Ring area. At 1500 m depth a 60 m thick high velocity layer is inserted to simulate a dolerite sill which intrudes the granite, and on top a 10 m thick low velocity layer simulates the glacial still present in the area.

Synthetic seismograms and real data

We have generated 2D synthetic seismograms using a finite difference method with 2^{nd} order finite difference operators in time and 4^{th} order ones in space [Levander, 1988], to model elastic waves. The algorithm uses the stress-velocity formulation of the elastic equations on a staggered grid. Absorbing boundary conditions were implemented at the bottom and sides of the grid and an accurate free surface boundary condition [Juhlin, 1995] was used at the top. The modeling was performed on a 1600×1000 grid, with 2 m grid spacing and 0.1 ms time step. The source is a Ricker wavelet with a main frequency of 50 Hz located at 16 m depth. The result is shown in Figure 5.16. The real (Figure 5.16a) and synthetic

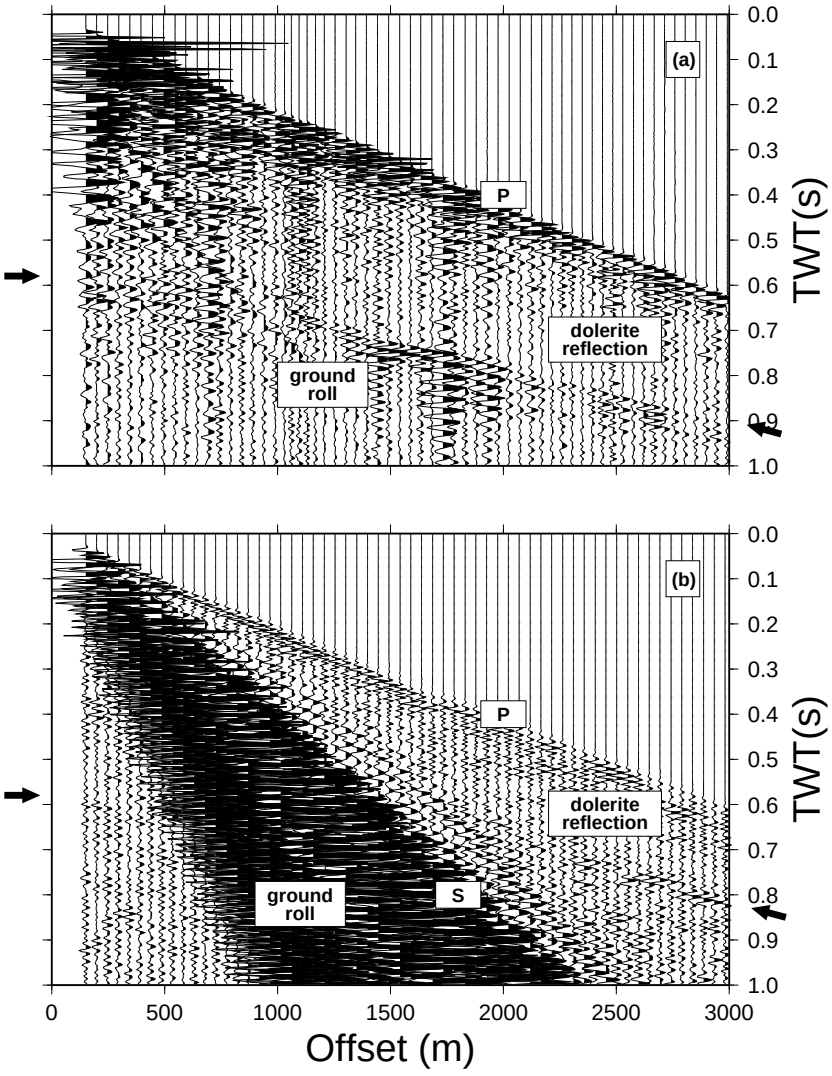

Figure 5.16. A comparison between a real surface seismic seismogram **(a)** and a synthetic seismogram produced with the finite difference method **(b)**.

(Figure 5.16b) seismograms differ primarily in that the wavefields are more scattered in the synthetics and that non-P-wave-energy is more prominent resulting in a poor match between the two. This may be caused by intrinsic attenuation being ignored, a Gaussian distribution of the random component was assumed, which is not really true, or the heterogeneities have a preferred orientation. We will investigate all of these possibilities in future work.

Summary

To perform modeling in 3D, in particular in the elastic case, and with models of reasonable size, a fair amount of memory is required. Using the thick nodes on the SP-2, it is possible to use models with $\sim 300 \times 300 \times 300$ gridpoints, which is enough to model some realistic geological structures. Also, the storage possibility of the output of the modeling is of great importance. The next step will be to include intrinsic attenuation, *i.e.*, perform viscoelastic modeling, at least for the 2D case. 3D viscoelastic modeling, which would be the ideal, will probably be too memory expensive, even for thick nodes.

6 Color Plates

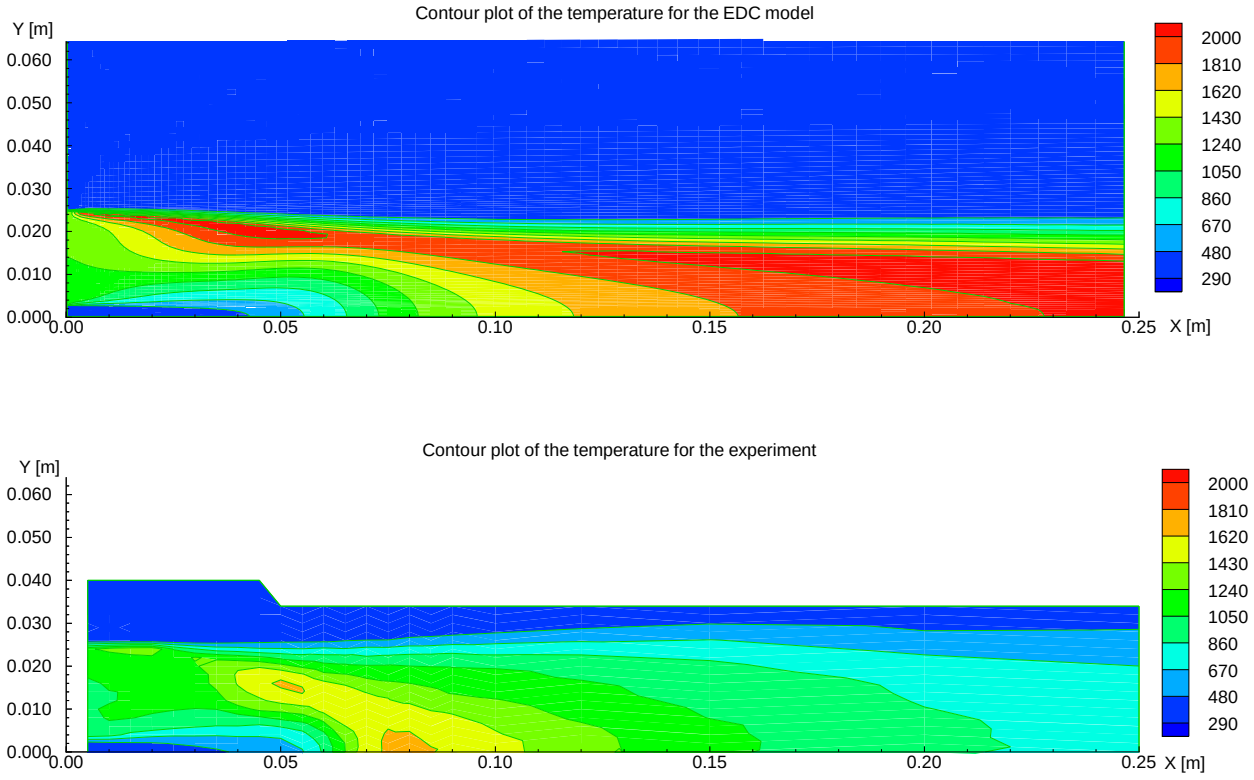

Figure 6.1. Bluff body configuration of a reacting flow field, temperature contour plots: Comparision between simulation and measurements. This computation was run on the IBM SP2 with the VOLSOL code developed by Volvo Aero Corporation. (See Section 4.5 on page 51.)

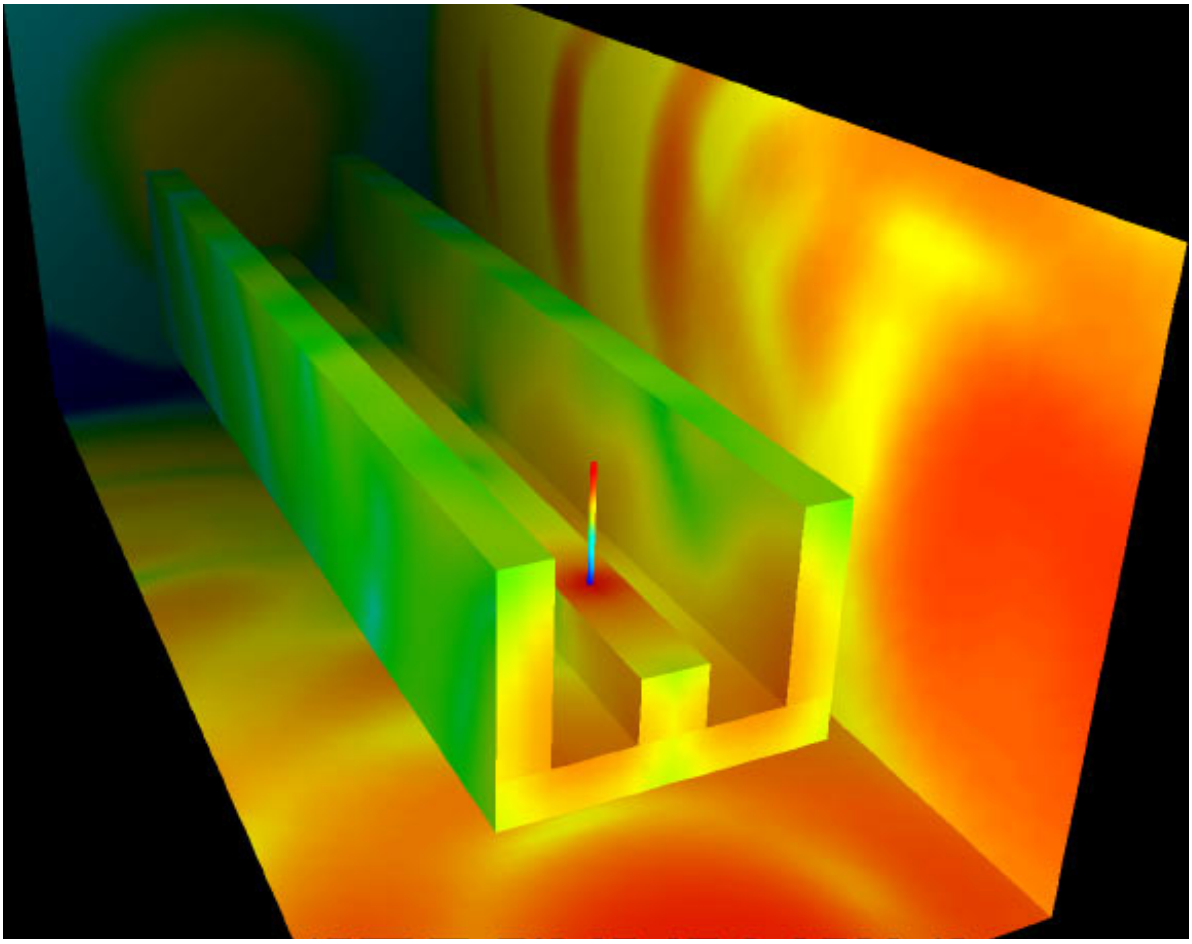

Figure 6.2. The Maxwell equations describes electromagnetic waves and can be solved numerically by using finite differences for space- and time-derivatives. This figure shows, for a distinct time, the solution of an open waveguide problem. An antenna is attached to an E-shaped waveguide and a current pulse is injected into the antenna. The antenna is modeled with a thin wire model. The purpose of this calculation is to study the fraction of energy propagating along the waveguide compared to the energy leaking out of the waveguide. By carefully choosing the sizes the waveguide can be optimized with respect to this fraction. The antenna current is shown on the antenna, surface currents on the waveguide surface and energy density (log scale) in the field, projected on three artificial outer surfaces. (See Section 5.1 on page 53.)

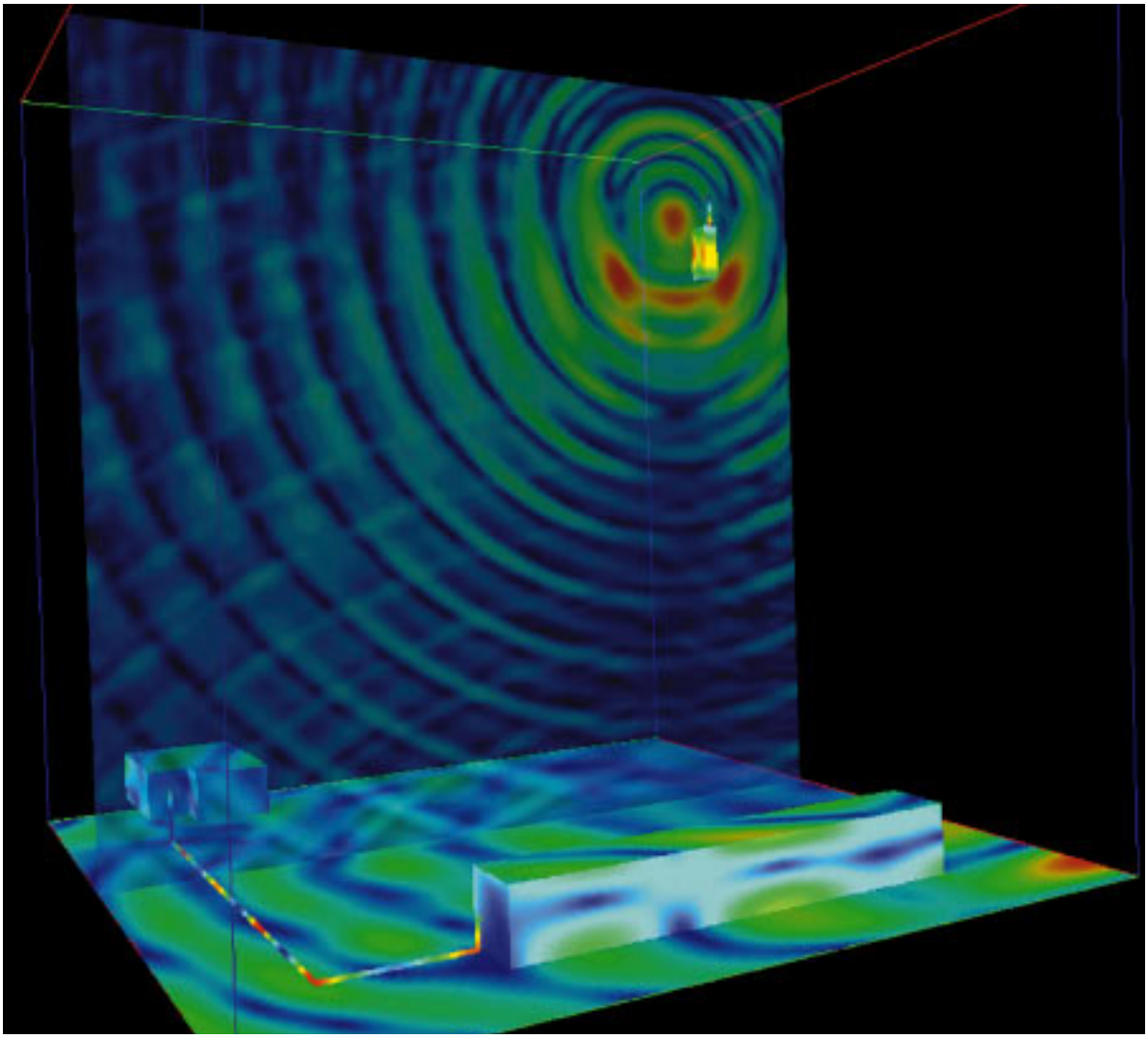

Figure 6.3. Electromagnetic compatibility concerns the interaction of different electronic devices. The goal is to design devices immune to influence from other devices and to suppress unnecessary electromagnetic emissions. This picture shows a setup for studying the induction of currents on a wire connecting two electronic devices in the presence of a transmitting cellular phone. The antenna on top of the telephone is driven by a current pulse and the picture shows a snapshot in time of the response. All color scales are linear and the colors represent: Cellular phone: antenna current $0-30\,\mathrm{mA}$, surface current $0-25\,\mu\mathrm{A/m}$; Devices and ground plane: surface current $0-2.5\,\mathrm{nA/m}$, wire current -20 – 20 μA; Semi transparent projection plane: energy density $0-50\,\mathrm{nJ/m^3}$. This problem was solved by using $200 \times 200 \times 200$ grid points and the code was executed on one vector processor on the Fujitsu VX/2 at PDC. Execution time was a few minutes and execution speed almost 900 Mflop/s. (See Section 5.1 on page 53.)

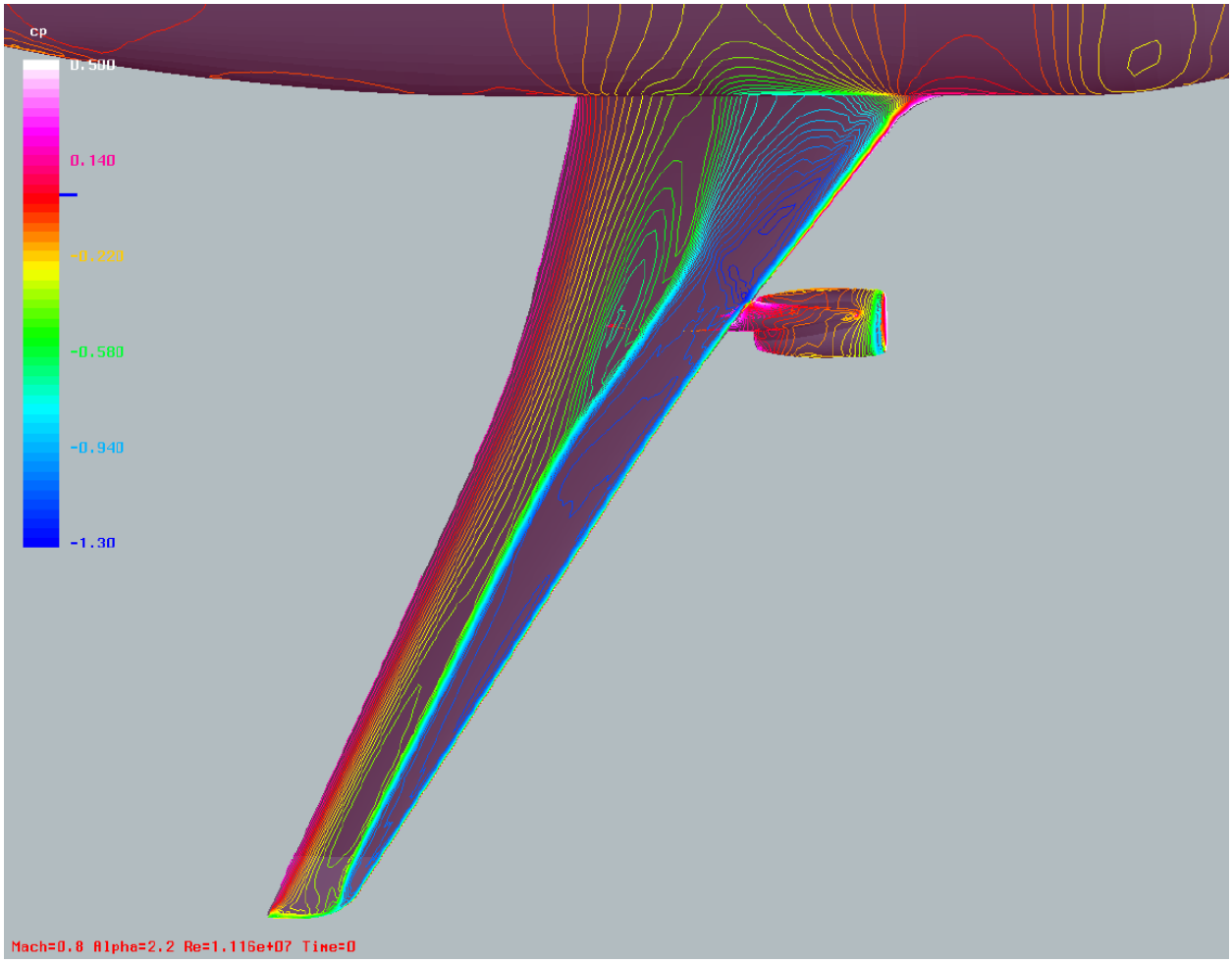

Figure 6.4. Isopressure lines ontop of the AS28G wing. The shock position is where the pressure-gradient is large (many lines close to each other). (See Section 4.3 on page 41.)

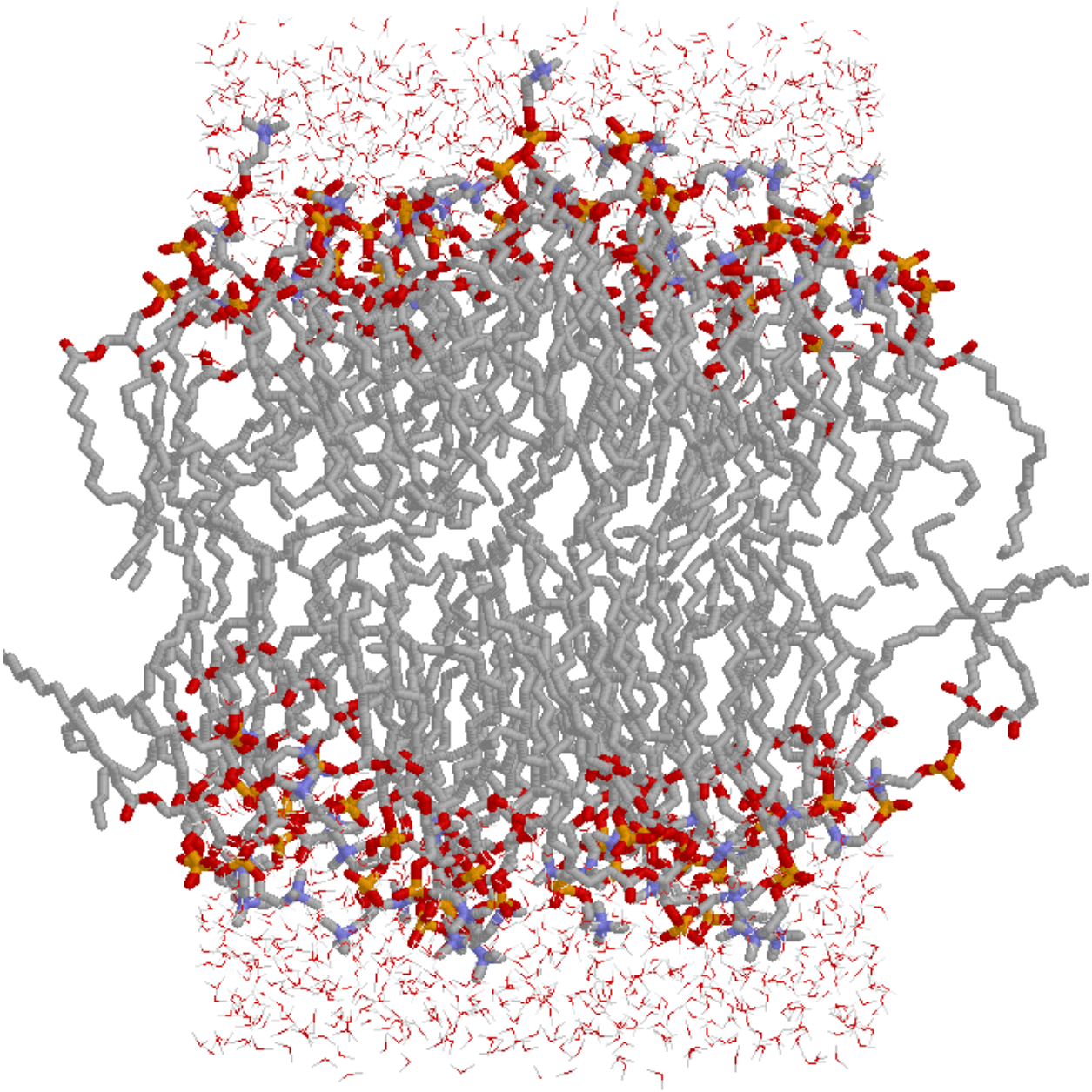

Figure 6.5. Side view of the equilibrated dipalmitoylphosphatidylcholine (DPPC) bilayer. The grey chains in the middle are the fatty acid chains, the read and yellow the lipid head groups while the water molecules further out are drawn with thin lines. (See Section 3.1 on page 19.)

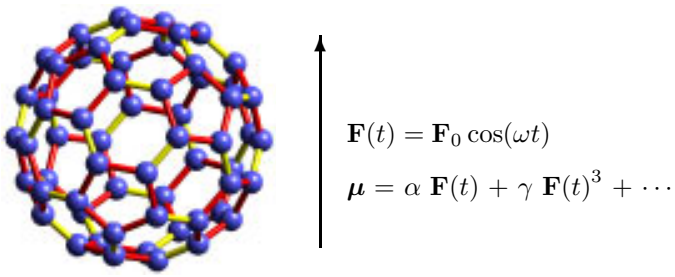

Figure 6.6. The fullerene C_{60} for which the induced dipole moment determined by the (hyper)polarizabilities have been computed at the *ab initio* level. (See Section 5.4 on page 64.)

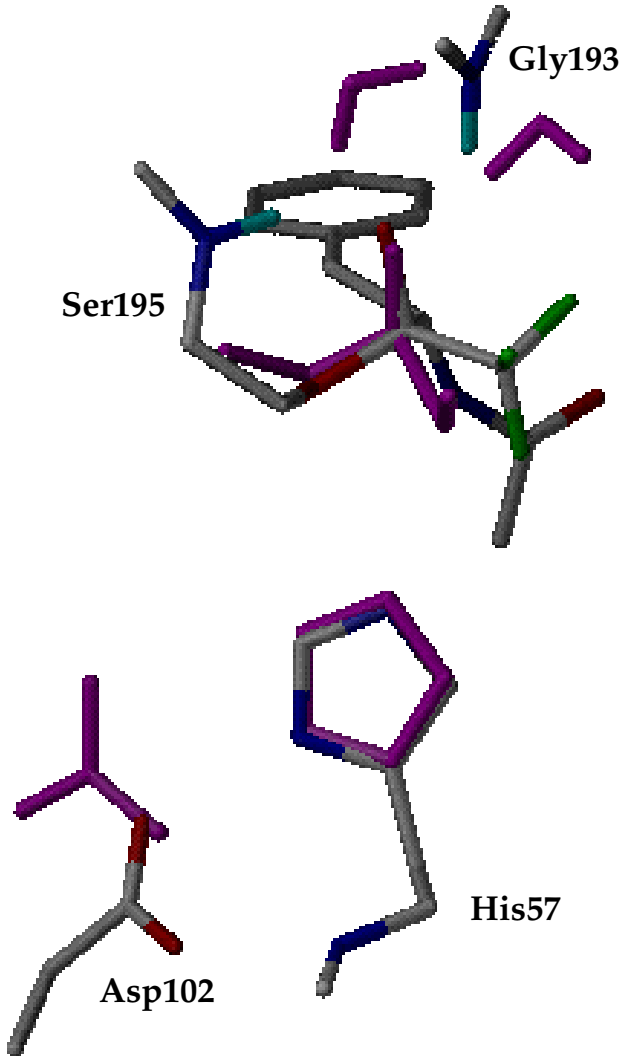

Figure 6.7. The optimized structure of the transition state in the acylation step for ester hydrolysis in serine hydrolases superimposed on the the crystal structure of the reaction center of chymotropsin with n-acetyl-l-phenylalanyl trifluoromethyl ketone bound as inhibitor. The computed transition state structure is colored all purple. The close similarity between the two structures supports the hypothesis that enzymes are optimized towards transition state stabilization. The optimized structure was computed at the DFT-B3LYP/6-31+G* level, while the crystal structure was taken from Brookhaven protein data bank (entry 6GCH). (See Section 3.2 on page 21.)

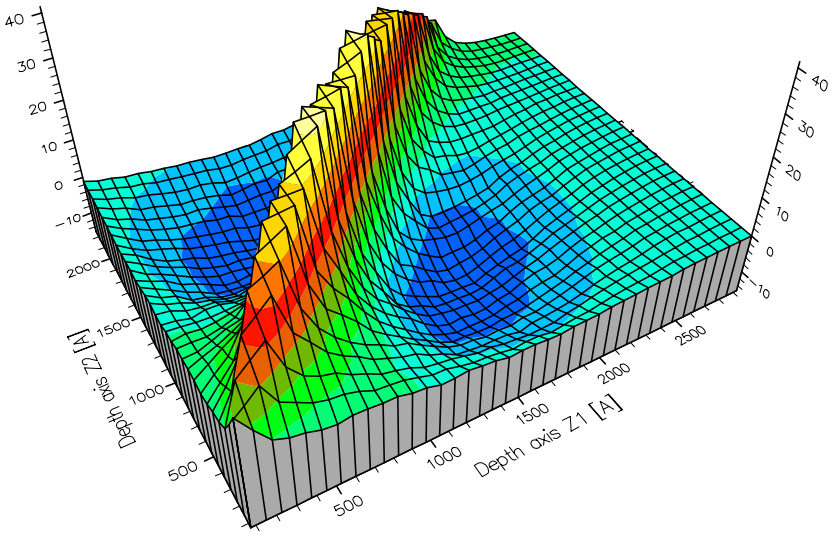

Figure 6.8. Depth correlations of vacancies created by irradiation of Si material with 100 keV Si ions. The ion beam is entering the material at point $Z_1 = Z_2 =$ perpendicularly to the material surface. (See Section 5.5 on page 70.)

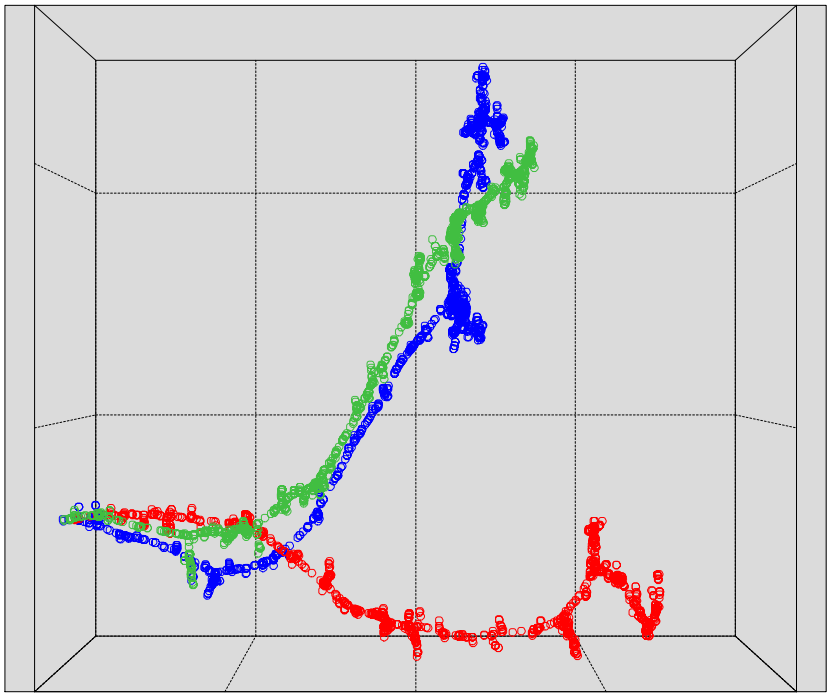

Figure 6.9. Space distribution of the vacancies in three cascade processes initiated by three 100 keV Si ions impinging on a Si material. (See Section 5.5 on page 70.)

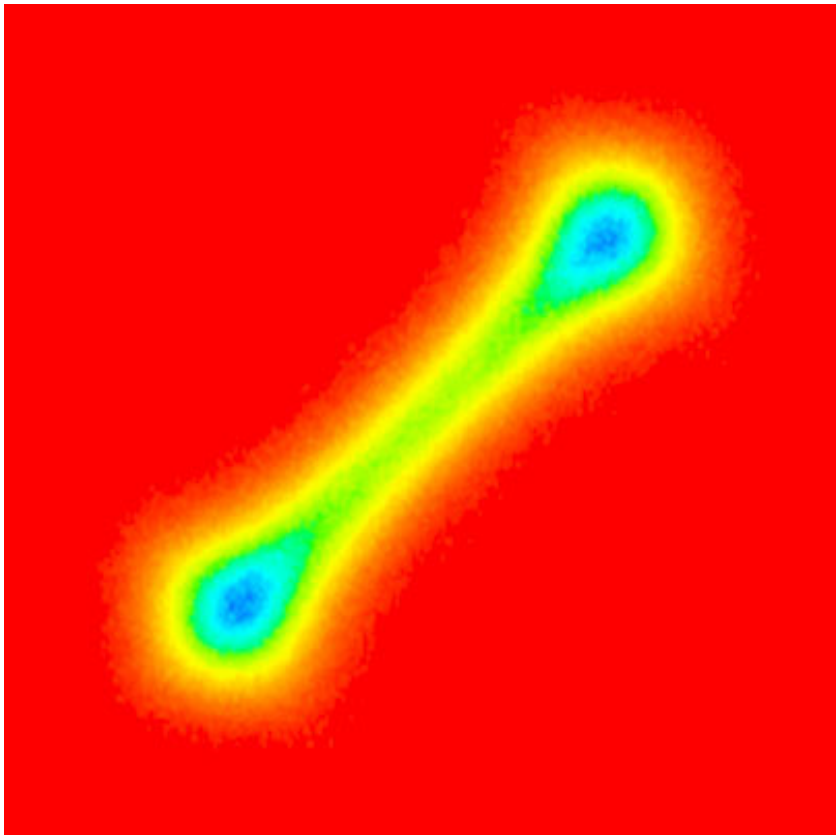

Figure 6.10. The distribution of the quantum path for a hydrogen atom adsorbed on a Ni(001) surface at 40 K. The centroid of the quantum path is located at the saddle point between two stable minima and the figure shows that the hydrogen for this configuration is quantum-mechanically delocalized. (See Section 5.10 on page 87.)

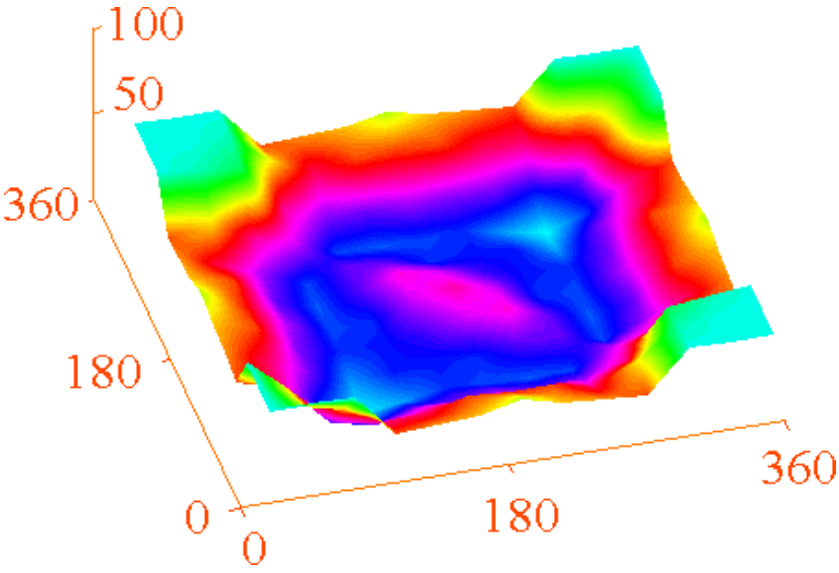

Figure 6.11. Map of the potential energy surface for the "PFSI" anion, $[(C_2F_5SO_2)_2N]^-$, for rotations about the central S–N bonds. The central part of the map comprising dihedral angles 90–270° with less than 15 kJ/mol difference. (See Section 7.3 on page 126.)

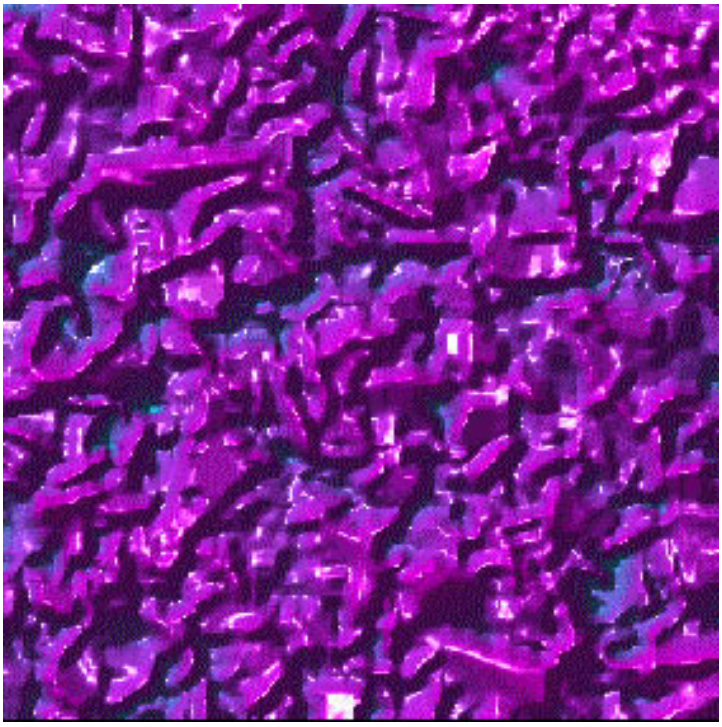

Figure 6.12. Surface of a simulated $6 \times 6 \times 6\,\mu\text{m}^3$ cubic cluster of clay particles having 30% porosity. The cluster includes about 7000 hexagonal flakes simulating clay particles in paper coatings. (See Section 5.11 on page 89.)

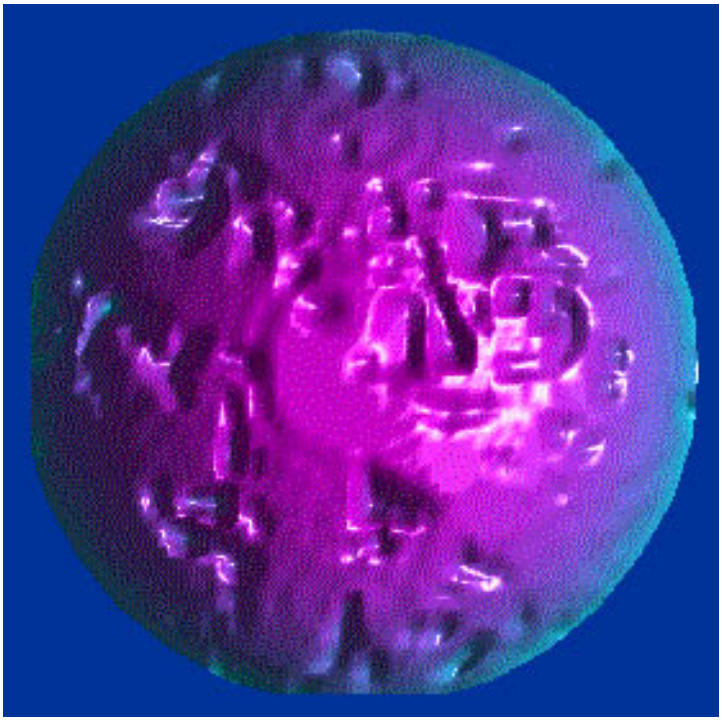

Figure 6.13. Spherical cluster, $4\,\mu$m diameter, cut from the cluster in Figure 6.12. (See Section 5.11 on page 89.)

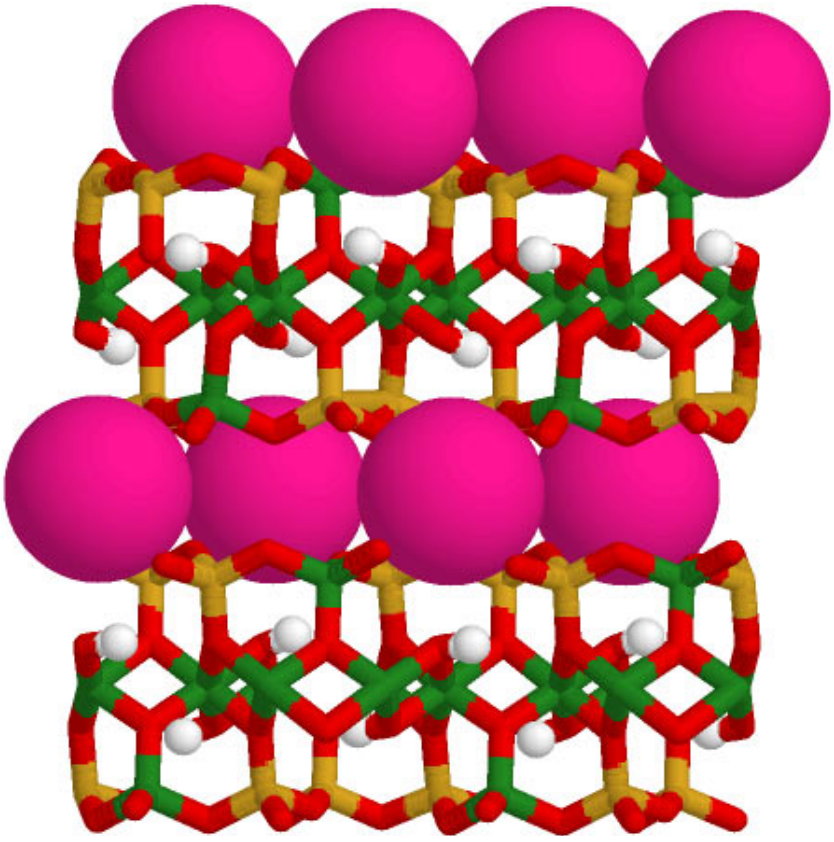

Figure 6.14. Colors represent: K^+: Magenta, Si^{4+}: Yellow, Al^+: Green, O^{2-}: Red, and H^+: White. In the $2M_1$-Muscovite structure, a layer of octahedrally coordinated Al^{3+} ions is sandwiched between two tetrahedral silicate layers, with vertices pointing towards the octahedral layer. The buckled basal plane of the tetrahedra forms distorted hexagonal rings of oxygens. Aluminium is randomly substituted for silicon with a ratio of 1:3, and for charge compensation potassium counterions are present at the center of all the hexagonal rings. The hydroxyl groups are located in the juction between the octahedral and tetrahedral layers, under the rings, and they form elongated hydrogen bonds to oxygens in the rings. (See Section 7.4 on page 129.)

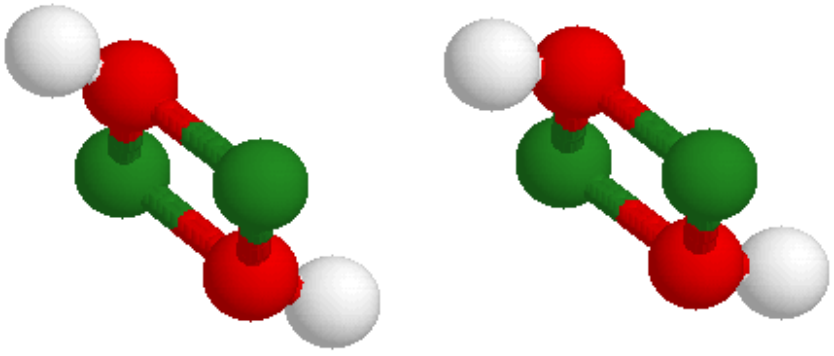

Figure 6.15. The formation of water in the dehydroxylation ($2OH^- \Rightarrow H_2O + O^{2-}$) can occur between hydroxyl groups bond to the same or to different Al^{3+} ions. The stiffness of the Al–O–Al–O square in the MD simulations suggests that the reaction within a Al_2O_2 group is less likely. (See Section 7.4 on page 129.)

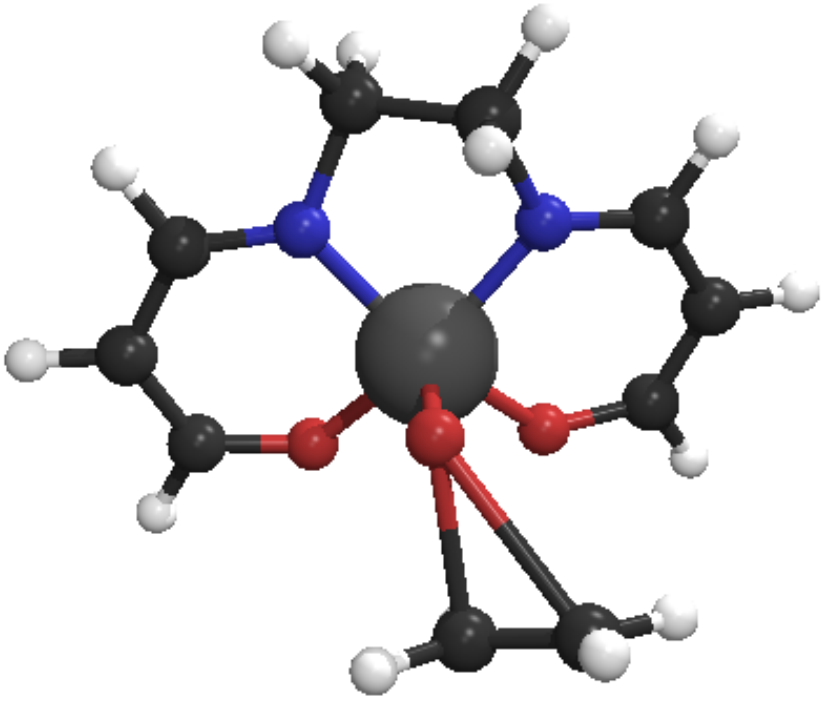

Figure 6.16. The addition of the alkene, shown in the lower part of the figure, is asymmetric. One carbon atom of the alkene interacts before the other with the oxo-group, represented in red above the central manganse atom. (See Section 7.8 on page 142.)

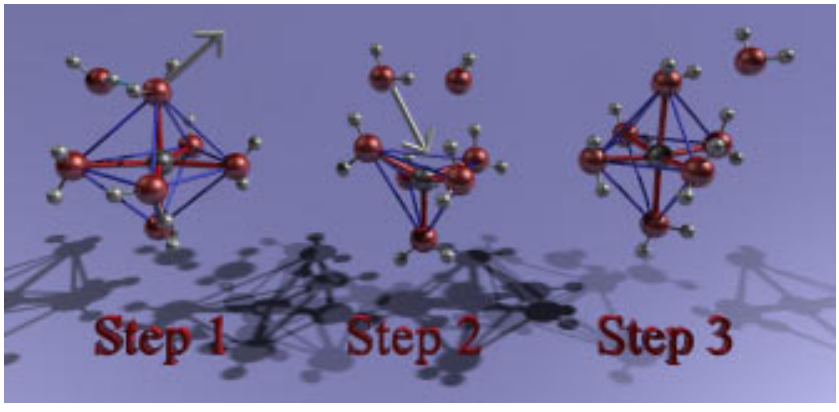

Figure 6.17. A sequence of snapshots for one of the exchange events found around $Li^+(aq)$. The mechanism is dissociative, and the intermediate complex forms a trigonal bipyramid. (See Section 7.7 on page 140.)

Figure 6.18. The spatial distribution functions of water atoms around a phosphate group of DNA. Atoms of phosphate group of DNA and neighbouring sugar and ester grours are displayed as spheres, the oxygen and hydrogen spatial distribution functions as correspondingly red and blue surfaces around. The surfaces are drawn at intensities 2.4 (solid) and 1.5 (net). (See Section 7.10 on page 146.)

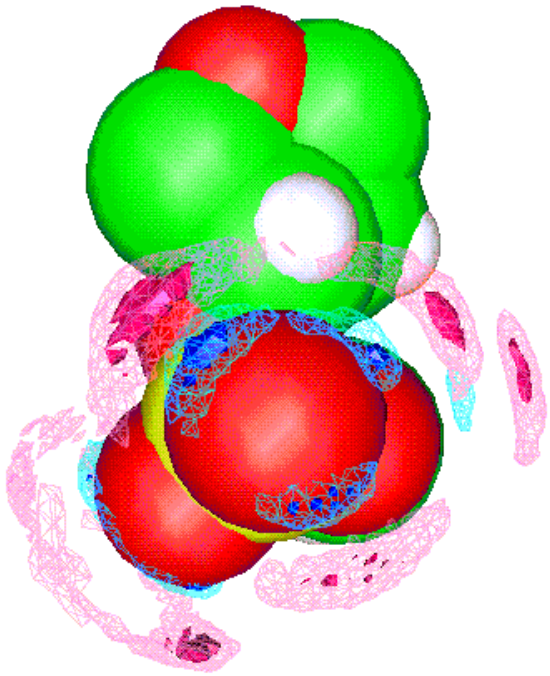

Figure 6.19. The spatial distribution functions of Li^+ ion around a phosphate group of DNA (blue surfaces). The surfaces are drawn at intensities 10 (solid) and 3 (net). (See Section 7.10 on page 146.)

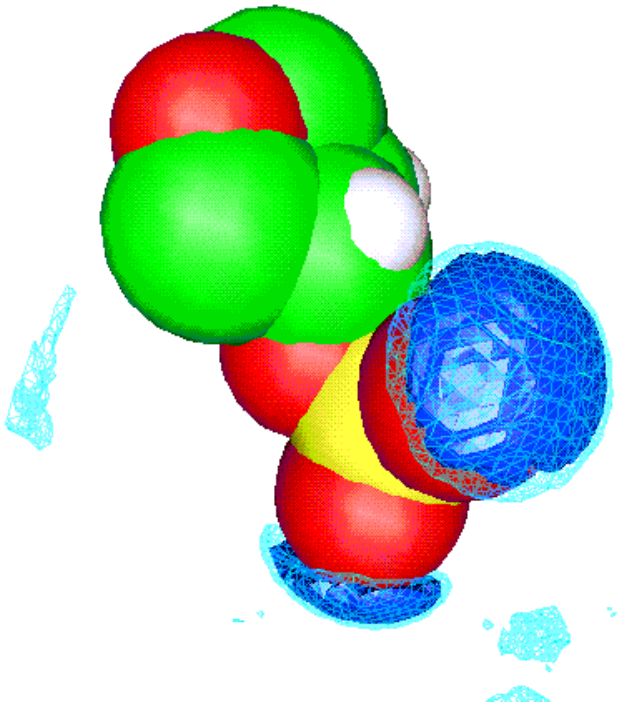

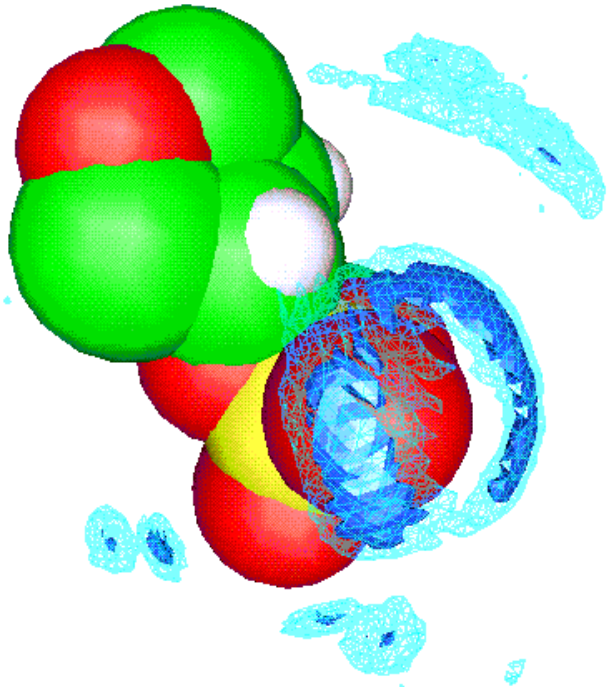

Figure 6.20. The spatial distribution functions of Na^+ ion around a phosphate group of DNA (blue surfaces). The surfaces are drawn at intensities 4 (solid) and 2 (net). (See Section 7.10 on page 146.)

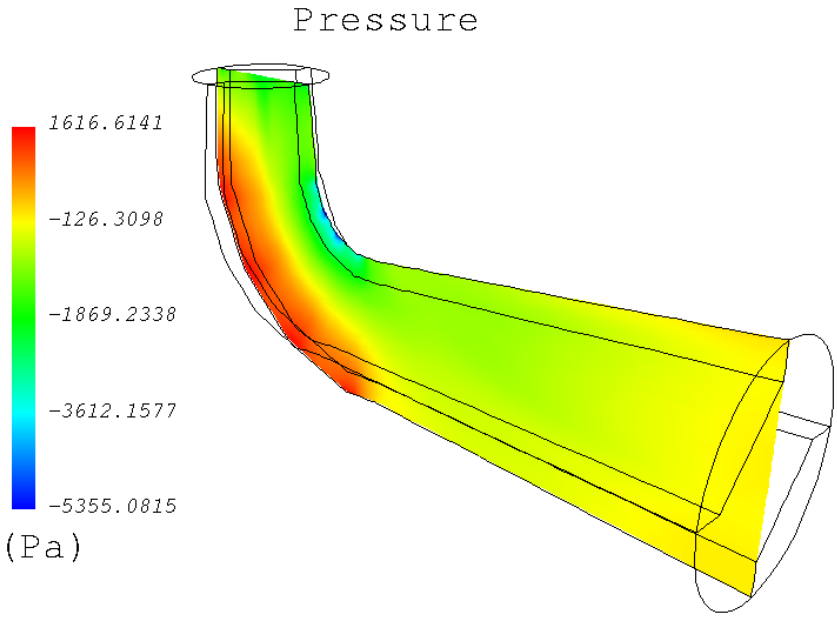

Figure 6.21. This is a picture of a draft tube (this particular geometry is from the GAMM Workshop at EPFL 13–15 September 1989, Lausanne, Switzerland). The draft tube is the last part of a hydro power turbine and the purpose is to convert some of the kinetic energy of the flow from the runner into pressure energy and thereby increase the efficiency of the turbine. The colors in the picture shows the pressure distribution in the midplane. (See Section 4.1 on page 39.)

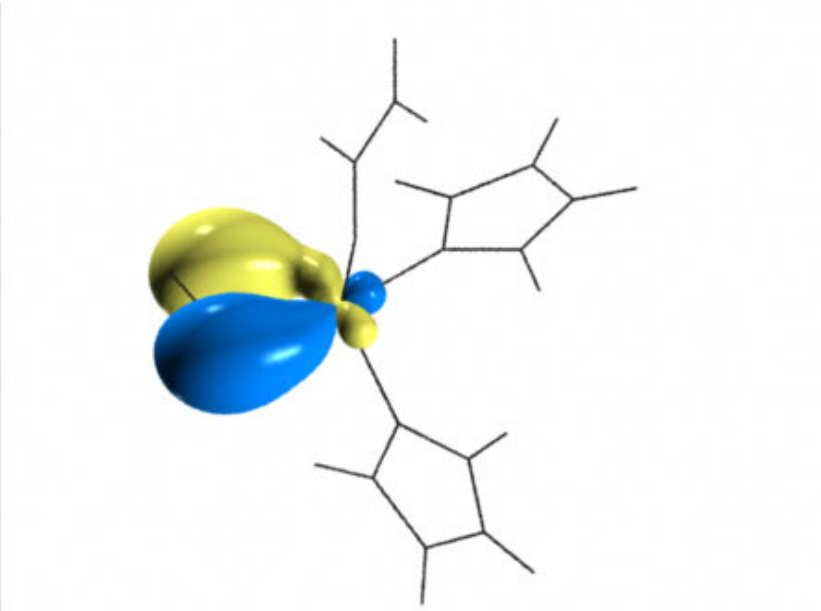

Figure 6.22. The singly occupied orbital corresponding to the absorption peak at 600 nm for stellacyanin. It is a π bonding orbital centered around the Cu-S_{Cys} bond, with 75% S_{Cys} $3p$ and 25% Cu $3d$ character. The orbitals were calculated by the *ab initio* multiconfigurational CASSCF method, using the crystal structure coordinates and including the pointcharges and solvent interactions of the surrounding protein. (See Section 7.20 on page 174.)

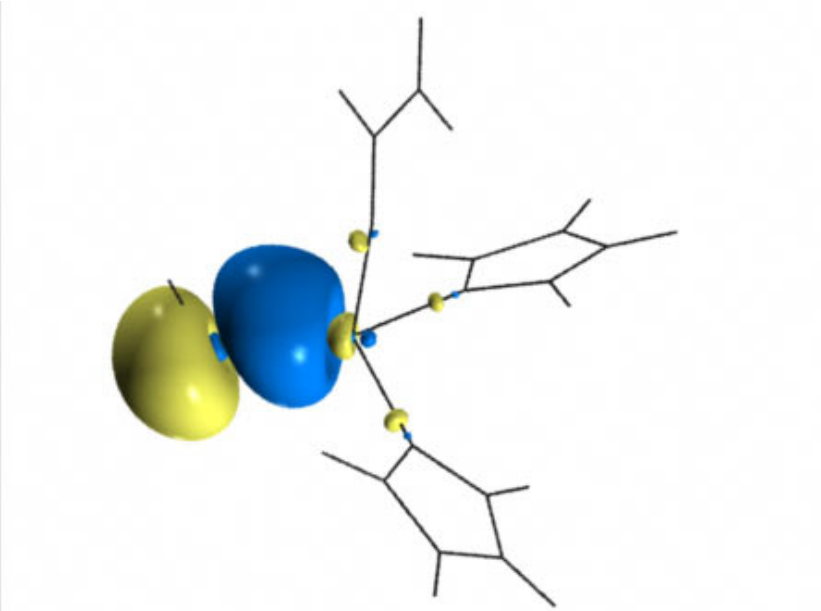

Figure 6.23. The singly occupied orbital corresponding to the absorption peak at 460 nm for stellacyanin. It is a σ bonding orbital centered around the Cu-S_{Cys} bond As for the π bonding excited state, the main character of this orbital is dominated by a S_{Cys} $3p$ orbital. (See Section 7.20 on page 174.)

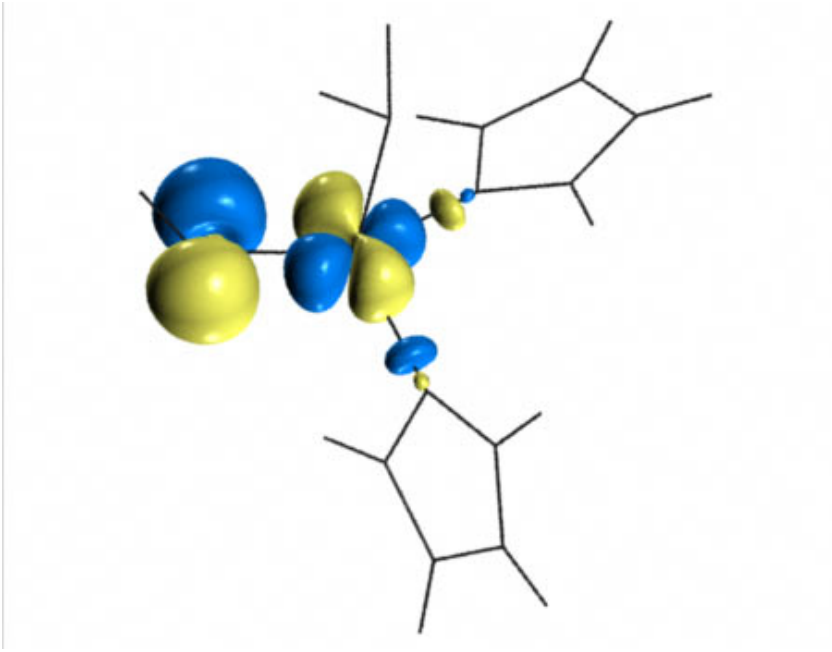

Figure 6.24. The singly occupied orbital in the ground state of plastocyanin. The two ligating imidazole histidine nitrogens form σ antibonds to the copper ion, while the S_{Cys} forms a π antibond to the copper. The bond between S_{Cys} and Cu has almost purely π antibonding character. The orbital composition is about 80% Cu $3d$ and about 20% S_{Cys} character,with only about 1% imidazole contributions. The overlap with the π bonding excited state is therefore very efficient, resulting in the strong absorption peak at 600 nm. (See Section 7.20 on page 174.)

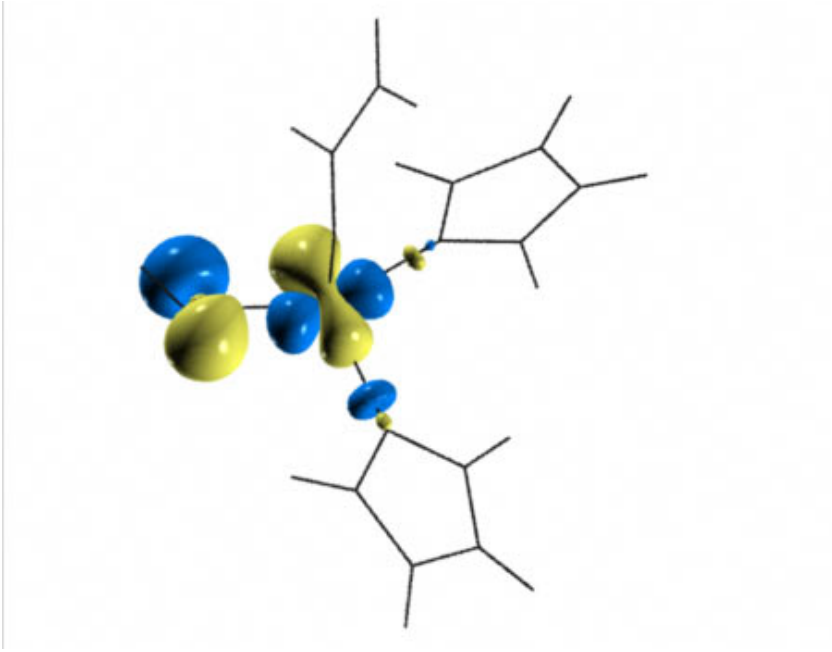

Figure 6.25. The singly occupied orbital in the ground state of stellacyanin. The orbital is not purely π antibonding as in plastocyanin, instead it is a mixture of π and σ antibonding interactions. The significant amount of σ character in the orbital increases the overlap with the σ bonding excited state, resulting in a more efficient charge transfer to this state. As a result the intensity of the peak at 460 nm is increased as compared to plastocyanin. (See Section 7.20 on page 174.)

Figure 6.26. The optimised structures (MP2) of the two alternative benzene coordination models for Hg_3^{2+}. (See Section 7.13 on page 160.)

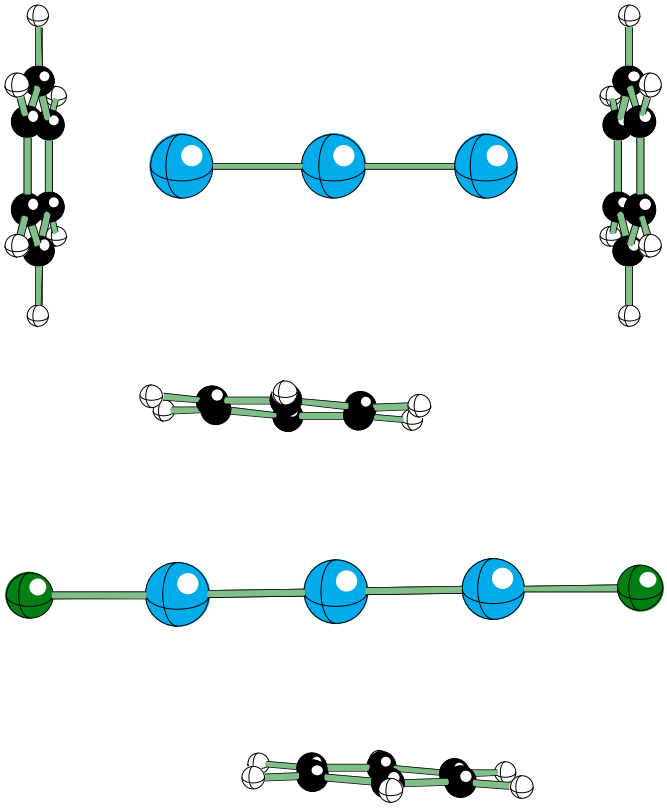

Figure 6.27. The optimised (B3LYP) overall staggered configuration for $[Pt_6(CO)_{12}]^{2-}$. (See Section 7.13 on page 160.)

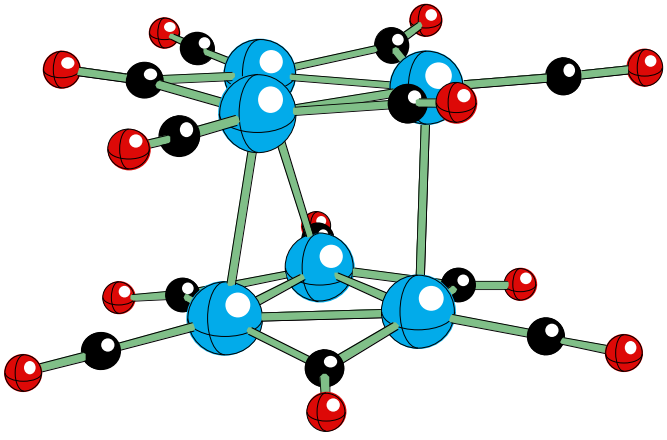

7 Applications in Chemistry

7.1 Nature of the Interactions between Polar β-Substituents and Palladium in (η^3-Allyl)palladium Complexes

Kálmán Szabó
Department of Organic Chemistry, Uppsala University

Allyl-palladium chemistry is one of the most successful areas of homogeneous catalysis. In particular, palladium catalysed allylic substitution and allylic oxidation reactions have proved to be very useful preparative methods. One of the most important aspects of this type of chemistry is the possibility of controlling the chemo-, regio- and stereoselectivity of the nucleophilic attack on the allyl moiety through the choice of reaction conditions and the ancillary ligands on palladium. However, furthering the development of allylic substitution and allylic oxidation reactions requires more information on the fundamental electronic and steric interactions, which govern the selectivity in these reactions. In this respect quantum chemical calculations can provide invaluable help in obtaining a better understanding of the nature of the electronic interactions occurring in (η^3-allyl)palladium intermediates.

The *ab initio* and DFT studies performed by the IBM SP-2 parallel computer facility of PDC were focused on the electronic interactions occurring between the allylic β-substituents (X) and palladium atom in (η^3-allyl)palladium complexes (1–7), see Figure 7.1. The calculations were carried out for small model systems (1) and experimentally investigated large cyclic species (2–7), which have great practical importance [Szabó *et al.*, 1997, Szabó, 1997, Aranyos *et al.*, 1997, Szabó, 1996].

Computational studies for (1) showed [Szabó *et al.*, 1997, Szabó, 1997, Szabó, 1996] that the electronic interactions, so called β-substituent effects, between palladium and X influence: (a) the structure of (η^3-allyl)palladium complexes; (b) the kinetic and thermodynamic stability of these species; (c) the regiochemistry of the nucleophilic attack on the allyl moiety. The structural changes are summarized as follows: (1) antiperiplanar Pd–C3 and C4–X bonds; (2) elongation of the C4–X bond; (3) shortening of the C3–

Figure 7.1. Seven different (η^3-allyl)palladium complexes, see Section 7.1.

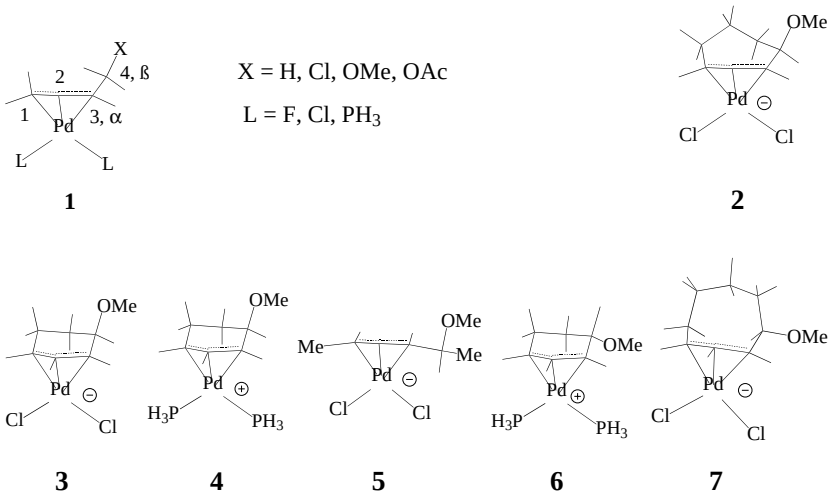

C4 bond; (4) shortening of the Pd–C3 bond; (5) shortening of the Pd–C4 distance; (6) charge accumulation on the X substituent. The β-substituent effects induce asymmetric electron distribution on both the allylic fragment and the C–X bond, which makes the less substituted allylic terminus more reactive towards nucleophilic attack.

The β-substituent effects thermodynamically stabilize the (η^3-allyl)palladium complexes by up to 8–10 kcal/mol. Weakening of the C–X bond, as shown by the C–X stretching force constants, facilitates its heterolytic fission, and therefore the β-substituent effects leads to a decrease of the kinetic stability of the complexes. This latter feature has been investigated in a combined experimental and theoretical study [Szabó *et al.*, 1997, Szabó, 1997] of (η^3-allyl)palladium species (2–7). These studies verified that strong β-substituent effects are present in six- and seven-membered ring species (2,3) and rather weak interactions in the eight membered ring complex (7), and also inspired some new synthetic applications.

Such studies could not been done without access to the parallel computer facility of PDC

In particular, theoretical studies for various conformers of (2–7) represent a computationally demanding problem. Such studies could not been done without access to the parallel computer facility of PDC.

7.2 Molecular Dynamics Simulation of Li^+ and Cl^- Ions in a PEO Surface

Alvo Aabloo, John O. Thomas
Angstrom Laboratory, Inorganic Chemistry Department,
Uppsala University

Poly(ethylene oxide) (PEO) based polymers have attracted considerable attention as potential polymer electrolytes in modern electrochemical devices; especially in high energy-density lithium-ion/polymer batteries. Mechanisms of ionic transport in a polymer surface have thus a special relevance, and yet are very poorly understood, largely because of the experimental difficulties involved in their study. In this work, potentials developed earlier to model crystalline and amorphous PEO [Neyertz *et al.*, 1994, Neyertz and Brown, 1995] and then applied to the simulation of a crystalline PEO surface, are used here to provide a model for the surface of a polymer host for Li^+ and Cl^- ions. A $2 \times 2 \times 8$ PEO unit-cell simulation box has been used with cell edges: $a = 16.10$ Å, $b = 26.08$ Å, $c = 155.84$ Å, $\beta = 125.4°$. The same highly asymmetric simulation box was created as in the earlier simulation of the PEO surface, comprising a 200 Å gap between 122 Å thick "crystalline" PEO sheets extending in the z-direction. The first sixteen CH_2-CH_2-O units of each chain were tethered on the one side of the PEO sheet. Three Li^+ and three Cl^- ions were introduced randomly into the untethered region. A Universal Force Field (UFF) was used to calculate the parameters for potentials involving Li^+ and Cl^-. An Ewald summation method was used in calculating the total potential. All calculations (made at 300, 400 and 500 K and at a pressure of 1 bar) used a local modification of the polymer MD program DL_POLY. The system was allowed to relax for an initial 200 ps using NVT ensemble simulation. The NpT Nose-Hoover barostat, with relaxation times of 0.1 ps and 1 ps was then used during the final 3 ns of simulation.

Subsequent analysis revealed a number of interesting features in the behaviour of the Li^+ and Cl^- ions in the region of the PEO surface: Li^+ ions were coordinated either by five ether oxygens ("5O"), with the PEO chain tending to enclose the Li^+ ion, or by one Cl^- ion and two ether oxygens ("1Cl2O") in a regular planar arrangement. The "5O" mode was preferred nearer the surface, going over to the "1Cl2O" mode deeper into the polymer host.

7.3 Ab Initio Calculations on Polymer Electrolyte Components

Patrik Johansson, Jan Lindgren
Angstrom Laboratory, Inorganic Chemistry Department,
Uppsala University

One of the most promising designs of new, high-energy density, environmentally safe, rechargeable batteries is based on lithium ion conduction in polymer electrolytes. The most often used system in polymer electrolyte studies is poly(ethylene oxide), $(\text{-}CH_2CH_2O\text{-})_n$ doped with various lithium salts. In the resulting mixtures the lithium ions are proposed to move using the segmental motion of the polymer chains and the anions are believed to more or less diffuse freely.

The three different projects presented here concern modelling, by *ab initio* quantum mechanical calculations, two different aspects of polymer electrolytes. The first models the internal flexibility of one of the anions suitable to be used as counter-ion to lithium, and the other two model the lithium ion coordination to the PEO polymer chain.

Potential energy surface of $[(C_2F_5SO_2)_2N]^-$

The anions used in polymer electrolyte systems are preferably large and bulky with a highly delocalized negative charge. The PFSI anion, $[(C_2F_5SO_2)_2N]^-$, is one of the suggested anions due to these properties and to its chemical and thermal stability. This anion is also thought to prevent crystallisation in PEO systems through its high internal flexibility. Crystallisation would result in multiphase systems, with a lower ion-conductivity.

To investigate this proposed flexibility and to determine the internal rotational barriers and , furthermore, to find the local and global minimum structures of the anion, a potential energy surface was calculated employing *ab initio* methods. Since earlier studies on the analogous TFSI anion, $[(CF_3SO_2)_2N]^-$, gave an incorrect central S-N-S angle using the 3-21+G* basis set, we have used the 6-31G* basis set. In general when anions are considered the use of diffuse functions is recommended. Model calculations however, showed them unnecessary to correctly describe this anion. This might be due to the distribution of the negative charge over five different atoms in the central part. Since the system contains

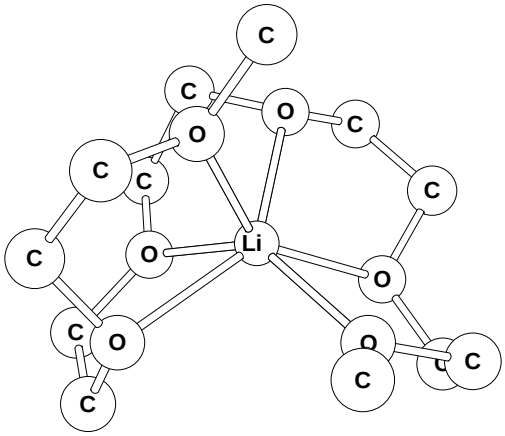

Figure 7.2. An *ab initio* calculated 1:1 lithium-pentaglyme complex with hexa-coordination of the lithium cation. Hydrogens omitted for clarity.

381 electrons and the surface to be calculated include at least 48 unique points each fully relaxed and optimized, the use of the capacity at PDC and the IBM SP-2 has made this study possible. Furthermore, we need the vibrational frequencies to be able to compare with spectroscopic data for real polymer electrolyte systems in which this anion is used as a counter-ion to lithium.

The IBM SP-2 has made this study possible

The results show the internal flexibility in terms of rotations around the central C-S-N-S bonds and the occurrence of two unique local minima, with the C_2 symmetry species having the lowest energy by 5.6 kJ/mol, see Figure 6.11 on page 114. However, no distinct differences as compared to the TFSI anion concerning charge distribution or internal flexibility can be found. The vibrational frequencies for both stable structures found have been calculated to assist interpretation of vibrational spectra of polymer electrolyte systems.

Ab initio calculations of penta- and hexa-glyme lithium complexes

To model the cation coordination in PEO polymer electrolyte systems we have performed *ab initio* calculations on 1:1 complexes of lithium with oligomers of PEO, penta- and hexa-glyme, see Figure 7.2. These oligomers have the formulas CH_3-O-$(CH_2CH_2O)_n$-CH_3, $(n = 5, 6)$. The calculations started from several different geometries obtained in a systematic way using knowledge from earlier calculations on shorter oligomers and pre-optimized using semi-empirical PM3 methods. Due to the high flexibility of the chains it is, not impossible, but extremely demanding to find all

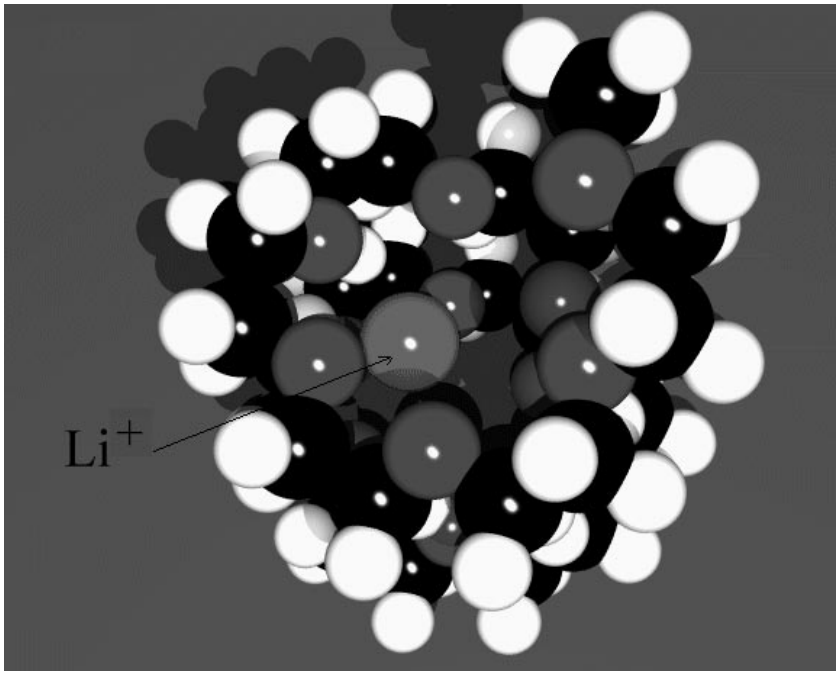

Figure 7.3. The picture shows the rigid PEO-helix used in the studies – nine monomers long – with a lithium ion coordinated in an optimized position.

stable structures. In this study the number of starting structures were 45 and 126 respectively, which should give results which reflects the nature of the cation coordination in these systems.

Thus the strength of the lithium interaction with a single PEO chain can be evaluated in a realistic environment

The results include several stable geometries and hereto belonging energies, relative total and bond energies, as a function of coordination number of lithium and chain length. Thus the strength of the lithium interaction with a single PEO chain can be evaluated in a realistic environment. The results show that lithium probably has an average coordination number of five in these systems, assuming that non-coordinating anions, such as $[(C_2F_5SO_2)_2N]^-$, are used as counter-ions.

Model calculations of the lithium ion transport in a poly(ethylene oxide) helix

The movement of lithium ions in polymer electrolytes is believed to occur mainly in the amorphous phase. A number of crystal structures have been determined of salt–PEO mixtures with O/M ratios 3 or 4. These are more concentrated than usual polymer electrolytes are. They do, however, provide some information about lithium ion coordination to the ether oxygens. The pur-

pose of the present study was to study lithium ion coordination inside a general helix of PEO. The helix with the same conformation sequence as found in most of the crystal structures and with no interaction to an anion. The results include the optimized lithium positions inside this rigid helix by moving the lithium in a volume-grid and performing *ab initio* single-point energy calculations for each point, see Figure 7.3. Furthermore, the lithium ion position was fully optimized and the bonding energies were calculated using DFT methods. The bonding energies compare well to the results from our earlier studies on lithium - di- and tri-glyme complexes.

7.4 A First Principles Study of the Dehydroxylation of $2M_1$-Muscovite

Michael Odelius
Department of Physical Chemistry, Uppsala University
Michele Parrinello
Dipartimento di Fisica, Universitá di Milano, Italy
Marco Bernasyyconi
Max-Planck Institut für Festkörperforschung, Stuttgart, Germany

The dehydroxylation of $2M_1$-Muscovite and other micas have been carefully studied by many different experimental techniques, which have been successful in characterising the difference between the $2M_1$-Muscovite crystal and its dehydroxylated form, see Figure 6.14 on page 116. However, the detailed mechanism for the reaction is still under debate. It is difficult to reach from the experimental information to a fully described mechanism.

It is difficult to reach from the experimental information to a fully described mechanism

It has been shown by X-ray diffraction and Mössbauer spectroscopy on dehydroxylated $2M_1$-Muscovite that the coordination in the "octahedral" layer is changed from six to five. The reaction occurs in a wide temperature range (800–1220 K), which has been interpretated as evidence both for the influence of the Al substitutions and for an inhibiting effect of the five coordinated Al^{3+} on neighbouring reaction sites. In IR studies the OH line has been observed to shift with the temperature before disappearing, suggesting that an intermediate state exists for the hydroxyl group. Also shifts in the vibrational spectra of K^+ has been observed. Electrical conductivity indicate that the ions diffuse before forming water, and the activation energy for the proton diffusion

is determined. Thus, a solid experimental ground exists for the study, and still valuable information on the mechanism of dehydroxylation is lacking, motivating the theoretical study.

The method is very suitable for studying crystals, since it is based on a plane wave description and periodic boundary conditions

Car and Parrinello [Car and Parrinello, 1985a] has developed an *ab initio* method to perform MD simulations for classical nuclei, based on density functional theory. It enables us to calculate accurate quantum mechanical forces on the nuclei, as an alternative to the use of model potentials (force fields). The method is very suitable for studying crystals, since it is based on a plane wave description and periodic boundary conditions. This excludes an explicit treatment of the core electrons, but with *ab initio pseudo potentials* and *gradient corrections to the energy functional* we get a highly accurate description of the system in general, and of the hydroxyl groups, in particular.

It offers a large number of possibilities for analysing the dehydroxylation process, since both the dynamics and the electron structure can be studied. We have seen in earlier structure calculations of $2M_1$-Muscovite [Odelius *et al.*, 199X] that the bond lengths and orientations of the hydroxyl groups depend strongly on the presence of the Al substitution sites, which will effect the reaction path way. (Some preliminar calculations on the $2M_1$-Muscovite crystal were also done in a recent study on the water adsorption on mica [Odelius *et al.*, 1997]).

In this study we will perform MD simulations at increasing temperatures, to study the motion of the hydroxyl groups, the formation of water and the transformation to the dehydroxylated form of $2M_1$-Muscovite, see Figure 6.15 on page 116. At this state, we have from high temperature (1000 K) MD simulations identified the initial stages of the dehydroxylation. The protons are very flexible at high temperature. However, the distribution of the O–H bonds is remarkably narrow, and the flexibility of the OH^- arises from the fluctuations in the Al^{+3}–OH^- bond and in the orientation of the OH^- groups. This indicates that the dehydroxylation is initiated by a hydroxyl group detaching from the Al^{+3} ion as a preserved entity.

The next step of the study is to predict the faith of the detached hydroxyl group. Does it react with the nearest proton, or could it diffuse through the crystal? The work also involves studies of how the crystal accommodates for the detachment of the hydroxyl group and the formation of water.

7.5 The Water Dimer Interaction Energy: Convergence to the Basis Set Limit at the Correlated Level

Martin Schütz, Steve Brdarski, Per-Olof Widmark, Roland Lindh, Gunnar Karlström
Department of Theoretical Chemistry, Lund University

Introduction

The study of the interactions between molecules is one of the fields of chemistry where quantum chemical methods have increased our understanding both in a quantitative and a qualitative way. While experimental techniques at best can provide information on (average) equilibrium geometries and corresponding binding energies of molecular complexes and clusters, quantum chemical *ab initio* methods can cover the entire potential energy surface, rendering valuable information *e.g.*, on local minima, transition states, isomerization pathways, *etc.*, which is a prerequisite for a deeper understanding of these systems.

The majority of calculations on clusters of molecules and complexes adopt the supermolecular approach, in which the interacting energy is computed as the difference between the energy of the complex, and the total energy of the (non-interacting) monomers, which form the complex. Such calculations are known to be sensitive to basis set extension effects, and in particular to the basis set superposition error (BSSE): The problem with the BSSE originates from the fact, that the wave function of a molecular complex is expanded in a set of basis functions that are linked to the individual centers of the interacting molecules. Boys and Bernardi (B&B) suggested an elegant method, which they named the counterpoise (CP) correction, to cope with this problem. The solution, according to B&B, is to study the individual monomers within the basis set of the complex, and to use the sum of the energies of the individual molecules in that composite basis as a reference. There has been quite a fierce discussion in the literature, whether more reliable interaction energies are obtained, if the CP procedure is employed or not.

Perhaps the most thoroughly studied model system for intermolecular interactions is the water dimer, both experimentally and theoretically. Its trans-linear geometry of C_s symmetry (see Figure 7.4) was established by molecular beam experiments and by several *ab initio* studies. The interaction energy of the complex

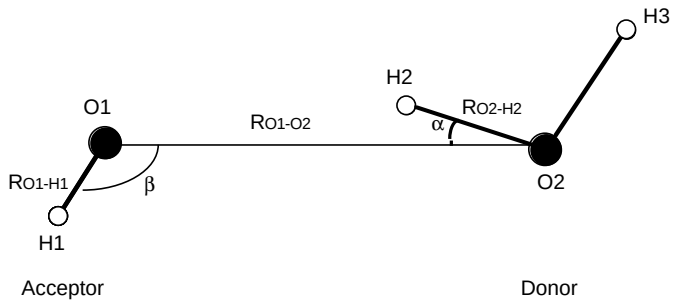

Figure 7.4. Translinear C_s minimum energy geometry of the water dimer. The relevant *intra-* and *intermolecular* coordinates are also indicated.

was in 1971 measured to $\Delta E = -5.4 \pm 0.7$ kcal/mol. A few years later, the same value was recommended with tighter error bars, *i.e.*, $\Delta E - 5.4 \pm 0.2$ kcal/mol. On the theoretical side numerous *ab initio* investigations have been devoted to accurately determine ΔE. It was observed, that correlation contributions beyond second order are rather insignificant at the equilibrium geometry, *i.e.*, about 0.05 kcal/mol or less for larger basis sets. The reason for this is a favourable cancellation of higher order terms with SDQ substitutions against the triples contribution. However, it has not yet been possible to achieve satisfactory agreement with the experimental value. Most of the studies performed so far ended up with a ΔE in the range of 4.4–4.8 kcal/mol after application of the CP correction.

In the present work a further attempt was made to assess ΔE_∞, employing a hierarchy of ANO-type and uncontracted basis sets: In the largest calculations a 1046 term basis including up to k-functions was used at the MP2 level, which is unprecedented so far by any of the previous calculation on the water dimer. All single-point calculations were carried out at a minimum energy geometry, which was determined on the CP corrected CCSD(T) intermolecular potential energy surface (PES). Based on these calculations and some elementary arguments from intermolecular perturbation theory a simple procedure was devised, which shifts the CP corrected interaction energies of small and moderate basis set calculations closer to the basis set limit. Some effort was invested also to accurately compute the contributions due to core correlation. So far, core correlation effects in the water dimer has been investigated only once, however merely with modest basis sets. As a consequence, the CP corrected and uncorrected core correlation contributions to the interaction energy varied between -0.01 and

-0.1 kcal/mol, while the recommended value was proposed to be -0.09 kcal/mol. In our calculations, we obtained a consistent contribution of -0.04 kcal/mol from the core electrons, significantly less than the previous estimate.

The high-end calculations reported in this work were made feasible by a novel integral direct, distributed-data parallel MP2 algorithm, recently implemented by us [Schütz and Lindh, 1997] and installed on the Strindberg IBM SP-2 machine at PDC. The present investigation involved several calculations using as much as 100 SP-2 nodes simultaneously. Hence, the present investigation may serve also as a practical application example demonstrating the usefulness of parallel algorithms in *ab initio* quantum chemistry.

The present investigation used up to 100 SP-2 nodes and may serve as a practical application example demonstrating the usefulness of parallel algorithms in ab initio quantum chemistry

Results and discussion

It has been argued occasionally, that the full CP correction should not be applied at the MP2 level, since it worsens the interaction energies by "overcorrecting" the BSSE. However, in view of all the evidence supporting the CP correction as the formally correct procedure to remove the BSSE from interaction energies, one may also investigate those sources of error, which cancel so favourably with the BSSE: In the present study we devised a simple scheme to improve the CP corrected correlation contributions $\Delta E(\mathrm{MP2}) - \Delta E(\mathrm{SCF})$ for the smaller ANO sets, which turned out to work surprisingly well. It is based on the following considerations:

- It is a general observation for moderate basis sets, that multipole moments are described adequately while polarizabilities come out too small.
- This deficiency in the polarizability has its major impact in the dispersion energy E_{disp}.

Assuming, that (i) the correlation contribution $\Delta E^{\mathrm{CP}}(\mathrm{MP2}) - \Delta E^{\mathrm{CP}}(\mathrm{SCF})$ is dominated by the dispersion energy and (ii) that the dipole polarizability term dominates E_{disp}, a simple scheme to improve $\Delta E^{\mathrm{CP}}(\mathrm{MP2}) - \Delta E^{\mathrm{CP}}(\mathrm{SCF})$ would be to scale this entity by

$$F \doteq \frac{\sum_{\alpha\beta\mu\nu}^{3} \tilde{\alpha}^{A}_{\alpha\beta} \tilde{\alpha}^{B}_{\mu\nu} T^{AB}_{\alpha\mu} T^{AB}_{\beta\nu}}{\sum_{\alpha\beta\mu\nu}^{3} \alpha^{A}_{\alpha\beta} \alpha^{B}_{\mu\nu} T^{AB}_{\alpha\mu} T^{AB}_{\beta\nu}}, \tag{7.1}$$

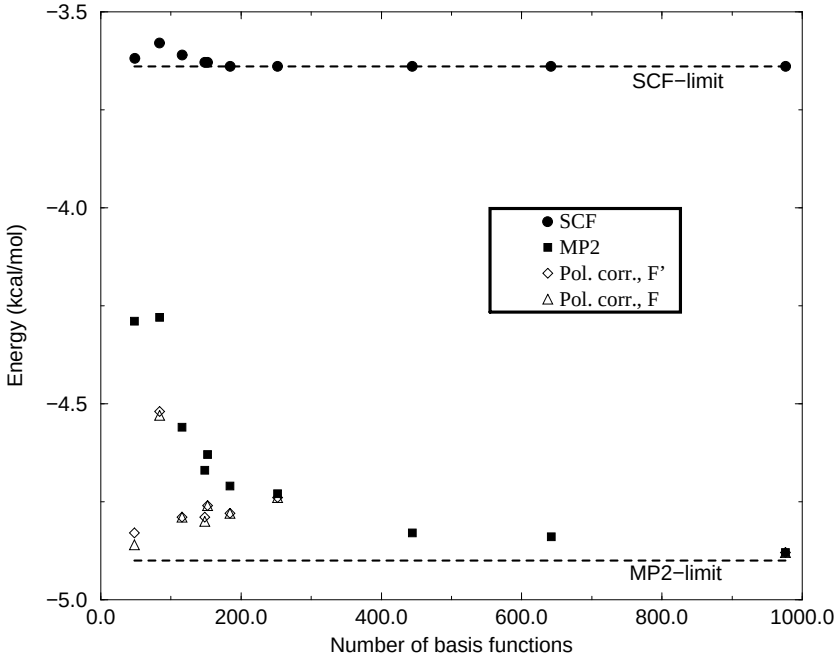

Figure 7.5. SCF and MP2,FC interaction energies as a function of the basis set size (*i.e.*, the number of basis functions). The ordinary, CP corrected SCF and MP2,FC data points are represented by filled circles and squares, respectively. The data points corresponding to CP and polarizability corrected interaction energies are represented by empty diamonds (orientation independent correction) and empty triangles (orientation dependent correction), respectively.

where $\alpha^A_{\alpha\beta}$ denote components of the dipole polarizability tensors of molecule A, respectively; $T^{AB}_{\alpha_1\ldots\alpha_n} = \nabla_{\alpha_1}\ldots\nabla_{\alpha_n}1/R$ are components of the multipole-propagator tensor, and $\tilde{\alpha}^A$ being the dipole polarizability tensor of monomer A at the basis set limit. If the polarizability tensor is not too anisotropic, F can be further simplified to

$$F' \doteq \frac{\tilde{P}^A\tilde{P}^B}{P^AP^B} \qquad \text{with} \qquad P \doteq \frac{1}{3}(\alpha_{xx}+\alpha_{yy}+\alpha_{zz}) \qquad (7.2)$$

The polarizability scaled and ordinary CP corrected interaction energies are plotted in Figure 7.5. The polarizability scaled interaction energies cluster around -4.75 – -4.8 kcal/mol and are surprisingly stable with respect to basis set extensions, apart from the very smallest sets. The discrepancies between F and F' scaled energies are small, as expected from the quite isotropic polarizability tensor obtained for the water monomer.

Summary and conclusions

In this work the structure and interaction energy of the water dimer have been accurately determined. It is found that the to-

tal binding energy of the dimer including corrections for the BSSE and for the deformation of the monomer structures in the complex is close to 4.98 kcal/mol. The remaining uncertainty of this estimate is of the order of 0.05 kcal/mol, and is primarily due to the uncertainty in the geometry of the complex, which naturally could not be optimized on equal footing with the single point calculations. The tendency of this source of error obviously is to increase the binding energy. The remaining BSSE in the most accurate calculation is -0.03– -0.04 kcal/mol.

The geometry of the dimer in the present investigation is characterized by an O–O distance of 2.925 Å, which was determined on the counterpoise corrected CCSD(T) potential energy surface. The discrepancy between the experimentally deduced distance of 2.95 Å and the present result is probably due to difficulties in the determination of the potential energy minimum from experimental data due to coupling of the intermolecular O–O stretch with other inter- or intramolecular modes orthogonal to the stretch.

We have further shown that the proper approach to calculate the binding energy involves the use of the counterpoise correction, but that truncation of the one particle basis set inevitably leads to a reduced dispersive coupling between the two water molecules. In the course of this analysis we also have seen that the high angular momentum AOs contribute primarily to the interaction energy via the short range, higher-order dispersion terms. Based on these considerations a simple correction procedure is proposed, which removes part of this problem by scaling the correlation energy contribution with the ratio of the products of the molecular polarizabilities obtained at the basis set limit, and within the basis used for the calculation of the interaction energy, respectively. This approach however does not involve any contributions from higher-order polarizabilities.

We can conclude that there is a cancellation between the ordinary BSSE and the lack of dispersive interaction in small and moderate basis sets, and that this cancellation is one of the major reasons for the long dispute about the proper way to evaluate the interaction energy of a molecular complex.

7.6 Ab Initio Molecular Dynamics Investigations of Transition Metal Clusters

Henrik Grönbeck, Wanda Andreoni
IBM Research Division, Zurich Research Laboratory, Switzerland
Arne Rosén
Department of Physics, Göteborg University and CTH

Computationally, the field of atomic clusters is challenging because of the large-scale quantum problems involving unknown ionic configurations. For clusters, the discretization of the electronic states results in electronic characteristics that are different from the bulk properties. Moreover, one might expect different structural motifs and coordinations than are present in the extended material. This is an issue that should be addressed from first principles. Model potentials derived from bulk or surface properties can most likely not account for the rehybridization in these finite systems. In our work at PDC, we are applying the density functional formalism [Hohenberg and Kohn, 1964, Kohn and Sham, 1965] using local minimization techniques, and the Car–Parrinello (CP) [Car and Parrinello, 1985b] method for molecular dynamics to investigate the electronic, geometric, and chemical properties of small transition metal clusters. Here we will give two examples from our research program at PDC. The calculations were performed using the parallel 2.5 IBM version of the CPMD code developed by J. Hutter.

The structures of atomic clusters is generally unknown and computationally challenging due to the large number of possible isomers

The structures of atomic clusters is generally unknown and computationally challenging due to the large number of possible isomers. We have performed calculations of the geometric properties of niobium clusters [Grönbeck *et al.*, 1997]. Niobium is a transition metal with several interesting features in the size evolution pattern of the cluster properties, for which the experimental evidence of existing isomers is one example. For Nb_8, we have obtained with the aid of molecular dynamics and standard geometry optimizations several minima on the energy potential surface. Three of them are shown Figure 7.6. These three isomers are within 0.6 eV in total energy. The lowest energy geometry (top panel) is a dodecahedron, whereas both (middle) and (bottom) have structures of bi-capped octahedra. These geometries represent all compact structures with a high coordination for all atoms in the cluster.

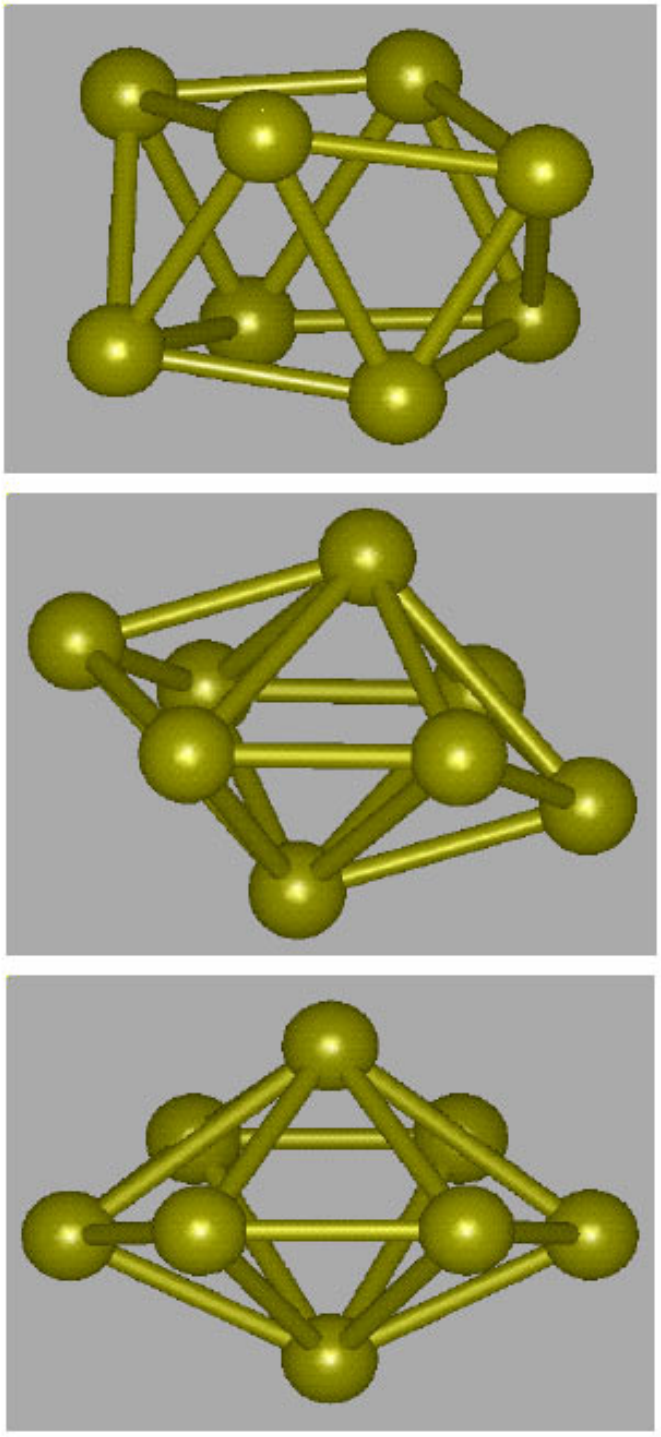

Figure 7.6. Low energy structures of Nb_8.

In addition to bare metal clusters, we have studied the adsorption of molecules such as O_2 and CO onto clusters of niobium and platinum. One example is $(CO)_n$ adsorbed onto Pt_3 [Grönbeck and Andreoni, 1997]. CO on Pt(111) is a textbook example of the interaction of CO on transition-metal surfaces, which essentially can be understood in terms of the Blyholder model for 5σ donation and 2π backdonation. What happens when the surface is reduced to only three atoms? Are, for example, the same geometric configurations preferred, and what are the characteristic binding energies? In our study, we have found that actually the "top" configuration is preferred for adsorption of CO on Pt_3, in agreement with CO onto Pt(111). However, the molecular binding energy is much higher ($\sim$1 eV). For the characterization of CO on surfaces, the stretching vibration frequency of CO is often measured. This has also been done in the case of clusters, using vibrational-resolved photoelectron spectroscopy (PES) [Icking-Konert *et al.*, 1996]. In this method, the vibrations are excited by removing one electron from an anionic cluster. Consequently, it is important where the last electron is localized. We find that for the anion of $Pt_3(CO)_6$ this orbital is delocalized over the entire molecule, see Figure 7.7. Removing this electron will excite two decoupled vibrations of the "top" and "bridge" bonded CO molecules. Our evaluation of the vibrational spectrum yields symmetric CO stretch vibrations at 2103 and 1930 cm^{-1} for the top and bridge positions, respectively. The PES experiments [Icking-Konert *et al.*, 1996] resolve one peak at 2020 cm^{-1} and, for a coverage of 0.5 at the Pt(111) surface, these vibrations are reported to be 2104 and 1885 cm^{-1} [Hoge *et al.*, 1988].

Having taken two examples from our research program, we have demonstrated issues currently of interest in the field of atomic clusters, and some of the possibilities of the methods we are using. The plane wave – pseudo potential method is powerful in handling dynamical properties of clusters. Currently, we have initiated a study of alkylthiole passivated nanoclusters of gold. Such stable systems have recently been produced experimentally [Whetten *et al.*, 1996] and show several interesting features, such as size effects in electronic and optical properties. So far, calculations of self-assembled metal nanoclusters have been made only with classical potentials. These studies have been of great importance to verify and interpret the experiments. It is, however, clear that quantum mechanical

These studies have been of great importance to verify and interpret the experiments

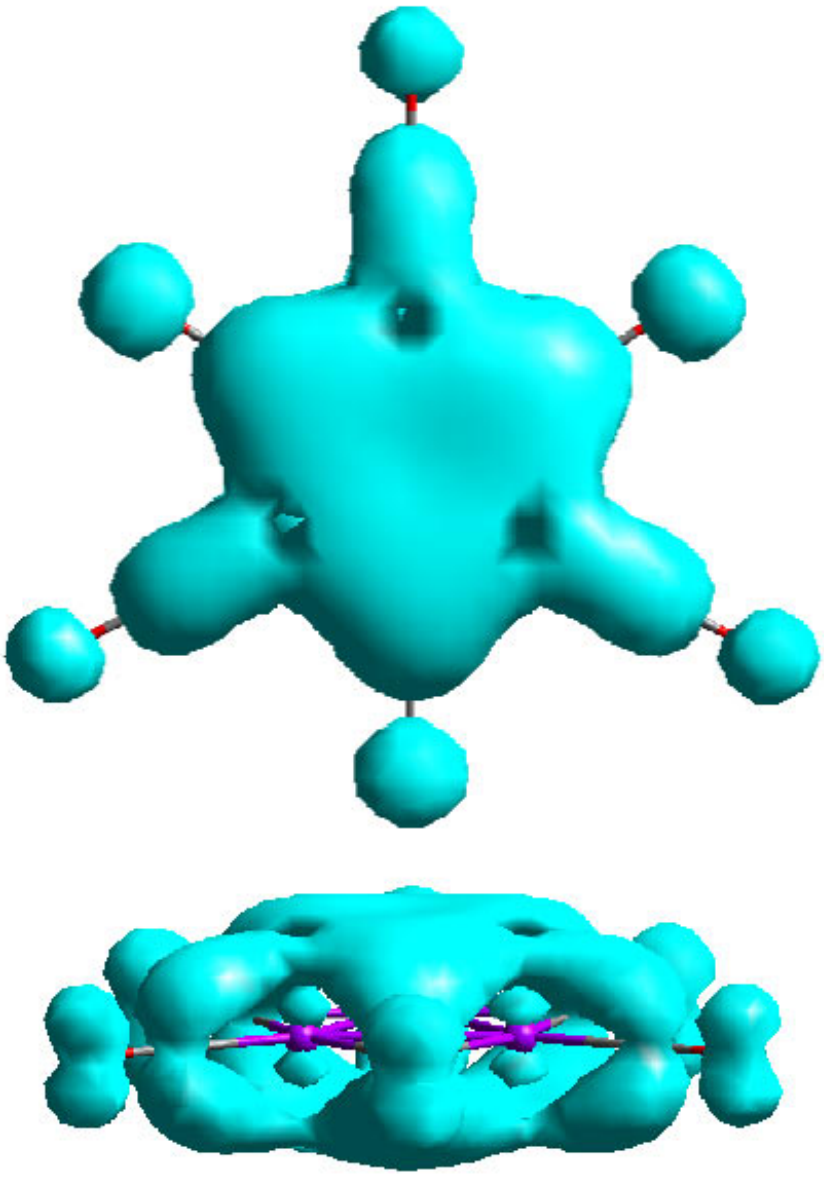

Figure 7.7. Two views of the $Pt_3(CO)_6^-$ HOMO probability density. The plotted surface corresponds to $0.001\,e/(a.u.)^3$. $Pt_3(CO)_6^-$ has a planar structure with three CO molecules in "top" and "bridge" positions, respectively.

calculations are necessary to understand and eventually control the size-evolutionary pattern of physical and chemical properties of such systems. Especially it is expected that the interaction between the thiol chains and the core of gold atoms needs an *ab initio* description.

7.7 MD Simulations of the Solvent Exchange Mechanism around Li^+ in Aqueous Solution[1]

Kersti Hermansson, Daniel Spångberg
Inorganic Chemistry Department, Angstrom Laboratory,
Uppsala University

The solvated metal ion is the precursor of all solution phase metal ion coordination chemistry. An understanding of the structure and dynamics of solvated metal ions is therefore essential for understanding the reactivity of ions in solution. The pure solvent exchange reaction in aqueous ionic solutions, for example, can be formulated like this:

$$M^{n+}(H_2O)_6 \; + \; H_2O^* \rightarrow M^{n+}(H_2O)_5(H_2O)^* \; + \; H_2O \qquad (7.3)$$

The detailed mechanisms for solvent exchange processes are often difficult to establish with certainty from experiment. From experiments like X-ray and neutron diffraction, NMR and IR, much is known about the hydration structure around metal ions in solution, but much less detailed information exists concerning the dynamics. Residence times for water exchange around metal cations have been measured using NMR and are found to span an enormous range: from picoseconds for the alkali ions up to several days for some of the highly charged d-metal ions. By varying temperature and external pressure in the experiments, exchange mechanisms can be proposed from derived properties like the activation volume and activation entropy. Establishing the correct mechanism is usually far from trivial, however, and for the very fast exchange processes around alkali cations the situation is even worse: experimental data is non-existant or very unprecise. In all these cases simulations can give valuable additional molecular level information.

In all these cases simulations can give valuable additional molecular level information

[1]This project is supported by the Swedish Natural Science Research Council NFR and the National Graduate School in Scientific Computing NGSSC through the Swedish Foundation for Strategic Research SSF.

MD simulations and results

We have performed constant–pressure constant–temperature MD simulations of a dilute solution of LiCl in water to establish the mechanisms for solvent exchange around the cation at room temperature and atmospheric pressure. The exchanges are very infrequent on the time scale of a normal MD simulation run, and long simulation runs are needed. The timestep used was 0.75 fs. The equations of motion were treated by Anderson's pulsating box method [Anderson, 1980]. The TIP4P potential [Jorgensen *et al.*, 1983] was used for the water–water interactions. The ion–water potentials were taken from [Bounds, 1985] and the ion-ion potentials from [Sangster and Atwood, 1978]. Electrostatic interactions were treated by the Ewald method.

Figure 6.17 on page 117 shows snapshots from an animation sequence of a solvent exchange event around Li^+. The Li^+ ion is normally surrounded by six water molecules in the simulation, as seen in "Step 1". The water molecules are dipoles and will therefore arrange themselves with the oxygen atom pointing towards the cation most of the time. The instantaneous coordination figure is a distorted octahedron as has been indicated in the figure. The picture also includes a seventh molecule, residing further out in the second shell.

Most of the time a cation in water moves together with its hydration shell, but sometimes one of the bound water molecules leaves the ion and joins the water molecules in the bulk solution - or a water molecule from the bulk first enters the hydration and creates a strained intermediate with seven neighbours before "an old" first-shell molecule leaves for the bulk. These two limiting processes are called *dissociative exchange* and *associative exchange*, respectively. In these simulations we are trying to establish which mechanism is predominating for the exchange around $Li^+(aq)$. We are also studying the rate of the exchange process and its pressure dependence as well as activation volumes and their mechanistic interpretation.

The arrow on one of the six bound water molecules in Step 1 is drawn to indicate that this molecule is soon going to move away from the ion. This has happened in Step 2, which shows the geometry of the intermediate complex in the exchange process around Li^+. We find that the intermediate complex consists of five molecules, *i.e.*, the exchange is dissociative, and the complex

is a fairly regular "trigonal bipyramid". The two molecules shown above the cation are not bound to the cation but reside much further out, in the second hydration shell. The intermediate complex lives for about half a picosecond, before a new water molecule enters the first hydration shell and an octahedron is once again formed (Step 3).

To summarize we find that:

- Most of the exchanges around lithium are of the dissociative type.
- There is an exchange around lithium about once every 30 picoseconds.
- The exchange event itself takes about 0.5–1 picosecond.

7.8 Theoretical Studies of Organometallic Reactions

Mats Svensson
Department of Chemistry, Organic Chemsitry, KTH

Computational based chemistry is a fast growing research field both in the academic world and in the industry. The speed of modern workstations together with the development of more efficient methods and algorithms have made computer based chemical research an interesting complement to experimental chemistry. In particular, the chemistry involving transition metals as catalysts is a field well suited for a theoretical study since many of the intermediates are hard to isolate under normal experimental conditions. In this project we use a hybrid density functional approach, the lately very popular B3LYP method as implemented in Gaussian94.

The chemistry involving transition metals as catalysts is a field well suited for a theoretical study since many of the intermediates are hard to isolate under normal experimental conditions

This project, which is a collection of several subprojects in collaboration with groups in our department and at other universities, is aiming for an understanding of the electronic and steric effects governing the reaction profiles of organometallic reactions. Projects presently under study are:

- Epoxidation of alkenes catalyzed by manganese-salen complexes. An in house collaboration in the organic chemistry group at KTH with professor Björn Åkermark, Ph.D. student Christian Linde and Assoc. professor Per-Ola Norrby (at the Royal Danish School of Pharmacy). The theoretical part of this project is aiming for an understanding of the mechanism behind the

isomerization and the selectivity of this important epoxidation reaction. The transition state, the highest energy structure on the reaction path, for the addition of the alkene to the oxo-ligand of the manganese complex is shown in Figure 6.16 on page 117. This transition state leads to the desired product of this reaction; the oxidated alkene, *i.e.*, the epoxide.

- Late transition metal complexes as catalysts for olefin polymerization. The initial steps, the complexation and migratory insertion of the olefin into the metal-alkyl bond is studied in detail in order to understand the influences of the substituent on the olefin and the role of the metal [Svensson *et al.*, 1997]. This is a very promising reaction for the development of new polymers. A collaboration between Dr. Krister Zetterberg and Dr. Staffan Strömberg.

- Regio control in the Heck reaction. A combined theoretical and experimental study of ligand and substrate effects on the regio selectivity in the Heck reaction using the biphosphine ligands dppe and dppp. A collaboration with professor Björn Åkermark, Dr. Maik Ludwig and Dr Staffan Strömberg.

- Nitrogen fixation by Nitrogenases. We have studied the fixation of nitrogen, step by step using a Fe(II)-dimer model for the active site in the nitrogenase. This projects is a collaboration with professor Per Siegbahn and Joakim Westerberg (Stockholm University) and professor Robert Crabtree (Yale University) [Siegbahn *et al.*, 1998].

7.9 Topics in Radical Chemistry Studied Using Quantum Chemical Methods

Sten Lunell, Torbjörn Fängström, David Edvardsson, Christer Enkvist
Department of Quantum Chemistry, Uppsala University

Radicals are a class of compounds which usually are characterised by exceptionally high reactivity. They often exist only as short-lived intermediates in chemical reactions, and are as such very difficult to study directly by experimental techniques. With the advent of modern supercomputers quantum chemical calculations have therefore become a powerful alternative and/or complement to experimental investigations on these systems.

In the present project, we are primarily studying the structure, hyperfine properties, and reactions of a number of radicals, employing Density Functional Theory (DFT) and *ab initio* methods [Fängström *et al.*, 1998a, Fängström *et al.*, 1998c, Shiotani *et al.*, 1998, Fängström *et al.*, 1998b].

As mentioned above radicals are difficult to study experimentally due to their high reactivity and natural tendency towards decomposition. In some cases inconclusive assignments are deducted in Electron Spin Resonance (ESR) spectra, which are known to be very sensitive to the geometry. The theoretical contribution hence demands very accurate geometry optimisation calculations. In this connection one example is the theoretical interpretation of the ESR spectrum for the dimethylether radical cation which has been studied in detail with *ab initio* and DFT methods.

A factor that may affect the interpretation of the spectrum is the formation of complexes between the radical and the surrounding solvent. In such cases the size of the system becomes a critical factor and accurate calculations at reasonable levels can only be managed in conjunction with powerful computer facilities.

One problem studied [Fängström *et al.*, 1998b] has been the determination of the potential energy surface (PES) for the reaction between aluminum and dimethylether, as well as hyperfine coupling constants for possible products of the reaction, using DFT methods. Two important one-dimensional cuts of this PES is depicted in Figure 7.8.

Another example of an ongoing project is the theoretical study of chlorine-oxygen compounds related to the ClO self-reaction [Fängström *et al.*, 1998a]. This reaction is known to be a crucial step in the reaction cycle mainly responsible for the spring-time ozone depletion over the Antarctic.

This reaction is known to be a crucial step in the reaction cycle mainly responsible for the spring-time ozone depletion over the Antarctic

Geometrical parameters, vibrational frequencies, relative stabilities, and dissociation energies of the three stable Cl_2O_2 isomers and the OClO and ClOO radicals were calculated using DFT. The present investigation showed that DFT using hybrid functionals is capable of describing these systems to at least the same degree of accuracy as *ab initio* methods.

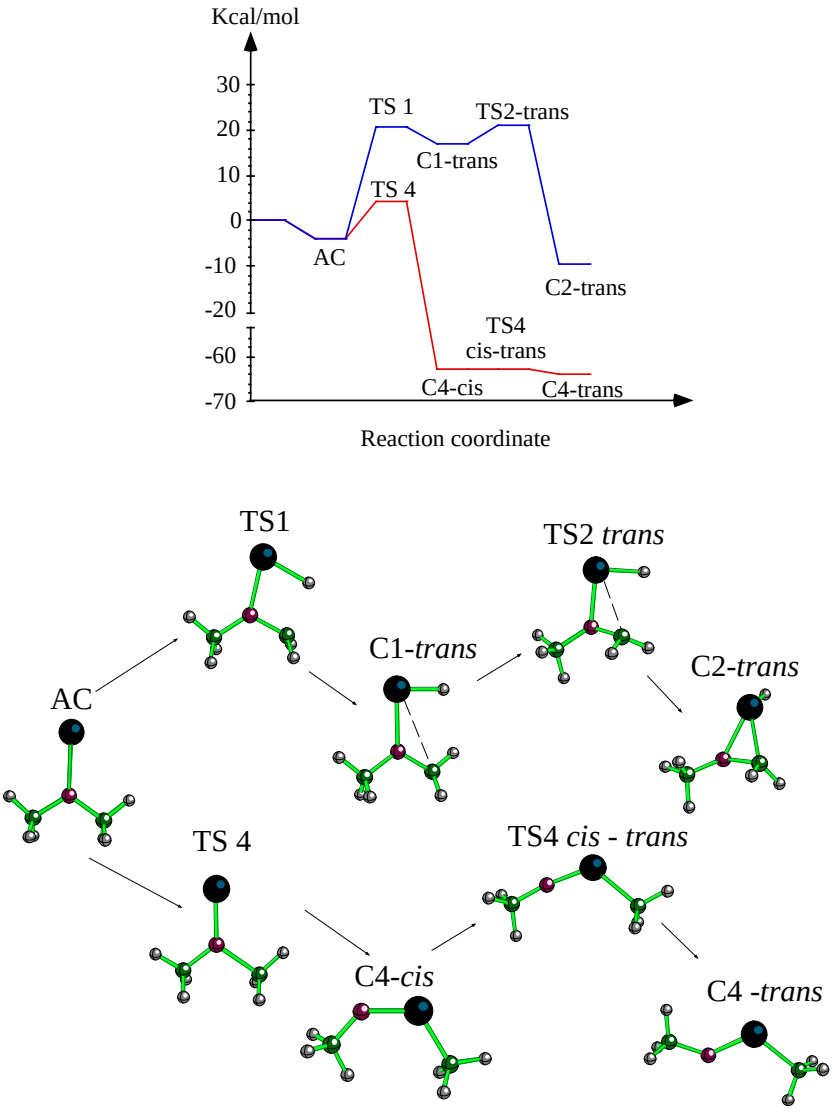

Figure 7.8. Energy reaction profile for the C-H and C-O aluminum-dimethylether insertion reactions and structures of C-H and C-O insertion products and transition state.

7.10 Parallel Molecular Dynamics Simulations of DNA Systems[2]

Alexander Lyubartsev, Aatto Laaksonen
Division of Physical Chemistry, Arrhenius Laboratory,
Stockholm University

Introduction

Computer simulation methods, such as, Molecular Dynamics (MD) and Monte Carlo (MC) have now become important techniques to study fluids and solids. These methods provide a link between theory and experiment and they are also the only way to study complex many-body systems when both experimental techniques and analytical theories are unavailable.

Now it is a standard routine procedure to simulate molecular systems consisting of the order of 100–1000 particles, which in some cases (*e.g.*, simple liquids) is sufficient to give a good description of the corresponding macrosystem. For other systems, a larger number of particles is needed in order to describe them in a realistic way. Complex bio- and organic molecules (*e.g.*, proteins, nucleic acids, membranes, carbohydrates, etc.) immersed into a solvent increase the number of involved atoms with one to two or more orders of magnitude. Also, the larger the molecular systems grow, the longer simulations are needed to follow low-amplitude motions and slow conformational transitions. It is clear that the rate of the progress towards more complex molecular models is set, to a large extent, by advances in microprocessor technology and computer architecture as well as by development of appropriate software.

Parallel algorithms

Computer simulations of many-particle systems are well suited for parallel computer systems. The basic reason for this is that the forces acting on each particle can be calculated independently in different processors. However, the most optimal parallel scheme for a particular problem depends both on the hardware in hand and on the system under investigation (size, type of interaction, etc.). Electrostatic interactions, fast intramolecular motions due

[2]The color pictures of the spatial distribution functions were produced using the `gOpenMol` package by Leif Laaksonen, Centre for Scientific Computing, Espoo, Finland.

to explicit modeling of hydrogens, angle and torsional angle forces of macromolecules—all these kinds of forces require a special treatment to create an effective parallel code.

There exists two main strategies in parallelization of a molecular dynamics code: replicated data and domain decomposition. The first scheme implies that all the nodes know the positions and velocities of all the atoms, and calculation of different forces goes in parallel. In the domain decomposition approach the atoms are distributed over the nodes, and each node calculates forces only for a certain set of atoms. Both schemes have *pros* and *cons*. We applied the replicated data method which is more suitable for simulations of macromolecules surrounded by a solvent. The effectiveness of this method does not depend critically on the system structure and the force field. The weak point of this approach is that it requires more communications between the processors. Still, the prevailing point of view is that for several or several dozens processors the replicated data method is preferable.

The MDynaMix program

During 1994–1996 we have developed a general purpose molecular dynamics code (MDynaMix) for simulations of arbitrary mixtures of rigid or flexible molecules employing the most modern simulation techniques: double time step algorithm for fast and slow modes, optimized Ewald method for electrostatic interactions, constant temperature–constant pressure algorithm. The program can be used for simulation of mixtures of molecules interacting with AMBER- or CHARMM-like force fields [Weiner *et al.*, 1986], [MacKerell *et al.*, 1995], which includes the following terms:

1. atom-atom short-range interactions (Lennard–Jones potential),
2. atom-atom electrostatic interactions,
3. intramolecular interactions: covalent bonds, covalent angles and torsional angles,
4. some optional terms (hydrogen bonds, etc.).

The code is highly universal and well suited for simulation of both simple molecules and complex biological macromolecules

The code is highly universal and well suited for simulation of both simple molecules and complex biological macromolecules. It can be easily made to run on a single-processor computer. In the latest version (4.2) additional features were included: separate pressure

control in different directions (for simulation of anisotropic systems), generalized reaction field method for electrostatic interactions, truncated octahedron or hexagonal simulation cell, parallel SHAKE algorithm for constrained dynamics, different types of torsion angle potential and a few other options.

The replicated data method implies that each node knows the positions of all the atoms. This easily allows one to distribute calculation of different forces over the nodes, providing equal load to all the nodes. After completing the calculations on each node all the forces acting on a given atom are transfered to the "home" node corresponding to this atom and summed up. This is done by an `MPI_Reduce_scatter` call from the MPI library. Then the atoms are moved according to a chosen integration scheme. After completing an MD step new positions of atoms are broadcasted to all nodes. The two global communication operation, `MPI_Reduce_scatter` and broadcast, cause some computational overhead. Other parts of the program are almost 100% scalable.

Benchmarks

The performance of the program was tested on several molecular systems qualitatively differing by the composition:

1. A periodic fragment of DNA in ionic aqueous solution: DNA (635 atoms), 1050 waters and 40 Na and Cl ions, 3825 atoms in total.

2. An NaCl ion solution: 20 NaCl ion pairs and 1960 water molecules, 5920 atoms in total.

3. A lipid bilayer. 64 DPPC lipid molecules (50 atoms each) and 1472 water molecules, 7616 atoms in total.

All the simulations were carried out with flexible molecular models employing the double time step algorithm with 0.2 fs small time step and 2 fs long time step. The Ewald method was applied for calculations of electrostatic contributions. Table 7.1 shows total CPU time on the IBM SP-2 for 1 ps simulations depending on the number of processors.

System	#atoms	Box sizes	R_{cut}	Nodes 1	4	8	16	32
1. DNA	3825	$33 \times 33 \times 34$	13	120	32	17	9	5.5
2. Ion	5920	$39 \times 39 \times 39$	13	220	57	28	17	9.5
3. Lipid	7616	$44 \times 44 \times 64$	14	300	77	45	23	14.0

Table 7.1. CPU time (in minutes) for 1 ps simulation of 3 different systems on the IBM SP-2 depending on number of processors. Box sizes and cutoff distance R_{cut} are given in Å.

Simulations of DNA system

We have used the developed software for large-scale molecular dynamics simulations of DNA system in aqueous ionic solution. The simulation cell includes a periodic fragment of DNA (10 base pairs), water molecules and different ions. At present we have carried out simulations with Na^+, Li^+ and Cs^+ counterions. We have employed the CHARMM-95 [MacKerell *et al.*, 1995] force field for DNA, flexible SPC model for water and rigid models for ions. The simulation were carried out in a rectangular box with periodic boundary condition and the Ewald summation method for the electrostatic interactions. Thus the model represents in fact an infinite array of DNA ordered in parallel. One should note that this model is closer, compared to an isolated DNA model, to DNA molecules *in vivo* where DNA are compactly packed in nucleosomes. The simulation time was 2 ns for Li and Na DNA and 400 ps for Cs DNA. Purposes of the molecular dynamics simulations were many-folds.

Hydration effects

Different ions and other small molecules exert a decisive influence on the behavior of DNA and its biological functionality. Molecular simulations can yield valuable information on how water molecules and ions are organized around different sites on the DNA surface. The modern 3D computer graphics allows one to display the *spatial* distribution functions which are proportional to the probability to find an atom in local coordinate system of another molecule.

Molecular simulations can yield valuable information on how water molecules and ions are organized around different sites on the DNA surface

Figure 6.18 on page 118 shows the spatial distribution functions of O and H water atoms relative to a phosphate group of DNA. One can see three clear maxima of O and H spatial distribution functions around each of the two oxygens of the phosphate group. Analyzing the distributions one can conclude that each oxygen from the phosphate group is surrounded by three water molecules, each with one OH bond directed straight to the oxygen of the

phosphate group and with another OH bond without preferential orientation.

Figure 6.19 on page 118 and Figure 6.20 on page 119 show the spatial distribution functions for Li^+ and Na^+ ions. For Li^+ ions the displayed contour surfaces are drawn at intensities 3 and 10 units, the maxima of the distribution function being above 100. This means that Li^+ ions are strongly bound to the phosphate groups. Indeed, the detailed analysis of the MD trajectories shows that some Li^+ ions were bound to a phosphate group during the whole simulation run.

The intensity of Na^+ spatial distribution function is lower compared to Li^+, the displayed surfaces are drawn at 2 and 4 units. One can notice an asymmetry of distribution of Na^+ between two different oxygens on the phosphate group. Na^+ prefer to bound to the oxygen which is close to the neighboring sugar group. Behind this group one can see another maximum in the spatial distribution function which corresponds to binding of Na^+ ions to the bases, in the large groove of DNA.

The spatial distribution function for Cs^+ ions does not show any specific binding to any DNA site. These ions are just moving around the DNA surface being attracted by the electrostatic forces.

Calculation of effective ion-DNA potentials

Molecular dynamics simulations can be used to construct effective (or low-resolution) potentials to describe ion-DNA interactions on a larger scale. These potentials allow one to carry out simulations of ion-DNA system without explicit representations of water molecules, but keeping the same structural properties. Removing of water molecules reduces greatly the complexity of the system and makes it possible to study another class of phenomena: polyelectrolyte properties of DNA, global conformational properties, association, etc.

To derive the effective potentials, we have calculated, from MD simulations, the radial distribution functions between the ions and some sites on the DNA surface. Then we use the inverse Monte Carlo procedure [Lyubartsev and Laaksonen, 1995] to reconstruct the interaction potentials from RDF-s. The results for effective potentials between ions and two different sites on DNA (P atoms of the phosphate groups and C4 atoms of base pairs) are shown in Figure 7.9.

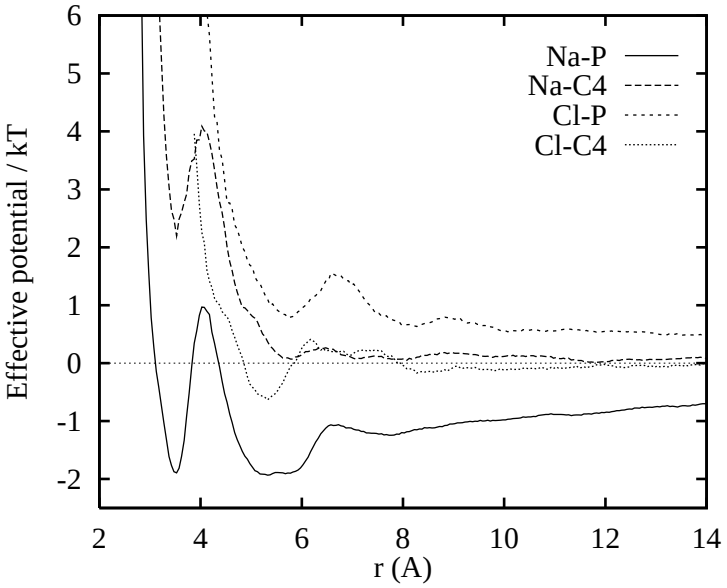

Figure 7.9. The effective potential between Na^+ and Cl^- ions and two sites of DNA (phosphates and C4 atom of the base pairs).

Diffusion of ions

The dynamics of ions near the DNA surface differs considerably from that of bulk solutions. The NMR experiments carried out at our laboratory show that the diffusion of ions in concentrated DNA solutions is essentially slower compared to the bulk solution. The retardation of the self-diffusion coefficient occurred to be strongly dependent on the ion type: it is very high for Li^+ ions and relatively low for Cs^+ ions. Our simulation results (Table 7.2) confirm these experimental data. On the first sight it may seem strange that the large and heavy Cs^+ ion moves much faster than light and small Li^+ ion, especially in concentrated DNA solutions or fibers where the mean distance between the DNA surfaces is a few Ånströms. The molecular dynamics simulations allow us to understand the reasons for this behavior. A Li^+ ion, being small, can approach closer to another charged atom and forms a rather stable bond. Some of Li^+ ions bind to the phosphate groups of DNA thus becoming almost immovable. Other Li^+ atoms, not bound to DNA, form a hydration shell of water molecules around themselves, thus its effective (hydrated) radius occurs greater than that of Cs^+ ion which does not have any stable hydration shell.

Table 7.2. Self-diffusion coefficients (in $10^{-9}m^2/s$) of ions in ordered DNA solution (distance between DNA 25 Å) and in the bulk phase (concentration 0.4 M).

Ion	DNA-solution	Bulk
Li^+	0.15	0.95
Na^+	0.55[a]	1.1
Cs^+	0.64	1.6

[a] Distance between DNA 33 Å.

Conclusion

We are planning to continue the present molecular dynamics study of DNA molecule in solution addressing to a number of important biophysical problems: effect of different ions on DNA conformation, interaction of DNA with molecular ligands, behavior of DNA in concentrated solution and ordered phase (fibers). The size and time scale of the planned simulations require the further use of parallel high-performance computers at PDC.

The size and time scale of the planned simulations require the further use of parallel high-performance computers at PDC

7.11 Molecular Dynamics Simulations of Nucleic Acids in Organic Solvents

Jan Norberg, Lennart Nilsson
Center for Structural Biochemistry, Karolinska Institutet

Nucleic acid base stacking

Base stacking is one of the driving forces responsible for the stabilization of the three-dimensional structure of DNA and RNA molecules. In contrast to the composition dependent hydrogen bonding energy of Watson-Crick base pairing, base stacking interactions are very sequence dependent. The base stacking phenomenon has been attributed to electrostatic interactions, hydrophobic effects, and dispersion interactions. The natural habitat for nucleic acids is an aqueous solution, containing a mix of salts as well as high molecular weight compounds, and structural properties of nucleic acids can be modulated by the dielectric nature of other molecular species with which they interact, proteins interacting with DNA and RNA may well exert a structural, or dynamic, influence and modify the properties of the nucleic acid by providing a hydrophobic environment shielding it from the aqueous solution. It is therefore of interest to study one of the basic determinants of nucleic structure, base stacking, in surroundings with different dielectric properties. In the present study the stack-

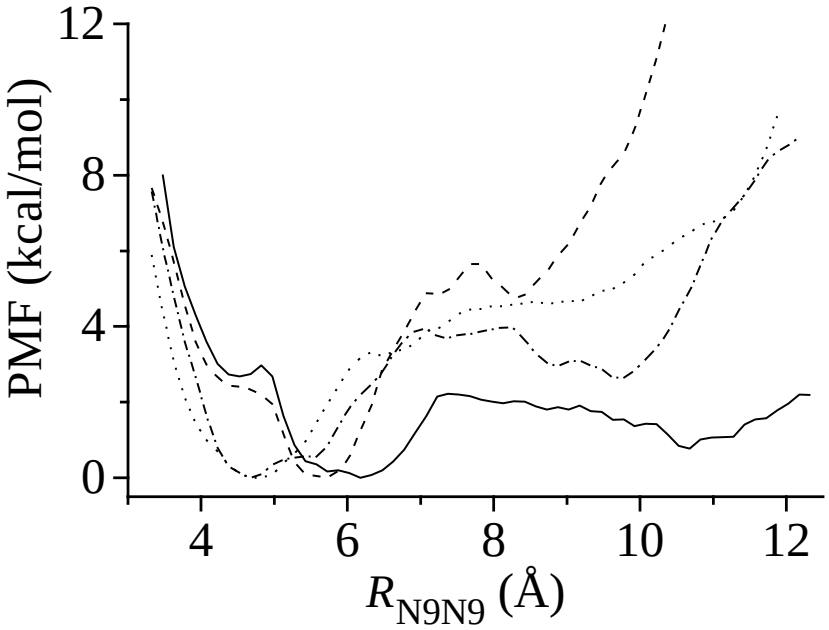

Figure 7.10. Free energy surfaces of stacking for the ribodinucleoside monophosphate rAprA in $CHCl_3$ (-), DMSO (- - -), MeOH (-.-.-) and aqueous (...) solution.

ing ability of ribo- and deoxyribodinucleoside monophosphates in aqueous and organic solutions are examined in the model systems rAprA and dTpdT, using extensive nanosecond unrestrained molecular dynamics simulations and potential of mean force calculations [Norberg and Nilsson, 1998]. The organic solvents investigated in the study were methanol (MeOH), dimethyl sulfoxide (DMSO), and chloroform ($CHCl_3$). For computational details see [Norberg and Nilsson, 1998].

Potential of mean force calculations

From potential of mean force calculations along a reaction pathway we obtained free energy surfaces for rAprA and dTpdT in aqueous and organic solutions. In aqueous solution a well defined minimum, which corresponds to a stacked A-RNA like conformation, was obtained at about 4.7 Å. A wider minimum located at about the same position was found for rAprA in MeOH, but the unstacked states were lower in free energy in MeOH compared to aqueous solution (Figure 7.10). For DMSO the minimum was shifted towards larger R_{N9N9} distances and unstacked states with quite high energies were obtained. In $CHCl_3$ the unstacked states

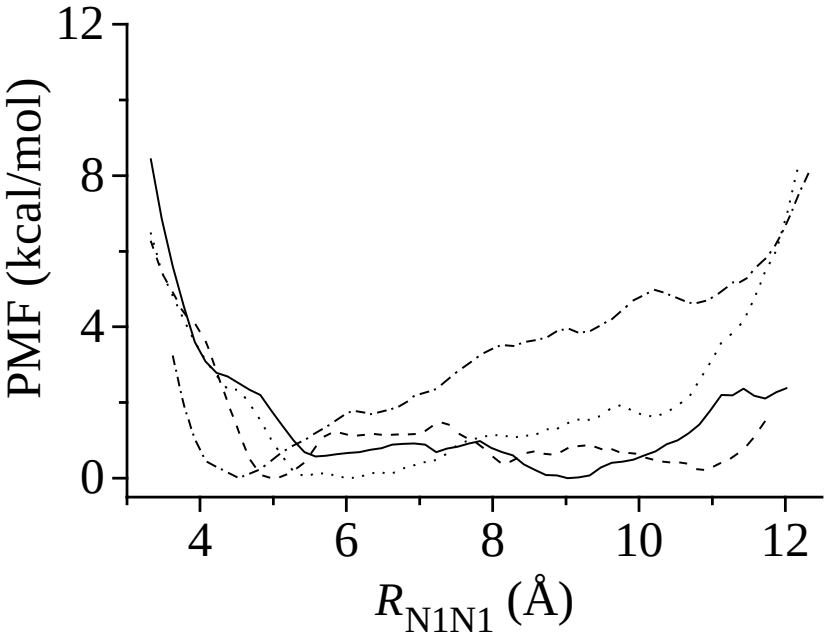

Figure 7.11. Free energy surfaces of stacking for the deoxyribodinucleoside monophosphate dTpdT in $CHCl_3$ (-), DMSO (- - -), MeOH (-.-.-) and aqueous (...) solution.

were of very low energy and no significant barrier between stacked and unstacked states was observed. From experiment the stacking ability of dTpdT has been found to be favored in aqueous solution compared to methanol. In Figure 7.11 the stacking free energy of dTpdT is displayed for aqueous and organic solutions. Only in aqueous solution a well defined minimum was observed for dTpdT and also the free energy of the unstacked states was higher than in the less polar solvents.

Unrestrained molecular dynamics simulations

The stability of MD simulations is often characterized by the root mean square (rms) displacement of atomic positions from a suitable reference structure, usually the starting structure. The time evolution of the rms deviations for rAprA in aqueous, chloroform, dimethyl sulfoxide and methanol solutions are displayed in Figure 7.12. In all four cases the rms deviation was found to be stable throughout the simulation. The smallest rms deviation from the initial structure for the non-hydrogen atoms of rAprA was obtained in methanol, 0.82 Å during the last 400 ps, and in aqueous solution the rms deviation was slightly larger (0.91 Å). In DMSO

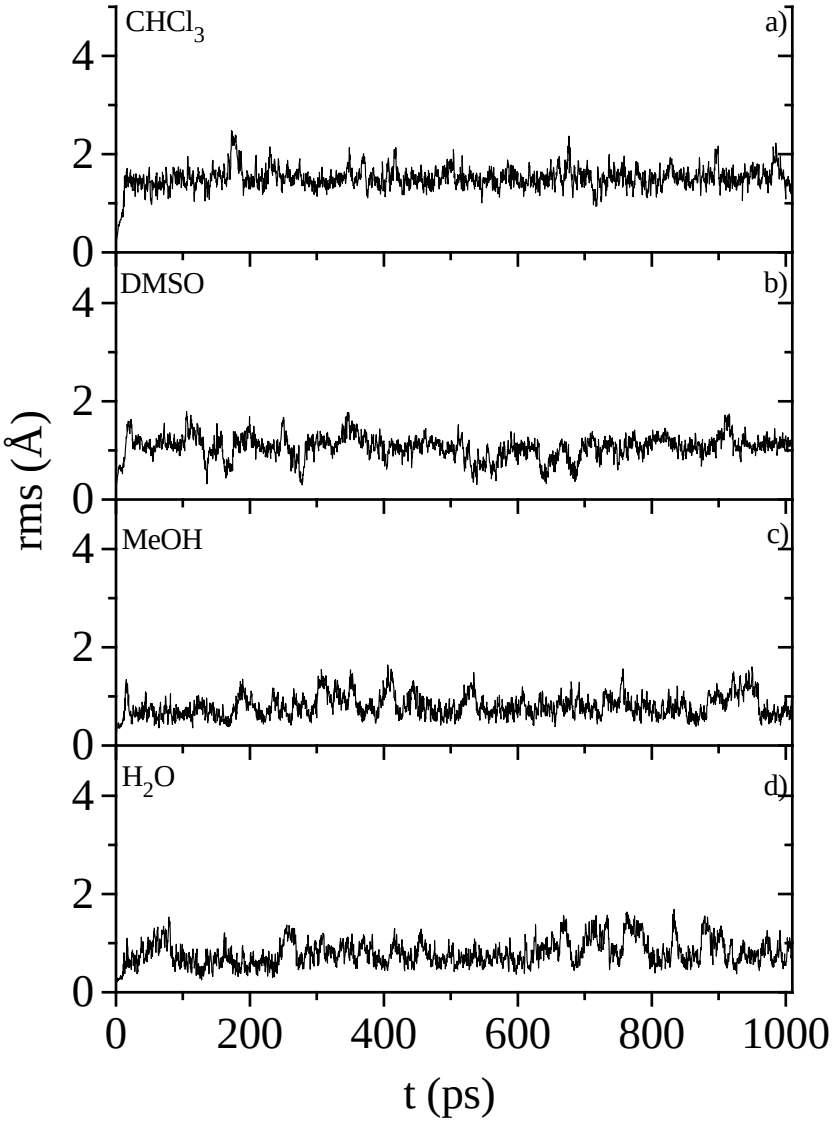

Figure 7.12. Root mean square atomic deviations as a function of time for all heavy atoms of the ribodinucleoside monophosphate rAprA in a) $CHCl_3$, b) DMSO, c) MeOH and d) aqueous solution.

the rms deviation for rAprA was 1.07 Å and a clearly larger value was determined in $CHCl_3$ (1.53 Å). When all atoms were included in the calculation of the rmsd, the rms deviation for rAprA in the four solvents increased by about 0.2 Å. In the different solvents the standard deviation of the rmsd of rAprA were found to be 0.19–0.28 Å. rAprA stacks very well in aqueous solution [Norberg and Nilsson, 1995b], and in this study rAprA showed good stacking ability in both aqueous and organic solutions, but with a rms deviation of 0.62 Å higher in the low dielectric solvent, $CHCl_3$, compared to the high dielectric aqueous solution. For dTpdT the rms deviation from the initial structure in aqueous solution was maintained stable during the whole simulation. A rms deviation of 1.03 Å was obtained for all heavy atoms of dTpdT in water and 1.34 Å including hydrogen atoms (Figure 7.13). In the organic solvents the rmsd for dTpdT still fluctuated on the nanosecond time scale, indicating a lower stability for the stacked state. Among the organic solvents the most stable rms deviation was found for dTpdT in MeOH, 2.50 Å for all the heavy atoms, and larger values of rmsd for dTpdT were observed in DMSO and $CHCl_3$. This is consistent with earlier investigations where the free energy of the unstacked states was found to be lower, with a less favorable base-base interaction energy, for dTpdT than for rAprA [Norberg and Nilsson, 1995a, Norberg and Nilsson, 1995b].

Results

We have demonstrated that the stacking free energy is favored in aqueous solution for both the rAprA and dTpdT molecules. From the rms deviation for both rAprA and dTpdT a clear indication that base stacking is favored in aqueous solution with high dielectric constant compared to organic solutions with low dielectric constants are shown. For rAprA, which has displayed a high stacking propensity in aqueous solution, a more or less stacked conformation was maintained even in low dielectric solvents, but for dTpdT with intermediate stacking ability the bases became much more flexible in the low dielectric solvents compared to the situation in aqueous solution. Taken together these results indicate that in the low-dielectric solvents the bases are more flexible which reduces the free energy cost of unstacking.

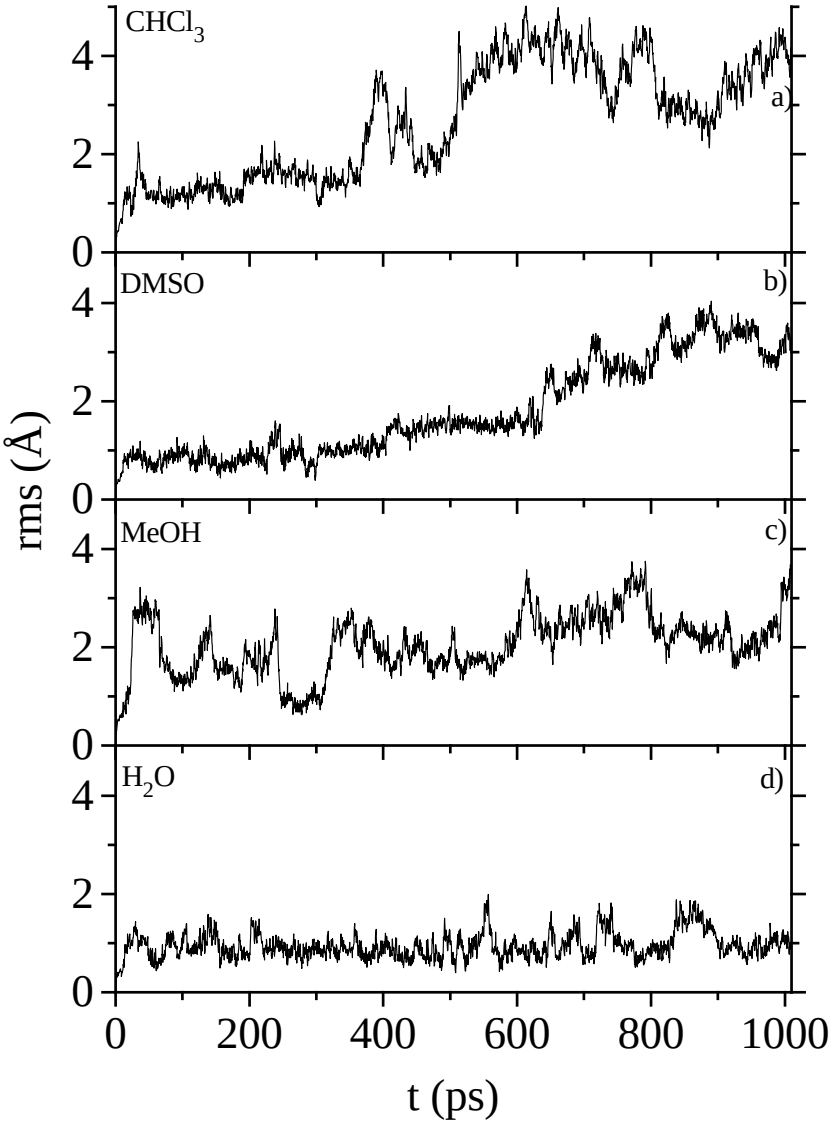

Figure 7.13. Root mean square atomic deviations versus time for all heavy atoms of the deoxyribodinucleoside monophosphate dTpdT in a) $CHCl_3$, b) DMSO, c) MeOH and d) aqueous solution.

7.12 MD Simulation of Binary Mixtures

Dan L. Bergman, Aatto Laaksonen
Division of Physical Chemistry, Arrhenius Laboratory,
Stockholm University

We are interested in the micro structure of binary liquid mixtures. By micro structure we mean the average spatial correlations extending usually less than ten molecular lengths around each molecule. The model system we use is a water–acetonitrile mixture. This system is known to phase separate at some compositions below $T_c = 272$ K. There is an ongoing discussion concerning the micro structure for $T > T_c$. There are some experimental indications that micro heterogenieties form, *i.e.*, regions with locally enhanced concentration of one of the specie.

Since our program vectorizes well we have been able to simulate systems consisting of up to 2048 molecules

In order to investigate the micro structure of this mixture we have performed MD simulations on the Fujitsu VX/2 machine at PDC. Since our program vectorizes well (it spends over eighty percent of the CPU time in the vector unit) we have been able to simulate systems consisting of up to 2048 molecules. To extract the relevant structural information from the MD trajectory we compute spatial distribution functions of atomic number densities (SDFs). They are defined as:

$$g_{AB}(\vec{r}) = \frac{\rho_B(\vec{r} \mid \vec{r}_A = 0)}{\rho_B} \tag{7.4}$$

Here A and B each denotes an atom type, ρ_B denotes the bulk density of type B atoms and, $\rho_B(\vec{r} \mid \vec{r}_A = 0)$ is the conditional density of type B atoms at the point $\vec{r}$ as measured in a coordinate system rigidly attached to the molecule containing atom A. The origin of this coordinate system is at the atom A. Casually one may describe this as the average distribution of B atoms an observer riding on an atom of type A would see.

The oxygen-oxygen distribution is shown in Figure 7.14. At the center is a water molecule and surrounding it is the iso-density surface $g_{OO}(\vec{r}) = 3.3$. At A and B the probability of finding oxygen atoms in the volume inside the isosurfaces, and they can be used to define hydrogen bonds. We have proposed in [Bergman and Laaksonen, 1998a] that spatial distribution functions of this type is a natural starting point for the analysis of micro structure in liquid mixtures, and in [Bergman and Laaksonen, 1998b] we use these functions to derive some properties of the hydrogen bond network in the mixtures.

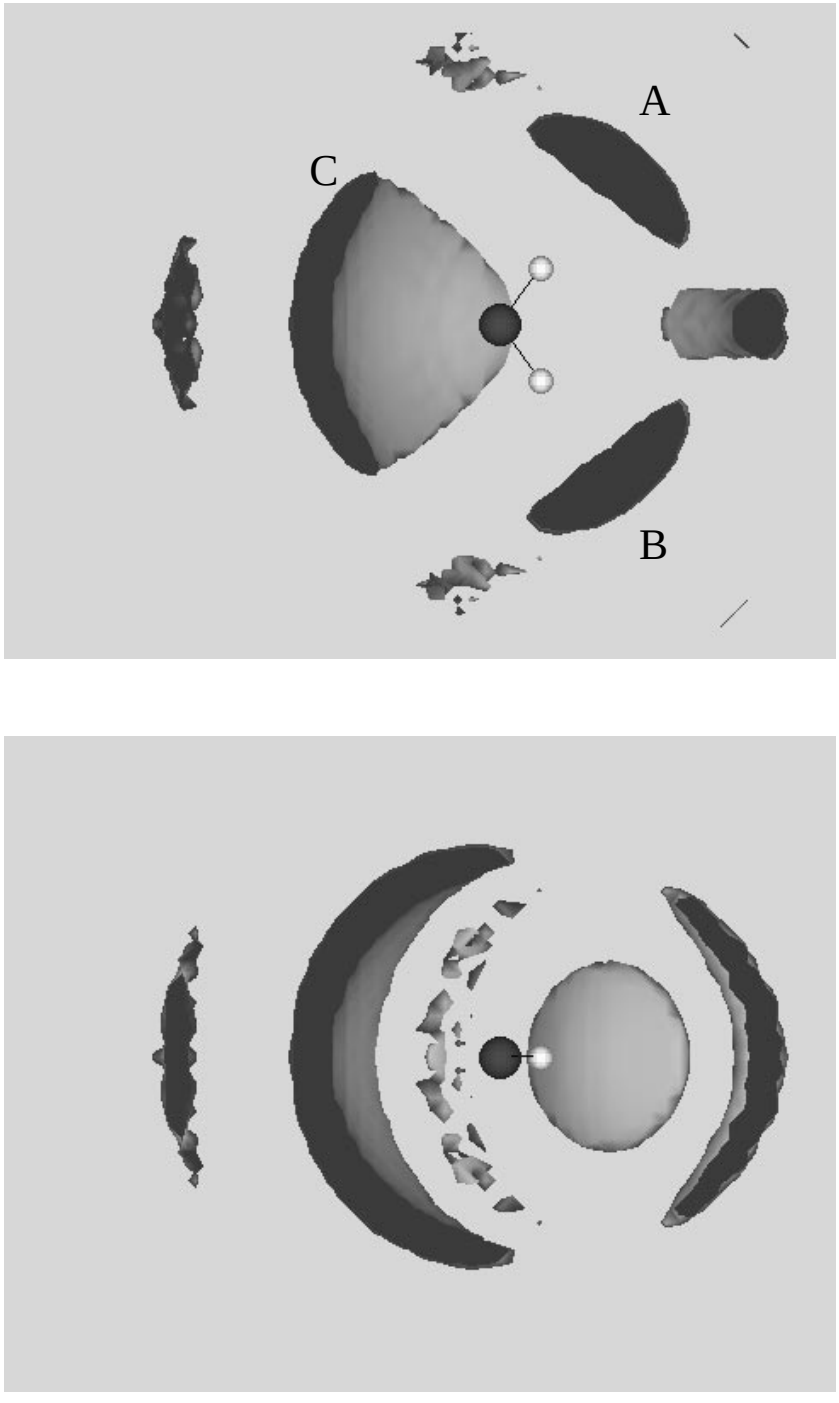

Figure 7.14. Two projections of the isosurface defined by $g_{OO} = 3.3$. The front half planes have been removed. A, B and C indicates the primary maxima which correspond to hydrogen bond sites. At A and B, the central water molecule donates a proton, and at C it accepts one, two, or three protons.

Heavily assisted by the PDC staff, we have also been able to study one of our systems using 3D animations

Heavily assisted by the PDC staff, we have also been able to study one of our systems using 3D animations. The possibility to interactively select the view point allowed us to zoom in on local processes.

7.13 Structure Bonding Relationships in Cluster Systems and Their Reaction Media

Lars Bengtsson-Kloo
Division of Inorganic Chemistry 1, Lund University

indexChemistry!cluster systems

This project is devoted to the combined experimental and theoretical study of discrete and extended inorganic clusters; the conditions of formation and the relationship between structure, bonding and physical properties. Clusters are essential model systems for the understanding of the relationship between microscopic and macroscopic properties of theoretically and technologically important compounds. Clusters are often found as fundamental structural units in compounds with special physical properties, such as super- or semiconductors. Traditional cluster chemistry is very much focused on clusters isolated in the solid state, but remarkably little (or nothing) is known about clusters present in the reaction media used; such information is vital for the understanding of the thermodynamic and/or kinetic conditions of cluster formation and stability. The drawback of studies of liquid systems is that in spite of extended spectroscopic, thermodynamic and X-ray scattering investigations, a few models can typically be applied to explain the body of experimental data. Here, applied theoretical analyses play an important role: the outcome of calculations give information about the chemical bonding and consequently provide adequate models for the interpretation of the experimental results, and also suggestions for future targets of synthesis as well as a deeper insight into the correlation between cluster fragments found in solution and extended solid compounds. The ultimate goal is thus to be able to design new materials that exhibit special conductivity properties in one or two dimensions and that are insulators in the other(s). The calculations are normally quite heavy, typically employing basis sets of about 1000 primitive functions contracted to about 400–500 basis functions. Since the calculations involve heavy atoms, the most important approximation is

the use of effective core potentials. Adapted basis sets are normally developed for each systems in order to obtain the optimal balance between calculational accuracy and effort. Because of the size of the basis sets needed, calculations are normally performed on HF, DFT and MP2 levels only. Gaussian94 is the main program employed; 8 nodes give an increase in speed of about 4 for calculations involving geometry optimization and vibrational frequency evaluation.

Reaction media

Recently, we have developed reaction media based on $GaCl_3$ in benzene for the synthesis of cationic clusters and low-dimensional compounds [Ulvenlund *et al.*, 1995]. Experimental results from X-ray scattering and vibrational spectroscopy of solutions of $GaCl_3$ and mixed-valence salts $Ga(GanCl_{3n+1})$ in benzene and mesitylene have been rationalized using applied theoretical calculations at HF and MP2 level [Bengtsson-Kloo and Ulvenlund, 1997]. The interaction between the aromatic molecules and Ga(III) is strongly suggested to be of $(1)\pi$ type. Benzene is indicated to form a mono-bridged $Ga_2Cl_6(C_6H_6)$ complex, whereas the stronger donor mesitylene seems to also form monomeric $GaCl_3(C_9H_{12})$ complexes in equilibrium with the mono-bridged, Ga_2Cl_6-mesitylene dimer complex (Figure 7.15). $Ga_2Cl_7^-$ is shown to have a preferred bent configuration with a Ga-Cl-Ga angle about 120 degrees. However, the potential surface is found to be very flat and weak interactions or packing effects in solid compounds are very likely to influence its conformation.

Cationic mercury clusters in solution

At first we regarded the $GaCl_3$-aromatic solvents as inert media, whose main effect was to bring down the working temperature of traditional molten reaction media for main-group cluster synthesis to room temperature, but now we have identified clear and specific cluster-benzene interactions. They can be seen for Bi_5^{3+} and are quite explicit for Hg_2^{2+} and Hg_3^{2+}. Experiment clearly shows that benzene thermodynamically stabilizes the mercury cluster cations. Evidence for interactions between Hg_m^{2+} cations and C_6H_6 are observed in the Raman spectra: The totally symmetric C_6H_6 band at $991\,cm^{-1}$ is found to split in the presence of Hg_m^{2+} ions and to give

Figure 7.15. The optimized structure (MP2) of dimeric $Ga_2Cl_6(C_6H_6)$ (upper) and monomeric $GaCl_3(C_9H_{12})$ (lower).

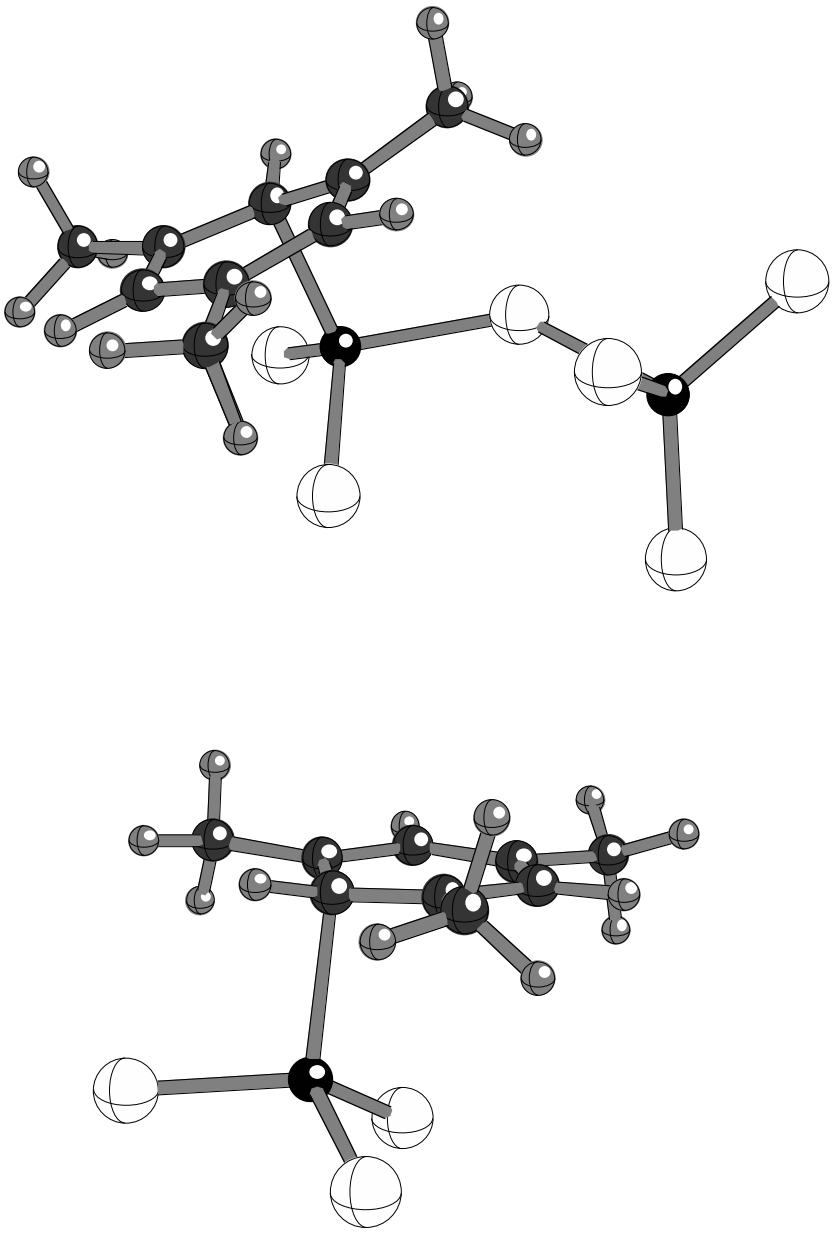

new peaks at 978 ($m = 2$) and 982 ($m = 3$) cm^{-1}. The subvalent mercury clusters are thus not only stabilized by the traditional, hard acidity provided by a Lewis acid, but also by the soft basicity provided by the direct coordination of the aromatic molecules to the clusters. Applied theoretical calculations were performed for the model compounds $Hg_m(C_6H_6)_2^{2+}$ and $Hg_mCl_2(C_6H_6)_2$, $m = 2$ and $m = 3$, with chloride as model for gallate (Figure 6.26 on page 122). The calculations show that both coordination models are feasible. However, the calculated "indicators", the C-C ring-breathing and all-in-phase C-H bending vibrational modes of coordinated benzene, for the $Hg_m(C_6H_6)_2^{2+}$ models with end-on coordination of the benzene molecules are most consistent with the body of experimental and literature data [Ulvenlund *et al.*, 1997].

Chini clusters of nickel and platinum

In the solid state the $[M_3(CO)_6]_2^{2-}$ clusters of Ni and Pt differ in that the nickel cluster has the triangular subunits in a staggered conformation (D_3d symmetry) whereas the platinum one has them in a nearly eclipsed geometry (D_3h symmetry). Larger $[M_3(CO)_6]_n^{2-}$ clusters also display an ambiguity concerning the stacking of the triangular subunits. Liquid X-ray scattering and vibrational spectroscopic studies on $[M_3(CO)_6]_n^{2-}$ (M=Ni, Pt; n=1, 2) clusters in dmf and thf solution have been performed. The structure of the M_6 clusters in solution differs from the solid state: in solution both clusters exhibit an overall staggered M3-M3 conformation as verified by theoretical calculations at B3LYP level (Figure 6.27 on page122). The monomeric M3 clusters have so far evaded crystallization, but in solution the structure is triangular with similar metal-metal and metal-carbonyl distances as found in the corresponding M6 clusters. Apical CO's have been suggested to be important for the stabilization of the M3 clusters. However, calculational results show that this is an unlikely explanation, and instead it is indicated that cations in the apical position can contribute to their stability as supported by the known compound $[Ni_3(CO)_6I]^-$ with a formal I^+ cation. An applied theoretical analysis of the inter-triangular rotational barrier in the M6 clusters has been performed showing that the barrier is very small, in particular for the Pt_6 cluster [Bengtsson-Kloo *et al.*, 1997].

7.14 Investigations of Surface and Gas Phase Reactions During Film Growth

Karin Larsson
Inorganic Chemistry Department, Angstrom Laboratory,
Uppsala University

Thin films of various materials play an important role in materials science today

Thin films of various materials play an important role in materials science today. Techniques to produce films with artificiell structures, *i.e.*, with desired combinations and distributions of the phases, are being developed. However, there may be large problems in the process of deposition of the different type of structures. In order to succeed in a well-controlled growth of materials there is a need to achieve a detailed understanding at the molecular level of the growth processes. This can be obtained by performing quantum mechanical calculations. The knowledge obtained may then be used to develop and optimize new processes of technological interest.

Vapor growth of materials is a very dynamic process since it involves the generation of surface vacancies and adsorption of different gaseous species (including the growth species) to various radical surface sites. Adsorption processes are, hence, of specific importance to investigate. Other interesting growth processes include surface migration, surface reactions, nucleation and a continued growth process.

There is generally a considerable interest in the cubic form of the primarily covalent compunds diamond, SiC and BN, respectively. These isostructural compounds have well-known similarities with respect to their physical and chemical properties (hardness, thermal conductivity and chemical stability). The aim with the present project is, firstly, to get a deep knowledge of the general growth processes for each compound and, secondly, to compare these growth processes.

Several theoretical subprojects have been finished in the period July 1996 up to now. For instance, a study of the adsorption of H, and important hydrocarbon species, to various growth edges on a growing diamond (111) surface have recently been completed [Larsson, 1997a]. It was then shown that different type of surface sites at different growth steps are energetically more in favor for the CH_3 species. Others are more in favor for the C_2H_2 species. These results make it impossible to preclude the C_2H_2 species from any role as a growth species during chemical vapor deposition of

diamond from a reaction mixture of methane and hydrogen.

The effect of neighboring surface-bonded species (H, CH_3, F, Na, OH) on the stabilization energy of diamond nucleation (on the edge atoms of the (100) plane of h-BN) were investigated in two different studies [Carbone *et al.*, 1997c, Carbone *et al.*, 1997b]. These adsorbates differed markedly in electronegativity and radii. The nucleation of diamond were found to be more energetically favored compared to a corresponding graphitic outgrowth, for all adsorbates investigated.

A study of adsorption of CH_3OH to a Si(100) 1×2 surface has also been performed. Different adsorption sites were then found to be preferred [Carbone *et al.*, 1997a]. The three papers [Carbone *et al.*, 1997c, Carbone *et al.*, 1997b, Carbone *et al.*, 1997a] have been performed in cooperation with a post-doc from Italy, Dr. Marilena Carbone.

The possibility for surface migration of H and different hydrocarbon species in the diamond (111) surface, have also been investigated [Larsson and Carlsson., 1997]. Potential surfaces were then calculated, and the transition states were located. It was observed that the strongly adsorbed CH_2 species also has the smallest barrier for migration.

The effects of surface composition on electron transfer in diamond (111), is another study that has very recently been finished [Larsson, 1997b]. Total atomic charges have then been calculated at the MP2 level of theory. A strong correlation between adsorption energy and electron transfer were observed.

The following sub-projects are presently running:

1. Adsorption of carbon- versus silicon-containing species on β-SiC surfaces.

2. Reconstructions of differently terminating c-BN (111) surfaces.

3. Adsorption of different species on the (111) surface of c-BN.

4. The effect of cluster sizes of β-SiC on, especially, the band gap. The corresponding effect on the stabilization energy is also investigated.

The second and third projects are running in cooperation with the PhD-student Björn Mårlid. The fourth project is running in cooperation with the Master Thesis student Christer Bäcklund.

The computing resources at PDC has been used for the subprojects reported in [Larsson, 1997a, Carbone *et al.*, 1997c, Carbone *et al.*, 1997b, Larsson and Carlsson., 1997, Larsson, 1997b] as well as in the four ongoing subprojects presented above.

7.15 Geometry and Spectroscopy of DNA bases in solution

Anders Broo
Department of Physical Chemistry, CTH

The free DNA bases can occur in more than one tautomeric form. The equilibrium between the different tautomeric forms depends on the character of the environment; for instance, base paring and hydrogen bonding can exclude one or several possible tautomers. Thus, it is important to model both specific solvent interactions (*e.g.*, hydrogen bonding) and continuum effects (polarity of the solvent). Broo and co-workers have studied solvent effects, tautomerism and other geometry effects of DNA bases and related molecules in a series of papers [Holmén and Broo, 1995, Broo and Holmén, 1996, Broo and Lincoln, 1997]. The effect of tautomerism and other geometry effects have also been studied [Broo and Holmén, 1997]. In all these works most of the geometry determination has been done on the IBM SP-2 at PDC. Inclusion of the solvent in quantum chemical calculations using continuum models has shown to be important for the description of tautomeric equilibrium and electronic- and vibration spectra. We have also shown that it is essential to use high quality geometries when calculating electronic and vibration spectra, especially when calculating transition moment directions. The electronic spectra of the DNA bases are very complicated from a theoretical point of view since many close lying transitions of $\pi \rightarrow \pi^*$ and $n \rightarrow \pi^*$ interacts. The $n \rightarrow \pi^*$ transitions can gain intensity by vibronic coupling with the close lying $\pi \rightarrow \pi^*$ transitions and/or if the DNA base is non-planar. We have shown that the degree of non-planarity depends on solvent effects, thus having an indirect effect on the absorption spectrum.

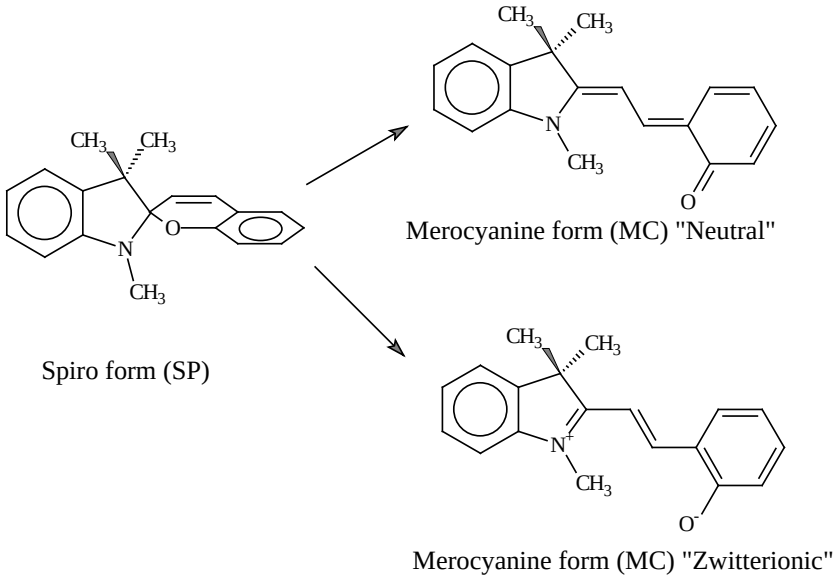

Figure 7.16. Spirobenzopyran reaction scheme.

7.16 A Quantum Chemical Investigation of the Photochemical Ring-Opening Mechanism of Indolospirobenzopyran

Anders Broo
Department of Physical Chemistry, CTH

It is well known that when a spirobenzopyran (SP) compound absorbs UV light, the C-O bond of the spiro moiety is broken and the ring is opened to form a merocyanine (MC) structure, see scheme in Figure 7.16. The MC form can either be of zwitterionic character or have a more neutral character. This reaction has been studied using the IBM SP-2 at PDC. The geometry of the SP and the MC forms has been determined using the AM1, the *ab initio* HF/3-21G and the B3LYP/3-21G methods. The excited state potential energy surface was investigated at the *ab initio* CIS/3-21G level of theory. The ring-opening reactions mechanism for the spiropyran with a hydrogen atom in the 6 position (SP-H) and a nitro group in the 6 position (SP-NO2) turned out to be different due to the low lying $n \rightarrow \pi^*$ excited states of the SP-NO2. The energetic and the geometry of the located stationary states are shown in Figure 7.17.

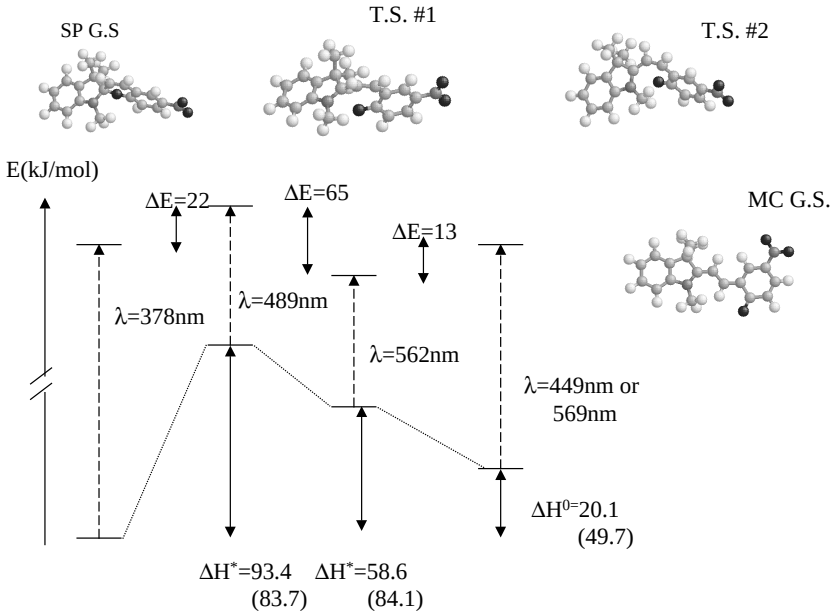

Figure 7.17. The reaction path for the ring-opening reaction of 6-nitro-1,3,3-trimethylspiro(2H-1-benzopyran-2,2-indole) Energies are in kJ/mol and numbers within parenthesis are the B3LYP/3-21G energies. The transition wavelengths for the merocyanine form correspond to the neutral form and the zwitterionic form, respectively.

7.17 A Theoretical Investigation of the Mechanism of the Intermolecular Proton Transfer in the Carbanion [1.1]ferrocenophane

Anders Broo
Department of Physical Chemistry, CTH

In 1981, Mueller-Westerhoff et al. reported what they claimed as the first evidences for an intramolecular C-H...-C hydrogen bond in carbanions of substituted [1.1]ferrocenophanes. Later, Ahlberg and co-workers used NMR spectroscopy and X-ray crystallography to further study the proposed intramolecular hydrogen bond and the structure of substituted [1.1]ferrocenophanes. The crystallographic structure of [1.1]ferrocenophanyllithium clearly shows that no intermolecular C-H...-C hydrogen bond is possible in the solid state. Recent results from NMR experiments, carried out in diethylether solution indicate that the lithium ion is bonded on top, exo-coordinated, of the anionic carbon, in accord with the solid state structure. However, endo-coordinated structures are not completely ruled out since ferrocenophanes are known to be very flexible and can undergo pseudo-rotation, resulting in several isomers, see scheme in Figure 7.18. In an recent study, partly carried out on the IBM SP-2 at PDC, the proton transfer reac-

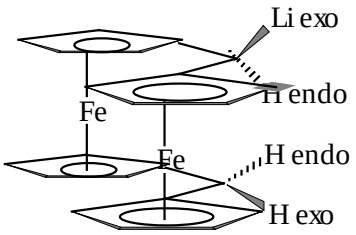

1a

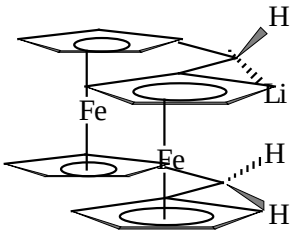

1b

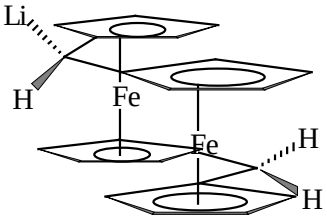

1c

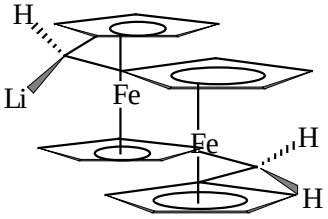

1d

Figure 7.18. Reaction scheme.

tion was studied by means of quantum chemical calculations. The B3LYP hybrid density functional method was used and turned out to be very accurate in reproducing the geometry of the sandwic complex. Ferrocene, the building block of ferrocenophane, is well known to be notoriously hard to describe with traditional methods. The theoretical proton transfer rate was calculated using traditional transition state theory, where all quantities were obtained form the DFT calculations. Nuclear tunneling was considered by correcting the theoretical calculated transfer rate with a transmission factor (so called Wigner correction). Nuclear tunneling turned out to be important for the proton transfer at rather high temperatures. A tunneling factor of 5.09 at 173 K was calculated.

Ferrocene is well known to be notoriously hard to describe with traditional methods

A surprisingly good scaling of the CPU time used for solving the SCF problem with increasing number of nodes were observed for this rather large molecule (356 contracted basis functions and 770 primitive functions C1-symmetry). The sad news is the bad

scaling in the geometry-determining step (which is not done in parallel mode). Thus, the overall performance was found to be good up to about 8 nodes. The speedup using more nodes was hurt by the slow geometry-determining step leading the an overall efficiency of only 37% with 32 nodes, giving a theoretical speedup of only 11.84 on 32 nodes compared with one node. With 64 nodes the geometry step required (15 minutes wall-clock time) as long time as the time to solve the SCF problem. The Gaussian94 program was used for all the DFT calculations.

7.18 Quantum Chemistry and Molecular Mechanics as Tools in Asymmetric Synthesis. Application to the Horner-Wadsworth-Emmons Reaction

Peter Korall
Department of Chemistry, KTH
Per-Ola Norrby
Department of Medicinal Chemistry, DFH, Denmark
Tobias Rein
Department of Organic Chemistry, DTH, Denmark

Introduction

In recent years the area of asymmetric synthesis has been intensely studied by organic chemists. This is largely due to that biological activity of, e.g., pharmaceuticals or pesticides rely upon the substrate binding to receptors. As this interaction is of look-key type it is inherently dependent on the three dimensional structure of the interacting species.

The objective of research in asymmetric synthesis is to design new and highly selective reactions where yield and purity of the desired product isomer should be optimal. Often, the methods employed for improving existing asymmetric reactions are based on accumulated empirical knowledge in combination with experimental trial and error. However, due to the fast development of computer hardware and important investments in supercomputers, molecular systems of impressive size can nowadays be handled accurately. This has led to a development where computational methods have become increasingly important in the understanding and design of asymmetric reactions. The theoretical tools we have employed are quantum chemistry in combination with molecular mechanics.

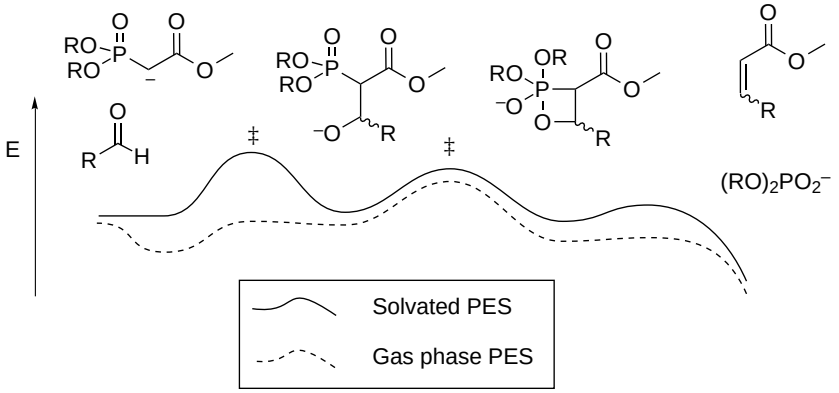

Figure 7.19. The mechanism of the HWE reaction. PES = Potential energy surface. The symbol ‡ points out the two transition states involved in the determining the selectivity of the process.

The initial phase in trying to understand and improve an asymmetric reaction is to perform a thorough quantum chemical investigation of the reaction mechanism. This will give information on which intermediates are involved and in which reaction step the selectivity is determined. This work directs the future molecular mechanics efforts and supply all the necessary input data for the next phase, the development of a molecular mechanics transition state force field. Molecular mechanics is computationally less demanding and could be performed on an ordinary workstation.

Once an accurate force field has been derived a more creative phase starts

Once an accurate force field has been derived a more creative phase starts. It is now possible to very rapidly evaluate new ideas on how to modify structures in order to improve the selectivity of the chemical reaction. In our case, to improve and to tailor make new reagents for asymmetric Horner-Wadsworth-Emmons (HWE) reactions.

Modelling of the Horner-Wadsworth-Emmons reaction

The HWE reaction is closely related to the Wittig reaction, and is used for formation of carbon-carbon double bonds. In the HWE reaction the nuclephile is a carbanion stabilized by a phosphonate ester and an additional anion-stabilizing group (frequently a carboxylic ester). The detailed mechanism of this reaction has recently been studied at PDC by us (schematically illustrated in Figure 7.19) [Brandt *et al.*, 1998]. This has resulted in a very comprehensive understanding of the reaction, and several molecular factors which are important for the final product selectivity have been identified.

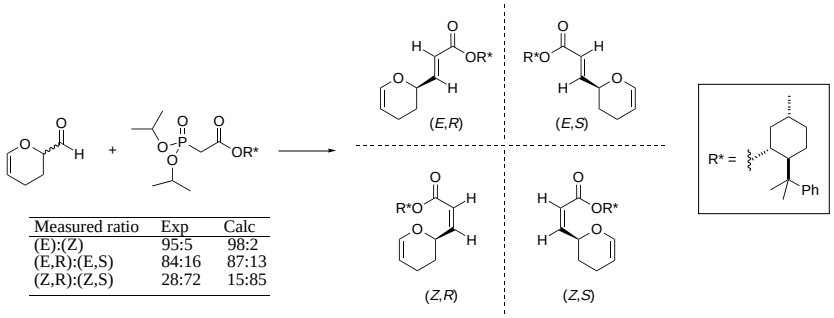

Measured ratio	Exp	Calc
(E):(Z)	95:5	98:2
(E,R):(E,S)	84:16	87:13
(Z,R):(Z,S)	28:72	15:85

Figure 7.20. An illustrative example of modelling of a so-called kinetic resolution. The selectivity of the reaction can be predicted using molecular mechanics.

Most pleasantly, our initial modelling results are very promising

With the reaction mechanism revealed it becomes possible to create molecular mechanics models of the selectivity-determining transition states. The input data used for such force field developments are molecular geometries and Hessians. Most pleasantly, our initial modelling results are very promising (see Figure 7.20) [Norrby *et al.*, 1998].

Further studies at PDC will involve quantum chemical calculations of reagents containing new anion-stabilizing groups (e.g., carboxamides) or phenoxy substituents on phosphorous. The molecular mechanics part of the project will focus on finding improved chiral handles (R* in Figure 7.20) and on evaluating new interesting substrates. This work is done in close collaboration with experimentalists.

7.19 Flow Properties of Liquid Crystals by Molecular Dynamics Calculations

Sten Sarman
Department of Physical Chemistry, Göteborg University

We study flow properties of liquid crystals at the molecular level by computer simulation methods. So far it is very hard to simulate realistic liquid crystal models. Therefore we use a model fluid known as the Gay-Berne fluid [Gay and Berne, 1981]. It consists of rigid prolate ellipsoidal bodies. This fluid has been shown to form isotropic phases as well as nematic and smectic liquid crystals. In a nematic liquid crystal there is orientational order, *i.e.*, the elongated molecules point in almost the same direction, but there is no translational order [Chandrasekhar, 1992]. In a smectic liquid crystal the molecules point in the same direction and they are ordered in layers, where the molecular axes are perpendicular to

the plane of the layer. There is no order within the layers, so that each layer can be regarded as a two-dimensional liquid. The properties of liquid crystals are consequently higly anisotropic.

Our particular interest is to study how the viscosities change when we go from the nematic phase to the smectic phase. In a liquid crystal the viscosity is a fourth rank tensor with seven independent components. This anisotropy gives rise to shear induced rotation and shear alignment.

In order to study this we apply molecular dynamics simulation methods, where one solves the Newtonian equations of motion for ther molecules. There are two different methods for evaluation of transport coefficients [Evans and Morriss, 1990]: Equilibrium molecular dynamics (EMD) where one evaluates the Green-Kubo relations for the viscosities. The second method are the SLLOD equations of motion for shear flow. The simulations are facilitated by the application of a constraint method that fixes the director in space [Sarman, 1995]. This means that a director based coordinate system becomes an inertial frame. One also finds that the Green-Kubo expressions for the various viscosity coefficients become much simpler when the director is fixed.

Both the EMD simulations and the shear flow simulations converge rather slowly, so it is necessary to use a fast computer like a parallel processor. Our system consists of 8000 particles. We use a dataparallel code to solve the equations of motion. The system is not large enough to justify the development of domain decomposition codes.

Both the EMD and the shear flow simulations converge rather slowly, so it is necessary to use a fast computer

So far we have studied three statepoints, one in the nematic phase, one in the smectic phase and one at the transition point. The transition point is particularly interesting because the nematic-smectic transition is a second order phase transition. There is consequently a critical point similar to the gas liquid critical point. According to theory some viscosity coefficients diverge at the transition point. We have managed to verify this.

In the future we plan to examine transport phenomena others than shear flow, such as heat conduction.

7.20 The Relation between Structure and Spectroscopy of the Blue Copper Protein Stellacyanin

Jan O. A. De Kerpel, Michaela Flock, Kristine Pierloo
Department of Chemistry, University of Leuven
Mats H. M. Olsson, Ulf Ryde, Björn O. Roos
Department of Theoretical Chemistry, Lund University

The blue copper proteins constitute a group of proteins that function as electron carriers in a large number of biochemical reactions [Adman, 1991]. They exhibit a number of unusual spectroscopic and structural properties. According to the widely accepted entatic state and induced rack theories, the reason for these properties is that the protein matrix enforces an unnatural geometry onto the Cu(II) coordination sphere, viz. a geometry that is close to the one preferred by Cu(I). In this way, the reorganization energy is reduced and the electron transfer is facilitated. However, we have optimised Cu(II) complexes with the same ligand as in the proteins with the density functional B3LYP method and showed that the optimised geometry in vacuum is closely similar to the one found in the proteins [Ryde *et al.*, 1996]. Thus, our results give no support to the strain hypotheses. Therefore, we have started to look for alternative explanations to the exceptional characteristics of the blue copper proteins.

The visual spectroscopy of most blue copper proteins is dominated by a strong absorption line around 600 nm, giving rise to the the deep blue colour of the proteins. The intensity of this line is about 100 times larger than the one of normal inorganic copper complexes. Most blue copper proteins also exhibit another absorption peak around 460 nm. The relative intensities of these two peaks vary widely among different blue copper proteins; the absorbance ratio of the peak at 460 nm to the peak at 600 nm (R_ϵ) ranges from 0.06 for plastocyanin to 1.22 for nitrite reductase.

Stellaycyanin is a blue copper protein from the laquer tree. It deviates from most other blue copper proteins by a different copper coordination sphere. All blue copper proteins have three strong copper ligands, one cysteine thiolate atom and two histidine nitrogen atoms. In addition, there is at least one weakly bound axial ligand. In normal blue copper proteins, it is a methionine residue, but in stellacyanin it is instead a glutamine residue that binds by its amide oxygen atom. The spectrum of stellacyanin exhibits the normal two lines around 600 and 460 nm, but the R_ϵ ratio is higher

(0.29) than what could be expected from its rather trigonal structure. Furthermore, the spectrum changes when the pH is increased and the reason for this change has been much debated. Therefore, we have investigated the relation between the spectrum and the structure of some realistic stellacyanin models. The geometries have been calculated using the B3LYP method at PDC, whereas spectra have been computed by multiconfigurational perturbation theory (CASPT2) on sequential machines.

The origin of the two absorption peaks in stellacyanin

The position of the two absorption lines around 460 nm and 600 nm depends on the electronic structure of the corresponding excited state. These excited states can be best described by their singly occupied orbitals. In Figure 6.22 on page 120, the singly occupied orbital of the excited state corresponding to the peak at 600 nm is shown. The orbital is a π bonding orbital between the cysteine S $3p$ orbital and a Cu $3d$ orbital. Similarily, in Figure 6.23 on page 120, the singly occupied orbital of the excited state corresponding to the transition of the peak at 460 nm is shown. Again, the orbital is strongly localized along the Cu–S_{Cys} bond, but this time it is a σ bonding orbital. In fact, both excited states have about 75% S_{Cys}character. The corresponding excited-state orbitals for plastocyanin are closely similar.

The intensity of a transition is determined by the overlap between the ground state and the corresponding excited state. Figure 6.24 on page 121 shows the ground-state singly occupied orbital in plastocyanin. The orbital clearly is π antibonding between S_{Cys} $3p$ and Cu $3d$. Figure 6.25 on page 121 shows the ground-state singly occupied orbital in stellacyanin. Here, the bond is no longer purely π antibonding, but it also contains a significant amount of a σ antibonding character. In fact, the ground state of plastocyanin has 96% π and 4% σ antibonding character, whereas the one of stellacyanin has only 68% π and 32% σ antibonding character.

From these numbers it follows that in plastocyanin the overlap between the ground state and the σ bonding excited state is poor, while the overlap with the π bonding excited state is strong. This explains the high intensity of the peak at 600 nm and the very low intensity of peak at 460 nm in plastocyanin. On the other hand, for stellacyanin the overlap of the ground state with the π bond-

ing excited state is weaker, and the overlap with the σ bonding excited state is stronger. Consequently, the 460 nm excitation in stellacyanin acquires a significant intensity.

The pH dependence of Stellacyanin

The absorption spectrum of stellacyanin is pH sensitive: at high pH, the most intense line is blue-shifted from 610 nm to 580 nm [Lu. *et al.*, 1993, Thomann *et al.*, 1991]. It has been suggested that this is due to a change in the coordinating atom of glutamine. At low pH, the O^{ϵ}_{Gln} atom coordinates to the copper atom, wheras at high pH, the N^{ϵ}_{Gln} atom might be deprotonated and may then become a good copper ligand. Yet, this suggestion has lately been challenged [Nersissian *et al.*, 1996].

In order to test this hypothesis, we optimized the geometries of $Cu(NH_3)_2(SH)(HCONH_2)^+$ with the oxygen atom as the fourth copper ligand and $Cu(NH_3)_2(SH)(HCONH)$ with the nitrogen amide atom as the fourth copper ligand. SH^- is a model of the cysteine thiolate ligand, NH_3 is a model of histidine, and $HCONH_2$ and $HCONH^-$ are models of the neutral and deprotonated glutamine residue, respectively. Earlier optimisations of similar systems [Olsson *et al.*, 1998] have shown that two different conformations are possible for such copper complexes, a trigonal, π bonded structure and a tetragonal σ bonded structure. Therefore, we optimised both structures for the two complexes.

As was expected from our previous calculations on models of plastocyanin, the energy of the trigonal and tetragonal structure of the $Cu(NH_3)_2(SH)(HCONH_2)^+$ model did not differ significantly (less than 10 kJ/mole). On the other hand, for the model of $Cu(NH_3)_2(SH)(HCONH)$, the tetragonal structure was 50 kJ/mole more stable than the trigonal structure. Inspection of the coordinates of the trigonal structures showed that the Cu–N_{Gln} bond is shorter than the Cu–O_{Gln} bond. As a consequence, the Cu–S_{Cys} bond length increases.

When we calculated the electronic spectra of the trigonal and tetragonal structures of $Cu(NH_3)_2(SH)(HCONH_2)^+$ and also $Cu(NH_3)_2(SH)(HCONH)$ it turned out that the trigonal structures exhibit an intense peak around 600 nm and a smaller peak around 460 nm. On the other hand, the tetragonal structures show a single peak around 460 nm and no intensity around 600 nm.

Two lines of evidence talk against the suggestion that N^{ϵ} coor-

dinates to copper at high pH. First, the negatively charged ligand would strongly stabilise a tetragonal structure (by 50 kJ/mole). In the spectrum of this structure, the 460 nm peak would be more intense than the peak at 600 nm. Therefore, a strong change in intensity of both peaks would be expected, but this is not observed in experiments. Second, even if the protein could stabilize the trigonal structure, the calculated spectra show that the blue line would be expected to be red-shifted by the change of the coordinating atom, not blue-shifted as is observed. Thus, we must conclude that the coordinating atom of the glutamine ligand does not change at high pH, in accord with the latest experiments [Nersissian *et al.*, 1996]. Instead, we suggest that the spectral shift is caused by a change in the electrostatic field near the copper ion probably due to deprotonation of an ionisable residue.

7.21 MD Simulation Studies of Ribonucleotide Reductase

J. Arvid Nilsson, Aatto Laaksonen
Division of Physical Chemistry, Arrhenius Laboratory,
Stockholm University

Ribonucleotide reductase (RNR) is an essential protein for all living cells, which synthesizes building blocks for the double stranded DNA molecule. Since the determination of the three-dimensional structure of RNR, the number of research projects in the area have grown rapidly. Several experimental and theoretical research groups are studying the underlying mechanisms of RNR's function. One of the crucial properties of the protein is the hydrogen transfer, where a hydrogen atom moves from the active site at the surface of the protein to a tyrosine radical, deep buried in the interior of the protein. Such mechanisms can be found in several different proteins (*e.g.*, the photosynthesis protein PSII) and this kind of mechanism is a target for a great interest. The present work is aiming at a connection between theoretical studies and experimental observations and the first step taken is a molecular dynamics (MD) simulation of one of the two monomers building up the R2 subunit of RNR.

An MD simulation of a system like this would be completely impossible without powerful computing resources

An MD simulation of a system like this would be completely impossible without powerful computing resources. The SP-2 system fits the application very well while the problem is naturally paral-

lel and the applied algorithm runs well with up to 32 nodes with a reasonable overhead. The estimated time for 1 nanosecond simulation of this system (approximately 21 000 atoms) is about 7000 node hours. This work has been started in 1997 and is progressing until the end of 1998.

8 Miscellaneous Projects

8.1 Radio Resource Management in Personal Communication Networks

Michael Liljenstam, Rassul Ayani
Department of Teleinformatics, Simulation Laboratory, KTH

Introduction

Personal Communication Networks (PCNs) provide wireless communication services to mobile users. Tremendous growth in the number of subscribers in cellular telephony networks over the last couple of years increases demands on network operators and manufacturers to efficiently utilize radio resources while maintaining acceptable quality of service. Hence, tools for the study of such systems are essential to the industry and telecommunications operators. Tractable analytical models of PCNs are often not general or flexible enough for these studies and simulation has consequently become widespread. However, detailed simulations of such networks are often highly resource demanding in terms of CPU time and memory requirements.

Detailed simulations are often highly resource demanding in terms of CPU time and memory requirements

We explore the possibility of tackling the large resource demands in simulations of cellular networks through the use of parallel discrete event simulation (PDES) techniques. The advantage of PDES compared to other techniques is that model fidelity is not compromised and the statistical properties of the output is not altered. Up to now our primary focus has been on applying PDES techniques to simulations of Radio Resource Management in wireless cellular networks.

Personal Communication Networks

The area covered by a Personal Communication Network is populated by a number of base stations (BSs), where the radio coverage of a BS is called a cell. Users carrying a mobile terminal (MT) can communicate with other parts of the system by transceiving with the BS covering the cell they are located in at that specific time. Available radio frequency spectrum is limited and it is important to utilize it efficiently. For this reason, radio channels are

reused in cells that are sufficiently spaced apart, since interference caused by transmission (on the same channel) will be negligible if the station is sufficiently far away. Different schemes exist to allocate channels to cells so as to ensure that interference falls below the limit of what is tolerable. In Fixed Channel Assignment (FCA) N cells are grouped into a cluster and a disjoint subset of the available channels are assigned to each cell in the cluster. Dynamic Channel Assignment (DCA) schemes strive to improve channel utilization compared to FCA by dynamically reassigning channels among cells based on the current state of the system in terms of *e.g.*, traffic load or measured interference.

As MTs move around it may become necessary to switch an ongoing call over to another BS or to use another channel on the same BS, this is referred to as a handover (HO). When moving closer to the BS, the interference caused to other stations can be reduced by reducing the transmission power, so called power control. An attempt to initiate a call may fail because there are no available channels in the cell, this is referred to as a blocked call. Similarly a HO may fail, due to unavailability of channels, which may result in poor reception for the MT for a prolonged time and eventually causing the call to be terminated. Such a forced termination is termed a dropped call. The fraction of blocked and dropped calls at a specific system load are used as quality of service measures for the network. The goal is to engineer the system to make best possible use of the available radio frequency spectrum while maintaining low probabilities of blocked or dropped calls (typically $< 1\%$).

Parallel Discrete Event Simulation

Parallel discrete event simulation (PDES) refers to the execution of a single Discrete Event Simulation (DES) program on a parallel computer. The common approach to PDES is to view the system being modeled, usually referred to as the physical system, as a set of sub-systems, each simulated by a logical process (LP). Thus, a parallel simulator is constructed as a set of N ($N > 1$) communicating LPs. Since time advances asynchronously in the different LPs, special care must be taken to ensure that events are executed in time order (*i.e.*, that causality errors are avoided). Two main paradigms have been proposed for synchronization of LPs in a PDES: conservative and optimistic methods. In conservative ap-

proaches, only safe events (*i.e.*, events that do not create causality error for other LPs) are executed. In this way, conservative methods strictly avoid any causality errors ever occurring. Optimistic approaches, on the other hand, assume that respective events at different LPs occur in correct order. However, optimistic methods employ a detect and recovery mechanism to correct causality errors, if they occur. The Time Warp mechanism is the most well-known optimistic protocol. The Time Warp approach allows an LP to simulate forward, in parallel with other LPs, until it receives an event message that causes rollback to an earlier simulated time. The event causing rollback is called a straggler. The method requires both time and space to maintain the past history of each LP, and to perform the rollback operation whenever necessary. State saving is an important issue in Time Warp and several optimizations, including incremental and sparse state saving, have been proposed. Time Warp has shown good performance for many applications, where the associated state saving and rollback costs lie within an acceptable range.

The MobSim++ Environment

The Mobile Telecommunication Simulator has been implemented in C++ to run on top of the Parallel Simulation Kernel (PSK). The simulator originated from an existing sequential simulator called MaDRAS developed at the Radio Communication Systems Laboratory, KTH in cooperation with Winlab at Rutgers University. An object oriented design approach was used for the simulator to make it flexible and to allow easy replacement of different submodels. A separate visualization tool written in C++ and TCL/TK is also provided.

The Parallel Simulation Kernel (PSK) was designed to be a common platform for research on parallel simulation applied to different areas (such as mobile telecommunications, computer architecture, and hardware simulations). The kernel handles synchronization on shared memory multiprocessors (such as SUN SparcCenter 2000) or in a distributed memory environment (such as IBM SP-2) using a common interface. The kernel was implemented in C++ to provide support for object oriented programming. The user creates a simulation application by creating an instance of the kernel and deriving objects from some of the kernel defined classes.

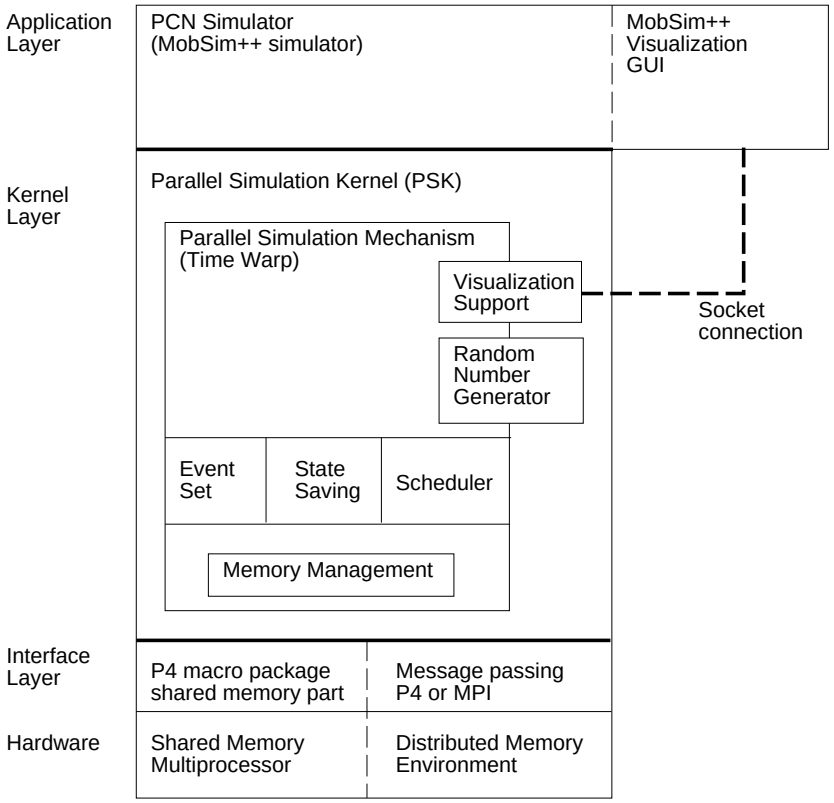

Figure 8.1. Structure of the Mobile Telecommunication Simulation Environment

Due to poor look-ahead in the PCN application and because optimistic synchronization mechanisms tend to offer a higher level of transparency for the user, it was decided that the kernel should employ optimistic synchronization by using the Time Warp mechanism.

The overall structure and different layers of a simulator, in this case the mobile telecommunications simulator, implemented on top of the PSK are shown in Figure 8.1. The PSK was designed to be portable across a number of platforms and to have a modular structure to allow easy replacement and experimentation with key components of the system. The kernel is internally made up of a parallel simulation mechanism (in this case Time Warp) and libraries for additional functionalities such as random number generation and visualization support that have some ties to the simulation mechanism. The random number generator uses separate random number streams for each of the LPs. The Time Warp

mechanism includes modules for key components of the system. Event set management, state saving mechanisms and Logical Process scheduling policies were determined to be mechanisms that may require modification to adapt to specific application requirements. Also, there is a low level memory management module that is common to all different parts of the Time Warp kernel.

In order to make applications portable, we have based the kernel on standards for concurrency control and message passing. On shared memory machines, we use the concurrency control primitives (locks, barriers, etc.) defined in the shared memory part of the Portable Programs for Parallel Processors (P4) macro package. This package has been ported to a wide range of shared memory multiprocessors. In the case of distributed memory environments it is possible to use either the message passing part of the P4 package or an implementation of the Message Passing Interface (MPI).

Our experiences to date, in the design and implementation of the simulation environment have been reported in [Liljenstam and Ayani, 1997].

Status

Experiments have previously been carried out on a shared memory machine (a Sun SparcCenter 2000 with 8 processors) with encouraging speed-ups [Liljenstam and Ayani, 1996]. The simulation environment has now been ported over to run on the IBM SP-2 and is currently undergoing tests and tuning. Since message latencies are important for the efficiency of the Time Warp synchronization mechanism and the latencies are substantially larger on a distributed memory machine such as the SP-2, this effort is more focused toward being able to make use of more available memory and thus being able to scale-up simulations.

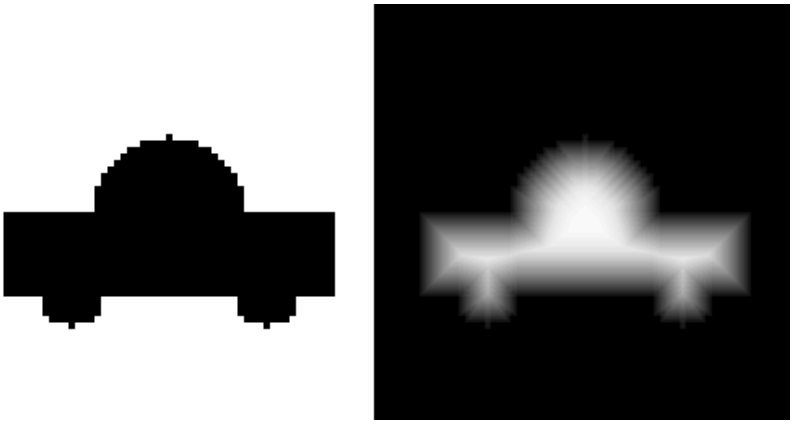

Figure 8.2. Left: Binary image of a car. **Right**: Distance transform, every pixel inside the car object is labeled with the distance to the background.

8.2 The Digital Distance Transform Algorithm on General Parallel Computers[1]

Anders Forsmoo, Gunilla Borgefors
Centre for Image Analysis,
Swedish University of Agricultural Sciences, Uppsala

Digital image analysis has been around as a scientific subject for about 30 years. Now some algorithms are used routinely in practical applications. Many applications produce large amounts of data, *e.g.*, MR-scanning in medicine and remote sensing, leading to long processing times. It is often suggested that this problem can be solved by using parallel computers. This sounds easy, but most image analysis algorithms are designed for serial computation and implemented on serial computers.

The purpose of this project is to develop parallel algorithms and implementations for image analysis, with a special emphasis on shape analysis, starting with distance transforms.

Consider a binary digital image, consisting of feature and non-feature pixels, *e.g.*, background pixels and object pixels. The distance transform is an operation that converts such a binary image to an image where each pixel has a value corresponding to the distance to the nearest feature pixel, see Figure 8.2. This structure is then used in various analysis tasks.

Shape analysis operations are global in the sense that information must be transferred long distances over the image. This is in

[1]Project partially financed by NUTEK (grant No. 8421-95-01823).

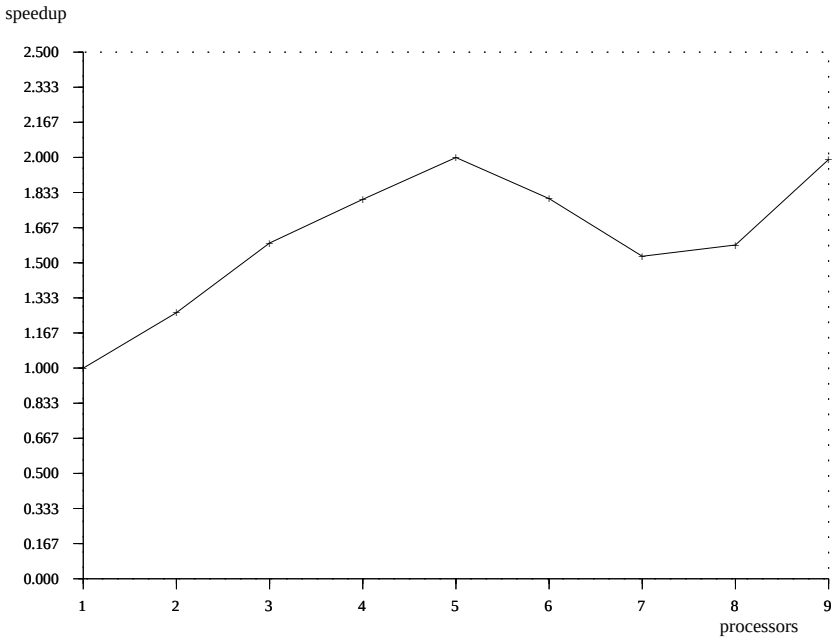

Figure 8.3. Speedup of pipeline algorithm.

sharp contrast to local filters, that are much simpler to implement in parallel. Distance transforms are used as part of many complex algorithms, *e.g.*, matching of images, morphological operations, finding binary skeletons and path planning.

We thus used the digital distance transform as a model global algorithm, because it is relatively simple and generally useful for practical image analysis applications. The results should be relevant for a large group of other global algorithms.

The parallel algorithms found in literature [Borgefors *et al.*, 1990] has been implemented on the SIMD CM200 computer Bellman, which is now retired. The results were promising [Forsmoo and Borgefors, 1997] concerning the SIMD architecture, but the CM200 was too slow, 10 MHz, and to small, 8192 procesors.

The parallel algoriths used in [Forsmoo and Borgefors, 1997] was not suited for MIMD implementations, instead the well-known sequential algorithm [Rosenfeld and Pfaltz, 1968] have been modified in two different ways (data-parallel, pipeline) and implemented on the IBM SP-2 computer Strindberg. The pipeline-algorithm scales reasonably well, see Figure 8.3, but the speedup (compared to a DEC workstation) is very poor.

SIMD computers are better suited for this type of algorithm

The reason is that the distance transform is not computationaly complex enough to perform well on a MIMD computer. SIMD computers are better suited, but unfortunately not developed any more, but we hope this will change in the future.

Bibliography

[Abenius, 1997] Abenius, E. (1997). Subcell Models in the Finite Difference Time Domain Method for the Maxwell Equations. Technical report, PSCI. To appear. 56

[Adman, 1991] Adman, E. T. (1991). Copper Protein Structures. *Adv. Protein Chem.* **42**: 145–197. 174

[Alvardo *et al.*, 1991] Alvardo, E., Nukada, T., Ogawa, T., and Ballou, C. E. (1991). *Biochemistry* **30**: 881–886. 33

[Anderson, 1980] Anderson, H. (1980). Molecular Dynamics Simulations at Constant Pressure and/or Temperature. *J. Chem. Phys.* **72**: 2384–2393. 141

[Andersson and Ledfelt, 1996] Andersson, U. and Ledfelt, G. (1996). Parallel Computations in Industrial Electromagnetics. In: *RadioVetenskap och Kommunikation 96*, edited by L. H. Zetterberg, S-971 87 Luleå, Sweden. SNRV, NUTEK, Luleå University of Technology, p. 450–454. 57

[Aranyos *et al.*, 1997] Aranyos, A., Szabó, K. J., Castaño, A. M., and Bäckvall, J.-E. (1997). Central versus Terminal Attack in Nucleophilic Addition to (^{1}-Allyl)palladium Complexes. Ligand Effects and Mechanism. *Organometallics* 1058. 123

[Aschenauer *et al.*, 1995] Aschenauer, E. C., Gabathuler, K., Hauser, P., Missimer, J., Badertscher, A., Goudsmit, P. F. A., Leisi, H. J., Schröder, H., Sigg, D., Zhao, Z. G., Chattellard, D., Egger, J.-P., and Markushin, V. E. (1995). Cascade Processes and the Kinetic-Energy Distribution of Pionic Hydrogen Atoms. *Phys. Rev. A* **51**: 1965–1979. 62

[Aschenauer and Markushin, 1996] Aschenauer, E. C. and Markushin, V. E. (1996). High-Velocity Components in Exotic Atoms, their Origin and Effects. *Hyp. Int.* **101/102**: 97–106. 62

[Ashcroft and Langreth, 1967] Ashcroft, N. W. and Langreth, D. C. (1967). *Phys. Rev.* **159**: 500. 84

[Badertscher *et al.*, 1997] Badertscher, A., Daum, M., Frosch, R., Goudsmit, P. F. A., Hajdas, W., Janousch, M., Kettle, P.-R., Markushin, V., Schottmüller, J., and Zhao, Z. G. (1997). Experimental Determination of the Kinetic Energy Distribution of $\pi^- p$ Atoms in Liquid Hydrogen. *Phys. Lett.* **B392**: 278–282. 62

[Baldwin and Lomax, 1978] Baldwin, B. S. and Lomax, H. (1978). Thin Layer Approximation and Algebraic Model for Separated Turbulent Flows. Technical Report AIAA 78-257, AIAA. 42

[Banci *et al.*, 1991] Banci, L., Bertini, I., and Luchinat, C. (1991). *Nuclear and Electron Relaxation.* Weinheim: VCH. 58

[Bäckbro *et al.*, 1997] Bäckbro, K., Löwgren, S., Österlund, K., Atepo, J., Unge, T., Hultén, J., Bonham, N. M., Schaal, W., Karlén, A., and Hallberg, A. (1997). Unexpected Binding Mode of a Cyclic Sulfamide HIV-1 Protease Inhibitor. *J. Med. Chem.* **40**: 898. 29

[Benetis *et al.*, 1983] Benetis, N., Kowalewski, J., Nordenskiöld, L., Wennerström, H., and Westlund, P.-O. (1983). Nuclear Spin Relaxation in Paramagnetic Systems: The Slow-Motion Problem for Electron Spin Relaxation. *Mol. Phys.* **48**: 329. 57

[Bengtsson-Kloo *et al.*, 1997] Bengtsson-Kloo, L., Iapalucci, C. M., Longoni, G., and Ulvenlund, S. (1997). The Solution Structures of Mono- and Ditriangular Chini Clusters of Nickel and Platinum. An X-ray Scattering and Quantum Chemical Study. *Inorg. Chem.* Submitted. 163

[Bengtsson-Kloo and Ulvenlund, 1997] Bengtsson-Kloo, L. and Ulvenlund, S. (1997). Arene Solutions of Gallium Chloride — Part 3. *Spectrochim. Acta, Part A* **53**: 2129. 161

[Berger *et al.*, 1997] Berger, O., Edholm, O., and Jähnig, F. (1997). Molecular Dynamics Simulation of a Fluid Bilayer of Dipalmiotylphosphatidylcholine at Full Hydration, Constant Pressure and Constant Temperature. *Biophys. J.* **72**: 2002–2013. 19

[Bergman and Laaksonen, 1998a] Bergman, D. and Laaksonen, A. (1998a). Angularly Resolved Density Distributions — A Starting Point for Analysis of Liquid Structure. *Mol. Simul.* In press. 158

[Bergman and Laaksonen, 1998b] Bergman, D. and Laaksonen, A. (1998b). Topological and Spatial Structure in the Liquid Water–Acetonitrile Mixture. In manuscript. 158

[Bergström and Gebart, 199X] Bergström, J. and Gebart, B. R. (199X). Estimation of Numerical Accuracy for the Flow Field in a Draft Tube. *Computers and Fluids* Submitted. 39

[Blétry, 1990] Blétry, J. (1990). *Phil. Mag.* **B62**: 469. 81, 84

[Borgefors *et al.*, 1990] Borgefors, G., Hartmann, T., and Tanimoto, L. (1990). Parallel Distance Transforms on Pyramid Machines: Theory and Implementation. *Signal Processing* **21**: 61–86. 185

[Bounds, 1985] Bounds, D. (1985). A Molecular Dynamics Study of the Structure of Water around the Ions Li^+, Na^+, K^+, Ca^{++}, Ni^{++} and Cl^-. *Mol. Phys.* **54**: 1335–1355. 141

[Brandt *et al.*, 1998] Brandt, P., Norrby, P.-O., Martin, I., and Rein, T. (1998). A Quantum Chemical Exploration of the Horner-Wadsworth-Emmons Reaction. *J. Org. Chem.* **63**: 1280. 171

[Broo and Holmén, 1996] Broo, A. and Holmén, A. (1996). Ab Initio MP2 and DFT Calculations of Geometry and Solution Tautomerism of Purine and Some Purine Derivatives. *Chem. Phys.* **211**: 147. 166

[Broo and Holmén, 1997] Broo, A. and Holmén, A. (1997). Calculations and Characterization of Electronic Spectra of the DNA Bases, based on Ab Initio MP2 Geometries of Different Tautomeric Forms. *J. Phys. Chem.* **101**: 3589. 166

[Broo and Lincoln, 1997] Broo, A. and Lincoln, P. (1997). Ab Initio and Semiempirical Calculations of Geometry and Electronic spectra of Ruthenium Organic Complexes, and Modeling of Spectroscopical Changes Upon DNA Binding. *Inorg. Chem.* **36**: 2544. 166

[Brooks *et al.*, 1983] Brooks, B. R., Bruccoleri, R. E., Olafsen, B. D., States, D. J., Swaminathan, S., and Karplus, M. (1983). CHARMM: A Program for Macromolecular Energy, Minimization, and Dynamics Calculations. *J. Comp. Chem.* **4**: 187–217. 24

[Bürgers and Bachau, 1997] Bürgers, A. and Bachau, H. (1997). On the Calculation of C^{4+} (4,4) Doubly Excited States. *J. Phys. B: At. Mol. Opt. Phys.* **30**: 4163. 101

[Bürgers *et al.*, 1998] Bürgers, A., Brandefelt, N., and Lindroth, E. (1998). The Inter-Electronic Angle in Doubly Excited States and the Quality of Approximate Quantum Numbers. In preparation. 101, 102

[Bürgers and Rost, 1996] Bürgers, A. and Rost, J.-M. (1996). Complex Expectation Values and Lewis Structures for Resonant States. *J. Phys. B: At. Mol. Opt. Phys.* **29**: 3825. 101, 102

[Bürgers and Wintgen, 1994] Bürgers, A. and Wintgen, D. (1994). Inhibited Autoionization of Planetary Atom States. *J. Phys. B: At. Mol. Opt. Phys.* **27**: L131. 101, 101

[Bürgers *et al.*, 1995] Bürgers, A., Wintgen, D., and Rost, J.-M. (1995). Highly Doubly Excited S States of the Helium Atom. *J. Phys. B: At. Mol. Opt. Phys.* **28**: 3161. 101, 101

[Caprara and Rosengren, 1997a] Caprara, S. and Rosengren, A. (1997a). Density-Matrix Renormalization Group for Fermions: Convergence to the Infinite-Size Limit. *Nucl. Phys. B* 640–650. 97

[Caprara and Rosengren, 1997b] Caprara, S. and Rosengren, A. (1997b). Ground-State Magnetic Properties of the Kondo Lattice Model at low Electron Densities. *Europhys. Lett.* **39**: 55–60. 97

[Car and Parrinello, 1985a] Car, R. and Parrinello, M. (1985a). *Phys. Rev. Lett* **55**: 2471. 130

[Car and Parrinello, 1985b] Car, R. and Parrinello, M. (1985b). Unified Approach for Molecular Dynamics and Density-Functional Theory. *Phys. Rev. Lett.* **55**: 2471. 136

[Caratzoulas *et al.*, 1997] Caratzoulas, S., Jackson, B., and Persson, M. (1997). *J. Chem. Phys.* **107**: 6420. 89

[Carbone *et al.*, 1997a] Carbone, M., K., L., and Carlsson, J. O. (1997a). Adsorption Geometry of CH_3OH on the Si(100)2 $\times$ 1 Surface: First-Principle Calculations. In manuscript. 165, 165

[Carbone *et al.*, 1997b] Carbone, M., K., L., and Carlsson, J. O. (1997b). Diamond Nucleation on Hexagonal Boron Nitride: A Theoretical Investigation of the Influence of CH_3 and Na Substituents. *J. Phys. Chem.* Submitted. 165, 165, 166

[Carbone *et al.*, 1997c] Carbone, M., K., L., and Carlsson, J. O. (1997c). Diamond Nucleation on Hexagonal Boron Nitride: A Theoretical Investigation of the Influence of Nearest Substituents. *J. Phys. Chem.* **101**: 9445. 165, 165, 166

[Caughey, 1988] Caughey, D. A. (1988). Diagonal Implicit Multigrid Algorithm for the Euler Equations. *AIAA Journal* **26**: 841–851. 42

[Cervinka, 1985] Cervinka, L. (1985). *J. Non-Cryst. Solids* **75**: 69. 81

[Cervinka, 1987] Cervinka, L. (1987). *J. Non-Cryst. Solids* **90**: 371. 81

[Chandrasekhar, 1992] Chandrasekhar, S. (1992). *Liquid Crystals.* Cambridge: Cambridge University Press. 172

[Crawford *et al.*, 1991] Crawford, J. F., Daum, M., Frosch, R., Jost, B., Kettle, P.-R., Marshall, R. M., Wright, B. K., and Ziock, K. O. H. (1991). Precision Measurement of the Pion Mass Difference $m_{\pi^-} - m_{\pi^0}$. *Phys. Rev. D* **43**: 46–58. 61, 62

[Draine, 1988] Draine, B. T. (1988). The Discrete-Dipole Approximation and its Applications to Interstellar Graphite Grains. *Astr. J.* **333**: 848–872. 90

[Draine and Flatau, 1994] Draine, B. T. and Flatau, P. J. (1994). Discrete-Dipole Approximation for Scattering Calculations. *JOSA* **11**: 1491–1499. 90

[Dwek, 1996] Dwek, R. A. (1996). *Chem. Rev.* 683–720. 32

[Dzugutov, 1992] Dzugutov, M. (1992). *Phys. Rev.* **A46**: R2984. 82, 82, 83, 86

[Dzugutov, 1993] Dzugutov, M. (1993). *Phys. Rev. Lett.* **70**: 2924. 82, 83, 86

[Dzugutov, 1994] Dzugutov, M. (1994). *Europhys. Lett.* **26**: 533. 82, 82, 82

[Dzugutov, 1995] Dzugutov, M. (1995). Phason Dynamics and Atomic Transport in an Equilibrium Dodecagonal Quasi-crystal. *Europhys. Lett.* **31**: 95–100. 86

[Ele, 1994] Electricite de France, Direction des Etudes et Recherche. (1994). *First Workshop on Aerodynamics of Steady State Combustion Chambers and Furnaces: Final Result*, Chatou, France, 1994. 51

[Elliott, 1990] Elliott, S. R. (1990). *Physics of Amorphous Materials.* London: Longman, 2nd edition. 81

[Elliott, 1991] Elliott, S. R. (1991). *Nature* **354**: 445. 80

[Elliott, 1992] Elliott, S. R. (1992). *J. Phys. Condens. Matter* **4**: 7661. 80, 80

[Engström and Rigdahl, 1992] Engström, G. and Rigdahl, M. (1992). Kompendium i bestrykningsteknik. Technical report, STFi, Stockholm. 92, 92

[Ericsson and Ruhe, 1980] Ericsson, T. and Ruhe, A. (1980). The Spectral Transformation Lanczos Method for the Numerical Solution of Large Sparse Generalized Symmetric Eigenvalue Problems. *Math. Comp.* **35**: 1251. 100

[Eriksson, 1997] Eriksson, L. A. (1997). Evaluation of the Performance of Non-Local Density Functional Theory for pi-Radical Hyperfine Structures. *Mol. Phys.* **91**: 827. 77

[Eriksson, 199X] Eriksson, L. A. (199X). The Sulfinylimine Radical in Azido-CDP and Azido-UDP Inhibited Ribonucleotide Reductase. Submitted. 77, 77

[Eriksson and Himo, 1997] Eriksson, L. A. and Himo, F. (1997). Radicals in Biophysical Systems — A Theoretical Perspective. *Trends in Physical Chemistry* **6**: 153. 77, 77

[Eriksson *et al.*, 1997] Eriksson, L. A., Himo, F., Siegbahn, P. E. M., and Babcock, G. T. (1997). Electronic and Magnetic Properties of Neutral and Charged Model Quinone and Plastoquinone Radicals. *J. Phys. Chem.* **101**: 9811. 77

[Eriksson, 1996] Eriksson, L.-E. (1996). A Preconditioned Navier-Stokes Solver for Low Mach Number Flows. In: *Computational Fluid Dynamics '96*, 1996. 51

[Evans and Morriss, 1990] Evans, D. J. and Morriss, G. P. (1990). *Statistical Mechanics of Nonequilibrium Liquids.* London: Academic Press. 173

[Fängström *et al.*, 1998a] Fängström, T., Edvardsson, D., Ericsson, M., Lunell, S., and Enkvist, C. (1998a). Density Functional Study of Chlorine-Oxygen Compounds Related to the ClO Self-Reaction. *Int. J. Quant. Chem.* **66**: 203. 144, 144

[Fängström *et al.*, 1998b] Fängström, T., Kirrander, A., Eriksson, L. A., and Lunell, S. (1998b). The Reaction Between Aluminium and Dimethyl Ether. Comparative Study of Density Functional Theory and EPR Results. *J. Chem. Soc., Faraday Trans.* **94**: 000. 144, 144

[Fängström *et al.*, 1998c] Fängström, T., Lunell, S., Kasai, P. H., and Eriksson, L. A. (1998c). Theoretical Study of the Insertion Reactions of Aluminium with H_2O, NH_3, HCl and Cl_2. *J. Phys. Chem.* **102**: 1005. 144

[Feagin and Briggs, 1986] Feagin, J. M. and Briggs, J. S. (1986). Molecular Description of Two-Electron Atoms. *Phys. Rev. Lett.* **57**: 984. 98

[Forsmoo and Borgefors, 1997] Forsmoo, A. and Borgefors, G. (1997). Parallel Distance Transform Algorithms on a General SIMD Computer. In: *The 10th Scandinavian Conference on Image Analysis, Lappeenranta, Finland, June 9-11*, volume 1, 1997, p. 471–478. 185, 185

[Froelich and Flores, 1993] Froelich, P. and Flores, A. (1993). Effects of Intramolecular Dynamics on Nuclear Fusion Rates and Sticking of the Molecular Ion $dt\mu$. *Phys. Rev. Lett.* **70**: 1595–1598. 62, 62

[Froelich and Wallenius, 1995] Froelich, P. and Wallenius, J. (1995). Resonance Side-Path in Muon Catalyzed Fusion. *Phys. Rev. Lett.* **75**: 2108–2111. 62, 62

[Gacherieu, 1996] Gacherieu, C. (1996). *Etude d'un modèl de turbulence algébrique 3D: Application au calcul Navier-Stokes de l'écoulement autour d'une installation motrice d'avion de transport.* Phd thesis no. 1248, Institut National Polytechnique de Toulouse. 43

[Gay and Berne, 1981] Gay, J. G. and Berne, B. J. (1981). Modification of the Overlap Potential to Mimic a Linear Site-Site Potential. *J. Chem. Phys.* **74**: 3316. 172

[Götze and Sjögren, 1992] Götze, W. and Sjögren, L. (1992). *Rep. Progr. Phys.* **55**: 241. 82

[Grönbeck and Andreoni, 1997] Grönbeck, H. and Andreoni, W. (1997). A Theoretical Study of CO_n Chemisorption on Pt and Pt_3: Electronic and Vibrational Properties. *Chem. Phys. Lett.* **269**: 385. 138

[Grönbeck *et al.*, 1997] Grönbeck, H., Rosén, A., and Andreoni, W. (1997). Theoretical Study of Chemisorption on Niobium Clusters: Carbon Monoxide and Oxygen. *Z. Phys. D* **40**: 206. 136

[Hafner, 1987] Hafner, J. (1987). *From Hamiltonians to Phase Diagrams.* Berlin: Springer-Verlag. 82, 82

[Hammer and Nielsen, 1995] Hammer, B. and Nielsen, O. H. (1995). In: *Proceedings from Workshop on Applied Parallel Computing in Physics, Chemistry and Engineering Science (PARA95)*, edited by J. Wasniewski, Lecture in Computer Science. Springer. 87

[Helgaker *et al.*, 1997] Helgaker, T., Jensen, H. J. A., Jørgensen, P., Olsen, J., Ruud, K., Ågren, H., Andersen, T., Bak, K. L., Bakken, V., Christiansen, O., Dahle, P., Dalskov, E. K., Enevoldsen, T., Heiberg, H., Hettema, H., Jonsson, D., Kirpekar, S., Kobayashi, R., Koch, H., Mikkelsen, K. V., Norman, P., Packer, M. J., Saue, T., Taylor, P. R., and Vahtras, O., (1997). DALTON, an Ab Initio Electronic Structure Program, Release 1.0. See: http://www.kjemi.uio.no/software/dalton/dalton.html. 65

[Herrick, 1983] Herrick, D. R. (1983). New Symmetry Properties of Atoms and Molecules. *Adv. Chem. Phys.* **52**: 1. 98

[Himo *et al.*, 199X] Himo, F., Babcock, G., and Eriksson, L. A. (199X). Conformational Analysis of Quinone Radical Anions in Photosystem II and Photosynthetic Bacteria. *J. Phys. Chem.* To be submitted. 77

[Himo and Eriksson, 1998] Himo, F. and Eriksson, L. A. (1998). On the Local Structure of Glycyl Radicals in Different Enzymes. *J. Chem. Soc. Perkin Trans.* **2**: 305. 77, 77

[Himo and Eriksson, 199X] Himo, F. and Eriksson, L. A. (199X). Reaction Mechanism of the Radical Controlled Catalysis in Anaerobic Escherichia Coli Pyruvate Formate Lyase. *J. Am. Chem. Soc.* To be submitted. 77, 77

[Hoge *et al.*, 1988] Hoge, D., Tüshaus, M., Schweitzer, E., and Bradshaw, A. M. (1988). The Metal-Carbon Stretch in the Vibrational Spectrum of CO Adsorbed on Pt(111). *Chem. Phys. Lett.* **151**: 230. 138

[Hohenberg and Kohn, 1964] Hohenberg, P. and Kohn, W. (1964). Inhomogenous Electrons Gas. *Phys. Rev* **136**: 864. 136

[Holliger, 1997] Holliger, K. (1997). Upper-Crustal Velocity Heterogeneities as Derived from A Variety of P-Wave Sonic Logs. *Geophys. J. Int.* **125**: 813–829. 102

[Holmén and Broo, 1995] Holmén, A. and Broo, A. (1995). A Theoretical Investigation of the Solution N(7)H↔N(9)H Tautomerism of Adenine. *Int. J. Quant. Chem.* **22**: 113. 166

[Hu *et al.*, 199X] Hu, C.-H., Brinck, T., and Hult, K. (199X). Ab Initio and Density Functional Theory Studies of the Catalytic Mechanism for Ester Hydrolysis in Serine Hydrolases. *Int. J. of Quant. Chem.* In press. 21

[Hultén *et al.*, 1997] Hultén, J., Bonham, N. M., Nillroth, U., Hansson, T., Zuccarello, G., Bouzide, A., Åqvist, J., Classon, B., Danielsson, U. H., Karlén, A., Kvarnström, I., Samuelsson, B., and Hallberg, A. (1997). Cyclic HIV-1 Protease Inhibitors Derived from Mannitol: Synthesis, Inhibitory Potencies, and Computational Predictions of Binding Affinities. *J. Med. Chem.* **40**: 885. 29

[Icking-Konert *et al.*, 1996] Icking-Konert, G. S., Handschuh, H., Ganteför, G., and Eberhardt, W. (1996). Bonding of CO to Metal Particles: Photoelectron Spectra of $Ni_n(CO)_m^-$ and $Pt_n(CO)_m^-$ Clusters. *Phys. Rev. Lett.* **76**: 1047. 138, 138

[Jameson, 1985] Jameson, A. (1985). Numerical Solution of the Euler Equations for Compressible Inviscid Fluids. In: *Numerical Methods for the Euler Equations of Fluid Dynamics*, edited by F. A. *et al.* SIAM, Philadelphia, 1985. 42

[Jonsson *et al.*, 1996] Jonsson, D., Norman, P., and Ågren, H. (1996). Cubic Response Functions in the Multi-Configuration Self-Consistent Field Approximation. *J. Chem. Phys.* **105**: 6401. 67

[Jonsson *et al.*, 1997] Jonsson, D., Norman, P., Ruud, K., Ågren, H., and Helgaker, T. (1997). The Electric and Magnetic Properties of Fullerenes. *J. Chem. Phys.* Submitted. 69

[Jorgensen *et al.*, 1983] Jorgensen, W., Chandrasekhar, J., Madura, J., Impey, R., and Klein, M. (1983). Comparison of Simple Potential Functions for Simulating Liquid Water. *J. Chem. Phys.* **79**: 926–935. 141

[Juhlin, 1995] Juhlin, C. (1995). Finite-Difference Elastic Wave Propagation. *Geophys. Prospecting* **43**: 843–858. 103

[Juozapavičius *et al.*, 1997] Juozapavičius, A., Caprara, S., and Rosengren, A. (1997). Quantum Ising Model in a Transverse Random Magnetic Field: A Density-Matrix Renormalization-Group Analysis. *Phys. Rev. B* **56**: 11097–11101. 97

[Kamimura, 1988] Kamimura, M. (1988). Nonadiabatic Coupled-Rearrangement-Channel Approach to Mouonic Molecules. *Phys. Rev. A* **38**: 621–624. 62

[Klopfer and Yoon, 1993] Klopfer, G. H. and Yoon, S. (1993). Multizonal Navier-Stokes Code with the LU-SGS Scheme. Technical Report AIAA paper 93-2965, AIAA. 42

[Kohn and Sham, 1965] Kohn, W. and Sham, L. J. (1965). Self-Consistent Equations Including Exchange and Correlation Effects. *Phys. Rev.* **140**: A1133. 136

[Kowalewski *et al.*, 1985] Kowalewski, J., Nordenskiöld, L., Benetis, N., and Westlund, P.-O. (1985). Theory of Nuclear Spin Relaxation in Paramagnetic Systems in Solution. *Prog. NMR Spectrosc.* **17**: 141. 57

[Kubelka, 1948] Kubelka, P. (1948). New Contributions to the Optics of Intensely Light-Scattering Materials. Part I. *JOSA* 448–457. 90

[Kubelka and Munk, 1931] Kubelka, P. and Munk, F. (1931). Ein Beitrag zur Optik der Farbanstriche. *Zeitschr. F. Techn. Physik* 593–601. 90

[Lam *et al.*, 1994] Lam, P. Y. S., Jadhav, P. K., Eyermann, C. J., Hodge, C. N., Ru, Y., Bacheler, L. T., Meek, J. L., Otto, M. J., Rayner, M. M., Wong, Y. N., Chang, C.-H., Weber, P. C., Jackson, D. A., Sharpe, T. R., and Erickson-Viitanen, S. (1994). Rational Design of Potent, Bioavailable, Nonpeptide Cyclic Ureas as HIV Protease Inhibitors. *Science* **263**: 380. 29

[Larsson, 1997a] Larsson, K. (1997a). Adsorption of Hydrocarbon Species on a Stepped Diamond (111) Surface. *Phys. Rev. B* Accepted. 164, 166

[Larsson, 1997b] Larsson, K. (1997b). Electron Transfer during Adsorption Processes on Diamond (111). To be submitted. 165, 166

[Larsson and Carlsson., 1997] Larsson, K. and Carlsson., J. O. (1997). Surface Migration During Diamond Growth. *Phys. Rev. B* Submitted. 165, 166

[Larsson *et al.*, 1994] Larsson, T., Westlund, P.-O., Kowalewski, J., and Koenig, S. H. (1994). Nuclear Spin Relaxation in Paramagnetic Complexes in the Slow-Motion Regime for the Electron Spin: The anisotropic Pseudorotation model for $S = 1$ and the Interpretation of Nuclear Magnetic Relaxation Dispersion Results for a Low-Symmetry Ni(II) Complex. *J. Chem. Phys* **101**: 1116. 57

[Lassmann *et al.*, 199X] Lassmann, G., Lendzian, F., Himo, F., Eriksson, L. A., and Lubitz, W. (199X). Structure and

Properties of Transient Histidine Radicals Formed by Oxidation in Aqueous Solution as Studied by EPR Spectroscopy and Density Functional Theory. To be submitted. 77, 77

[Levander, 1988] Levander, A. R. (1988). Fourth-Order Finite-Difference P-SV Seismograms. *Geophysics* **53**: 1425–1436. 103

[Leyland *et al.*, 1995] Leyland, P., Vos, J. B., Kemenade, V. V., and Ytterström, A. (1995). NSMB: A Modular Navier-Stokes Multiblock Code for CFD. Technical Report AIAA 95-0568, AIAA. 42, 42

[Lidmar *et al.*, 1997] Lidmar, J., Wallin, M., Wengel, C., Girvin, S. M., and Young, A. P. (1997). *Phys. Rev. B* Submitted. 79

[Liljenstam and Ayani, 1996] Liljenstam, M. and Ayani, R. (1996). A Model for Parallel Simulation of Mobile Telecommunication Systems. In: *Proceedings of the International Workshop on Modeling, Analysis and Simulation of Computer and Telecommunication Systems*, San José, CA. 183

[Liljenstam and Ayani, 1997] Liljenstam, M. and Ayani, R. (1997). MobSim++, An Environment for Parallel Simulation of PCNs. In: *Proceedings of the World Congress on Systems Simulation (WCSS'97) (2nd Joint Conference of International Simulation Societies)*, Singapore. 183

[Lin and Gomer, 1991] Lin, T. S. and Gomer, R. (1991). *Surf. Sci.* **41**: 255. 88

[Loncharich and Brooks, 1989] Loncharich, R. J. and Brooks, B. R. (1989). The Effects of Truncating Long-Range Forces on Protein Dynamics. *Proteins* **6**: 32–45. 24

[Lu. *et al.*, 1993] Lu., Y., Lacroix, L. B., Lowery, M. D., Solomon, E. I., Bender, C. J., Peisach, J., Roe, J. A., Gralla, E. B., and Valentine, J. S. (1993). *J. Am. Chem. Soc.* **115**: 5907. 176

[Luo *et al.*, 1997] Luo, Y., Norman, P., Ruud, K., and Ågren, H. (1997). Molecular Length Dependence of Optical Properties of Hydrocarbon Oligomers. *Chem. Phys. Letters* Accepted. 69

[Lyubartsev and Laaksonen, 1995] Lyubartsev, A. P. and Laaksonen, A. (1995). Calculation of Effective Interaction Potentials from Radial Distribution Functions: A Reverse Monte Carlo Approach. *Phys. Rev. E.* **52**: 3730. 150

[Lyubartsev and Laaksonen, 1997] Lyubartsev, A. P. and Laaksonen, A. (1997). "M.DynaMix", A Scalable, Parallel General Purpose MD Simulation Program for Arbitrary Molecular Mixtures. Technical report, Stockholm University. 20

[MacKerell *et al.*, 1995] MacKerell, A. D., Wiorkiewicz-Kuczera, J., and Karplus, M. (1995). An All-Atom Empirical Energy Function for the Simulation of Nucleic Acids. *J. Am. Chem. Soc.* **117**: 11946. 147, 149

[Magnussen, 1989] Magnussen, B. F. (1989). The Eddy Dissipation Concept. In: *Task Leaders Meeting*, Lund, Sweden. 51

[Mattila *et al.*, 1996] Mattila, T., Nieminen, R., and Dzugutov, M. (1996). *Phys. Rev. B* **53**: 192. 86

[Mattsson *et al.*, 1995] Mattsson, T. R., Engberg, U., and Wahnström, G. (1995). *Phys. Rev. B* **51**: 1885. 88

[Mattsson and Wahnström, 1997a] Mattsson, T. R. and Wahnström, G. (1997a). In: *Surface Diffusion: Atomistic and Collective Processes*, edited by M. Tringides. New York: NATO-ASI, Plenum. 88

[Mattsson and Wahnström, 1997b] Mattsson, T. R. and Wahnström, G. (1997b). *Phys. Rev. B* 56. 88

[Mattsson *et al.*, 1997] Mattsson, T. R., Wahnström, G., Bengtsson, L., and Hammer, B. (1997). *Phys. Rev. B* **56**: 2258. 87

[Mer *et al.*, 1996] Mer, G., Hietter, H., and Lefevre, J.-F. (1996). *Nature Struc. Biol.* **3**: 45–53. 32

[Moss and Price, 1985] Moss, S. and Price, D. L. (1985). In: *Physics of Disordered Materials*, edited by D. Adler, H. Fritzsche, and S. R. Ovshinsky. New York: Plenum, p. 77. 80, 80

[Nersissian *et al.*, 1996] Nersissian, A. M., Mehrabian, Z. B., Nalbandyan, R. M., Hart, P. J., Fraczkiewicz, G., Crernuszewicz, R. S., Bender, C. J., Peisach, J., Hermann, R. G., and Valentine, J. S. (1996). *Protein Sci.* **5**: 2184. 176, 177

[Neyertz and Brown, 1995] Neyertz, S. and Brown, D. (1995). A Computer Simulation Study of the Chain Configurations in Poly(ethylene oxide)-Homologue Melts. *J. Chem. Phys.* **102**: 9725–9735. 125

[Neyertz *et al.*, 1994] Neyertz, S., Brown, D., and Thomas, J. O. (1994). Molecular Dynamics Simulation of Crystalline Poly(ethylene oxide). *J. Chem. Phys.* **101**: 10064–10073. 125

[Nishida *et al.*, 1984] Nishida, Y., Ohuri, H., and Meguro, H. (1984). *Tetrahedron Lett.* **25**: 1575–1578. 35

[Norberg and Nilsson, 1995a] Norberg, J. and Nilsson, L. (1995a). Potential of Mean Force Calculations of the Stacking-Unstacking Process in Single-Stranded Deoxyribodinucleoside Monophosphates. *Biophys. J.* **69**: 2277–2285. 156

[Norberg and Nilsson, 1995b] Norberg, J. and Nilsson, L. (1995b). Stacking Free Energy Profiles for all 16 Natural Ribonucleoside Monophosphates in Aqueous Solution. *J. Am. Chem. Soc.* **117**: 10832–10840. 156, 156

[Norberg and Nilsson, 1998] Norberg, J. and Nilsson, L. (1998). Solvent Influence on Base Stacking. *Biophys. J.* **71**: 294–304. 153, 153

[Norman *et al.*, 1996a] Norman, P., Jonsson, D., Ågren, H., Dahle, P., Ruud, K., Helgaker, T., and Koch, H. (1996a). Efficient Parallel Implementation of Response Theory: Calculation of the Second Hyperpolarizability of the Polyacenes. *Chem. Phys. Lett.* **253**: 1. 67

[Norman *et al.*, 1996b] Norman, P., Jonsson, D., Vahtras, O., and Ågren, H. (1996b). Nonlinear Electric and Magnetic Properties Obtained from Cubic Response Functions in the Random Phase Approximation. *Chem. Phys.* **203**: 23. 67

[Norman *et al.*, 1997] Norman, P., Luo, Y., Jonsson, D., and Ågren, H. (1997). Ab Initio Calculations of the Polarizability and Hyperpolarizability of C_{60}. *J. Chem. Phys.* **106**: 8788. 69

[Norrby *et al.*, 1998] Norrby, P.-O., Brandt, P., and Rein, T. (1998). A New Method for Transition State Modelling and its Application to Asymmetric Horner-Wadsworth-Emmons Reactions. Submitted. 172

[Norrby and Liljefors, 1998] Norrby, P.-O. and Liljefors, T. (1998). Automated Molecular Mechanics Parameterization with Simultaneous Utilization of Experimental and Quantum Chemical Data. *J. Comput. Chem.* In press. 31

[Odelius *et al.*, 1997] Odelius, M., Bernasconi, M., and Parrinello, M. (1997). *Phys. Rev. Lett.* **78**: 2855. 130

[Odelius *et al.*, 199X] Odelius, M., Bernasconi, M., and Parrinello, M. (199X). A First Principles Study of the Structure of $2M_1$-Muscovite. To be published. 130

[Olsson *et al.*, 1998] Olsson, M. H. M., Ryde, U., Roos, B. O., and Pierloot, K. (1998). *J. Biol. Inorg. Chem.* In press. 176

[Paulsson and Ehrenberg, 1998] Paulsson, J. and Ehrenberg, M. (1998). Segregational Stability and Metabolic Burden of Plasmid ColE1 – a Mathematical Model. Submitted. 26, 26

[Paulsson *et al.*, 1998] Paulsson, J., Nordström, K., and Ehrenberg, M. (1998). Requirements for Rapid Plasmid ColE1 Copy Number Adjustments – a Mathematical Model of Inhibition Modes and RNA Turnover Rates. *Plasmid* In press. 25

[Payne *et al.*, 1992] Payne, M. C., Teter, M. P., Allan, D. C., Arias, T. A., and Joannopoulos, J. D. (1992). *Rev. Mod. Phys.* **64**: 1045. 87

[Pazsit and Chakarova, 199X] Pazsit, I. and Chakarova, R. (199X). Fluctuations in Atomic Collision Cascades with Power Law Scattering. *Transport Theory and Statistical Physics* In press. 70

[Quinteros and Bjuggren, 1998] Quinteros, T. and Bjuggren, M. (1998). The Discrete-Dipole Approximation Used to Model the Optical Behavior of Clusters of Pigments in Paper Coatings. In:

3rd. Workshop on Electromagnetic and Light Scattering - Theory and Applications, Bremen, Germany. To be published. 91

[Rettner and Auerbach, 1995] Rettner, C. T. and Auerbach, D. J. (1995). *Phys. Rev. Lett.* **74**: 4551. 89

[Rosenfeld and Pfaltz, 1968] Rosenfeld, A. and Pfaltz, J. (1968). Distance Functions on Digital Pictures. *Pattern Recognition* **1**: 33–61. 185

[Rost and Briggs, 1991] Rost, J.-M. and Briggs, J. S. (1991). Saddle Structure of the Three-Body Coulomb Problem; Symmetries of Doubly-Excited States and Propensity Rules for Transitions. *J. Phys. B: At. Mol. Opt. Phys.* **24**: 4293. 101

[Ryde *et al.*, 1996] Ryde, U., Olsson, M. H., Pierloot, K., and Roos, B. O. (1996). *J. Mol. Biol.* **261**: 586. 174

[Sangster and Atwood, 1978] Sangster, M. and Atwood, R. (1978). Interionic Potentials for Alkali Halides: II Completely Crystal Independent Specification of Born-Mayer Potentials. *J. Phys. C: Solid State Phys.* **11**: 1541–1555. 141

[Sarman, 1995] Sarman, S. (1995). Molecular Dynamics of Biaxial Nematic Liquid Cxrystals. *J. Chem. Phys.* **104**: 342. 173

[Schuster, 1905] Schuster, A. (1905). Radiation through a Foggy Atmosphere. *Astroph. J.* **21**: 1–22. 90

[Schütz and Lindh, 1997] Schütz, M. and Lindh, R. (1997). An Integral Direct, Distributed-Data, Parallel MP2 Algorithm. *Theor. Chim. Acta* **95**: 13. 133

[Shiotani *et al.*, 1998] Shiotani, M., Isamoto, N., Hayashi, M., Fängström, T., and Lunell, S. (1998). Deuterium Isotope Effects on Rotation of Methyl Hydrogens – A Study of the Dimethylether Radical Cation by ESR Spectroscopy and Ab Initio and Density Functional Theory. 144

[Siegbahn *et al.*, 1998] Siegbahn, P. E. M., Westerberg, J., Svensson, M., and Crabtree, R. H. (1998). Nitrogen Fixation by Nitrogenases: A Quantum Chemical Study. *J. Phys. Chem. B* 102. 143

[Stenutz and Widmalm, 1998] Stenutz, R. and Widmalm, G. (1998). *Glucoconjugate J.* In press. 33

[Stillinger and Weber, 1984] Stillinger, F. H. and Weber, T. A. (1984). *Science* **225**: 983. 83

[Strömquist *et al.*, 199X] Strömquist, J., Bengtsson, L., Persson, M., and Hammer, B. (199X). *Surf. Sci.* Accepted. 88

[Svensson *et al.*, 1997] Svensson, M., Stromberg, S., and Zetterberg, K. (1997). The Binding of Ethylene to Anionic, Neutral and Cationic Ni(II), Pd(II) and Pt(II) Cis/Trans Cloro-Ammonia Complexes. A Theoretical Study. *J. Am. Chem. Soc.* **16**: 3165–3168. 143

[Szabó, 1996] Szabó, K. J. (1996). Effects of β-Substituents and Ancillary Ligands on the Structure and Stability of (η^3-Allyl)palladium Complexes. Implications for the Regioselectivity in Nucleophilic Addition Reactions. *J. Am. Chem. Soc.* **118**: 7818. 123, 123

[Szabó, 1997] Szabó, K. J. (1997). Nature of the Interactions between Polar β-Substituents and Palladium in (η^3-Allyl)palladium Complexes. A Combined Experimental and Theoretical Study. *Chem. Eur. J.* **3**: 592. 123, 123, 124

[Szabó *et al.*, 1997] Szabó, K. J., Hupe, E., and Larsson, A. L. E. (1997). Stereoelectronic Control on the Linetic Stability of β-Acetoxy Substituted (η^3-Allyl)palladium Complexes in Mild Acidic Medium. *Organometallics* **16**: 3779. 123, 123, 124

[Taflove, 1995] Taflove, A. (1995). *Computational Electrodynamics: The Finite-Difference Time-Domain Method.* Artech House. 55

[Tasaki *et al.*, 1993] Tasaki, K., Mcdonald, S., and Brady, J. W. (1993). Concerning the Treatment of Long-Range Interactions in Molecular Dynamics Simulations. *J. Comp. Chem.* **14**: 278–284. 24

[Thomann *et al.*, 1991] Thomann, H., Bernardo, M., Baldwin, M. J., Lowery, M. D., and Solomon, E. I. (1991). *J. Am. Chem. Soc.* 113. 176

[Ulvenlund *et al.*, 1997] Ulvenlund, S., Rosdahl, J., Fischer, A., Schwerdtfeger, P., and Kloo, L. (1997). Hard Acid and

Soft Base Stabilisation of Di- and Trimercury Cations in Benzene Solution. A Spectroscopic, X-ray Scattering and Quantum Chemical Study. *Eur. J. Inorg. Chem.* Submitted. 163

[Ulvenlund *et al.*, 1995] Ulvenlund, S., Wheatley, A., and Bengtsson, L. A. (1995). Arene Solutions of Gallium Chloride - Part 1 & 2. *J. Chem. Soc., Dalton Trans.* **245**: 255. 161

[Vos *et al.*, 1997] Vos, J. B., Leyland, P., Lindberg, P. A., Kemenade, V. v., Gacherieu, C., Duquesne, N., Lötstedt, P., Weber, C., and Ytterström, A. (1997). *NSMB Handbook Version 4.0*, deliverable RD 21 parallel aero project edition, February 1997. 42, 42

[Wallenius and Froelich, 1995] Wallenius, J. and Froelich, P. (1995). Muon Transfer via Meta-Stable $dt\mu^*$ Molecules and the Kinetics of μCF. *Phys. Lett.* **A206**: 73–80. 62

[Wallenius and Froelich, 1996] Wallenius, J. and Froelich, P. (1996). Formation of Meta-Stable $dt\mu^*$ Molecules in $t\mu(2s) + D_2$ Collisions. *Phys. Rev. A* **54**: 1171–1182. 62, 62

[Weber, 1996] Weber, C. (1996). Implementation of the Lower-Upper Symmetric Gauss-Seidel (LU-SGS) Implicit Method into the Navier-Stokes Multiblock Flow Solver NSMB. Technical Report TR/CFD/96/43, CERFACS, Toulouse. 42

[Weiner *et al.*, 1986] Weiner, S. J., Kollman, P. A., Ngyuen, D. T., and Case, D. A. (1986). An All Atom Force Field for Simulations of Proteins and Nucleic Acids. *J. Comput. Chem.* **7**: 230. 147

[Wetmore *et al.*, 199Xa] Wetmore, S. D., Boyd, R. J., and Eriksson, L. A. (199Xa). Radiation Products of Thymine, 1-Methyl Thymine and Uracil Studied by Density Functional Theory. *J. Phys. Chem.* Submitted. 78

[Wetmore *et al.*, 199Xb] Wetmore, S. D., Himo, F., Boyd, R. J., and Eriksson, L. A. (199Xb). Effects of Ionizing Radiation on Crystalline Cytosine Monohydrate; The Importance of OH Radicals. *J. Phys. Chem.* Submitted. 78

[Whetten *et al.*, 1996] Whetten, R., Khoury, J., Alvarez, M., Murthy, S., Vezmar, I., Wang, Z., Stephens, P., Cleveland, C., Luedtke, W., and Landman, U. (1996). Nanocrystal Gold Molecules. *Adv. Mat.* **8**: 428. 138

[Wriedt, 1998] Wriedt, T. (1998). A Review of Elastic Light Scattering Theories. *Part. Part. Syst. Charact.* **15**: 2. 90

[Yoon and Jameson, 1986] Yoon, S. and Jameson, A. (1986). A Multigrid LU-SSOR Scheme for Approximate Newton Iteration Applied to the Euler Equations. Technical Report NASA-CR-179524, NASA. 42

[Ytterström, 1997] Ytterström, A. (1997). A Tool For Partitioning Structured Multiblock Meshes For Parallel Computational Mechanics. *The International Journal of Supercomputer Applications and High Performance Computing* **11**: 336–343. 43

[Zhu *et al.*, 1992] Zhu, X., Lee, A., Wong, A., and Linke, U. (1992). *Phys. Rev. Lett.* **68**: 1862. 88

Index